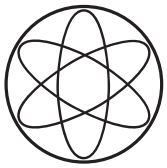

Search for Supersymmetry in Multi-Leptonic Final States with the ATLAS Detector at the LHC and Construction of New Precision Muon Tracking Detectors for the High-Luminosity LHC Upgrade

MARIAN BENEDIKT RENDEL

Dissertation

München 2023

TECHNISCHE UNIVERSITÄT MÜNCHEN
Fakultät für Physik

Max-Planck-Institut für Physik
(Werner-Heisenberg-Institut)

Search for Supersymmetry in Multi-Leptonic Final States with the ATLAS Detector at the LHC and Construction of New Precision Muon Tracking Detectors for the High-Luminosity LHC Upgrade

Marian Benedikt Rendel

Vollständiger Abdruck der von der Fakultät für Physik der Technischen Universität München zur Erlangung des akademischen Grades eines

Doktors der Naturwissenschaften (Dr. rer. nat.)

genehmigten Dissertation.

Vorsitzender:

Prüfer der Dissertation:

1.

2.

Die Dissertation wurde am bei der Technischen Universität München eingereicht und durch die Fakultät für Physik am angenommen.

Search for Supersymmetry in Multi-Leptonic Final States with the ATLAS Detector at the LHC and Construction of New Precision Muon Tracking Detectors for the High-Luminosity LHC Upgrade

Marian Benedikt Rendel

Abstract

Supersymmetry (SUSY) is one of the best-studied extensions of the Standard Model (SM) of particle physics answering several open questions of the SM. SUSY postulates a superpartner differing in spin by one half for each of the Standard Model particles.

This thesis presents two searches for Supersymmetry using 139 fb^{-1} of proton-proton collision data recorded by the ATLAS experiment at the Large Hadron Collider (LHC) at $\sqrt{s}$ = 13 TeV. The first search focuses on final states with at least four charged leptons. Due to the low SM background, four-lepton final states promises good sensitivity to several supersymmetric models. The first type of models assumes R-parity violation via lepton number violating interactions, which allows the lightest supersymmetric particle (LSP) to decay into two charged leptons and a neutrino. The second type of SUSY models assumes gauge mediated SUSY breaking. In this models pair produced higgsinos decay into a gravitino LSP and a Z or Higgs boson. No significant deviations from the SM predictions have been observed. Exclusion limits on the masses of the SUSY particles and the branching ratios of the higgsino decaying into Z bosons have been set. The second search presented in this thesis targets the supersymmetric partners of the electron and muon. Especially light smuons are of particular interest, because such SUSY scenarios are capable of providing an explanation for the observed deviation of the measured value of the anomalous of the anomalous magnetic moment of the muon to the SM prediction. The search concentrates on a region of the parameter space with differences in mass of the slepton and the LSP between 20 and 60 GeV, which is not covered by previous searches.

The LHC will be upgraded to the High Luminosity LHC, increasing the instanteneous luminosity by a factor of 7, in order to collect much more data to increase the sensitivity for physics beyond the SM. A major upgrade of the ATLAS detector is required to cope with the increased data rate. This thesis presents the construction of new small-diameter Monitored Drift Tube (sMDT) chambers that together with integrated resistive plate chambers (RPC) will replace the existing Monitored Drift Tube (MDT) chambers in the small sectors of the inner layer of the central detector region of the ATLAS muon spectrometer. Several measurements of the chamber geometry are performed during the production of each chamber, since precise knowledge of positions of sense wires of a sMDT chamber is crucial to achieve the target 10% momentum resolution for muons at $p_{\text{T}} \approx 1$ TeV.

Table of Contents

CHAPTER ONE

INTRODUCTION

The Standard Model (SM) of particle physics describes the known elementary particles and their interactions. With the discovery of the Higgs boson in 2012 with the ATLAS and CMS experiments at the Large Hadron Collider (LHC) [1, 2], the last missing particle of the SM was found. So far the SM was successfully in numerous precision experiments and no significant deviation from its predictions have been found.

Despite its success, there are many open questions, that the SM cannot answer, such as it can't provide a valid cold dark matter candidate, the observed asymmetry between matter and antimatter in the universe and the hierarchy problem.

Supersymmetry (SUSY) is one of the best-studied extensions of the SM. It postulates a symmetry between bosons and fermions, which in its simplest realization yields a new superpartner for every SM particle, with spin differing by $\frac{1}{2}$. Typically SUSY models assume a new conserved quantity, R-parity, which prohibits baryon and lepton violating interaction and therefore, prohibits proton decay and lead to a stable lightest supersymmetric particle (LSP), which is an ideal dark matter candidate if it is electrically neutral. However, the proton decay can already be avoided if either baryon or lepton number is conserved. It is therefore important to search for R-parity violating (RPV) SUSY as well, which leads generally to totally different phenomenologies at collider experiments.

This thesis discusses two search for SUSY using pp collisions at $\sqrt{s} = 13$ TeV recorded by the ATLAS experiment in 2015-2018, corresponding to an integrated luminosity of 139 fb^{-1}. The first search focuses on events with final states with at least four charged leptons. Due to the low SM background rates, final states with four leptons are an excellent channel for the search for SUSY. One type of SUSY scenarios studied by this search considers R-parity violation via lepton number violating interactions, which leads to the LSP decaying into a pair of charged leptons and a neutrino. With the next to lightest supersymmetric particle (NLSP) produced in pairs in the pp collisions decaying into the LSP, this leads to final states with four charged leptons. The four-lepton final state provides also sensitivity to R-parity conserving SUSY. The search considers the pair production of higgsinos which decay into a

Z or Higgs boson and a gravitino LSP, the superpartner of the graviton. Furthermore, the analysis searches for new physics in final states with at least five charged leptons. This region does not target any SUSY model specifically, but is used for a general search for new physics in five-lepton final states. The second search discussed in this thesis, focuses on the supersymmetric partners of the electron and muon. Light smuons may explain the measured value of the anomalous magnetic moment of the muon, which differs significantly from the SM prediction. Therefore, the search for sleptons is well motivated. Sleptons were already targeted by several other searches using the same data set. However, there is still a gap in sensitivity for scenarios where the difference in mass between the slepton and the LSP is between 20 and 80 GeV. This sensitivity gap is targeted by this search.

In order to collect much more data which facilitates to improve the precision measurements of the SM and increase the sensitivity for physics beyond the SM, the LHC will be upgraded to the High Luminosity LHC [3, 4] which will increase the instantaneous luminosity by a factor of 7.

A major upgrade of the ATLAS detector is required to cope with the increased pile-up conditions. For the ATLAS muon spectrometer the existing Monitored Drift Tube (MDT) chambers in the small sectors of the inner layer of the central detector region will be replaced by new small-diameter Monitored Drift Tube (sMDT) chambers with integrated resistive plate chambers (RPC).

In total 112 chambers need to be built for the upgrade. 16 BIS78 were constructed in 2017-2019 and installed in the ATLAS detector in 2020. The serial production of 96 BIS1-6 chambers started 2020 at two production sites. The production of each chamber is accompanied by several measurements that ensures the quality of the constructed chambers. The thesis describes the production of the sMDT chambers and the quality measurements on the chambers with focus on measurements of the chamber geometry. This ensures that the positioning accuracy of the sense wires fulfills the requirements, since precise knowledge of the position of the active detector elements within the detector is crucial to achieve the target 10% momentum resolution for muons at $p_{\mathrm{T}} \approx 1$ TeV. This requirement on the momentum resolution translates to required positioning accuracy of the sense wire of < 20 μm. The chambers deform under the influence of gravity and other external forces. Each chamber is equipped with an optical in-plane alignment system that allows to monitor such deformations during the detector operation. The deformations measured with the in-plane alignment system is compared to the mechanical measurements of the chamber geometry.

The first part of this thesis gives an overview of the SM and its supersymmetric extensions. Chapter 3 and 4 describe the LHC and the ATLAS experiment. Chapter 5 describes the production of the new sMDT chambers for the upgrade of the ATLAS muon spectrometer for the high luminosity LHC. The search for SUSY in final states with at least four charged leptons is described in Chapter 6. Chapter 7 describes the search for sleptons. A brief summary is given in Chapter 8.

CHAPTER TWO

THEORY

2.1 The Standard Model of particle physics

The Standard Model of particle physics (SM) [5–9] describes the elementary particles and their interactions. The SM is a relativistic quantum field theory which describes three of the four fundamental forces based on the local gauge symmetry group

$$SU(3)_C \times SU(2)_L \times U(1)_Y \tag{2.1}$$

, where C, L and Y denote the associated quantum numbers color, weak isospin and hypercharge. The $SU(3)_C$ gauge group describes the strong interaction. Electromagnetic and weak forces are unified into the electroweak interaction and described by the $SU(2)_L \times U(1)_Y$ gauge group.

2.1.1 Particle Content of the Standard Model

The particles of the SM can be classified according to their spin in fermions with half-integer spin and bosons with integer spin. The fermions with spin $\frac{1}{2}$ form matter and are further categorized into quarks and leptons and appear in three generations with increasing mass but same quantum numbers. The three lepton generations consist each of a charged lepton, electron, muon and tau, and an associated uncharged massless neutrino: ν_e, ν_μ and ν_τ. The neutrinos and charged leptons interact via the weak interaction, while the charged leptons with their electric charge of -1 also interact via the electromagnetic interaction. The quarks also interact through the weak and electromagnetic forces, but they also carry the so-called color charge, which comes in three different types denoted as red, $green$ and $blue$, and are therefore also interacting via the strong interaction. Each quark generation consists of an up-type quark with electric charge $+\frac{2}{3}$ (up, charm and top) and a down-type quark with electric charge $-\frac{1}{3}$ (down, strange and bottom). For each fermion there is also an anti-particle with the same mass but opposite charge. The interactions are mediated via gauge bosons with spin 1. The strong

interaction is mediated via eight massless gluons. Each gluon carries one color and one anti-color. The electroweak interaction is mediated with the massless photon γ and three massive gauge bosons, the two charged W^+, W^- and the neutral Z boson. The masses of the fermions and gauge bosons arises from the interaction with the Higgs field which is associated with the Higgs boson carrying spin 0.

2.1.2 Gauge Invariance

The SM is a quantum field theory, where particles are describes as excitations of quantized fields [10]. The equation of motion for a field ϕ is derived using the Lagrangian density $\mathcal{L}(\phi)$ together with the Euler-Lagrange equations from Hamilton's principle

$$\partial_\mu \frac{\partial \mathcal{L}(\phi)}{\partial(\partial_\mu \phi)} - \frac{\partial \mathcal{L}(\phi)}{\partial \phi} = 0. \tag{2.2}$$

Spin-0 particles are described by a scalar field $\phi(x)$. Spin-$\frac{1}{2}$ particles are described by spinor fields $\psi(x)$ and spin-1 particles are described by vector fields $A_\mu(x)$. The interactions of fermions with the gauge bosons is generated by requiring the Lagrangian density to be invariant under a local symmetry transformation. For example, the electromagnetic interaction is described by the theory of quantum electrodynamics (QED). The Lagrangian for a free fermion field ψ with mass m, $\mathcal{L}_0 = \bar{\psi}(i\gamma^\mu \partial_\mu - m)\psi$, with $\bar{\psi} = \psi^\dagger \gamma^0$ and the Dirac matrices γ^μ, is invariant under the global $U(1)$ transformation:

$$\psi(x) \rightarrow \psi^{'}(x) = e^{i\alpha}\psi(x), \tag{2.3}$$

with constant α. However, it is not invariant under a local transformation

$$\psi(x) \rightarrow \psi^{'}(x) = e^{i\alpha(x)}\psi(x). \tag{2.4}$$

In order to achieve invariance under local transformation, a vector field A_μ is required and the derivative in the Lagrangian has to be replace with the covariant derivative D_μ

$$\partial_\mu \rightarrow D_\mu = \partial_\mu + ieA_\mu, \tag{2.5}$$

where A_μ is a vector field corresponding to the electromagnetic field potential. The field A_μ couples to the fermion fields with the electric charge e as coupling strength. The local transformation of A_μ is given by

$$A_\mu(x) \rightarrow A^{'}_\mu(x) = A_\mu(x) - \frac{1}{2}\partial_\mu \alpha(x). \tag{2.6}$$

The invariant Lagrangian for the QED is given by:

$$\mathcal{L} = \bar{\psi}(i\gamma^\mu D_\mu - m)\psi - \frac{1}{4}F_{\mu\nu}F^{\mu\nu}, \tag{2.7}$$

where $F_{\mu\nu} = \partial_\mu A_\nu - \partial_\nu A_\mu$ is the field strength tensor that describes the kinematics of the vector field. This concept can be generalized to non-Abelian gauge symmetries, described by $SU(n)$ groups. For a non-interacting multiplet of n fermion fields $\Psi = (\psi_1, ..., \psi_n)^T$ with mass m the Lagrangian is given by

$$\mathcal{L}_0 = \bar{\Psi}(\gamma^\mu \partial_\mu - m)\Psi, \tag{2.8}$$

with $\bar{\Psi} = (\bar{\psi}_1, ..., \bar{\psi}_2)$. This Lagrangian is invariant under the global transformations

$$\Psi(x) \rightarrow U(\alpha^1, ..., \alpha^N)\Psi(x), \tag{2.9}$$

where U is a n-dimensional unitary matrix, parametrized by N real parameters $\alpha^1, ..., \alpha^N$. U is a representation of a non-Abelian Lie group $SU(n)$. The matrices U can be written in terms of the generators of the group $T_1, ..., T_N$, by

$$U(\alpha^1, ..., \alpha^N) = e^{i(\alpha^1 T_1 + ... + \alpha^N T_N)}. \tag{2.10}$$

The $n^2 - 1$ generators of a $SU(n)$ group fulfill the commutation relation

$$[T_a, T_b] = i f_{abc} T_c, \tag{2.11}$$

where the structure constants f_{abc} characterize the group and are real numbers. In order to achieve local invariance, i.e. by converting the constants α^a to real functions $\alpha^a(x)$, $a = 1, ..., N$, the derivative in the Lagrangian has to be changed to the covariant derivative

$$\partial_\mu \rightarrow D_\mu = \partial_\mu - ig\mathbf{W}_\mu(x), \tag{2.12}$$

with a vector field $\mathbf{W}_\mu$ and the coupling constant g. $\mathbf{W}_\mu$ can be expressed in terms of the generators

$$\mathbf{W}_\mu(x) = T_a W_\mu^a(x). \tag{2.13}$$

The local gauge transformation for W_μ^a expanded for infinitesimal $\alpha^a(x)$ is given by

$$W_\mu^a \rightarrow W_\mu^{'a} = W_\mu^a + \frac{1}{g}\partial_\mu \alpha^a + f_{abc} W_\mu^b \alpha^c. \tag{2.14}$$

These fields W_μ^a enter the Lagrangian and induce an interaction term

$$\mathcal{L}_{\text{int}} = g\bar{\Psi}\gamma^\mu \mathbf{W}_\mu \Psi. \tag{2.15}$$

The kinetic term of the W fields is obtained by a generalization of the electromagnetic field strength tensor

$$F_{\mu\nu}^a = \partial_\mu W_\nu^a - \partial_\nu W_\mu^a + g f_{abc} W_\mu^b W_\nu^c. \tag{2.16}$$

The kinetic term added to the Lagrangian is given by

$$\mathcal{L}_W = -\frac{1}{4} F_{\mu\nu}^a F^{a,\mu\nu}, \tag{2.17}$$

which contains a quadratic term a quadratic part describing the free propagation of the W fields. However the Lagrangian contains also cubic and quartic terms describing self-interactions of the gauge fields. The gauge fields in the Lagrangian have to be massless. Adding mass terms $\frac{1}{2}m^2 W_\mu^a W^{a,\mu}$ does not leave the Lagrangian invariant and breaks the gauge symmetry.

2.1.3 Quantum Chromodynamics

The strong interaction is described by Quantum Chromodynamics (QCD) with $SU(3)_C$ as gauge group [11]. The quarks carry a color charge labeled by red, $green$ and $blue$. They quarks appear in triplets under $SU(3)_C$

$$q = \begin{pmatrix} q_R \\ q_G \\ q_B \end{pmatrix}. \tag{2.18}$$

The eight generators T_a of the group are expressed in terms of the Gell-Mann matrices λ_a

$$T_a = \frac{1}{2}\lambda_a. \tag{2.19}$$

The covariant derivative acting on the quark triplets is given by

$$D_\mu = \partial_\mu - \frac{1}{2} i g_s \lambda_a G_\mu^a \,, \tag{2.20}$$

with the strong coupling constant g_s and the eight gauge fields, the gluon field G_μ^a. The kinetic term of the gluon fields in the Lagrangian is given by:

$$\mathcal{L}_{\text{QCD,kin.}} = -\frac{1}{4} G_{\mu\nu}^a G^{a,\mu\nu}, \tag{2.21}$$

with the field strength tensor:

$$G^a_{\mu\nu} = \partial_\mu G^a_\nu - \partial_\nu G^a_\mu + g_s f_{abc} G^b_\mu G^c_\nu \,. \tag{2.22}$$

The cubic and quartic terms in the gluon fields correspond to the self-interactions of the gluons. The self-interaction of the gluons leads to the phenomenon of confinement of colored particles [12]. Except for extreme conditions in a quark-gluon plasma [13], quarks are not free but only occur in colorless bound states, so called hadrons. Hadrons consists of either quark-antiquark pairs (mesons) or three quarks (baryons). However, hadrons consisting of more quarks, like tetra- and pentaquarks have been recently discovered [14–16].

2.1.4 The Electroweak Interaction

The electromagnetic and the weak interactions were unified to the electroweak interaction using the symmetry group $SU(2)_L \times U(1)_Y$ [5]. The gauge bosons of the weak interaction are massive. Therefore, the symmetry is broken leaving the electromagnetic gauge subgroup $U(1)_{\text{em}}$ unbroken. The quantum numbers associated with this symmetry are the weak isospin I and the weak hypercharge Y. The Gell-Mann-Nishijima relation connects the weak hypercharge and the third component of the weak isospin I_3 with the electric charge Q

$$Q = I_3 + \frac{Y}{2}. \tag{2.23}$$

The weak interaction couples only to left-handed fermions and right-handed anti-fermions. Therefore, the left-handed fermions are arranged in doublets with weak isospin $I = \frac{1}{2}$, where the upper components have $I_3 = \frac{1}{2}$ and the lower components have $I_3 = -\frac{1}{2}$

$$\begin{pmatrix} \nu_e \\ e \end{pmatrix}_L, \begin{pmatrix} \nu_\mu \\ \mu \end{pmatrix}_L, \begin{pmatrix} \nu_\tau \\ \tau \end{pmatrix}_L, \qquad \begin{pmatrix} u \\ d \end{pmatrix}_L, \begin{pmatrix} c \\ s \end{pmatrix}_L, \begin{pmatrix} t \\ b \end{pmatrix}_L . \tag{2.24}$$

The right-handed components are arranged in singlets with weak isospin $I = 0$

$$e_R, \mu_R, \tau_R, \qquad u_R, d_R, c_R, s_R, t_R, b_R \,. \tag{2.25}$$

. There are no right-handed neutrinos in the SM. The left- and right-handed components of a Dirac spinor ψ are given by:

$$\psi_L = \frac{1-\gamma_5}{2}\psi, \qquad \psi_R = \frac{1+\gamma_5}{2}\psi, \tag{2.26}$$

with $\gamma^5 = i\gamma^0\gamma^1\gamma^2\gamma^3$. The $SU(2)_L$ and $U(1)_Y$ gauge groups are associated with three vector fields $W_\mu^{1,2,3}$ and one vector field B_μ, respectively. The covariant derivatives are different for left-handed and right-handed fields and are given by:

$$D_\mu^L = \partial_\mu + ig_1\frac{Y}{2}B_\mu - ig_2\frac{\sigma_a}{2}W_\mu^a, \qquad D_\mu^R = \partial_\mu + ig_1\frac{Y}{2}B_\mu \,, \tag{2.27}$$

where $I_a = \frac{\sigma_a}{2}$ and σ_a are the three Pauli matrices. The parameters g_1 and g_2 are the coupling constants associated with $U(1)_Y$ and $SU(2)_L$. The Lagrangian is then given by:

$$\mathcal{L}_{EW} = \sum_f \bar{\psi}_L^f i\gamma^\mu D_\mu^L \psi_L^f + \sum_f \bar{\psi}_R^f i\gamma^\mu D_\mu^R \psi_R^f - \frac{1}{4}W_{\mu\nu}^a W^{\mu\nu,a} - \frac{1}{4}B_{\mu\nu}B^{\mu\nu}, \tag{2.28}$$

where the index f runs over the quark and lepton generations. The field strength tensors of the gauge fields is given by

$$W_{\mu\nu}^a = \partial_\mu W_\nu^a - \partial_\nu W_\mu^a + g_2\epsilon_{abc}W_\mu^b W_\nu^c \,, \tag{2.29}$$

$$B_{\mu\nu} = \partial_\mu B_\nu - \partial_\nu B_\mu \,, \tag{2.30}$$

where the Levi-Cevita symbol ϵ_{abc} provides the structure constants of the gauge group.

2.1.5 The Higgs Mechanism

The gauge bosons of the weak interaction are massive. However, adding mass terms to the Lagrangian violates gauge invariance. Masses for the bosons can be introduced by breaking the electroweak symmetry $SU(2)_L \times U(1)_Y$. This is described by the Brout-Englert-Higgs mechanism [17–19]. For this, the Brout-Englert-Higgs mechanism introduces an isospin doublet of complex scalar fields with hypercharge $Y = 1$

$$\Phi(x) = \begin{pmatrix} \phi^+(x) \\ \phi^0(x) \end{pmatrix}. \tag{2.31}$$

The Lagrangian is given by

$$\mathcal{L}_H = (D_\mu\Phi)^\dagger(D^\mu\Phi) - V(\Phi) \,, \tag{2.32}$$

with the covariant derivative

$$D_\mu = \partial_\mu + i\frac{g_1}{2}B_\mu - ig_2\frac{\sigma_a}{2}W_\mu^a \tag{2.33}$$

and the Higgs potential

$$V(\Phi) = -\mu^2\Phi^\dagger\Phi + \frac{\lambda}{4}(\Phi^\dagger\Phi)^2, \tag{2.34}$$

where λ and μ^2 are the dimensionless self-coupling and Higgs mass parameter, respectively. For $\mu^2, \lambda > 0$, V has a minimum for field configurations with $\Phi^\dagger\Phi = \frac{2\mu^2}{\lambda}$. Choosing the minimum such

that the charged component of the Higgs doublet is zero, gives the vacuum expectation value

$$\langle \Psi \rangle = \frac{1}{\sqrt{2}} \begin{pmatrix} 0 \\ v \end{pmatrix} \tag{2.35}$$

with $v = \frac{2\mu}{\sqrt{\lambda}}$. The Lagrangian is invariant under $SU(2)_L \times U(1)_Y$ symmetry transformations, but the vacuum configuration $\langle \Psi \rangle$ breaks the symmetry spontaneously. However, $\langle \Psi \rangle$ is still invariant under transformations of the electromagnetic subgroup $U(1)_{\text{em}}$. The Higgs doublet can be written as

$$\Phi(x) = \frac{1}{\sqrt{2}} \begin{pmatrix} \phi_1(x) + i\phi_2 \\ (v + H(x) + i\chi(x)) \end{pmatrix}, \tag{2.36}$$

with fields $\phi^+ = \phi_1 + i\phi_2$, H and χ, each with a vacuum expectation value of zero. The Higgs potential expanded around the vacuum configuration has a mass term for H, but not for ϕ_1, ϕ_2 and χ. Using the unitary gauge, the massless Goldstone bosons are absorbed in the longitudinal polarization degrees of freedom of the weak gauge bosons, giving them their masses. The Higgs doublet in unitary gauge is given by

$$\Phi(x) = \frac{1}{\sqrt{2}} \begin{pmatrix} 0 \\ v + H(x) \end{pmatrix}. \tag{2.37}$$

The potential V is given now by

$$V = \frac{M_H^2}{2} H^2 + \frac{M_H^2}{2v} H^3 + \frac{M_H^2}{8v^2} H^4. \tag{2.38}$$

The field $H(x)$ describes a neutral scalar particle with mass $M_H = \sqrt{2}\mu$, the Higgs boson. The Higgs boson was discovered in 2012 by the ATLAS and CMS experiments [1, 2] V contains also cubic and quartic self-interactions proportional to M_H^2. The kinetic part of the Higgs Lagrangian yields mass terms for the vector bosons

$$\frac{1}{2}(\frac{g_2}{2}v)^2(W_1^2 + W_2^2) + \frac{1}{2}(\frac{v}{2})^2(W_\mu^3, B_\mu) \begin{pmatrix} g_2^2 & g_1 g_2 \\ g_1 g_2 & g_1^2 \end{pmatrix} \begin{pmatrix} W^{3,\mu} \\ B^\mu \end{pmatrix}. \tag{2.39}$$

The fields W_μ^a, B_μ can be transformed to the physical fields $W_\mu^\pm$, Z_μ and A_μ

$$W_\mu^\pm = \frac{1}{\sqrt{2}}(W_\mu^1 \mp W_\mu^2) \tag{2.40}$$

$$\begin{pmatrix} Z_\mu \\ A_\mu \end{pmatrix} = \begin{pmatrix} \cos\theta_W & \sin\theta_W \\ -\sin\theta_W & \cos\theta_W \end{pmatrix} \begin{pmatrix} W_\mu^3 \\ B_\mu \end{pmatrix}. \tag{2.41}$$

This way the mass terms in equation 2.39 are diagonalized:

$$\frac{M_W^2}{2} W_\mu^+ W_\mu^- + \frac{1}{2}(A_\mu, Z_\mu) \begin{pmatrix} 0 & 0 \\ 0 & M_Z^2 \end{pmatrix} \begin{pmatrix} A_\mu \\ Z_\mu \end{pmatrix}. \tag{2.42}$$

The masses for the weak gauge bosons are given by

$$M_W = \frac{1}{2} g_2 v, \qquad M_Z = \frac{1}{2}\sqrt{g_1^2 + g_2^2}\, v \ . \tag{2.43}$$

while the photon remains massless. The electroweak mixing angle θ_W is given by

$$\cos\theta_W = \frac{g_2}{\sqrt{g_1^2 + g_2^2}} = \frac{M_W}{M_Z} \ . \tag{2.44}$$

The photon field A_μ couples via the electric charge e to the electron which can be written in terms of the gauge couplings as

$$e = \frac{g_1 g_2}{\sqrt{g_1^2 + g_2^2}}, \qquad e = g_2 \sin\theta_W, \qquad e = g_1 \cos\theta_W \ . \tag{2.45}$$

The spontaneous symmetry breaking does allow also the fermions to acquire mass by adding Yukawa interactions between the fermion fields and the Higgs field. For one generation of fermions the Lagrangian is given by

$$\mathcal{L}_Y = -G_l \bar{L}_L \Phi l_R - G_d \bar{Q}_L \Phi d_R - G_u \bar{Q}_L \Phi^c u_R + h.c. \ , \tag{2.46}$$

where $L_L = (\nu_L, l_L)^T$ and $Q_L = (u_L, d_L)^T$ are the left-handed lepton and quark doublets. As before, Φ is the Higgs field and $\Phi^c = i\sigma_2 \Phi = (\phi^{0*}, -\phi^-)^T$ is its charge-conjugate, with ϕ^- the adjoint of ϕ^+. G_f are the Yukawa couplings. In the unitary gauge the Yukawa Lagrangian is given by:

$$\mathcal{L}_Y = -\sum_f m_f \bar{\psi}_f \psi_f - \sum_f \frac{m_f}{v} \bar{\psi}_f \psi_f H \ , \tag{2.47}$$

with the fermion masses connected to the Yukawa coupling by $m_f = \frac{1}{\sqrt{2}} G_f v$. The Lagrangian contains now mass terms for the fermions and interactions between the fermions and the Higgs field with a coupling constant proportional to the fermion masses. Adding additional fermion generations, flavor mixing has to be taken into account. The Yukawa couplings are replaced by matrices with complex entries, $G_l = (G_{ij}^l)$, $G_u = (G_{ij}^u)$, $G_d = (G_{ij}^d)$. The matrix $G_l = (G_{ij}^l)$ is diagonal. Therefore, electroweak and mass eigenstate are equal, if the neutrinos are assumed massless. In the quark sector the matrices are not diagonal and have to be diagonalized to obtain mass eigenstates. This is described

by the unitary Cabibbo-Kobayashi-Maskawa (CKM) matrix, which off-diagonal elements allows for electroweak transitions between the quark generations [20, 21]. The CKM matrix has four independent physical parameters, three angles and one complex phase. The complex phase parameter is responsible for CP violation in weak decays.

2.2 Limitations of the Standard Model

Despite the enormous success of the SM predicting the outcome of particle physics experiments, there are several problems that the SM cannot address. A few examples are presented in the following.

Neutrino masses: In the SM neutrinos are assumed to be massless. However, the observation of neutrino oscillations requires the neutrinos to have mass [22–24]. Currently, only upper limits exist for the mass values. Recently, the KATRIN experiment set an upper limit on the neutrino mass of $m_\nu < 1.1$ eV (90% CL) [25].

Dark matter and dark energy: Astrophysical observations indicate the existence of matter that does not interact electromagnetically, so called dark matter [26–28]. Only 4.8% of the energy content of the universe consists of baryonic matter, while about 26% are dark matter. The remaining 68% are attributed to dark energy which is responsible for the observed accelerated expansion of the universe [29]. First evidence for the existence of dark matter originates from the observation of the rotation curves of spiral galaxies [27]. From Newtonian dynamics, the circular velocity $v(r)$ of an object in a galaxy is given by

$$v(r) = \sqrt{\frac{GM(r)}{r}}\,, \tag{2.48}$$

where r is the distance to the galactic center, G is the gravitational constant and $M(r) = 4\pi \int \rho(r) r^2\, dr$ is the enclosed mass of the galaxy with mass density $\rho(r)$. Beyond the galactic disc the circular velocity is expected to fall proportional to $1/\sqrt{r}$. However, the circular velocity was observed to be approximately constant. Assuming the validity of Newtonian dynamics, it implies a dark halo with $M(r) \propto r$ and $\rho(r) \propto r^{-2}$. Dark matter has to be massive, electrically neutral and stable on cosmological timescales. The neutrinos in the SM extended by neutrino masses are a candidate for dark matter. However, their density is too low to be a dominant component of dark matter [28]. In many models dark matter consists of weakly interacting massive particles (WIMPs).

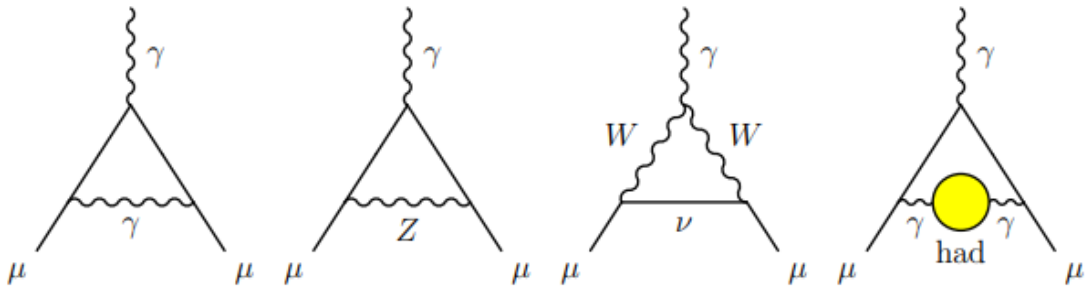

Figure 2.1: Representative Feynman diagrams contributing to a_μ [30].

The Anomalous Magnetic Moment of the Muon: The magnetic moment of the muon shows a deviation between measurement and the SM prediction [30]. The magnetic moment of the muon, predicted by the Dirac equation, is given by

$$\vec{M} = g_\mu \frac{e}{2m_\mu} \vec{S}\,, \tag{2.49}$$

with the gyromagnetic ratio $g_\mu = 2$. Quantum loop corrections cause a small deviations from this value [30], which are parametrized by the anomalous magnetic moment:

$$a_\mu = \frac{g_\mu - 2}{2}\,. \tag{2.50}$$

The anomalous magnetic moment of the muon can be precisely predicted with the SM and also measured with high precision. The loop correction of the SM can be divided into three types: QED loops with leptons and photons, weak loop contributions with $W^\pm$, Z and Higgs bosons and hadronic loops. Examples for Feynman diagrams contributing to a_μ are shown in Figure 2.1. The anomalous magnetic moment was measured by the E821 experiment at Brookhaven National Lab (BNL) by using muons in a storage ring and measuring their precession in a constant external magnetic field [31]. The same storage ring was later setup at the Fermilab National Accelerator Laboratory (FNAL) with a cleaner and more intense muon beam and improved detectors. First results from FNAL in 2021 confirmed the results from BNL [32]. The combined experimental average is

$$a_\mu(\text{Exp}) = 116592061(41) \times 10^{-11}. \tag{2.51}$$

The difference to the value predicted by the SM is

$$a_\mu(\text{Exp}) - a_\mu(\text{SM}) = (251 \pm 59) \times 10^{-11}, \tag{2.52}$$

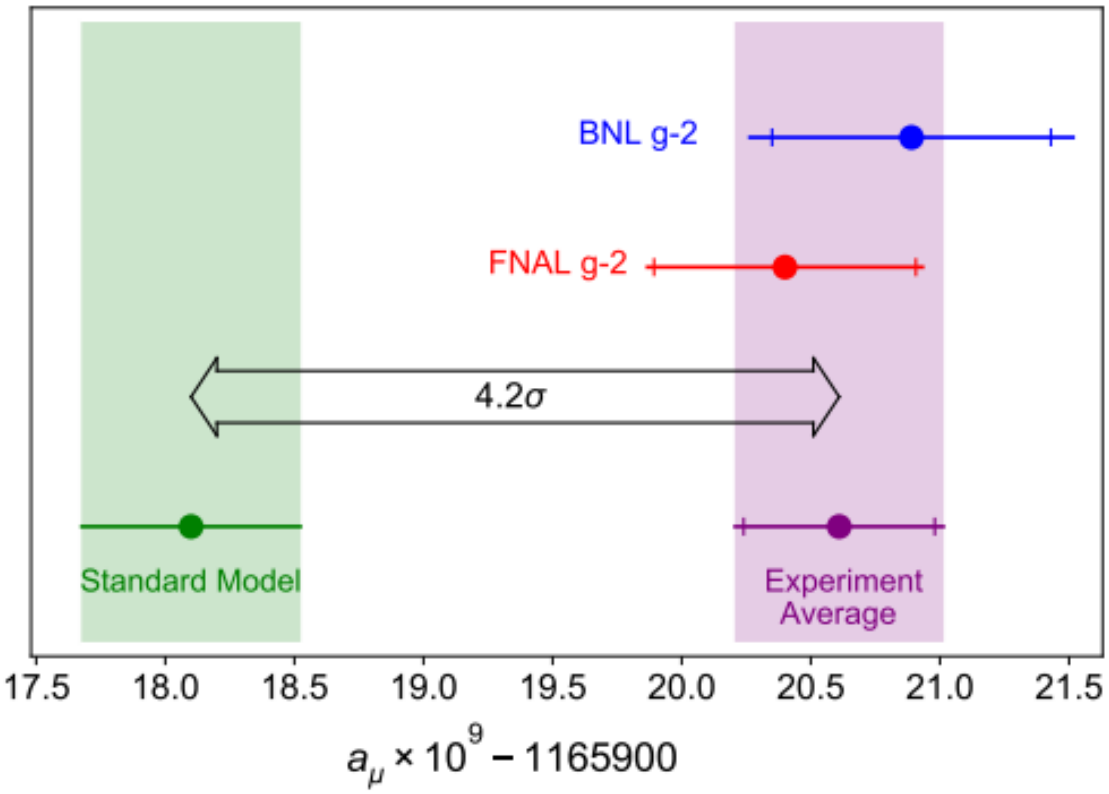

Figure 2.2: Experimental values for the anomalous magnetic moment of the muon from BNL and FNAL and the combined average in comparison to the SM prediction. [32].

which has a significance of 4.2σ. The results are shown in Figure 2.2. Extensions to the SM with new particles may lead to additional loop corrections that can explain the observed deviation.

The Hierarchy Problem: The mass of the Higgs boson receives loop corrections from every particle that couples directly or indirectly to the Higgs field [33]. The Feynman diagrams of the leading order corrections from a Dirac fermion f and a scalar particle S are shown in Figure 2.3. The fermion loop yields a correction

$$\Delta m_H^2 = -\frac{|\lambda_f|^2}{8\pi^2}\Lambda_{\mathrm{UV}}^2 + \dots , \tag{2.53}$$

while the scalar loop gives a correction

$$\Delta_H^2 = \frac{\lambda_S}{16\pi^2}[\Lambda_{\mathrm{UV}}^2 - 2m_S^2 \ln(\frac{\Lambda_{\mathrm{UV}}}{m_S}) + \dots] , \tag{2.54}$$

where λ_f and λ_S are coupling constants of the fermion and scalar particle to the Higgs field. Λ_{UV} is an ultraviolet momentum cutoff used to regulate the loop integral. Λ_{UV} is considered as the energy scale at which new physics enters the theory. If Λ_{UV} is of order of the reduced Planck scale $M_P = \sqrt{1/8\pi G_{\mathrm{Newton}}} = 2.4 \times 10^{18}$ GeV, the quantum correction is 30 orders of magnitude larger than the observed Higgs mass. This requires extreme fine-tuning which is not considered natural. Although quantum corrections to the fermion and gauge boson masses do not have the direct quadratic sensitivity to Λ_{UV}, the particles of the SM all obtain their masses from Higgs field and are therefore still indirectly sensitive to the cutoff scale Λ_{UV}. Furthermore, there are corrections from any hypothetical heavy particle.

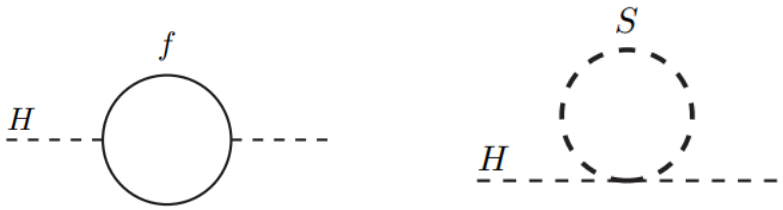

(a) (b)

Figure 2.3: One-loop quantum corrections to the Higgs squared mass parameter, due to (a) a Dirac fermion f and (b) a scalar S.

A possible solution to the hierarchy problem is the introduction of a new symmetry between bosons and fermions. Assuming that each of the fermions of the SM is accompanied by two complex scalars with $\lambda_S = |\lambda_f|^2$, the corrections proportional to Λ^2_{UV} will cancel due to the opposite sign of the corrections. Such additional scalar particles are predicted by Supersymmetry (SUSY) [33].

2.3 Supersymmetry

Supersymmetry [33–38] postulates a symmetry between bosons and fermions. An anti-commuting spinor operator Q transforms bosonic states into fermionic states and vice versa

$$Q\,|\text{boson}\rangle = |\text{fermion}\rangle\,, \qquad Q\,|\text{fermion}\rangle = |\text{boson}\rangle\,. \tag{2.55}$$

The operator Q and hermitian conjugate $Q^\dagger$ satisfy the (anti-)commutation relations with the schematic form:

$$\{Q, Q^\dagger\} = P^\mu, \tag{2.56}$$

$$\{Q, Q\} = \{Q^\dagger, Q^\dagger\} = 0, \tag{2.57}$$

$$\tag{2.58}$$

with the four-momentum generator of spacetime translations P^μ. The fermions and bosons that are related via the SUSY transformation are called superpartners. They form supermultiplets, that are the irreducible representations of the supersymmetry algebra. The squared-mass operator $-P^2$ commutes with Q, $Q^\dagger$ and all spacetime rotation and translation operators. Therefore, the particles of the same supermultiplet have the same eigenvalues of $-P^2$ resulting in equal mass. The operators Q and $Q^\dagger$ commute with the generators of the gauge transformations. Consequently, the particles in the same supermultiplet have the same electric charges, weak isospin and color degrees of freedom. A chiral supermultiplet consists of a Weyl spinor and a complex scalar field. A gauge supermultiplet contain a spin-1 vector boson and a Weyl spinor. In both cases the spin of the superpartners differs by $\frac{1}{2}$.

2.3.1 The Minimal Supersymmetric Standard Model

The Minimal Supersymmetric Standard Model (MSSM) contains the minimal number of new particles for a supersymmetric extension of the SM. The spin-0 superpartners of the fermions are called sfermions or squarks $\tilde{q}$ and sleptons $\tilde{\ell}$ and are arranged with their SM partners in chiral supermultiplets. The gauge bosons and their spin-$\frac{1}{2}$ superpartners, the gauginos, called wino, bino and gluino, are arrangend in gauge supermultiplets. Two chiral Higgs supermultiplets H_u and H_d with hypercharge $Y = \frac{1}{2}$ and $Y = -\frac{1}{2}$, respectively, are needed to cancel gauge anomalies. H_u and H_d give masses to the up-type and down-type fermions and sfermions, respectively. Due to the second Higgs doublet, there is not only one Higgs boson after electroweak symmetry breaking, but five Higgs bosons, two neutral scalars h and H, two charged bosons $H^\pm$ and one pseudoscalar A. The spin-$\frac{1}{2}$ superpartners of the Higgs bosons are called higgsinos. The electroweak gauginos and the higgsino form mixed mass eigenstates, four neutral neutralinos $\tilde{\chi}_i^0$ ($i = 1, 2, 3, 4$ increasing in mass) and four charged charginos $\tilde{\chi}_i^\pm$ ($i = 1, 2$). The chiral and gauge supermultiplets of the MSSM are shown in Table 2.1.

Since no partners of the SM particles that differ only in spin have been discovered, SUSY has to be a broken symmetry leading to masses of the SUSY particles well above their SM partners. In order to keep the cancellations of the corrections to the Higgs boson mass, SUSY is assumed to be softly

Table 2.1: Chiral and gauge supermultiplets of the MSSM

Supermultiplet ($i = 1, 2, 3$)	Sfermions spin 0	Fermions spin 1/2
Q_i	$\tilde{Q}_i = \begin{pmatrix}\tilde{u}\\ \tilde{d}\end{pmatrix}, \begin{pmatrix}\tilde{c}\\ \tilde{s}\end{pmatrix}, \begin{pmatrix}\tilde{t}\\ \tilde{b}\end{pmatrix}$	$Q_i = \begin{pmatrix}u\\ d\end{pmatrix}_L, \begin{pmatrix}c\\ s\end{pmatrix}_L, \begin{pmatrix}t\\ b\end{pmatrix}_L$
$\bar{U}_i$	$\tilde{u}^* = \tilde{u}^*, \tilde{c}^*, \tilde{t}^*$	$u_i^\dagger = u_R^\dagger, c_R^\dagger, t_R^\dagger$
$\bar{D}_i$	$\tilde{d}_i^* = \tilde{d}^*, \tilde{s}^*, \tilde{b}^*$	$d_i^\dagger = d_R^\dagger, s_R^\dagger, b_R^\dagger$
L_i	$\tilde{L}_i = \begin{pmatrix}\tilde{\nu}_e\\ \tilde{e}\end{pmatrix}, \begin{pmatrix}\tilde{\nu}_\mu\\ \tilde{\mu}\end{pmatrix}, \begin{pmatrix}\tilde{\nu}_\tau\\ \tilde{\tau}\end{pmatrix}$	$L_i = \begin{pmatrix}\nu_e\\ e\end{pmatrix}_L, \begin{pmatrix}\nu_\mu\\ \mu\end{pmatrix}_L, \begin{pmatrix}\nu_\tau\\ \tau\end{pmatrix}_L$
$\bar{E}$	$\tilde{e}_i^* = \tilde{e}^*, \tilde{\mu}^*, \tilde{\tau}^*$	$e_i^\dagger = e_R^\dagger, \mu_R^\dagger, \tau_R^\dagger$
Supermultiplet	Higgs fields spin 0	Higgsino fields spin 1/2
H_u	$H_u = \begin{pmatrix}H_u^+\\ H_u^0\end{pmatrix}$	$\tilde{H}_u = \begin{pmatrix}\tilde{H}_u^+\\ \tilde{H}_u^0\end{pmatrix}$
H_d	$H_u = \begin{pmatrix}H_d^0\\ H_d^-\end{pmatrix}$	$\tilde{H}_d = \begin{pmatrix}\tilde{H}_d^0\\ \tilde{H}_d^-\end{pmatrix}$
Supermultiplet	Gauge boson spin 1	Gaugino spin 1/2
	Gluon g	Gluino $\tilde{g}$
	$W^\pm, W^0$	Winos $\tilde{W}^\pm, \tilde{W}^0$
	B^0	Bino $\tilde{B}^0$

broken. After SUSY breaking the remaining correction to the Higgs boson mass is

$$\Delta m_H^2 = m_{\text{soft}}^2 [\frac{\lambda}{16\pi^2} \ln(\Lambda_{\text{UV}}/m_{\text{soft}}) + \dots] , \tag{2.59}$$

where λ is a dimensionless coupling and m_{soft} the SUSY mass scale [33]. In order to still solve the hierarchy problem the masses of the lightest few SUSY particles should not be much greater than the TeV scale and are therefore accessible by the LHC.

2.3.2 R-Parity

The superpotential, describing interactions between particles in chiral supermultiplets, may contain interaction terms that violate lepton number (L) and baryon number (B) conversation

$$W_{\Delta L=1} = \frac{1}{2}\lambda^{ijk} L_i L_j \bar{e}_k + \lambda'^{ijk} L_i Q_j \bar{d}_k + \mu'^i L_i H_u , \tag{2.60}$$

$$W_{\Delta B=1} = \frac{1}{2}\lambda^{''ijk}\bar{u}_i\bar{d}_j\bar{d}_k \ , \tag{2.61}$$

where i, k and k denote the generations, λ^{ijk}, $\lambda^{'ijk}$ and $\lambda^{''ijk}$ are dimensionless Yukawa couplings and $\mu^{'i}$ has the dimension of a mass [33]. The couplings λ^{ijk} are antisymmetric in i and j, while the couplings $\lambda^{''ijk}$ are antisymmetric in j and k. The simultaneous existence of baryon and lepton number violating terms would lead to a rapid proton decay. The current experimental limits on the life time of the proton is $\tau_{\text{proton}} > 10^{34}$ years [39]. In order to prevent baryon and lepton number violation and therefore keep the proton stable, a new multiplicative symmetry called R-parity is introduced

$$P_R = (-1)^{3(B-L)+2s}, \tag{2.62}$$

where s is the spin of the particle. SM particles have positive R-Parity, $P_R = +1$ and SUSY particles $P_R = -1$. R-parity conservation (RPC) has the following consequences:

- The lightest supersymmetric particle (LSP) must be stable. The LSP is a viable candidate for DM if it is electrically neutral. In most SUSY scenarios the LSP is assumed to be the lightest neutralino $\tilde{\chi}_1^0$.
- With exception of the LSP, SUSY particles eventually decay into states with an odd number of LSPs.
- SUSY particles are produced in even numbers at colliders.

R-parity conservation forbids all B and L violating couplings. However, the proton decay can be already avoided if either lepton or baryon number is conserved. R-parity violating (RPV) scenarios, that violates either lepton or baryon number, lead generally to totally different phenomenologies at collider experiments [40]. The search presented in chapter 6 considers scenarios with the coupling $\lambda^{ijk} \neq 0$, which allows the LSP to decay into two charged leptons and a neutrino. All other RPV coupling constants are considered to be zero.

CHAPTER THREE

THE LARGE HADRON COLLIDER

The Large Hadron Collider (LHC)[41] is the world's largest particle accelerator, hosted by CERN near Geneva. It is located in a tunnel with a circumference of 26.7 km. The tunnel previously housed the Large Electron Positron Collider (LEP). The LHC accelerates two proton beams (heavy ions are also possible) in opposite directions and collides them at four collision points. At these collision points the four large detectors, ATLAS[42], CMS[43], LHCb[44] and ALICE[45], are located. ATLAS and CMS are general purpose detectors, designed to cover many potential signatures in order to search for the Higgs boson, performing SM precision measurement and search for beyond SM physics. LHCb focuses on b-hadron decays and CP violation. ALICE focuses on heavy ion collisions and studies the properties of the quark-gluon plasma.

The LHC is part of a larger accelerator complex, shown in Figure 3.1, where protons are pre-accelerated in several steps before injection into the LHC. Hydrogen atoms are stripped from the electrons and accelerated by the linear accelerator, LINAC-2 to 50 MeV. The protons are further accelerated to 1.4 GeV by the Proton Synchrotron Booster, followed by the Proton Synchrotron increasing the energy to 25 GeV (PS). The protons are then injected in the Super Proton Synchrotron (SPS) accelerating the protons to 450 GeV. The protons are then filled in the LHC and accelerated to their final energy.

In 2010 and 2011, the LHC tooks proton-proton collision data at a center-of-mass energy of $\sqrt{s} = 7$ TeV. In 2012 it was increased to $\sqrt{s} = 8$ TeV. The operation at 7 and 8 TeV is called the Run 1. Between 2015 and 2018 the LHC was operated with an increased center-of-mass energy of $\sqrt{13}$ TeV. This period is called Run 2. In 2022 the LHC started the Run 3 at $\sqrt{s} = 13.6$ TeV. Besides the center-of-mass energy, the luminosity is an important quantity of an accelerator. For a process with cross section σ, the event rate this process is given by:

$$\dot{N} = \sigma \mathcal{L} \tag{3.1}$$

, with the instantaneous luminosity $\mathcal{L}$. The total number of expected events over the time of operation is given by:

$$N = \sigma L = \int \sigma \mathcal{L}(t) dt \tag{3.2}$$

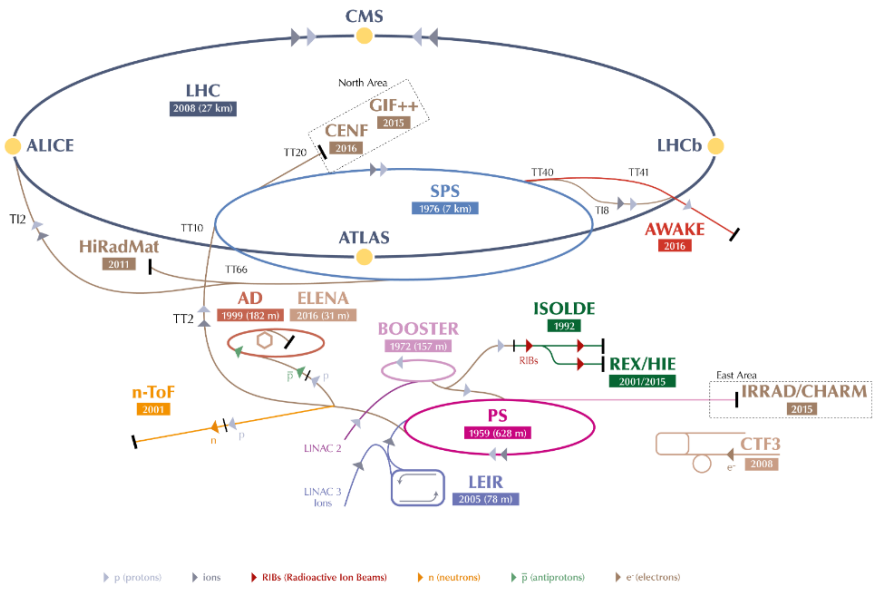

Figure 3.1: The accelerator complex at CERN with the LHC [47].

with the integrated luminosity L. The instantaneous luminosity is given by:

$$\mathcal{L} = \frac{N^2 k_b f}{4\pi\sigma_x^* \sigma_y^*} F \tag{3.3}$$

where N is the number of particles per bunch, k_b is the number of bunches, f is the revolution frequency, σ_x^* and σ_y^* are the horizontal and vertical beam size at the interaction point and F is the geometrical reduction factor from the crossing angle. At the LHC, the proton beams consist of 2808 bunches with up to 10^{11} protons per bunch. The bunches are collided every 25 ns. The LHC is designed to operate with an instantaneous luminosity of $\mathcal{L} = 10^{34}$ cm^{-2}s^{-1}, but but more than twice of the design value was reached in 2017.

During the Run 1 the LHC delivered an integrated luminosity of 5.46 (22.8) fb^{-1} at 7 (8) TeV, out of which 5.08 (21.3) fb^{-1} were recorded by ATLAS with 4.57 (20.3) fb^{-1} have a good enough quality for physics analyses. During the Run 2, the LHC delivered collisions with an integrated luminosity with 156 fb^{-1}, of which 147 fb^{-1} were recorded by ATLAS and 139 fb^{-1} of the data being good for physics analyses[46] as seen in Figure 3.2. Run 3 aims for an integrated luminosity of about 450 fb^{-1} until end of 2025. At the high instantaneous luminosity of the LHC, multiple proton-proton collisions happens during bunch crossing. These additional collisions are referred as pile-up. Also collisions from adjacent bunch crossings may overlay with the recorded event, adding to the pile-up. During Run 2 the average number of collisions per bunch crossing was $< \mu >= 33.7$, as seen in Figure 3.2.

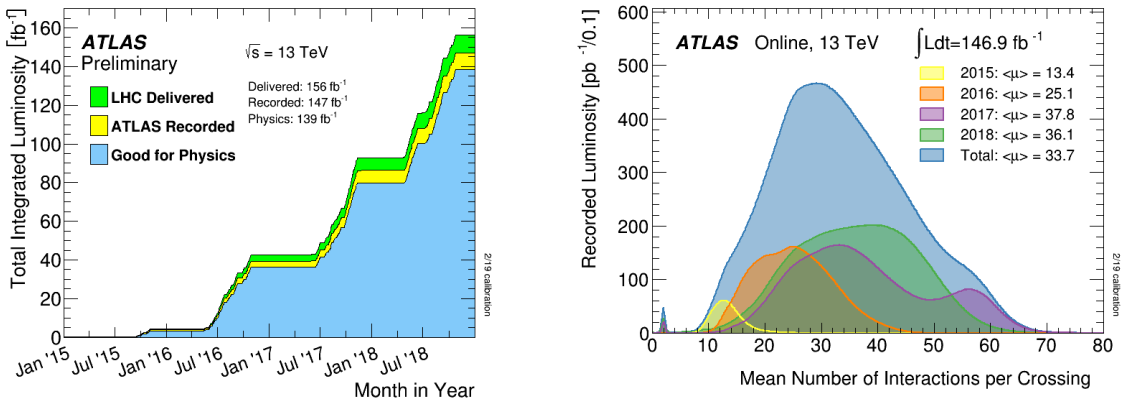

(a) (b)

Figure 3.2: Integrated luminosity during Run 2 (a) and distribution of the average number of interactions per bunch crossing (b) during Run 2 [48].

CHAPTER FOUR

THE ATLAS EXPERIMENT AT THE LARGE HADRON COLLIDER

The ATLAS detector is one of the four main LHC experiments [42]. It has a cylindrical shape with a length of 44 m and a diameter of 25 m. The detector covers almost the full solid angle. The detector consists of three main subsystems, with the Inner Detector (ID) in the center, surrounded by the Calorimeter System and the Muon Spectrometer (MS) as the outermost system. The ID and MS are immersed in a magnetic field that is generated by two independent magnetic systems. A schematic cut-away view of the ATLAS detector is shown in Figure 4.1. The description below follows Ref [42]

4.1 Coordinate System

The coordinate system used for ATLAS is a right-handed coordinate system with origin at the nominal interaction point. The z-axis points along the beam, the x-axis points towards the center of the LHC ring and the y-axis points upwards. Conveniently, spherical polar coordinates are used. The azimuthal angle ϕ is defined around the beam axis with respect to the positive x-axis. The polar angle θ is defined with respect to the positive z-axis. Instead of the polar angle the pseudorapidity η given by:

$$\eta = -\ln(\tan\frac{\theta}{2}) \ . \tag{4.1}$$

In the massless limit the pseudorapidity is equivalent to the rapidity y:

$$y = \frac{1}{2}\ln\frac{E + p_z}{E - p_z} \ , \tag{4.2}$$

with the energy E and the longitudinal momentum p_z of a particle. The transverse momentum p_{T} is the momentum of the particle perpendicular to the beam axis and is defined as

$$p_{\mathrm{T}} = p\sin\theta \ . \tag{4.3}$$

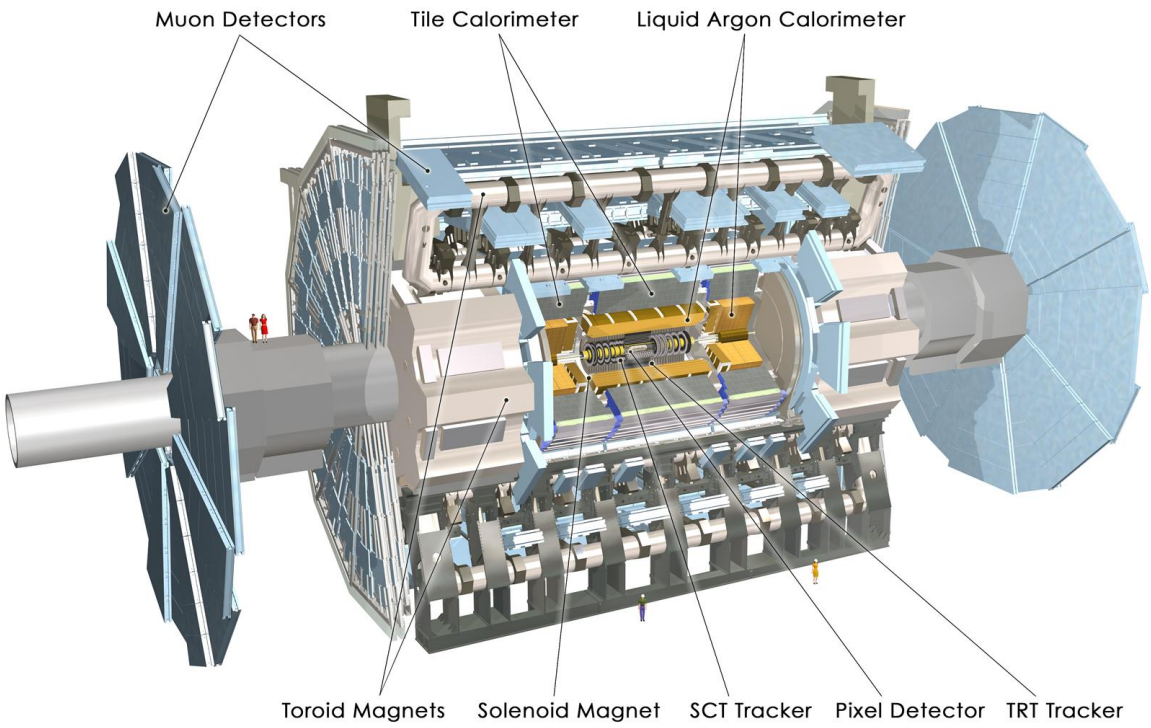

Figure 4.1: Schematic cut-away view of the ATLAS detector [42].

Analogous the transverse energy is defined as

$$E_T = E \sin\theta \, . \tag{4.4}$$

The angular separations ΔR and ΔR_y between two particles in the η-ϕ and in the y-ϕ plane, respectively, are defined as

$$\Delta R = \sqrt{(\Delta\eta)^2 + (\Delta\phi)^2} \tag{4.5}$$

and

$$\Delta R_y = \sqrt{(\Delta y)^2 + (\Delta\phi)^2} \, . \tag{4.6}$$

The angular separations are invariant under Lorentz boosts in the z-direction.

4.2 The Inner Detector

The innermost part of the ATLAS detector is the ID. The ID is used to measure the tracks of charged particles within the range of $|\eta| < 2.5$. Furthermore it allows the reconstruction of vertices. The trajectories of charged particles are bend by a 2T magnetic field produced by a cylindrical

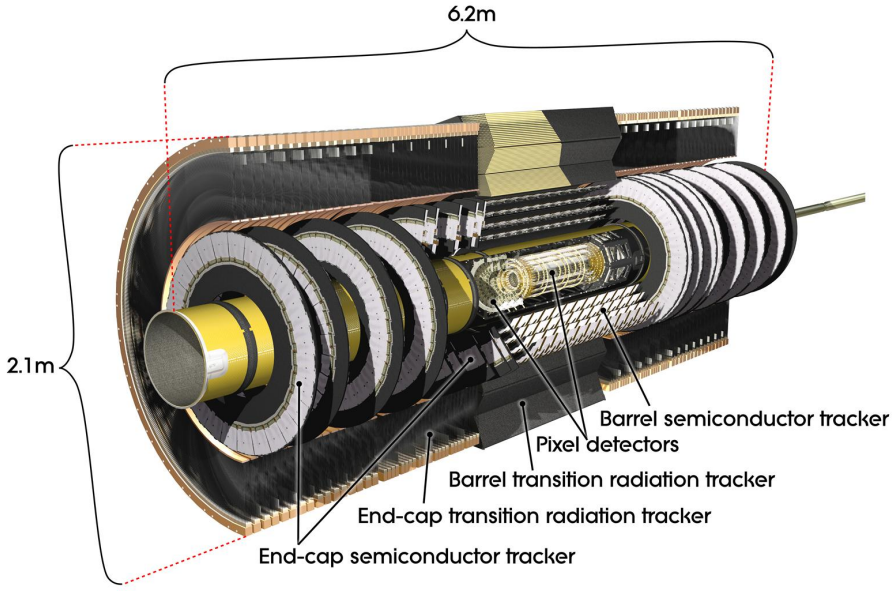

Figure 4.2: Schematic cut-away view of the ATLAS Inner Tracking Detector [49].

superconducting solenoid magnet. The magnetic field is orientated along the z-axis. The curvature of the tracks allows the measurement of the momentum and sign of the charge of charged particles. The ID is divided into three subsystems, the pixel detector, the Semiconductor Tracker (SCT) and the Transition Radiation Tracker (TRT). The ID is shown in Figures 4.2 and 4.3.

4.2.1 The Pixel Detector

The pixel detector is the innermost part of the ID. It consists of pixel sensors arranged in four layers in the barrel and three discs in each endcap. The layers in the barrel are at a distance of 33, 51, 89 and 123 mm from the beam. The discs in the endcap region are mounted in a distance of 495, 580 and 650 mm of the nominal interaction point. The typical size of the pixels is 50×400 μm. The innermost layer, the Insertable B-Layer (IBL) was installed during the first long shutdown before the start of Run 2 [51][52].

4.2.2 The Semiconductor Tracker

The Semiconductor Tracker (SCT) surrounds the Pixel detector. It consist of silicon semiconductor detectors, arranged in four cylinders in the barrel and nine discs in each endcap. It is composed of silicon microstrip sensors in double layers with a small angle between the two layers, allowing the

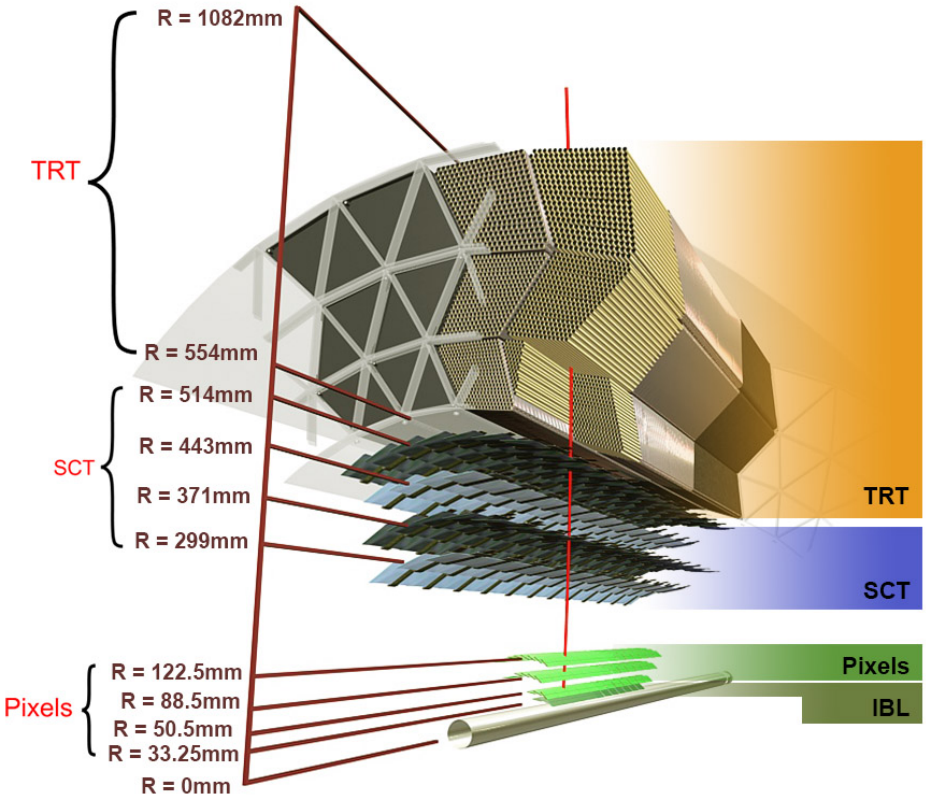

Figure 4.3: The tracking layers of the ATLAS Inner Detector [50].

measurement of a two-dimensional position of the traversing particle. The layers of the barrel have a distance of 299, 371, 443 and 514 mm of the beam. The endcap discs are mounted in distances between 853 mm and 272 mm.

4.2.3 The Transition Radiation Tracker

The outermost part of the ID is the transition radiation tracker (TRT) [53]. It covers the region of $|\eta| < 2.0$ The TRT consists of straw drift tubes filled with a $Xe/CO_2/O_2$ gas mixture. In the center of each straw tube there is a 31 μm diameter tungsten anode wire. In between the straw tubes the space is filled with a polypropylene radiator material. The straw tubes in the barrel region are aligned parallel to the beam while the straw tubes in the endcaps are oriented radially. The resolution of each straw tube is about 130 μm in the R-ϕ plane. Traversing tracks leave typically about 36 hits per track in the TRT. Traversing charged particles emit transition radiation in the radiator material that is detected by the straw tubes. Since it is much more likely for electrons to emit transition radiation than for heavier particles, the TRT helps identifying electrons [54, 55].

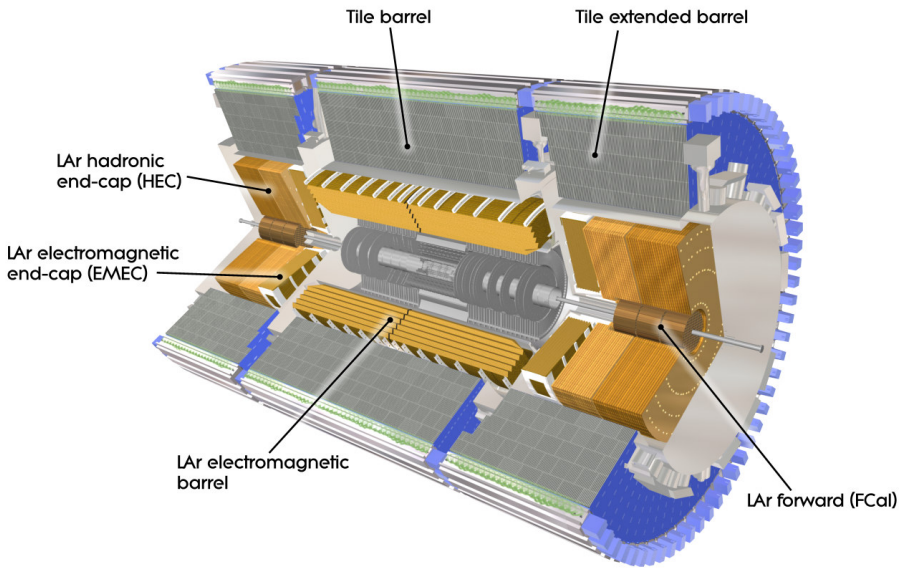

Figure 4.4: The ATLAS Calorimeter System [42].

4.3 The Calorimeter System

The ID is surrounded by the calorimeter. It covers the pseudorapidity range of $|\eta| < 4.9$. It is divided into three main subsystems the electromagnetic calorimeter, the hadronic calorimeter and the forward calorimeter [42][56][57][58]. The calorimeter is shown in Figure 4.4. The calorimeter measures primarily the energy of electrons, photons and hadrons. Electrons, photons and hadrons interact with high-density absorber layers, forming showers of secondary particles. The deposited energy is measured in the active material in between the passive layers.

4.3.1 The Electromagnetic Calorimeter

The electromagnetic calorimeter consists of alternating layers of lead as passive and liquid Argon (LAr) as active material arranged in an accordion-like shape. The LAr is ionized by electromagnetic showers produced in the absorber plates. The electromagnetic calorimeter is divided into a barrel part, covering the range of $|\eta| < 1.475$, and the two endcaps covering the range of $1.375 < |\eta| < 3.2$. The thickness of the electromagnetic calorimeter is more than 22 and 24 radiation lengths in the barrel and endcap region, respectively. In the range $|\eta| < 1.8$ a presampling detector is installed in front in the cryostat of the solenoid magnet of the ID. This allows corrections due energy losses in the detector material before the calorimeters, especially the solenoid coil. The $\Delta\eta \times \Delta\phi$ granularity of the calorimeter radially decreases.

4.3.2 The Hadronic Calorimeter

The electromagnetic calorimeter is surrounded by the hadronic calorimeter which uses layers of steel plates as passive material with scintillator tiles in between as active material. It covers the region of $|\eta| < 1.7$ consisting of a central barrel with a length of 5.8 m and two extended barrels, 2.6 m in length. Each barrel is built from 64 modules of size $\Delta\phi \sim 0.1$. The thickness of the barrel is approximately 7.4 interaction lengths. The hadronic calorimeter is extended by two LAr calorimeter endcaps covering the region of $1.5 < | eta| < 3.2$.

4.3.3 The Forward Calorimeter

The pseudorapidity range of $3.1 < |\eta| < 4.9$ is covered by two forward calorimeters (FCal). Each endcap consists of one electromagnetic and two hadronic modules. The inner module uses cooper as passive material. The other modules uses tungsten instead. All modules use LAr as active material.

4.4 The Muon Spectrometer

The outermost subsystem of the ATLAS detector is the MS [59]. The MS is shown in Figure 4.5. In contrast to electrons, photons and hadrons, muons pass the calorimeters depositing only a small fraction of their energy. The MS is used to identify tracks of mouns and to measure their momenta with high precision. The MS is immersed in a magnetic field produced by superconducting toroid magnets with average field strengths of 0.5 T and 1 T in the barrel and the endcaps, respectively. Each toroid magnet consists of eigth coils symmetrically arranged in ϕ around the beam axis. The magnetic field bends the muon trajectories in the η direction. The MS covers the region $|\eta| < 2.7$. Three layers of Monitored Drift Tube (MDT) chambers are used to measure the muon trajectories. The MDTs are arranged in 16 sectors in ϕ in the MS barrel and are complemented in the middle and outer layer by three layers of Resistive Plate Chambers (RPC) for triggering. Each endcap of the MS consists of three wheels of MDT chambers. The innermost rings of the inner wheels consists of Cathode Strip Chambers (CSC) replacing MDTs because of their higher rate capability. The triggering in the endcaps is performed by Thin Gap Chambers (TGC) in the inner and middle wheels.

4.4.1 The Monitored Drift Tubes

The MDT chambers consists of 400 μm thin aluminum tubes with a diameter of 30 mm filled with a Ar/CO_2 (93%/7%) gas mixture of 3 bar. Traversing muons ionize the gas. The ionization electrons drift towards the anode wire in the center due to the electric field between wire and tube wall. By

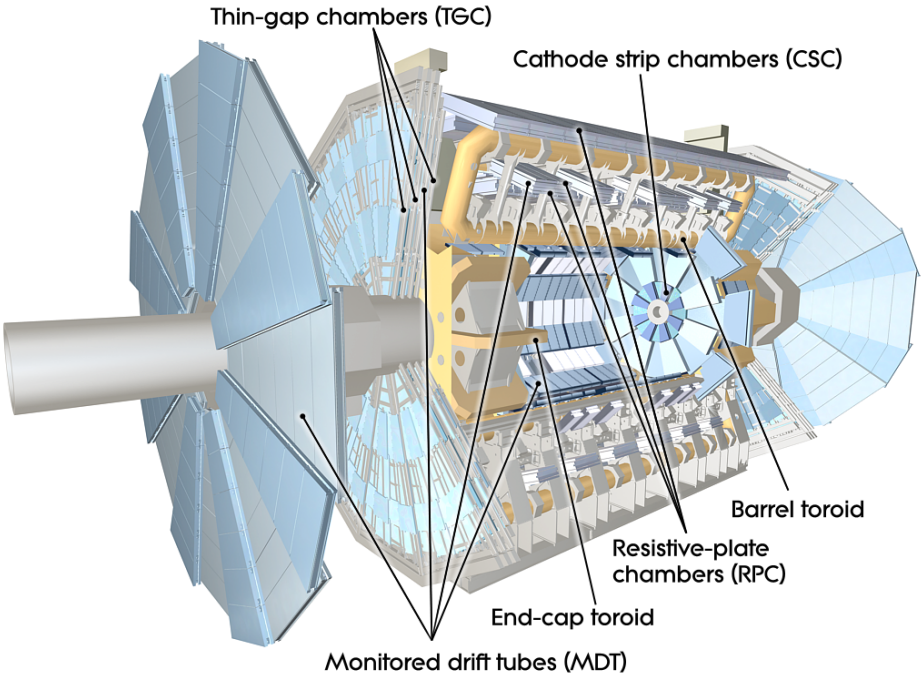

Figure 4.5: Schematic cut-away view of the ATLAS Muonspectrometer [42].

measuring the time the electrons need to reach the wire, the distance of the muon trajectory from the wire, the drift radius, can be determined with high precision. For the high-luminosity LHC, MDTs in the inner barrel layer will be replaced by small-diameter Monitored Drift Tube (sMDT) chambers with a tube diameter of 15 mm. This upgrade is described in Chapter 5. The functionality of the MDTs is described in more detail in Section 5.2.1.

4.4.2 The Cathode Strip Chambers

The CSCs are multi-wire proportional chambers consisting of four layers of radially orientated anode wires. Each wire layer is enclosed by two cathode strip layers. The readout strips are orientated parallel and perpendicular to the wires measuring the η and ϕ coordinates.

4.4.3 The Resistive Plate Chambers

The RPCs consists of two resistive electrode plates with a 2 mm gas filled gap in between. A high voltage of 10 kV is applied between the plates. On both sides of the gas gap, orthogonal readout strip panels are mounted, allowing for measurement of the η and ϕ coordinates of traversing muon tracks. The time resolution is about 1 ns.

4.4.4 The Thin Gap Chambers

The TGCs are multi-wire proportional chambers with wires in a thin gas gap between two parallel resistive plates. Readout strip panels measure the ϕ coordinate while the η coordinate is measured from the signals on the wires. The time resolution is better than 25 ns.

4.5 The Trigger System

During operation the LHC collides proton bunches at a rate of 40 MHz. This rate exceeds the computing and storage capacities. However, most of the collision events are interactions without large momentum transfer and are not interesting for physics analysis. The trigger system is designed to reduce the recorded event rate by selecting those events that are interesting for further studies, such as events with high p_{T} leptons, jets or $E_{\mathrm{T}}^{\mathrm{miss}}$. The trigger systems works in two stages, the level-1 (L1) trigger and the High-Level-Trigger (HLT) [60][61][62–65]. The hardware-based L1 trigger reduces the event rate from the originally 40 MHz to approximately 100 kHz. The L1 trigger uses information from the trigger chambers of the MS to identify high energetic muons and from the calorimeters to identify energy clusters from high energetic electrons, photons, τ leptons and jets or to identify large imbalances in transverse momentum. The L1 trigger then defines Regions of Interest (ROI) that are then processed by the HLT. Events accepted by the L1 trigger are then processed by the software-based HLT. The HLT reconstructs the Event using the ROIs defined by the L1 trigger. The HLT reduces the event rate to about 1 kHz. Events selected by the HLT are then permanently stored. The rate of the individual triggers depend on the instantaneous luminosity as well as the p_{T} threshold and quality requirements on the selected object. Triggers that exceed their rate limit are prescaled with a factor n, by selecting only every n-th event for this trigger. Therefore, during analysis data events selected by prescaled triggers have to be weighted with its prescale factor. With the increased luminosity during the later years of Run 2, the p_{T} threshold of the lowest unprescaled trigger increased. Most analyses used only unprescaled triggers. However, the search for sleptons presented in Chapter 7 utilizes prescaled lepton triggers for the estimation of the fake background.

4.6 Object Reconstruction and Identification

The raw signals measured by all the detector elements during data taking, are used to reconstruct and identify the particles that are then used as inputs for the physics analyses. A illustration of the interactions of different particle types with the subsystems of the ATLAS detector is shown in Figure 4.6.

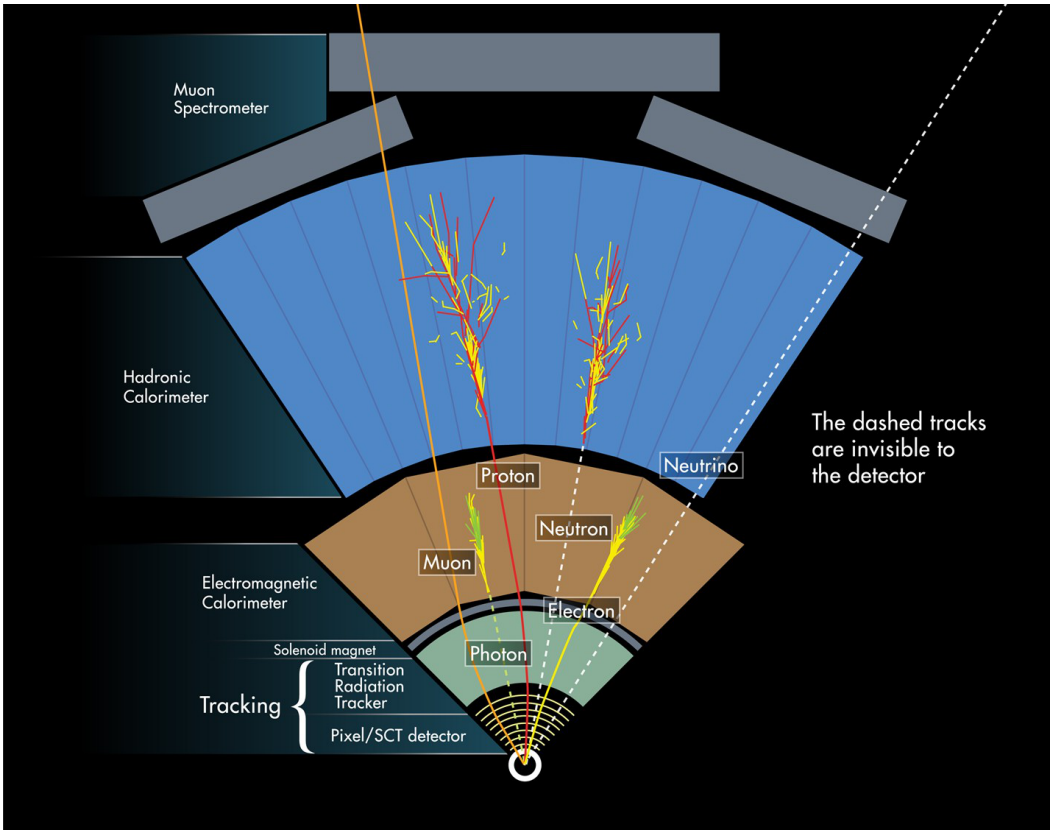

Figure 4.6: Particle signatures in the ATLAS detector [66].

4.6.1 Tracks and Vertices

The trajectories of charged particles are reconstructed using hits in the ID [67–70]. From the curvature of the track within the magnetic field, the transverse momentum as well as the sign of the charge of the particle can be obtained. The reconstruction starts by assembling the raw measurements of the Pixel Detector and the SCT into clusters. Three-dimensional measurements called space-points are created, representing the point where the charged particle traversed the active material of the ID. Track candidates are built using a combinatorical Kalman filter [71] from seeds formed from sets of three space-points. Ambiguities among the track candidates are resolved based on the number of pixel and SCT clusters and by using a neural network to identify merged clusters [72]. The remaining tracks are extrapolated to the TRT. A second approach starts from hits in the TRT that are then extrapolated to the silicon detectors. This approach is more efficient to reconstruct tracks from secondary vertices or from photon conversions that may not have enough hits in the silicon detector. The tracks in the ID are than used to reconstruct the primary and secondary vertices [73, 74]. The primary vertex is typically defined to be the one with the highest Σp_{T}^2. The longitudinal and transverse impact parameters z_0 and

d_0 are the closest distances of a track to the primary vertex.

4.6.2 Electrons

Electrons deposit the majority of their energy in the electromagnetic calorimeter. Therefore, electrons are reconstructed using clusters in the electromagnetic calorimeter. Furthermore, electrons as a charged particle are required to have a track in the ID matched to the energy deposit in the calorimeter. The electron reconstruction starts with clusters in the electromagnetic and hadronic calorimeters, so called topo-clusters, using neighbouring calorimeter cells with deposited energies above a noise threshold. The energies in the cells are measured at the EM scale accounting for the energy deposited by electromagnetic showers. Tracks in the ID are loosely matched to the clusters. Electrons require at least on matched track. Additional requirements are used to select the primary electron track in case multiple tracks matches the cluster. The EM topo-clusters with a matched track are used as seed to build super clusters. EM topo-clusters near the seed cluster which may emerge due to bremsstrahlung are added as satellite clusters if they satisfy criteria. The final superclusters define the electrons. The electron energy is calibrated using $Z \rightarrow e^+e^-$ events [75].

In order to reject misidentified hadrons and converted photons selected electrons have to fulfill quality and identification requirements [76]. A likelihood discriminator is constructed using properties of the primary electron track, the shape electromagnetic shower in the electromagnetic calorimeter and the compatibility of the electron track with the reconstructed cluster. The discriminator is used to define three working points, called LooseLLH, MediumLLH and TightLLH. The identification efficiencies are 93%, 88% and 80%. For the LooseLLH working point, there is an additional variant (LooseAndBLayerLLH) that requires additional hits in the IBL.

4.6.3 Photons

Similar to electrons, photons deposit their energy in the electromagnetic calorimeter. Therefore, photons are reconstructed starting from the same clusters and track as electrons. Photon conversion vertices are build. Photons are classified as converted photons if they are matched to a track from a conversion vertices. Otherwise photon have no matched track. The energy of photons is calibrated using $Z \rightarrow e^+e^-\gamma$ events [75]. In order to reject backgrounds from hadronic jets additional quality requirements are applied. The photon identifcation use a cut-based selection using the shape of the shower in the electromagnetic calorimeter. Three working points are defined, called Loose, Medium and Tight. The Loose working point is used in the trigger algorithms in 2015 and 2016, while the Medium working point is used in 2017 and 2018.

4.6.4 Muons

Muons are passing the calorimeter, because compared to electrons and photons they are are less subject to undergo bremsstrahlung, due to their much higher mass. Also, unlike hadrons they do not participate in the strong interaction. There are different approaches to reconstruct muons. They can be reconstructed using only a track in the MS (Standalone muon), by requiring a track in the ID and corresponding energy deposits in the calorimeter, compatible with that from a minimal ionizing particle (Calorimeter tagged muon), by requiring a track in the ID matched to a track in the innermost layer of the MS (Segment tagged muon) or by requiring a track in the ID matched to a track in MS (combined muons). The analyses in this thesis use combined muons only. Muons are calibrated in $Z \rightarrow \mu\mu$ and $J\psi \rightarrow \mu\mu$ events. In order to reject muons from semileptonic hadron decays quality criteria are applied to the muon candidates. Five working points are defined. The three working points Loose, Medium and Tight are designed to cover a wide range of analyses and cover the whole p_{T} spectrum. The working points low-p_{T} and high-p_{T} are optimized for low and high p_{T} regions [77].

4.6.5 Jets

Quarks and gluons produce a shower of secondary particles, that are moving in the same direction. These particles are reconstructed as a jet. Jets are reconstructed using the anti-k_t algorithm [78] with a radius parameter of $\Delta R = 0.4$. As input for the anti-k_t algorithm either topo-clusters or a combination of charged particle tracks and calorimeter energy deposits are used [79]. The latter of the two is referred as particle-flow reconstruction technique [80]. In the analysis described in Chapter 6 jets reconstructed from topo-clusters are used, while the analysis described in Chapter 7 uses jets reconstructed with the particle-flow reconstruction technique. Topo-clusters are build by clustering neighbouring calorimeter cells with energy deposits above a noise threshold [81]. The particle flow algorithm combines tracks from the ID and energy deposits in the calorimeter. Energy deposits from charged particles are substracted from the topo-cluster and replaced by momenta of tracks to those topo-clusters. This technique improves energy and angular resolution as well as reconstruction efficiency and pile-up stability. The jet energy scale (JES) calibration restores the jet energy to that of jets reconstructed at the particle level. In the first step contributions from pile-up are removed. In the absolute JES calibration, the energy and direction are corrected to truth jets from simulated events. In the global sequential calibration, the jet p_{T} resolution and associated uncertainties are improved using information from the tracking, calorimeter and muon chamber detector systems. In the final step, remaining differences between data and simulation are corrected by applying a residual in-situ calibration using well-measured objects such as photon and Z bosons [79]. Jets from pile-up are rejected by the jet vertex tagger (JVT) that utilizes the tracks associated with the jet [82].

Jets originating from b-quarks are identified using multivariate techniques, utilizing the long lifetime of b-hadrons of about 1.5 ps. It uses impact parameters of the tracks associated with the jet as well as the secondary vertices formed by these tracks. Jets identified as originating from b-quarks are called b-tagged jets [83].

4.6.6 τ leptons

In contrast to electrons and muons, τ leptons decay before interacting with the detector and are therefore identified using their decay products. τ leptons that decay leptonically into a light lepton are reconstructed as electron or muon and are not distinguished from them. The reconstruction of τ leptons that decay into hadrons takes anti-k_t with a radius parameter of $\Delta R = 0.4$ as input [84]. Compared to jets originating from quarks and gluons, a τ_{had} has a narrow shower shape with 1 or 3 tracks in its center ($\Delta R < 0.2$) and a total charge of ± 1. These tracks are used to reconstruct the τ decay vertex. The number of associated tracks in the inner core defines the prongness. A Recurrent Neural Network (RNN) is used to distinguish τ leptons from quark and gluon jets utilizing the shower shape in the calorimeter, the energy deposit in the core and outer region of the jet and the track impact parameters [85]. Three working points are defined, called Loose, Medium and Tight with an identification efficiency of 70% (60%), 60% (55%) and 40% (35%), respectively, for 1-prong (3-prong) τ leptons.

4.6.7 Missing transverse Momentum

Neutrinos and potential beyond the Standard Model particles, that are only interacting very weakly with the detector material, escape the detector undetected. However, due to the momentum conservation, particles leaving the detector undetected cause an imbalance in the total transverse momentum. This imbalance is called missing transverse momentum $p_{\mathrm{T}}^{\mathrm{miss}}$ and is calculated using the momenta of reconstructed particles as well as energy deposits not associated with any physics object, the so called soft-term

$$p_{x(y)}^{\mathrm{miss}} = -\sum_{i=e,\mu,\tau,\mathrm{jets}} p_{x(y)}^{i} + p_{x(y)}^{\mathrm{miss,\,soft}} \,. \tag{4.7}$$

The magnitude of the missing transverse momentum is called missing transverse energy [86]

$$E_{\mathrm{T}}^{\mathrm{miss}} = \sqrt{(p_x^{\mathrm{miss}})^2 + (p_y^{\mathrm{miss}})^2} \,. \tag{4.8}$$

4.6.8 Lepton Isolation

Prompt leptons are typically isolated from hadronic activity in the detector, while leptons from semi-leptonic decays of b and c hadrons are usually in the vicinity of jets and therefore additional hadrons. The separate prompt electrons and muons from non-prompt leptons isolation criteria are defined using either the transverse momenta of ID tracks or the transverse energies of calorimeter clusters in a cone around the lepton. The radius of the cone ΔR is either of fixed size or of variable size $\Delta R = \min(\frac{10}{p_{\mathrm{T}}}, \Delta R_{\mathrm{max}})$ where ΔR_{max} is the maximum cone size. Typically a cone size of 0.2, 0.3 or 0.4 are chosen. In the case of a variable radius, the cone size shrinks with increasing lepton p_{T}. Several isolation working points are defined based on the amount of transverse momenta of ID tracks or the transverse energies of calorimeter clusters inside the cone compared to the lepton p_{T} [75, 77]. Some of the SUSY models considered in the analysis described in Chapter 6 have collimated lepton pairs, which isolation cones may overlap. In order to prevent such lepton pairs to fail the isolation criteria, the contributions to the isolation variables from nearby leptons are not taken into account. The search described in Chapter 7 uses a BDT to identify prompt leptons. This approach was already used in several analysis, such as the one in Ref. [87].

4.7 Event Simulation

Monte Carlo simulations are used to model potential signals, estimating the background from SM processes or assisting the development and optimization of algorithms for reconstruction and identification of particles. It is crucial that the data is described well by the simulated events.

The Monte Carlo simulation is done in several steps. The first step, the event generation, simulates the production of particles as well as their decay chain in pp collisions. Typically, hundreds of particles covering a wide range of energies are produced in these collisions. The hard-scattering event, where heavy particles are created, can be calculated perturbatively [88]. Protons are not elementary particles, but consist of quarks and gluons which carry fractions x of the total momentum of the proton. The cross-section of two protons producing a final state X, $\sigma(pp \to X)$ can be described, according by the factorization theorem, by the perturbatively calculated hard-scattering cross-section of two partons a and b producing X, convoluted with the parton density functions (PDF) f_a and f_b

$$\sigma(pp \to X) = \sum_{a,b} \int_0^1 dx_a dx_b \int f_a(x_a, \mu_F) f_b(x_b, \mu_F) d\sigma_{ab\to X}(\mu_F, \mu_R) \,, \tag{4.9}$$

where $d\sigma_{ab\to X}(\mu_F, \mu_R)$ is the differential parton-level cross-section, which is calculated from the matrix element squared $|\mathcal{M}_{ab\to X}|^2$ [89]. The matrix element can be calculated from the Feynman

diagrams of the given process. The parton-level cross-section depends on the factorization scale μ_F and the renormalization scale μ_R. The choice for μ_F and μ_R are in principle arbitrary but the logarithmic structure of QCD defines limits on reasonable values [88]. The PDFs $f(x, \mu_F)$ are the probability that a parton has a fraction x of the proton momentum and depend on the factorization scale μ_F. The PDFs can not be calculated perturbatively, but are obtained from measurements in $ep/pp/p\bar{p}$ collisions [90–95]. After the hard-scattering, parton showers, that are produced by partons radiate gluons, that radiate further gluons or split into quark-antiquark pairs. This includes initial-state radiation (ISR) and final-state radiation (FSR). Parton shower creation, the hadronization of quarks and gluons, forming colorless hadrons, happens at low energies where α_s is large and therefore pertubation theory is not valid. The interactions of the remaining partons, not taking part in the hard-scattering process is added. These interactions are referred to as the underlying event. In the next step the hadronization of the parton showers into hadrons is simulated. Unstable hadrons are decayed into lighter particles with lifetimes long enough to reach the detector material. Furthermore, electromagnetic radiation, originating from charged particles is added. A pictorial representation of a $t\bar{t}H$ event is shown in Figure 4.7.

After the event generation, the propagation of the generated particles through the detector is simulated. GEANT4 [96] is used to simulate the interaction of the particles with the detector material as well as the deflection of the charged particles in the magnetic field. The energy deposits in the active sensors are stored. Using GEANT4 for the whole detector simulation (the so-called full simulation) is computationally expensive. Therefore, to reduce the computing time the fast simulation uses a parametrized model for the calorimeter response and GEANT4 for the ID and MS [97]. In the analyses described in this thesis the SM backgrounds are simulated using the full simulation while the SUSY signal models are simulated with the fast simulation.

The events are overlayed with simulated pile-up interactions. In the digitization step, the simulated energy deposits in the active sensors are converted into detector responses. The events are then reconstructed with the same algorithms used for the real data. Additional information about the generator-level particles corresponding to the reconstructed particles, the so called truth-information, is added.

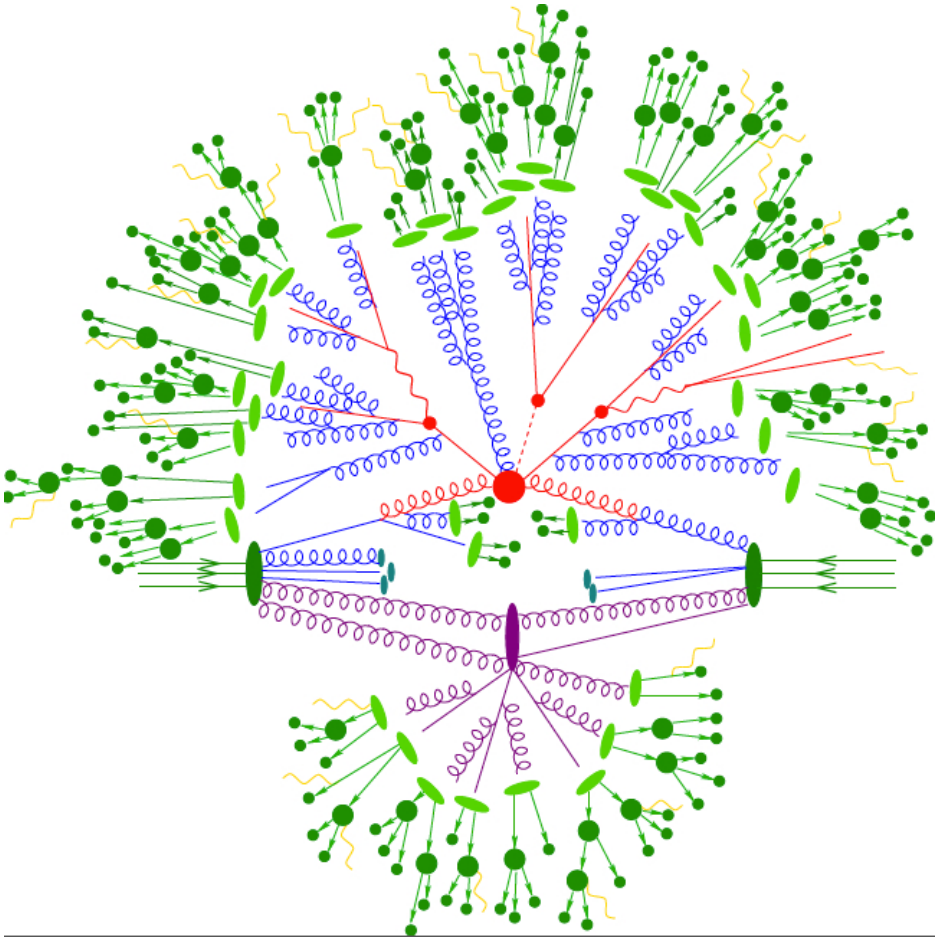

Figure 4.7: Pictorial representation of a $t\bar{t}H$ event. The hard scattering (big red blob) produced the top quark pair as well as the Higgs boson, which decay immediately indicated by the small red blobs. Initial and final state radiation is shown in red and blue. The underlying event is indicated in purple. The hadronization of the partons is shown as light green blobs while hadron decays are indicated as dark green blobs. Photons are depicted in yellow. [98, 99].

CHAPTER FIVE

UPGRADE OF THE ATLAS MUONSPECTROMETER

5.1 Overview

The LHC will be upgraded to the High Luminosity LHC, which will increase the luminosity [3, 4]. In order to be able to cope with the increased data rate the ATLAS detector will undergo major upgrades. The current schedule is shown in Figure 5.1.

These upgrades are divided into two phases: Phase-I happened during the Long Shutdown 2 (LS2) of the LHC from 2019 to 2021. Phase-II is scheduled between 2026 and 2028.

A major upgrade during Phase-I is the New Small Wheel (NSW) project [100], where the CSC and MDT chambers of the inner endcap wheels are replaced with small-strip TGC and Micro-Mesh Gaseous Structure (Micromegas) for triggering and precision tracking. For the phase-I and phase-II, new integrated sMDT+RPC chambers will installed in the inner barrel layer, which is described in section 5.2 in more detail [101–111].

5.2 The Barrel Upgrade Project

New thin-gap resistive plate chambers (RPC) will be installed in the inner barrel layer (BI) to improve the acceptance and efficiency at increased background rate capability. In the small sectors (BIS) in front of the toroid magnet coils, the present MDT chambers will be replaced with thinner sMDT chambers, in order to make space for the new RPCs and to increase the background rate capability [101]. The locations of the new sMDT and RPC chambers in the small sectors is shown in Figure 5.2. The sMDT chambers consist of drift tubes with half the tube diameter of the MDT chambers. A detailed description of the sMDT chambers is given in section 5.2.1.

The MDT and sMDT chambers use the following naming scheme. Chamber in the barrel are denoted with a B, an I, M or O indicate whether the chamber is in the inner, middle or outer layer. A S or L

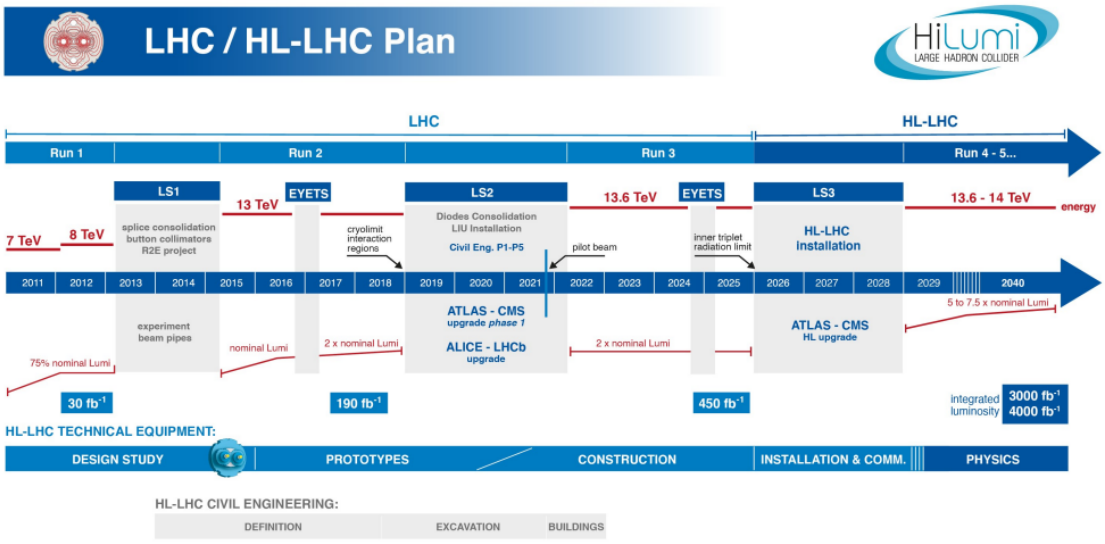

Figure 5.1: The LHC upgrade schedule [112].

indicates whether the chamber is in the small sectors, where the coils of the magnets are located, or the chamber is in the large sectors in between. Furthermore, the chambers within a half layer of each sector are numbered, starting with the chamber closest to the interaction point. an A or C indicates whether the chamber is on the detector side with positive or negative z coordinates. The name is finalized with a number indicating the ϕ sector. Even numbers corresponds to small sectors and odd numbers corresponds to large sectors. Consequential, the chamber closest to the interaction point in the inner layer, in the first small sector on the A side is called: BIS1-A02.

The replacement of the BIS MDT chambers by sMDT chambers proceeds in two stages. In the first stage, the Phase 1 upgrade in LS2, the BIS7 and BIS8 MDT chambers have been replaced by new combined BIS78 chambers. In the second stage, the chambers in the position 1 to 6 (see Figure 5.2) will be replaced in the Phase 2 upgrade in LS3.

5.2.1 Working Principle of sMDT chambers

The sMDT chambers consist of 400 μm thin aluminium tubes with a wire in the tube center. The drift tubes are filled with a Ar/CO_2 (93/7) gas mixture at 3 bar. A high voltage of 2730 V is applied between the anode wire and the tube wall. Muons traversing the drift tube ionize the Argon atoms along its trajectory creating free electrons and positive ions. In the electric field, the electrons drift

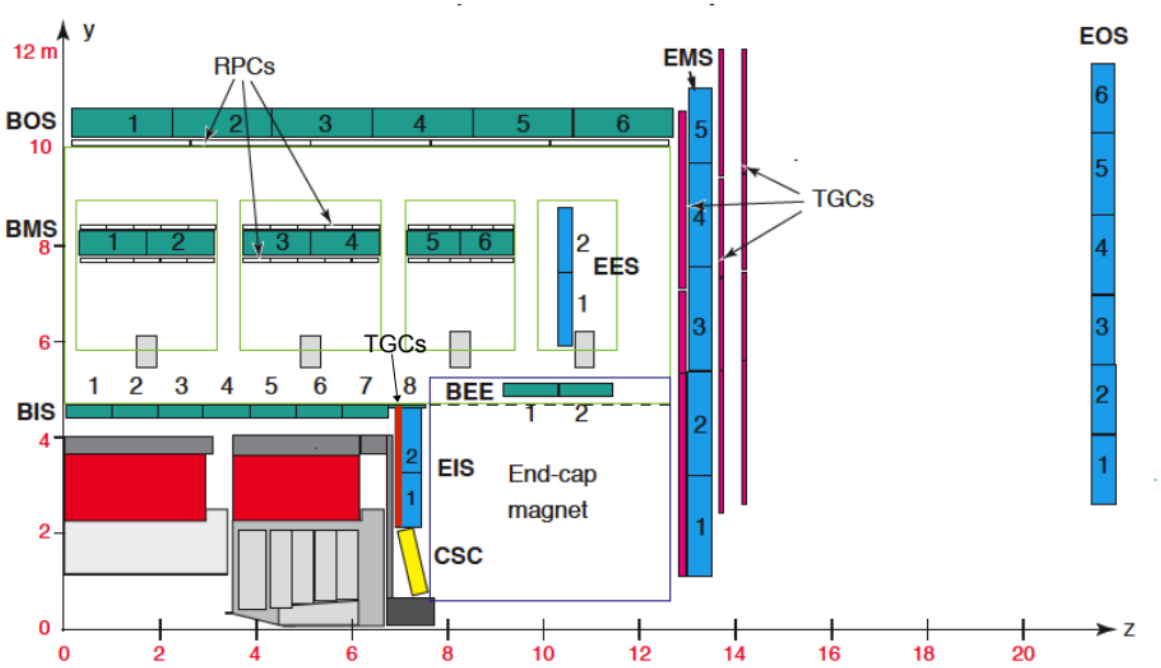

(a) ATLAS Muon Spectrometer in Run 1 and 2.

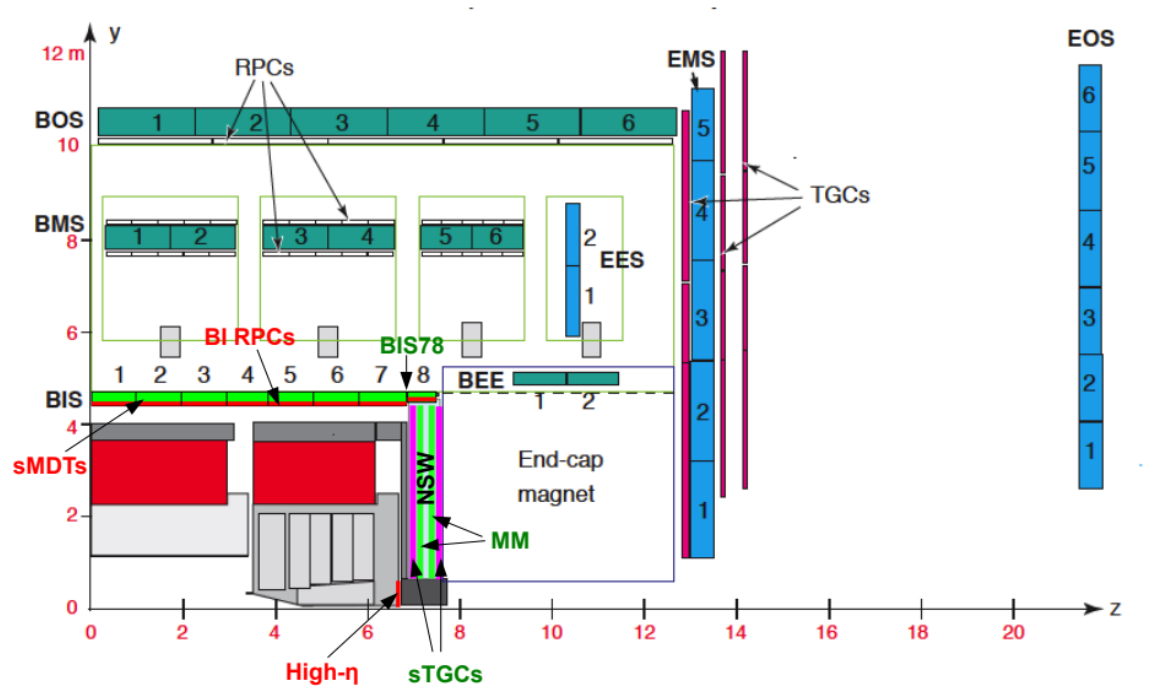

(b) ATLAS Muon spectrometer after Phase 2 upgrade for HL-LHC.

Figure 5.2: *R-z* cross sectional view of a quadrant of the ATLAS muon spectrometer showing a small sector (a) before and (b) after the upgrade for the HL-LHC [101].

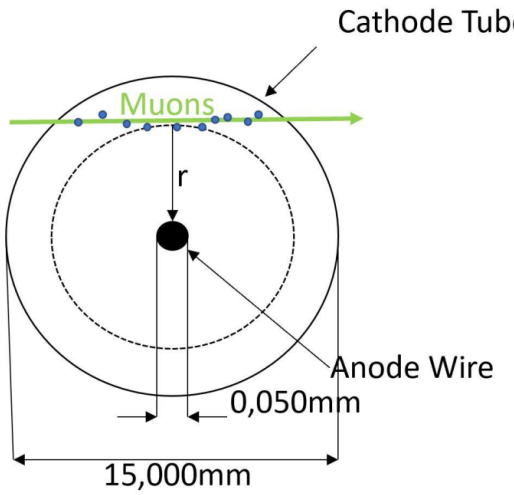

Figure 5.3: Cross section of a drift tube with the trajectory of a muon ionizing the drift gas.

towards the wire, while the positive ions drift to the tube wall. The drift velocity

$$\vec{v} = \mu\vec{E} \tag{5.1}$$

with charge mobility μ is much higher for electrons than for the ions, due to the much lower mass [113].

The radial electric field in the tube is given by:

$$E(r) = \frac{U}{\ln\frac{R}{r_{min}}}\frac{1}{r} \tag{5.2}$$

with the radius of the anode wire r_{min}, the inner radius of the tube R and the applied voltage U between wire and tube wall. Electrons near the wire gain sufficient high kinetic energy between collisions to ionize gas atoms amplifying the primary ionization charge in an avalanche.

The gas gain G is the ratio of charge in the avalanche and the amount of primary ionization. It is described by the Diethorn formula

$$\ln(G) = \ln(2)\frac{r_{min}E(r_{min})}{\Delta V}\ln(\frac{E(r_{min})}{E_{min}(\rho_0)}\frac{\rho}{\rho_0}) \tag{5.3}$$

where ρ is the charge density, ΔV the potential difference an electron passes between two successive ionizations and $E_{min}(\rho_0)$ the electric field required to start an avalanche in the drift gas [114]. For the MDT and sMDT gas mixture used the values are: $\Delta V = 34$ V and $E_{min} = 24\ \frac{\text{kV}}{\text{cm}}$.

The ATLAS MDT and sMDT chambers have a gas gain of $2 \cdot 10^4$ by choosing a potential of 3080 V

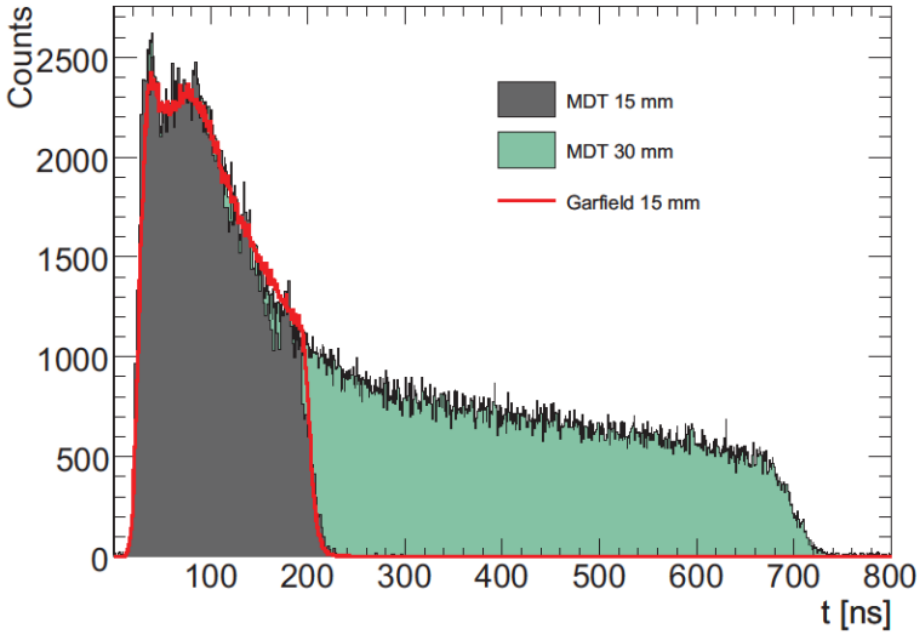

Figure 5.4: Drift time spectra of 30 mm and 15 mm diameter drift tubes [101].

and 2730 V, respectively, between wire and tube wall.

The drift time is the time difference between a trigger signal, indicating that a muon passed the tube, and the arrival of the first electrons at the wire. The drift time spectra of MDT and sMDT tubes are is shown in Figure 5.4. The drift time is translated into the drift radius, the distance between the muon trajectory and the wire using the measured space-to-drift-time relation shown in Figure 5.5.

The sMDT chambers consist of eight layers of drift tubes arranged in two multilayers with four layers each separated by a spacer frame. Using the measured drift radii in the drift tube layers traversed by the muon, the muon trajectory can be reconstructed. A cross section through the layers of a sMDT chamber is shown in Figure 5.6.

5.2.2 The Muon Chamber Alignment System

Knowledge of the relative positions of the muon chambers within the spectrometer is crucial in order to accurately reconstruct the muon tracks. For this purpose the chambers are equipped with an optical alignment monitoring system [115, 116]. The alignment system uses light rays from LED light sources illuminating a chess like pattern which are projected by lenses onto pixel cameras. By measuring the positions of the patterns on the cameras relative to reference positions for several such light rays connecting the chambers, the relative chamber positions can be monitored during the

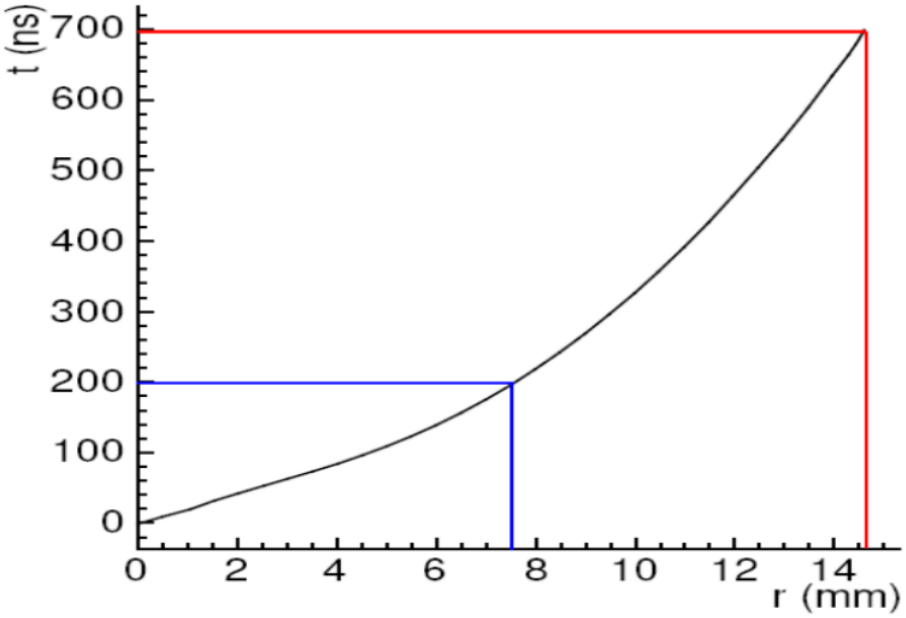

Figure 5.5: Space-to-drift-time relation of the MDT drift tubes. The maximum drift radii of the MDT chambers and the sMDT chambers are indicated in red and blue, respectively [101].

detector operation. The alignment system consists of projective alignment rays connecting chambers in the three layers of the spectrometer, and so called ”axial-praxial” sensors connecting neighbouring chambers within the same sector, and so called CCC sensors connecting the neighbouring sectors. The sensors are mounted on platforms that are glued on the chambers. The optical paths of the barrel alignment system are shown in Figure 5.7.

In addition, the MDT and sMDT chambers are equipped with ”in-plane” alignment systems which monitor deformations of the chambers, sagitta along or transverse to the tubes and torsion of the chamber around the tube axis. The chambers deform under the influence of gravity and other external forces. The following dominant deformations are considered for the sMDT chambers:

- Parabola-like bow on each chamberend transverse to the tubes, the readout (RO) and high-voltage (HV) supply side. The chambers are kinematically supported in two points on the RO side and in one point in the center of the HV side. Consequently, the bow is in opposite directions on both sides.

- Parabola-like bow along the tubes.

- Torsion of the chamber, i.e. relative rotation of the readout and high-voltage sides by a torsion angle.

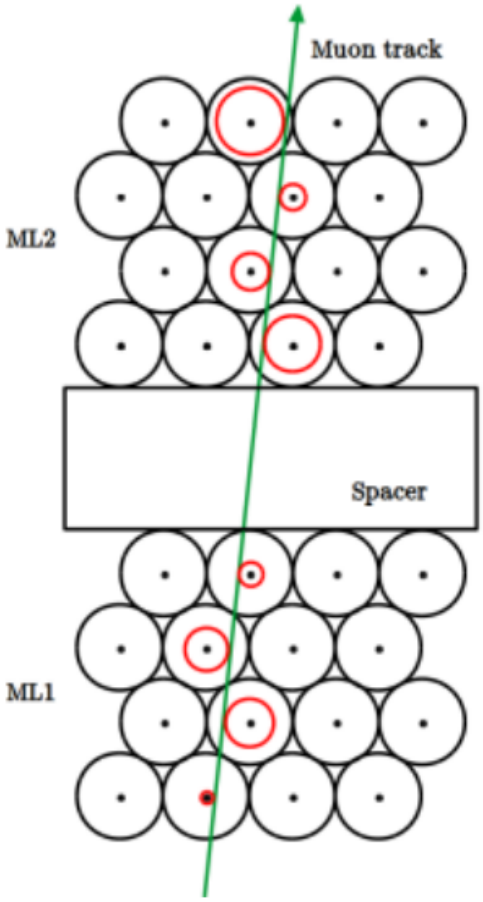

Figure 5.6: Schematic cross section of a sMDT chamber. The muon trajectory is reconstructed from a fit to the measured drift radii in 2×4 tube layers.

The in-plane alignment system consists four optical paths each with a pixel camera (CCD), a LED and a lense half-way between them [117]. In case of the BIS1-6 chambers, the in-plane alignment system is integrated into the spacer frame separating the two tube multilayers, while for the BIS78 chambers, the optical elements are positioned on the outer multilayer. Two parallel longitudinal paths measuring chamber sag while two diagonal paths measure torsion. In case of the BIS78 chambers, the longitudinal paths are along the readout and high-voltage side, perpendicular to the tubes, while for the BIS1-6 chambers they are along the tubes. The LEDs illuminate a chess like pattern (shown in Figure 5.9(c)) which is projected onto the CCDs via the lenses. By measuring the shift of the pattern with respect to a reference position, the deformation is determined. The measurement of the reference position is performed during the chamber assembly on a flat granite table. The ATLAS ARAMyS software [118] is used to determine the deformation from the data of the in-plane system. The torsion

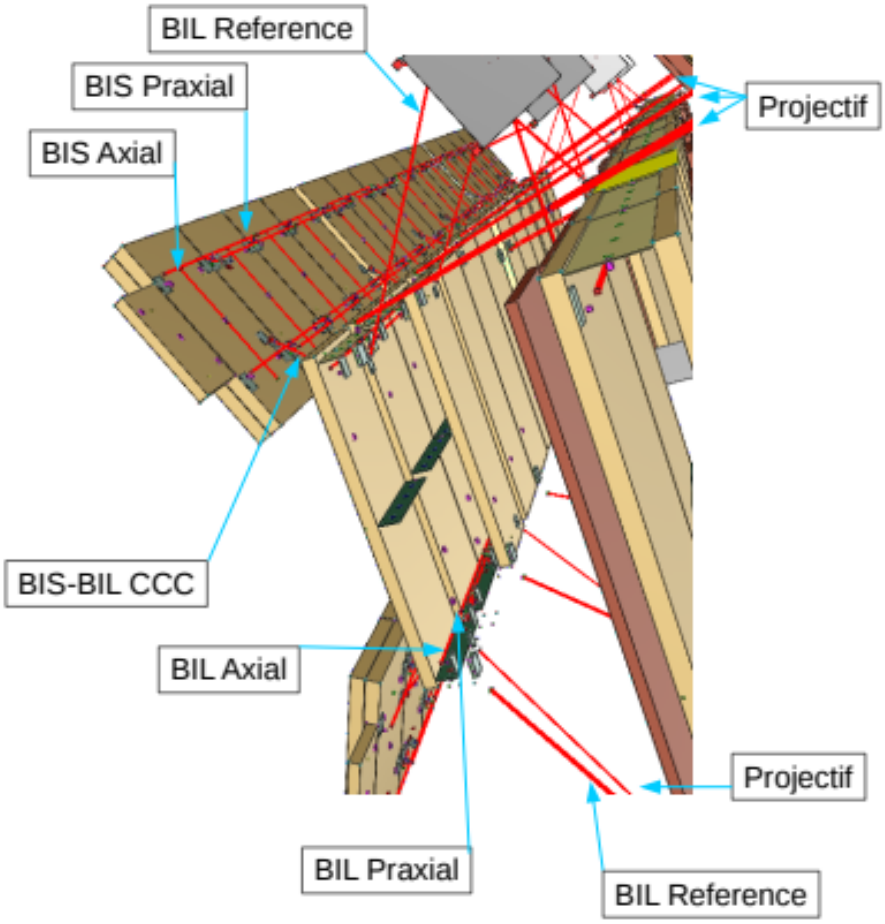

Figure 5.7: The optical alignment paths in two neighbouring sectors of the barrel MS [101].

angle α is obtained from the shifts in the two diagonal path y_{12} and y_{21}:

$$\alpha = \frac{(y_{12} - y_{21})}{d_{CCD}}, \tag{5.4}$$

where d_{CCD} is the distance between the two CCDs on the RO side and the y coordinate measured by the CCD is in the direction perpendicular to the tube layers. A drawing of the spacer frame of the BIS1-6 chambers with the integrated in-plane alignment system is shown in Figure 5.8. The assembled spacer frame with the LED, CCD and the chess like pattern that is used to determine the deformation is shown in Figure 5.9.

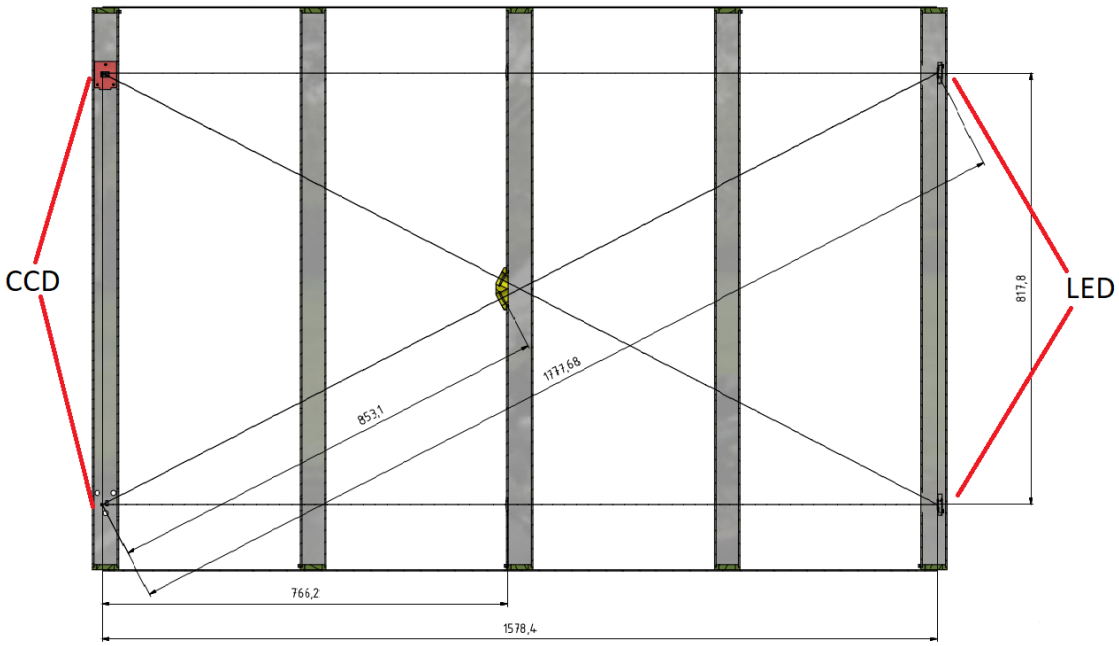

Figure 5.8: Drawing of the spacer frame of the BIS1-6 chambers with the integrated in-plane alignment system.

5.2.3 The BIS78 chambers

The BIS7 and BIS8 MDT chambers at the edges of the small sectors in the barrel in the layer are the first chambers that have first been replaced by new sMDT BIS78 chambers in the LS2 [109]. The BIS78 sMDT chamber upgrade serves as pilot project for the Phase 2 BIS1-6 sMDT upgrade. The 16 BIS78 chambers were produced at the Max-Planck-Institute for Physics (MPI) in 2017-2019 and installed in ATLAS for Run 3 end of 2020 [119]. Each BIS78 chamber consists of eight layers of drift tubes arranged in two multilayers separated by a spacer structure. While the inner multilayer only covers the area of the BIS7 chamber, the outer multilayer covers the area of both the BIS7 and BIS8 chambers. The layers of a chamber are numbered starting from the innermost layer. The tubes within one layer are numbered starting with the tube closest to the interaction point. The BIS78 chambers come in different sizes. 3 chambers on A and the C side have 78 and 96 tubes with length 1660 mm per layer in the inner and the outer multilayer 1 and 2, respectively. Other 5 chambers on A and C side are shorter, with 66 and 84 tubes per layer with shorter tube lengths of 1630 mm for 2 chambers on each side. In 4 of the chambers on each side, 30 tubes per layer in multilayer 2 towards BIS8 are shortened to 1530 mm as cutouts for structural elements of the endcaps inner wheel. Furthermore, each chamber has additional 12 tubes per layer in multilayer 2 as part BIS8 with a shorter length of 1000 mm overlapping with the inner endcap wheels [120]. On one end of the tubes, referred to as readout (RO), the readout electronic is mounted side. On the opposite end referred to as high voltage

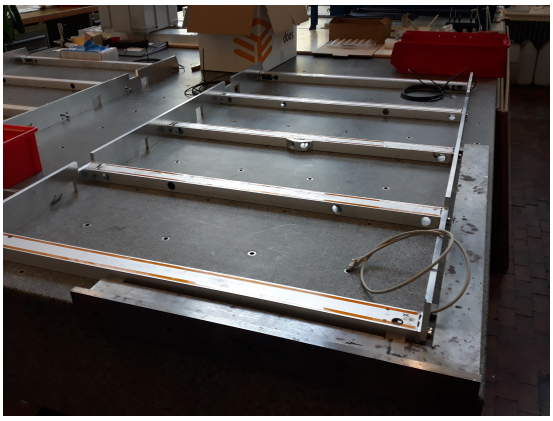

(a) Assembled spacer frame

(b) LED within the spacer bar

(c) chess like pattern

(d) CCD within the spacer bar

Figure 5.9: (a) The assembled spacer frame of a BIS1-6 chamber with the integrated in-plane alignment system. (b) LED within the spacer bar that projects a chess like pattern (c) onto the CCD (d) on the opposite side of the spacer frame.

(HV) side, the high voltage supply is connected. On the outermost layer of the chamber two support structures are glued, for mounting the chamber on rails on one- and two-points on the HV and RO side, respectively, in the ATLAS detector as well as in the frame for transporting.

On the outer multilayer, also the platforms for the global alignment sensors, the sensors of the in-plane alignment system and 4 B-field sensors mounting platforms are glued. There are four platforms for axial-praxial sensors and two platforms for CCC sensors. Additional 4 platforms are glued to the innermost first tube layer for alignment sensors connecting to the inner endcap wheels. The in-plane alignment system consists of 4 optical paths with 2 pixel sensors, 2 LEDs and 4 lenses. Two longitudinal optical paths are oriented perpendicular to the tubes on the HV and RO side next to the support structure. The other two paths are diagonal across the chamber sharing LEDs and pixel sensors with the longitudinal paths.

In the chamber coordinate system, the x-axis is parallel to the tubes, the z-axis parallel to the tube layers, perpendicular to the tubes and the y-axis perpendicular to the tube layers.

A 3D sketch of a BIS78 sMDT chamber is shown in Figure 5.12. The tube layout of a BIS78 chamber with a cutout region is shown in Figure 5.11

5.2.4 The BIS1-6 Chambers

The 96 BIS1-6 chambers all have rectangle shape. They consist of eight layers with 70(58) tubes per layer for the BIS1(BIS2-6) chambers arranged in two multilayers of four tube layers each separated by a spacer structure containing the sensors of the in-plane alignment system [120]. This allows for moving the sensors close to the corners of the chamber, to improve reconstruction of the chamber deformations. The pixel sensors of the in-plane system are mounted in the spacer bar on the RO side, the LEDs in the spacer bar on the HV side and the lenses in the middle bar of the spacer. Two optical paths are along on the sides of the chamber, parallel to the tubes. The other two paths are diagonal across the chamber. The distances between the optical elements are the same for all the BIS1-6 chambers and the LEDs and CCDs are closer to the edges for the BIS2-6 chambers. This allows for using lenses with the same focal lengths for all BIS1-6 chambers. All tubes have a length of 1615 mm. The layers and tubes are numbered in the same way as the BIS78 chambers.

On the outermost layers, the global alignment and B-field platforms are mounted. Each chamber carries 4 axial-praxial (AP) platforms in each corner and 2 B-field sensor platforms. Some of the chambers are equipped with 1 or 2 CCC sensor platforms. While the positions of the AP platforms with respect to the first tube in the first layer are the same for all chambers, the positions of the CCC and B-field platforms vary. Furthermore, some of the chambers are equipped with additional CCC platforms in order to make them interchangeable.

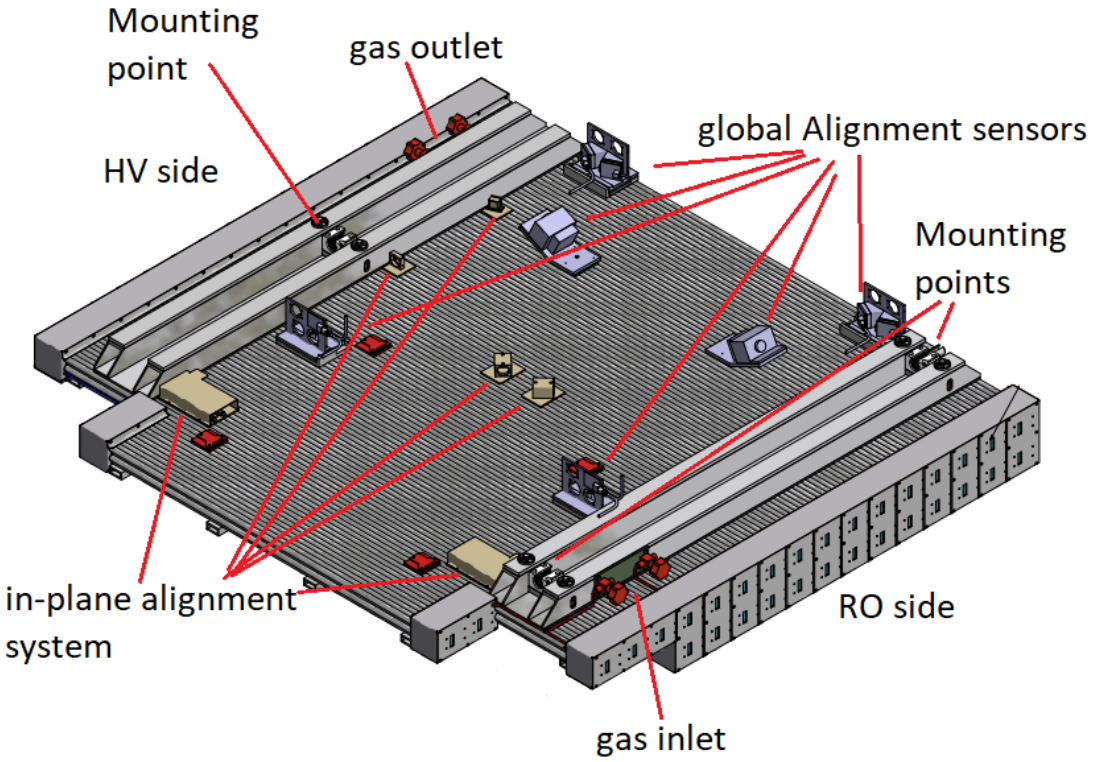

Figure 5.10: 3D sketch of a BIS78 sMDT chamber [120].

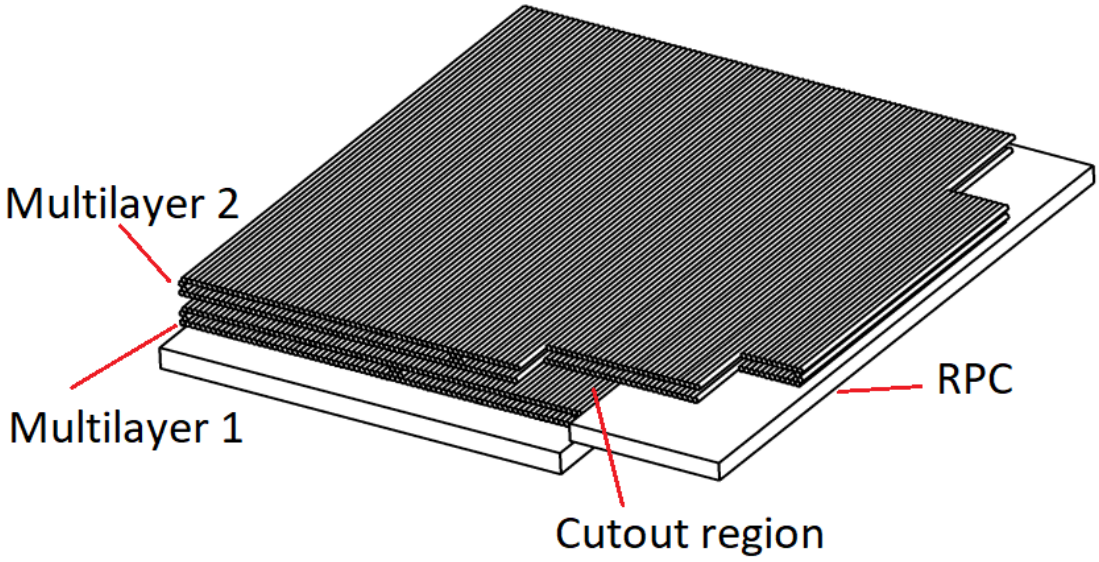

Figure 5.11: Tube layout of a BIS78 chamber with a cutout region (BIS78-C02) [120].

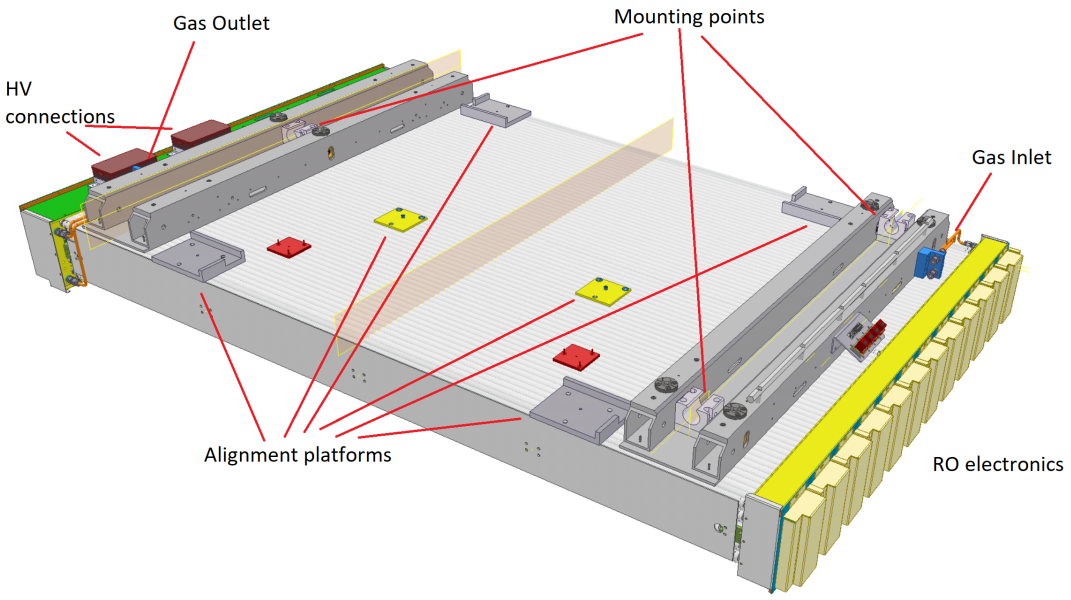

Figure 5.12: 3D sketch of a BIS1 sMDT chamber.

The chambers have been designed at MPI. Half of the 96 chambers are produced at MPI while the other half is produced at the University of Michigan (UM) and the Michigan State University (MSU).

A 3D sketch of a BIS1 sMDT chamber is shown in Figure 5.12.

5.3 Construction of sMDT Chambers

Drift tube production

For the 48 BIS1-6 sMDT chambers built at MPI, 23040 drift tubes, with a length of 1615 mm and 15 mm diameter are needed. An important component of the drift tubes are the endplugs which position the wire with high precision relative to the external reference surfaces of the central brass inserts of the injection molded plastic endplugs. The reference surfaces are later used to precisely position the tubes within the chamber and can be also used to measure the relative position of the wires. The wires are fixed with 350 g tension by crimping in copper tubelets in the brass inserts. The endplug design is shown in Figures 5.13 and 5.14.

The drift tubes are assembled in a clean room with a constant temperature of 20 °C. First the tube is on one end swaged to the endplug with its two O-rings. The sense wire is then inserted from the opposite end through the drift tube into this endplug using air flow at a pressure of 5 bar. Once the

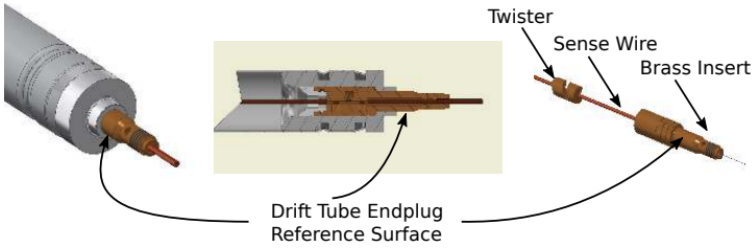

Figure 5.13: Wire positioning in the endplugs of the sMDT drift tubes with spiral wire locator (twister) inside the tube centered with respect to the external reference surface on the central brass insert of the endplug [105].

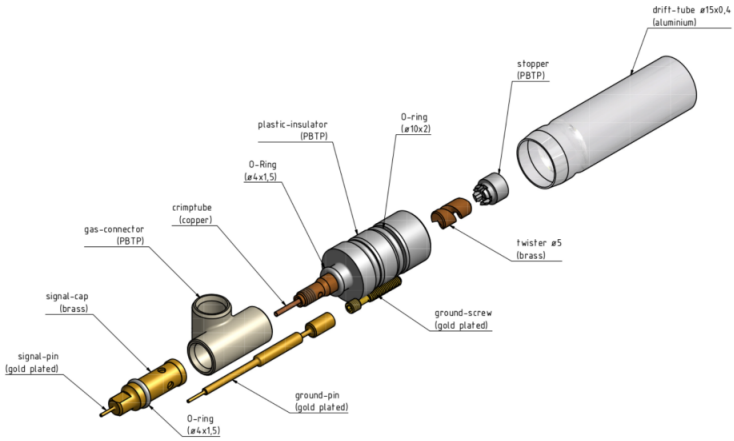

Figure 5.14: Exploded view of an sMDT endplug [121].

wire is routed through the spiral wire locator in the brass insert of the endplug, the wire is fixed by crimping it in a copper tubelet. In the next step, the second endplug is inserted in the tube. The wire is then overtensioned to 400 g and swaged after the wire has been fed through the wire locator . After 10 s, tension is relaxed to 360 g. After that, the wire is crimped at the second endplug. The nominal final tension of 350 g is reached after 13 days. Each drift tube is tested for its length, the wire tension after crimping and two time intervals, gas tightness and the dark current under high voltage of 3015 V. The results of these measurements are stored in a MySQL database which allows for the monitoring of the drift tube production. The experts receive daily updates on the drift tube production including the measurement results via e-mail, allowing to react when necessary.

The wire tension is measured by sending an an alternating current through the wire in an external magnetic field of a permanent magnet exciting vibratioms which modulate the current. By measuring the resonance frequency f of the wire, the tension T of the wire can be obtained, using the following relation:

$$T = \frac{\pi L^2 d^2 f^2 \rho}{g}, \tag{5.5}$$

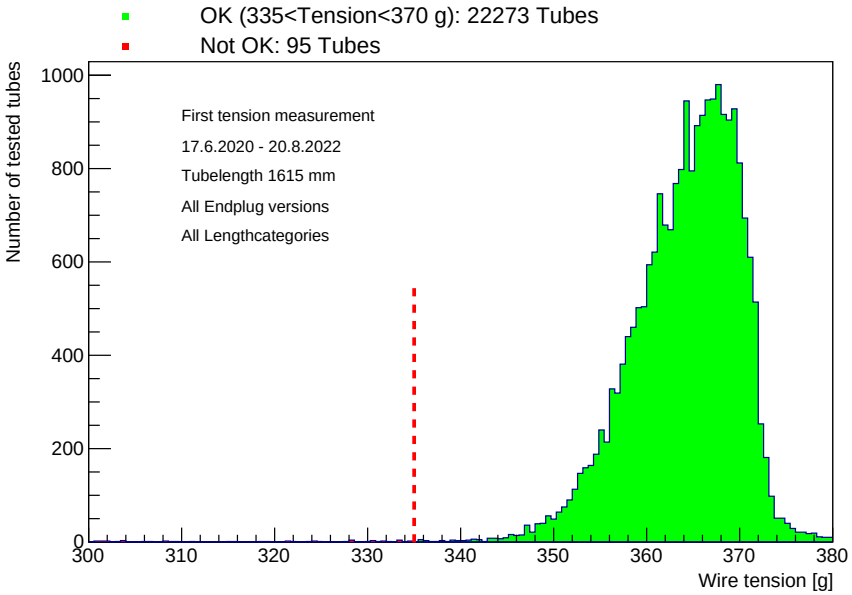

Figure 5.15: Wire tension of the drift tubes measured directly after the production.

with the wire diameter d, the effective wire length L, the density of the wire ρ and the gravitational acceleration g. The values used for the calculation are shown in Table 5.1. As wire relaxes over time, at the beginning the tension is measured directly after the assembly of the tube, a second time after at least 2 weeks. The final tension has to be between 335 g and 370 g, while the tension loss between first and the last measurement is required to be less than 18 g. The wire tension distributions from the first measurement is shown in Figure 5.15 and from the last measurement in Figure 5.16. Figure 5.17 shows the tension loss between the two measurements. The average tension loss is about 10 g.

Table 5.1: Wire parameters used in the calculation of the wire tension using equation 5.5.

Constant	Value
L [mm]	1597
d [mm]	5×10^{-2}
ρ [g/cm^3]	19.3

During the first wire tension measurement, the length of the assembled tube is measured. The length varies within a range of approximately 1 mm. Too large length variations can cause problems with the gas tightness of the gas distribution system and the mounting of the electronics boards. The length is measured between the fronts of the endplugs with respect to a reference tube of nominal length of 1624.4 mm (see Figure 5.18). The tubes are separated into 3 length categories:

- Short: -0.75 mm < $\Delta l_{\text{reference}}$ < -0.25 mm.
- Medium: 0.75 mm < $\Delta l_{\text{reference}}$ < 0.25 mm.

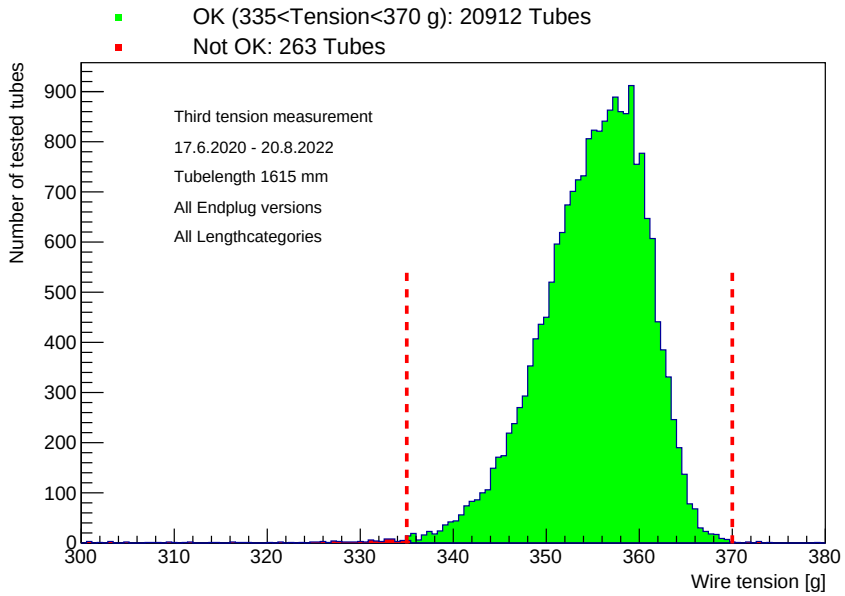

Figure 5.16: Wire tension of the drift tubes measured at least 2 weeks after the production.

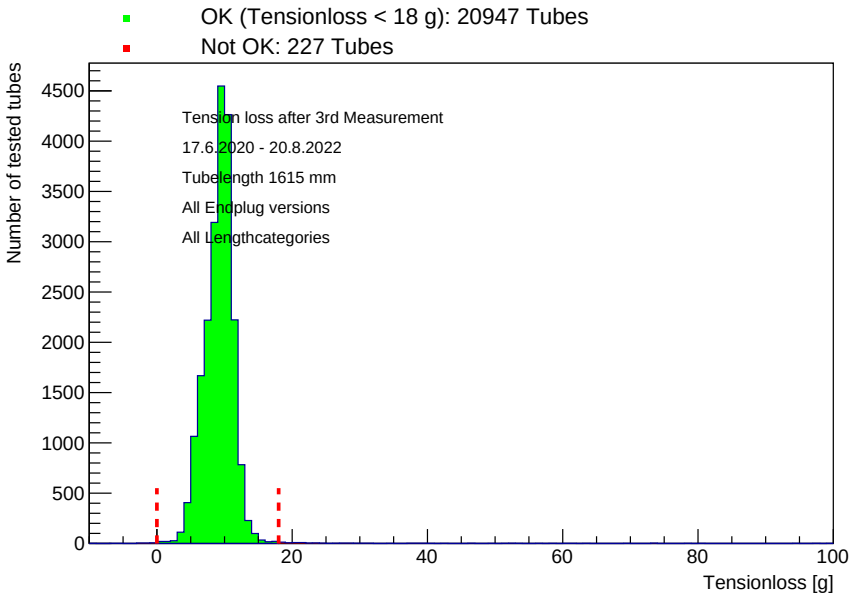

Figure 5.17: Loss of wire tension between the first and last measurements.

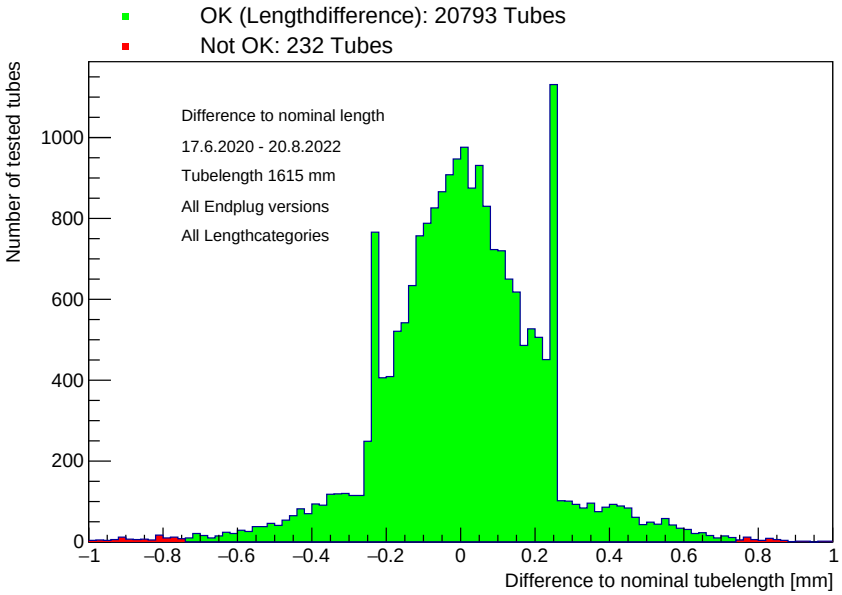

Figure 5.18: Length difference distribution of the assembled drift tubes relative to a reference tube.

- Long: 0.25 mm $< \Delta l_{\text{reference}} <$ 0.75 mm.

Tubes with larger deviation in length are rejected. For the gluing of a multilayer, only tubes from the same length category are used, assuring length variations within a multilayer below 0.5 mm. The majority of the tubes fall in the medium length-category.

In order to measure the gas leak rate, the tube is placed in a test cylinder which is then evacuated. The drift tube is filled with a mixture of 95% Ar and 5% He at a pressure of 3 bar. A He leak detector, measures the amount of He leaking into the evacuated cylinder. The measurement is corrected for the difference between the argon and helium atom sizes. The argon leak rate of a tube is required to be less than 10^{-5} $\frac{\text{mbar}\cdot\text{l}}{\text{s}}$. Figure 5.19 shows the measured leak rate distribution. The leak rates of almost all tubes are below the sensitivity of the leak detector and well below the requirement.

For the high voltage stability test, the tube is flushed with high purity N_2 for at least two minutes to remove remaining humidity, evacuated and afterwards filled again with the nominal gas mixture of Ar/CO_2 (93/7) at 3 bar. A high voltage of 3015 V (10 % above the nominal voltage) is applied between the wire and the tube wall. The dark current is continuously measured. The dark current is required to stay below 2 nA for several minutes. Figure 5.20 shows the measured dark current distribution. For most of the tubes, the dark current is below the requirement.

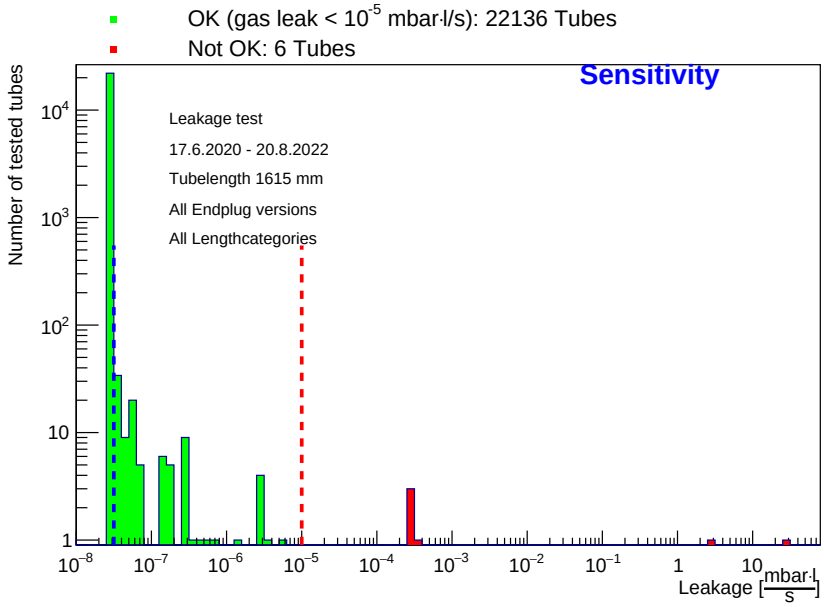

Figure 5.19: Leak rate distribution of the assembled drift tubes.

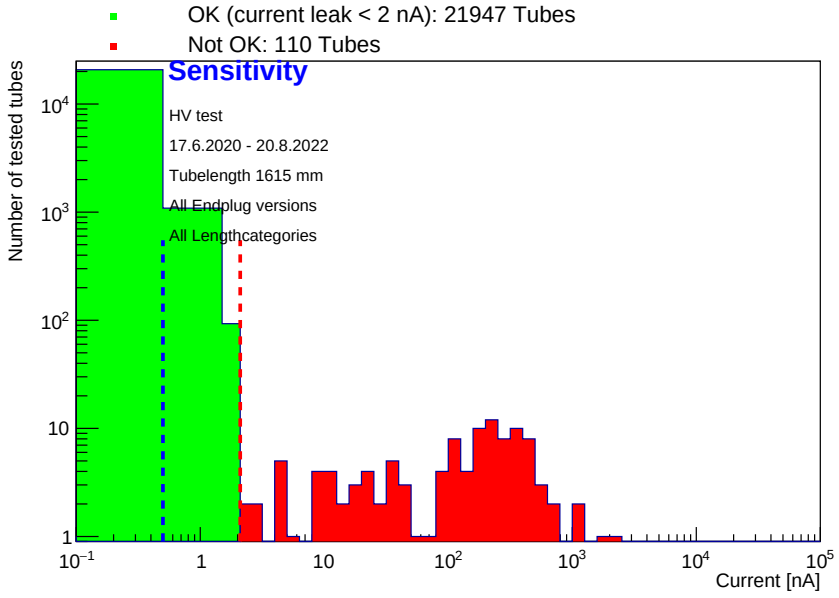

Figure 5.20: Dark current of drift tubes.

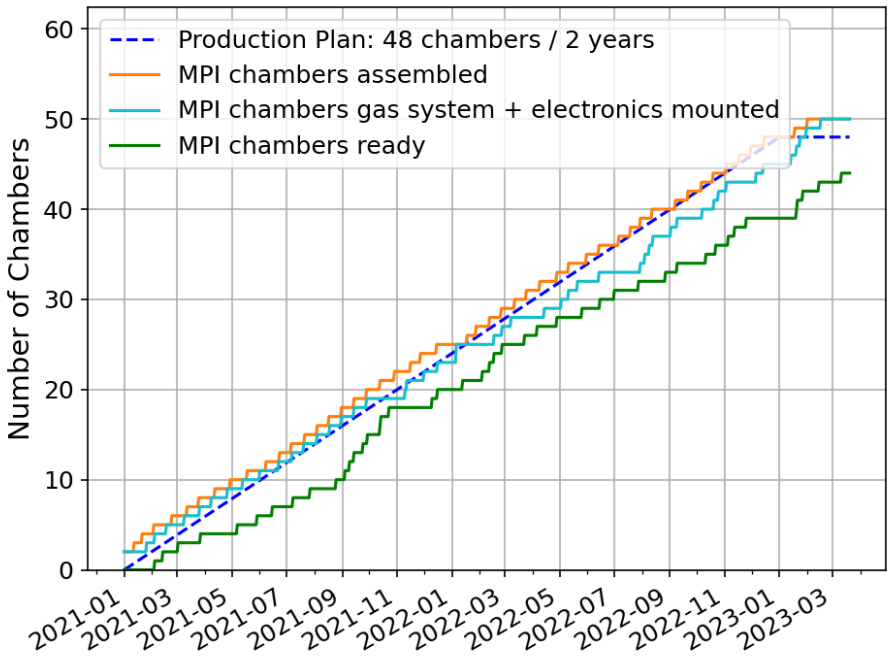

Figure 5.21: Number of sMDT chambers as a function of time at the MPI production site.

5.3.1 Assembly of the sMDT chambers

The assembly of a sMDT chamber is performed in three major steps. In the first step drift tubes are glued together. In the second step the gas distribution system is mounted and in the last step, the electronics and Faraday cages are installed. The work on these three steps is performed in parallel on different chambers. Therefore the production rate is constrained by the slowest of these steps, which is the gluing of the chamber (9 days). Figure 5.21 shows in orange the number of produced chambers as a function of its production date. The blue line indicates the production plan with 48 chambers produced in two years. The production rate is one chamber every two weeks and the production is perfectly within the planned schedule.

The gluing of the drift tubes into a sMDT chamber is performed in a temperature controlled clean room. Precise aluminum combs are used which have boreholes that define the positions of the external reference surfaces of the drift tube endplugs with a precision of 5 μm and thus define the positions of the sense wires. The assembling comb is shown in Figure 5.22. The combs are mounted on granite blocks placed on to a flat granite table. The base combs for the first layer mounted on the granite blocks stay fixed during the production campaign. The chamber is then assembled layer by layer. Starting from layer 2, the drift tubes are glued together with the neighbouring drift tubes of the preceding layer. For each tube, the results of the quality control measurements, described in section 5.3, are checked

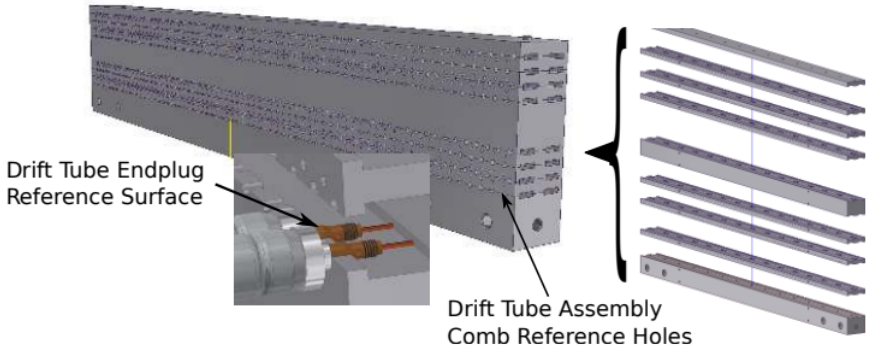

Figure 5.22: Principle of the sMDT chamber assembly jigging.

in order to assure that only good tubes are used for the chamber. The position of each tube within the chamber is registered in the database. In each layer, the tubes are pushed against the comb on the RO side to assure that there are no variations in the x position of the endplugs. The next layer of the assembly combs are then screwed to the previous layer. In between the drift tubes grounding screws are inserted that allow to connect the tube walls to the electronics. Between layers 4 and 5, the spacer housing the in-plane alignment system is glued. After each layer the glue is left to cure over night for one day. Thus the gluing of all eight layer requires seven working days. The gluing of a drift tube layer is shown in Figure 5.23. The gluing of the spacer is shown in Figure 5.24. After the gluing of all layers and before the disassembly of the aluminum comb for removal of the glued chamber, the support structures are glued on top of the chamber as well as the platforms for the global alignment and the B-field sensors. The four axial-praxial platforms at the four chamber corners are positioned with respect to the tube assembly comb using four separate precise mounting brackets. Another mounting plate is used to position the CCC and B-field sensor platforms with respect to the axial-praxial platforms. Like the gluing of the drift tubes, the glue for the support structures and platforms is left for curing over night. After the platforms are glued, their positions are measured as described in section 5.4.3 with 10 μm resolution. In parallel the reference measurement of the in-plane alignment system is taken, while the chamber is still muonted in the assembling combs without gravitational deformations. Before the assembly of the gas distribution system, the positions of the sense wires are measured via the endplug reference surfaces using an automated coordinate measuring machine (CMM) as described in section 5.4.4.

Like the gluing of the drift tubes into a sMDT chamber the assembly of the gas distribution system is performed in a temperature controlled clean room. The gas distribution system consists of plastic gas connectors for each endplug which connect them to a gas distribution bar for each multilayer where the connectors of neighbouring endplugs in the four layers of a multilayer are interconnected. At the connections of the different components O-ring seals are used. The gas connectors with the gas

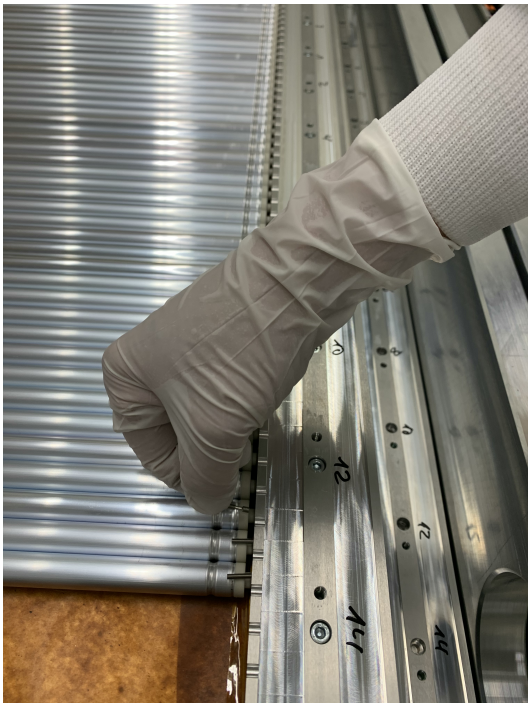

(a) Placing the grounding screws.

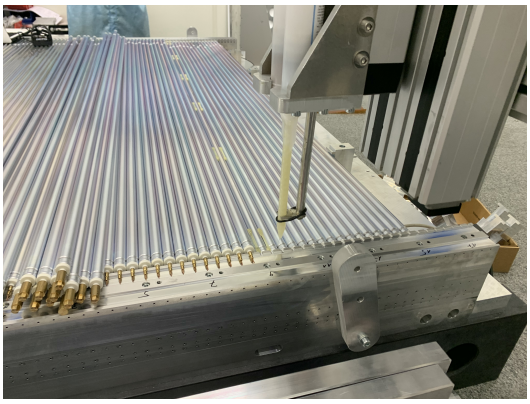

(b) Gluing of a drift tube layer.

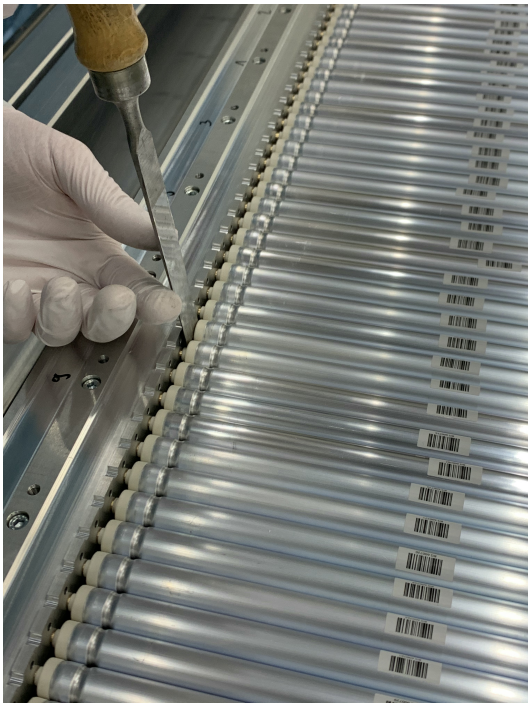

(c) Pushing the tubes against the comb on the RO side.

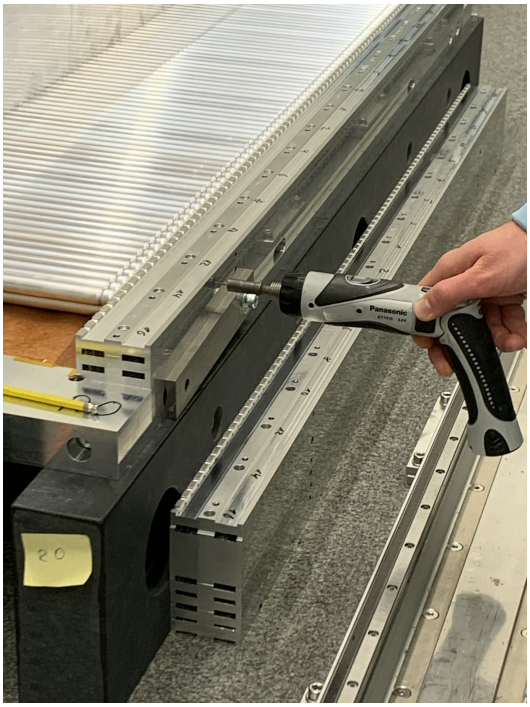

(d) Turning the grounding screws into the chamber.

Figure 5.23: (a) Grounding screws are placed between the tubes and inserted into the corresponding drill holes of the assembly combs. (b) Gluing of a drift tube layer. The glue is distributed by a automatic glue dispenser. (c) Drift tubes are pushed against the comb on the RO side. (d) Grounding screws are screwed into the the chamber after the curing of the glue.

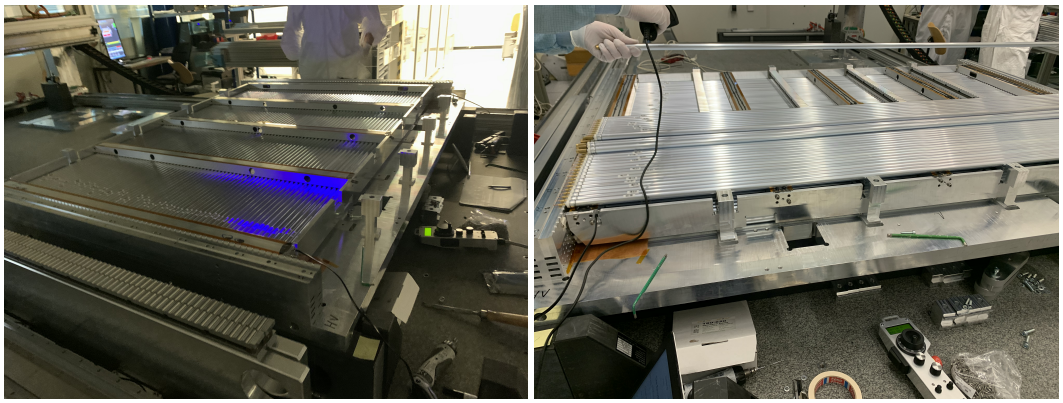

(a) Test of the in-plane alignment system. (b) Gluing of a drift tube layer on top of the spacer.

Figure 5.24: Gluing of the spacer between the two multilayers. (a) Functionality test of the in-plane alignment system before the gluing of the spacer. (b) Gluing of the drift tube layer on top of the spacer.

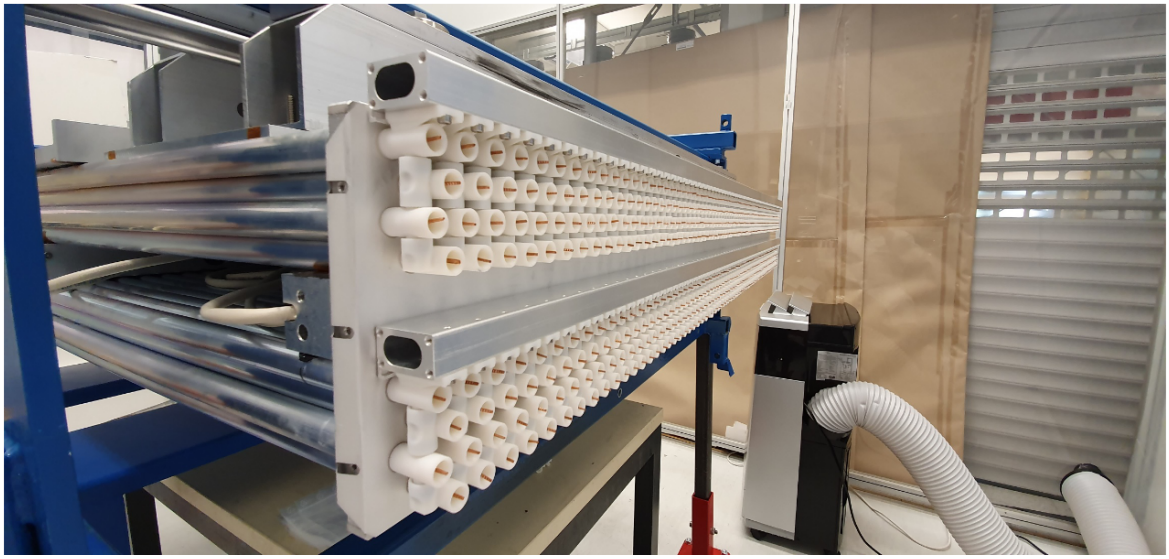

Figure 5.25: Chamber with installed gas connectors and gas distribution bars.

distribution bars are shown in Figure 5.25. Each gas distribution bar is connected to a in- or outlet valve on the chamber via stainless steel pipes. During the installation of the gas system additional grounding screws are installed as well as a ground foil per multilayer on each chamber side. The chambers with N_{tubes} drift tubes have to reach a gas leak rate below $2N_{\text{tubes}} \cdot 10^{-5} \frac{\text{mbar} \cdot \text{l}}{\text{s}}$ with about $2N_{\text{tubes}} \cdot 5$ O-ring seals per chamber. The installed gas distribution system is tested by measuring the pressure drop over night. The installation and test of the gas distribution system takes about one week.

After the installation and leak rate test of the gas system, the sMDT electronics consisting of RO and

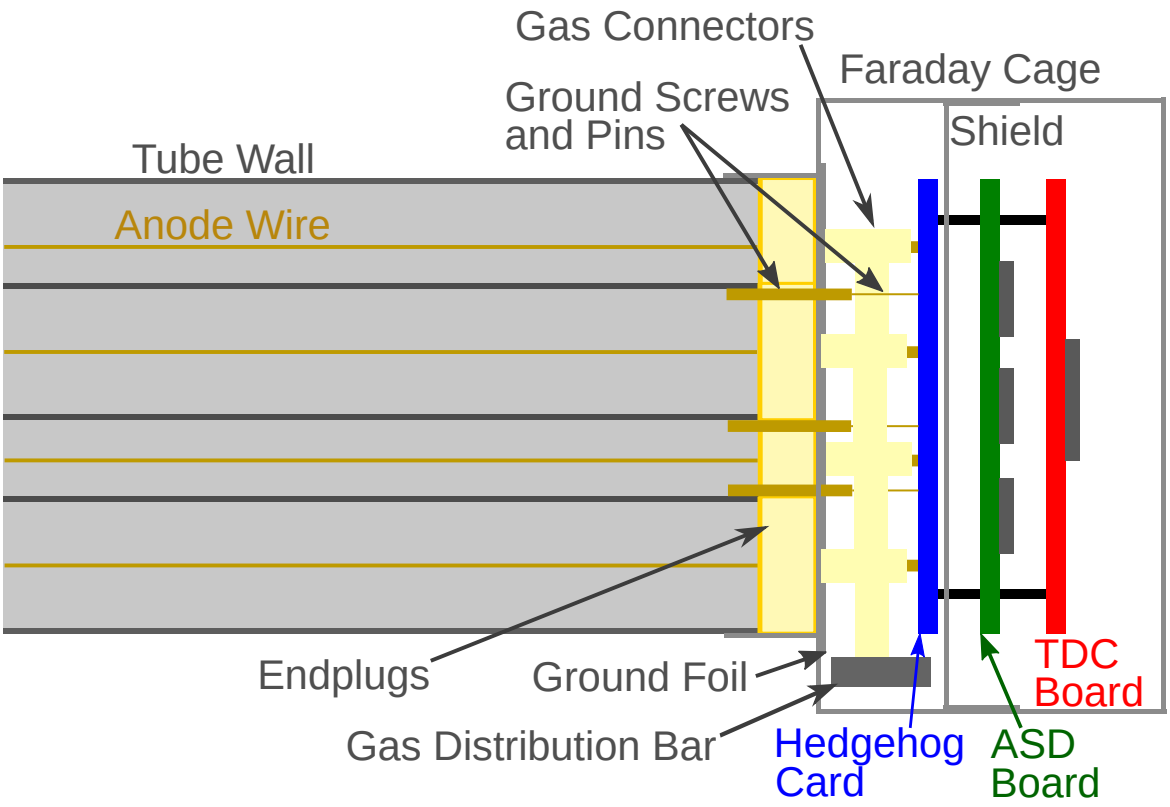

Figure 5.26: Schematic view of the sMDT readout electronics [109].

HV electronics is mounted onto the drift tubes on their corresponding side. Both sides are covered by a Faraday cage. Also 12 temperature sensors are installed on the chamber. The RO and HV electronics are implemented on boards serving up to 6×4 drift tubes within a multilayer. The electronics of the RO side are stacked on top of each other. The signal distribution hedgehoge board is mounted on the signal and ground pins of the drift tubes, followed by a layer with 3 Amplifier-Shaper-Discriminator (ASD) chips which passes the amplified, shaped and digitized signal to a Time-to-Digital Converter (TDC) chip on another layer. The TDC stores the arrival time of the signal and sends it to the off-chamber electronic. The RO electronics is illustrated in Figure 5.26. After the installation of the electronics the now complete chamber is tested in the cosmic ray test stand.

5.4 Mechanical Measurements of the sMDT Chambers

During the chamber construction, for each chamber several measurements are performed in order to assure that each chamber fulfills the requirements on precision of the sense wire positioning (± 20 μm rms) including deformations and platform positioning (± 200 μm rms) as well as gas leak rate, HV

stability and electronics performance and to spot potential problems in the production process that need to be fixed. While for the BIS78 chamber production at MPI the measurements still had to be analyzed manually and there was no cumulative display of the results, for the production of the BIS1-6 sMDT chambers a web based application was developed [122]. The raw data of these measurements are uploaded to a web page. The data is stored in a MySQL database and analyzed and the results displayed on the webpage automatically. The experts receive a notification via e-mail about the results allowing for reaction when necessary. The web page collects the measurement results of both the production sites at MPI and in Michigan. This thesis focuses on the mechanical measurements. However, the final performance tests are summarized at the end of this chapter.

5.4.1 Wire Position Measurements of the BIS78 Chambers

In order to verify the measurements of the in-plane alignment system, the chamber deformations predicted from them were compared to mechanical measurements of the wire position and geometry of the chambers. For the BIS1-6 chambers at MPI the 2D positions of each wire on RO and HV side are measured with a Coordinate Measuring Machine (CMM), as shown in section 5.4.4. The BIS78 chambers however, are to large to fit on the CMM available. Therefore, instead of measuring the chambers with the CMM, the BIS78 chambers were placed on a flat granite table and the height (y coordinate) of the reference surfaces of the endplugs measured with respect to the table surface using a height measurement device as shown in Figure 5.27. The wire z positions (horizontal on the assembly and measurement table) were assumed to be correct. The y coordinate are more critical due to successive assembly and gluing of the tube layers and gravitational sag. The same procedure is used for the BIS1-6 chambers produced in Michigan where no CMM is available.

The gravitational deformations on each side are approximately described by parabolas. Since the HV side is mounted on one point in the middle, the bow is upwards corresponding to a positive sag. The RO side on the other hand is mounted on two points at the ends and bows downwards corresponding to a negative sag. The wire coordinates for each tube layer are first linearly fitted and rotated such that fitted line is parallel to the z-axis, as the chambers are not perfectly parallel to the measurement table. In the case of the chambers with cutout regions, the heights of the endplugs on the opposite side are used to linearly extrapolate the measured cutout coordinates to the length of the longer tubes. The average height is subtracted to compare different layers. Afterwards, a parabola is fitted for each layer. The resulting sag values are then compared to the predictions of the in-plane alignment system.

In order to compare the torsion, the height measurements are fitted linearly on both sides and are rotated such that the fitted line on the RO side is parallel to the z-axis. The angle between the two fitted lines at each end gives the torsion angle.

These measurements are repeated with the chamber turned upside down. Since the coordinate system of the in-plane alignment system is rotated with respect to the height measurement, the signs of the sags and torsion of the in-plane alignment system are inverted.

The results of the measurements for the BIS78-A10 chamber are shown in Figure 5.30. The measurement confirm that deformation on each can be described by a parabola and the signs of the sags are as expected. The sags are between 30 and 80 μm consistent for 0° and 180° orientation of the chamber. The in-plane alignment system predicts the deformation with the correct sign of the sag and similar magnitude. The agreement is not perfect because the in-plane sensors measure only the region between the support bar and are mounted on layer 8. With exception of the RO side for the chamber upside down, the absolute values of the in-plane alignment system predicted sags is slightly larger than the mechanically measured sags. Also, the torsion angle is measured with the correct sign by the in-plane alignment system. Typically values of the torsion angle are in the range of 100-200 μrad. The precision of the reconstruction of the torsion angle by the in-plane alignment system measurements of about 50% is sufficient for the chamber geometry reconstruction for the required track reconstruction precision. While the sag values are stable independent of the exact support of the chambers on rails in the ATLAS experiment and on the measurement table in the transport frame, and are negligible for the average wire positioning accuracy, the torsion values are very sensitive because the chambers with very small spacer height of only 5 cm have little stiffness against torsion deformations. In particular the torsion values depend strongly on chamber installation angle and therefore has to be continuously monitored during chamber operation.

Figure 5.27: Height measurement device to measure the height of the reference surfaces of the endplugs with respect to the surface of a flat granite table.

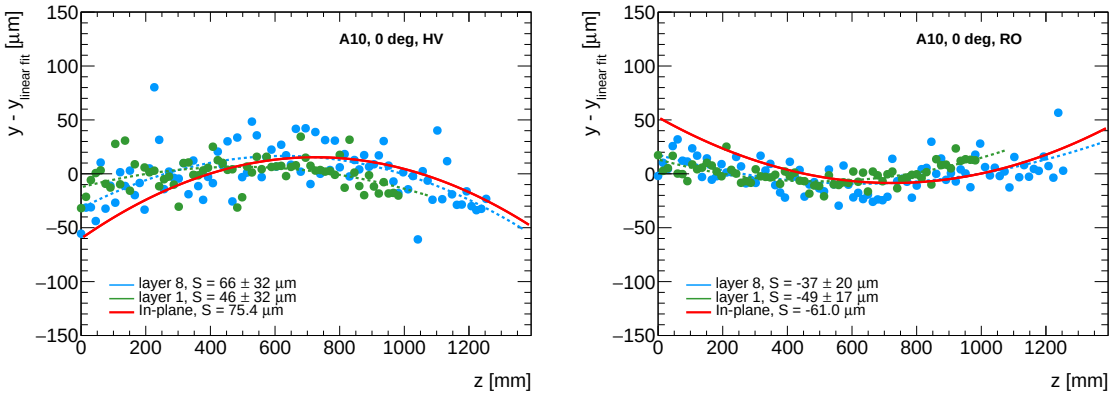

(a) HV side, 0°

(b) RO side, 0°

Figure 5.28: Results of the height measurements of the endplugs (wires) for the BIS78-A10 chamber in 0° position in comparison with the predictions from the in-plane alignment system for bottom layer 1 (ML1) and top layer 8 (ML2) where the in-plane sensors are mounted. The dashed curves show the parabola fits to the long tubes in each layer.

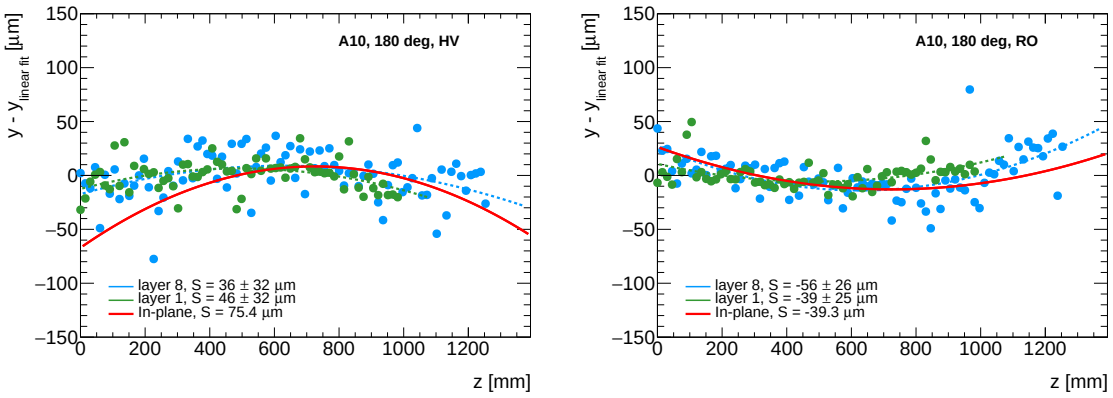

(a) HV side, 180° (b) RO side, 180°

Figure 5.29: Results of the height measurements of the endplugs (wires) for the BIS78-A10 chamber in 180° position in comparison with the predictions from the in-plane alignment system for bottom layer 1 (ML1) and top layer 8 (ML2) where the in-plane sensors are mounted. The dashed curves show the parabola fits to the long tubes in each layer.

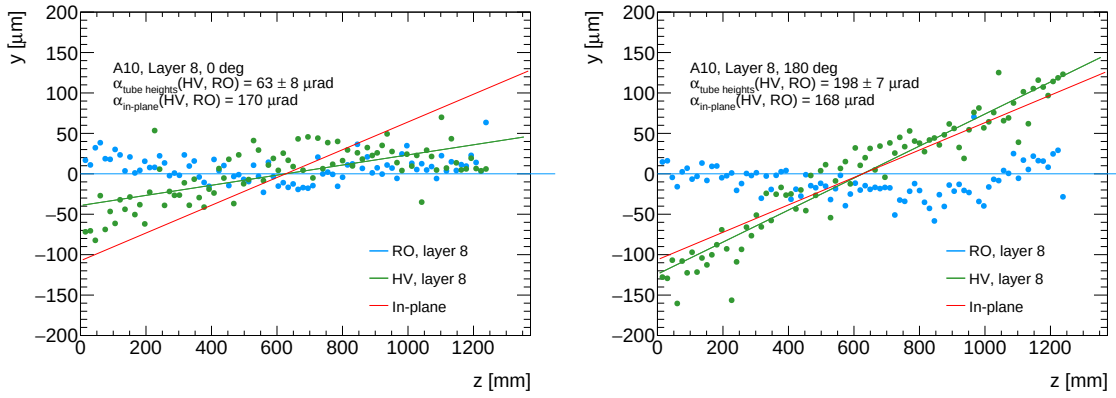

(a) Torsion 0° (b) Torsion 180°

Figure 5.30: Torsion angle measured with the height measurements of the endplugs (wires) for the BIS78-A10 chamber compared to the predictions from the in-plane alignment system.

5.4.2 In-plane alignment Measurement of the BIS78 chambers under different angles

The consistency of the in-plane system measurements under different installation angles has been tested. During the installation of the readout electronics the chambers are installed in a special frame that allows the chamber to be rotated in different positions around 360°. A sMDT chamber in the frame rotated in a 125° position is shown in Figure refFig:rotation. For one of the BIS78 chambers, BIS78-C04, the in-plane alignment system was read out while the chamber was rotated into different angles through two times 360°. The evaluated sags on the RO and HV sides as well as the torsion angles as a function of the rotation angle is shown in Figure 5.32. The sags and torsion angle follow approximately sine functions. The sags vary between −100 and +80 μm and the torsion angle varies between −50 murad and +250 μrad. The chamber returns to the same deformation after each 360° rotation.

5.4.3 Alignment and B-Field Sensor Platform Positions

Precise knowledge of the positions of the alignment sensors relative to the sense wires is crucial to monitor the relative positions of the chambers in the ATLAS detector. Therefore, the positions of the platforms are measured immediately after they have been glued, on the granite table before the

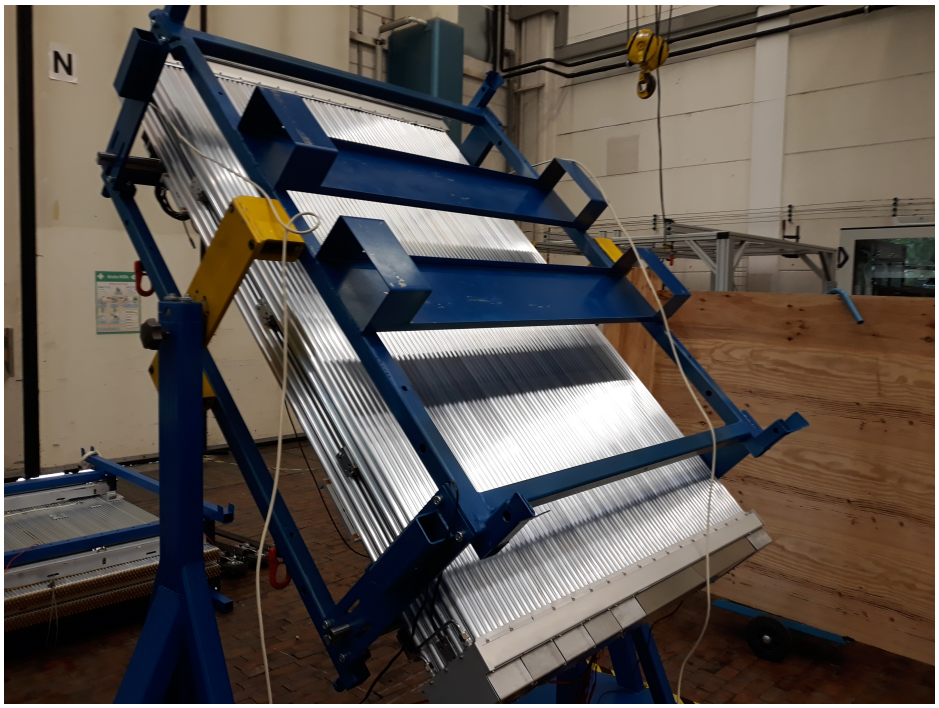

Figure 5.31: sMDT chamber rotated in a 125° position.

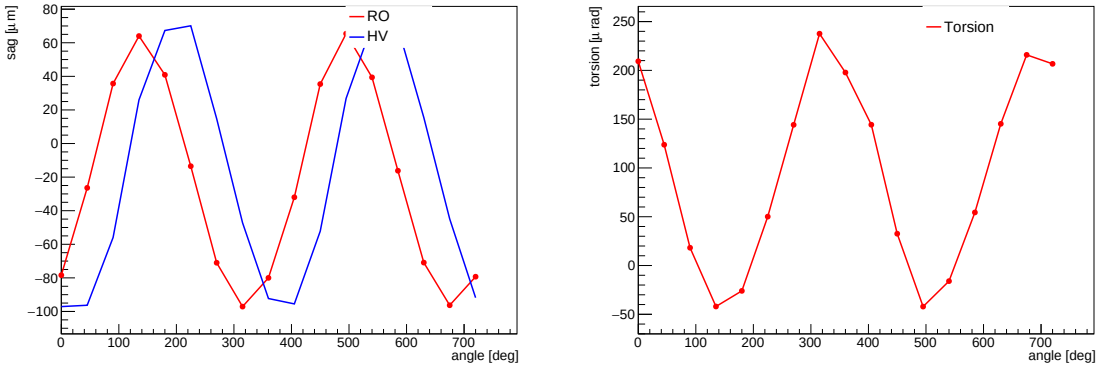

(a) Sags (b) Torsions

Figure 5.32: Torsion and sags evaluated as a dependence of the rotation angle.

assembly combs are removed where there are no chamber deformations. The naming scheme used for the platforms is shown in Figure 5.33.

The positions of the platforms are determined in three dimensions (3 coordinates, 3 angles) using a electro-mechanical feeler arm, called FARO arm after the brand name. The positions are measured with respect of the granite blocks that serve as the bases for the combs. The FARO arm precision decreases with increasing distances. Therefore, the platforms of one corner of the chambers are measured independently with respect to the closest granite block minimizing the distances. The measurement of the platforms with the FARO arm are illustrated in Figure 5.34.

The coordinate system of the FARO arm is defined by the plane of the granite table and the reference granite blocks. The z-axis is perpendicular to the front surface of the reference granite and along the tubes of the assembled chamber, while the y-axis is perpendicular to the surface of the granite table.

The Axial-Praxial platforms have reference surface defining the x- and the z-coordinate. Three steel insert surfaces on the platform define the y-coordinates. In case of the CCC platforms spheres on the CCC alignment sensors as well as for the FARO arm measurement are inserted into three holes in the platform one defining x, y, z, one y, z and one only y. By measuring several points on the surfaces of the spheres, their centers can be evaluated. The edges of the B-field platforms define its x- and z-coordinates, while the platform surface defines the y-coordinate. Figure 5.35 shows the points measured on the platforms . Blue points indicate points corresponding to the x-coordinate. Green and red points correspond to the y and z coordinates, respectively. The measured spheres on the CCC platforms are shown in purple, since they determine several coordinates each. For each coordinate, the positions of the corresponding points are measured relative to the respective reference surface on the table. Since the position of the assembly combs to the reference surfaces is known from measurements

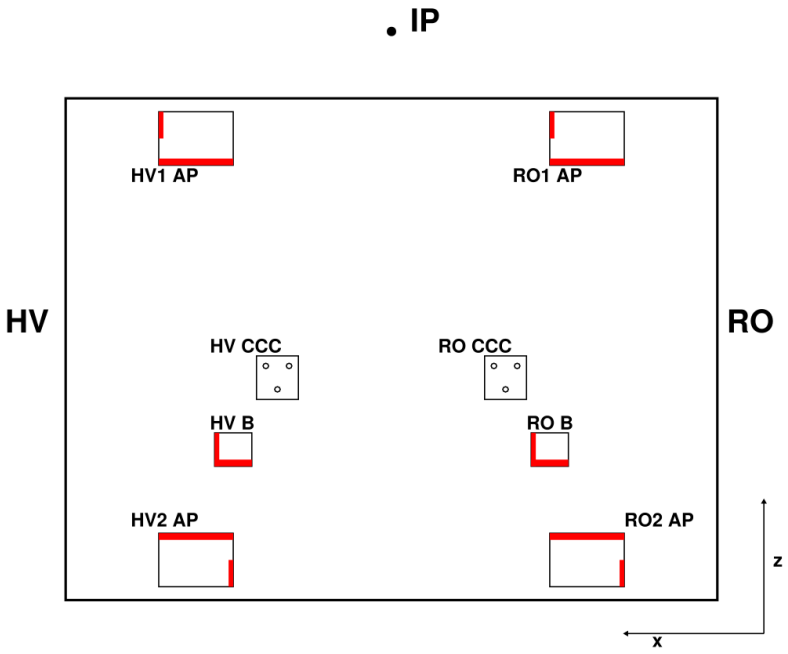

Figure 5.33: Naming scheme used for the alignment platforms for BIS78 and BIS1-6 chambers. The interaction point (IP) direction is indicated.

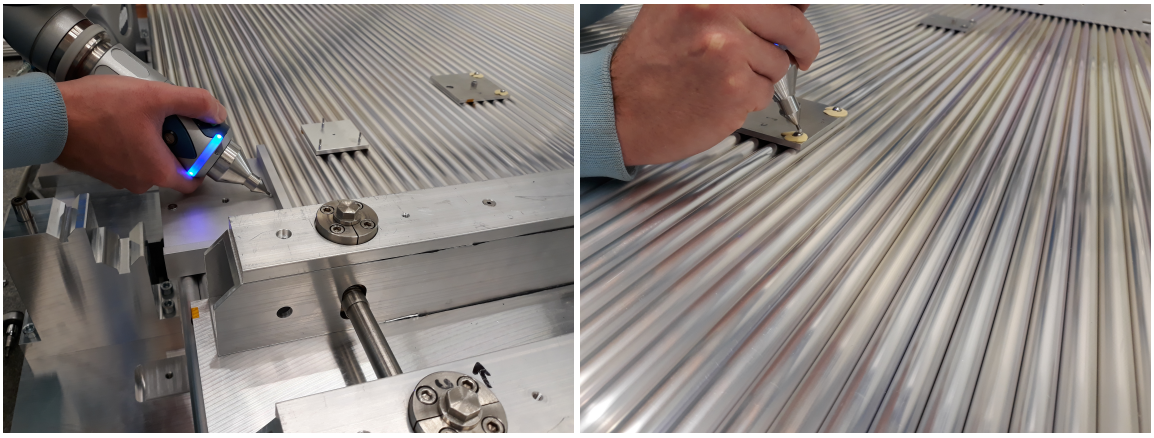

(a) AP platforms (b) CCC platforms

Figure 5.34: Measurement of the AP and CCC sensor platforms using a electro-mechanical feeler arm.

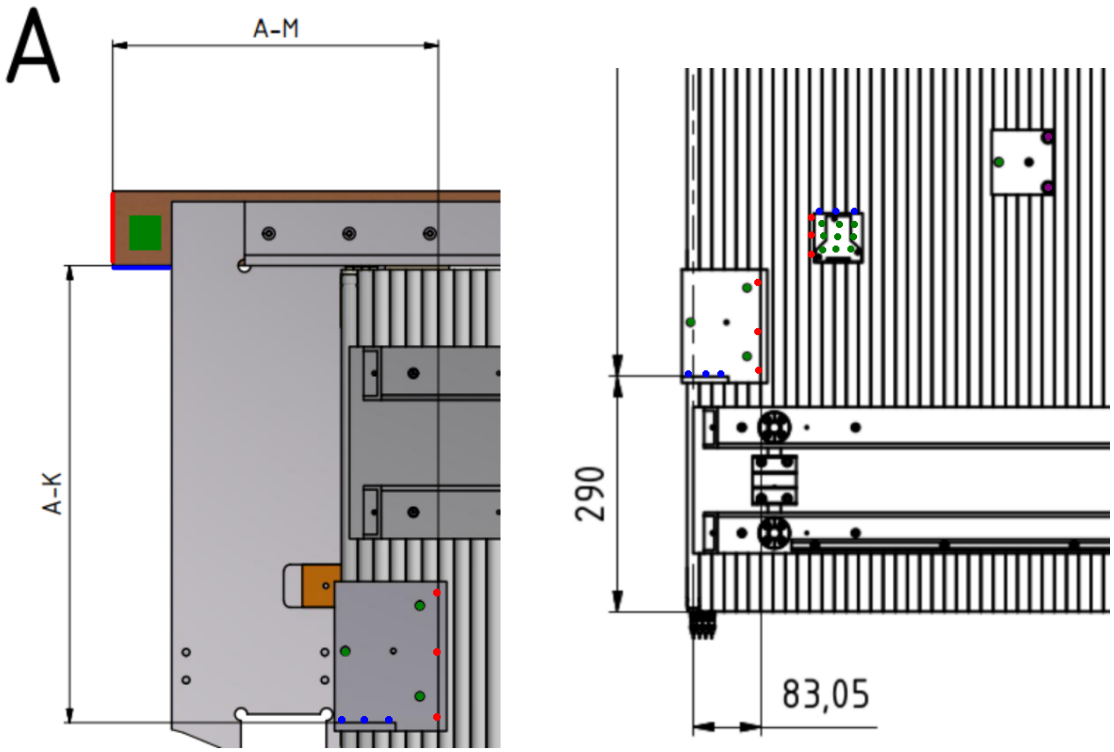

(a) (b)

Figure 5.35: Measured points (blue, red and green) on the alignment platforms. (a) The reference surfaces and measured points on the Axial-Praxial platforms. (b) The measured points on the Axial-Praxial, the B-field sensor and the CCC platforms. The colors indicate the measured coordinates. Blue points correspond to the x-coordinate, while green and red points correspond to the y- and z-coordinates, respectively. On the CCC platforms the spheres are used for several coordinates and are marked in purple.

with the coordinate measuring machine, the measured positions relative to the reference surfaces can be transformed to positions relative to the sense wire grid of each chamber end. Each measurement is repeated at least 8 times and the results are averaged. The resulting statistical measurement precision is about 10 μm. By fitting lines through the different measurement points on the platforms, also the angles of the platforms in the x-y, y-z and x-z planes, can be evaluated.

The measured platform positions relative to their nominal positions are shown for all assembled BIS1-6 chambers in Figures 5.36-5.41 for the axial-praxial platforms, in Figures 5.48-5.50 for the CCC platforms, and in Figures 5.54-5.56 for the B-field sensor platforms. The axial-praxial platforms are typically positioned within ±0.1 mm of the nominal position. However, occasionally the positions shifted increasingly for subsequent chambers, for example for the RO2 AP platforms in the z direction, to negative values at beginning of the production and later to positive values. When such systematic deviations are observed, the positions of the platform mounting brackets are readjusted. The measured

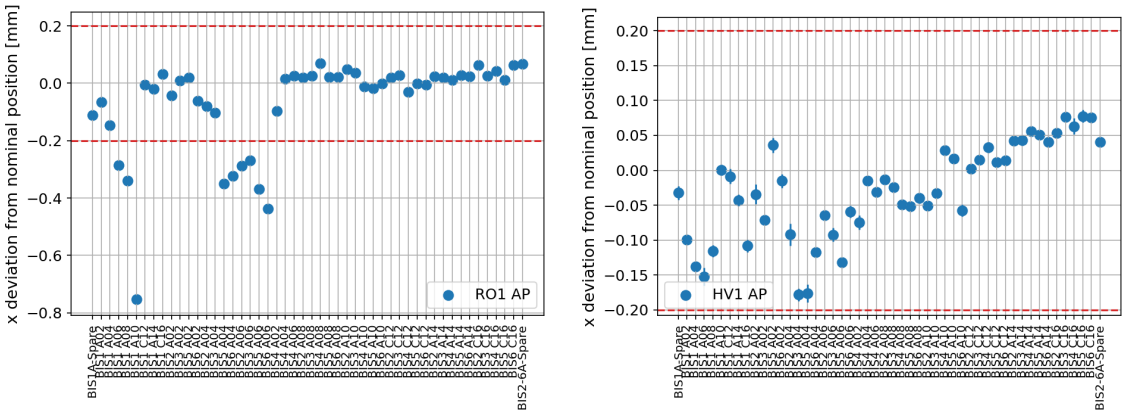

(a) RO1 AP x

(b) HV1 AP x

Figure 5.36: Measured AP alignment platform positions in x for the different BIS1-6 chambers in the serial production.

angular orientations of the AP platforms are shown in Figures 5.42-5.46. Typical angles relative to nominal are below ±1 mrad. Some chambers carry two sets of CCC platforms, named CCC1 and CCC2 in the plots. In most cases, the CCC platforms are positioned within ±0.1 mm of the nominal position. The CCC platform positioning relative to the AP platforms depends on the precision of the AP platform positioning. In case of larger deviations on the CCC platforms, AP platform mounting tools are, therefore, readjusted. The measured angular orientation of the CCC platforms are shown in Figures 5.51-5.53. Like for the CCC platforms, for chambers with two sets of B-field sensor platforms the two sets are labeled B1 and B2 in Figures 5.54-5.56. The required positioning accuracy of the B-field sensor platforms is much coarser. The corresponding positioning accuracy is typically ±0.4 mm.

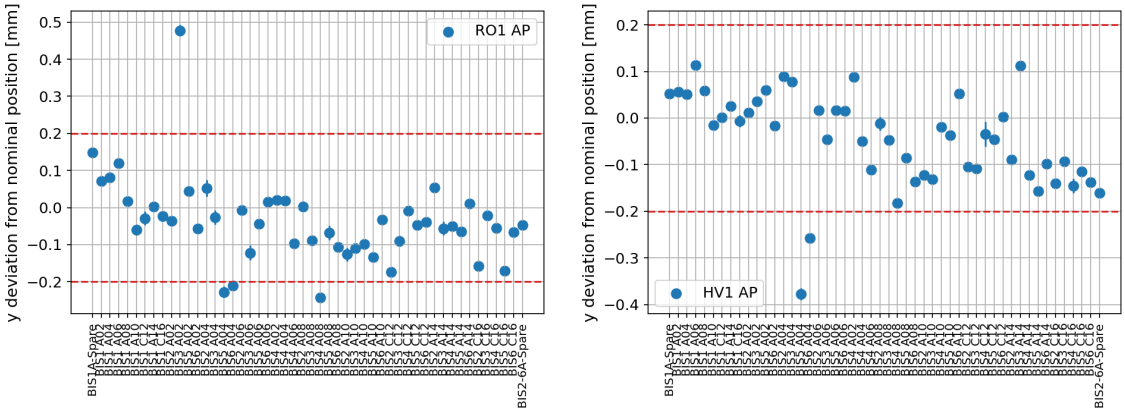

(a) RO1 AP y (b) HV1 AP y

Figure 5.37: Measured AP alignment platform positions in y for the different BIS1-6 chambers in the serial production.

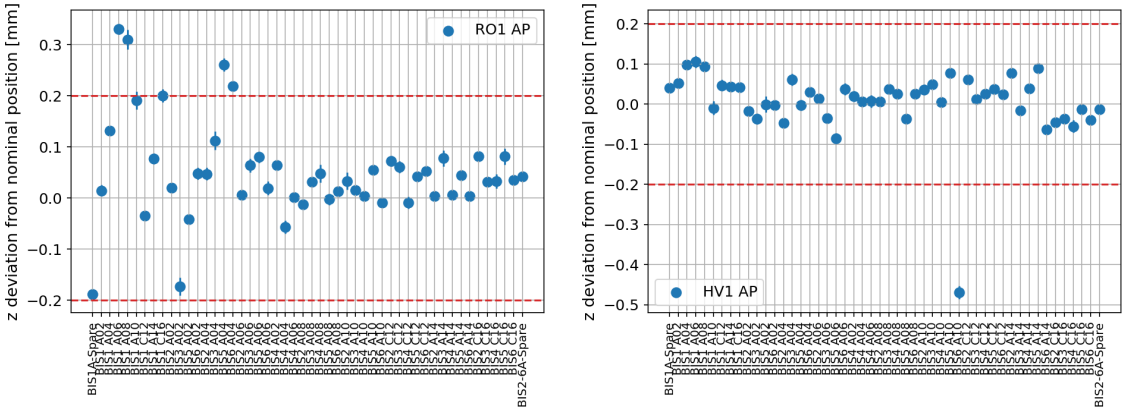

(a) RO1 AP z (b) HV1 AP z

Figure 5.38: Measured AP alignment platform positions in z for the different BIS1-6 chambers in the serial production.

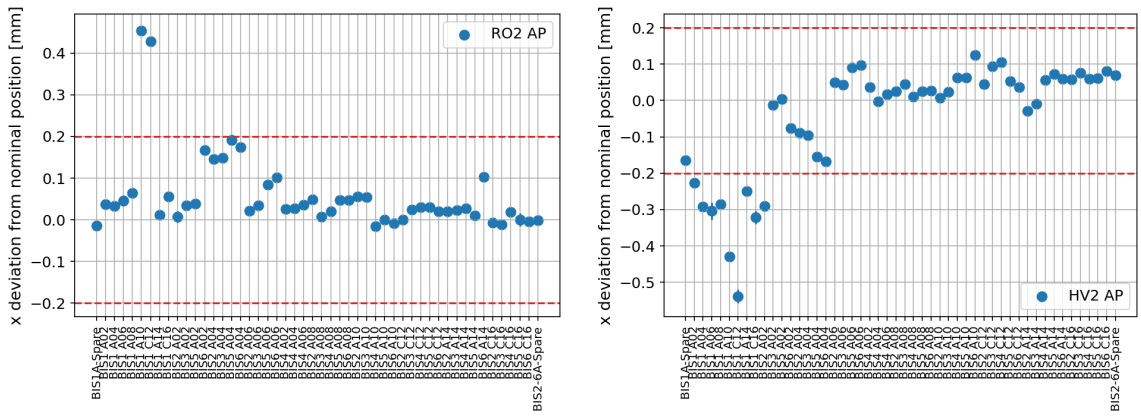

(a) RO2 AP x (b) HV2 AP x

Figure 5.39: Measured AP alignment platform positions in x for the different BIS1-6 chambers in the serial production.

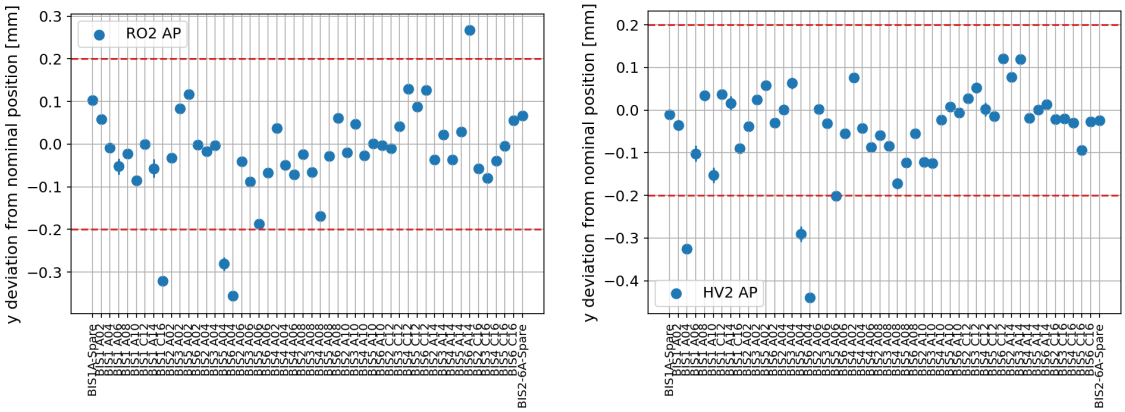

(a) RO2 AP y (b) HV2 AP y

Figure 5.40: Measured AP alignment platform positions in y for the different BIS1-6 chambers in the serial production.

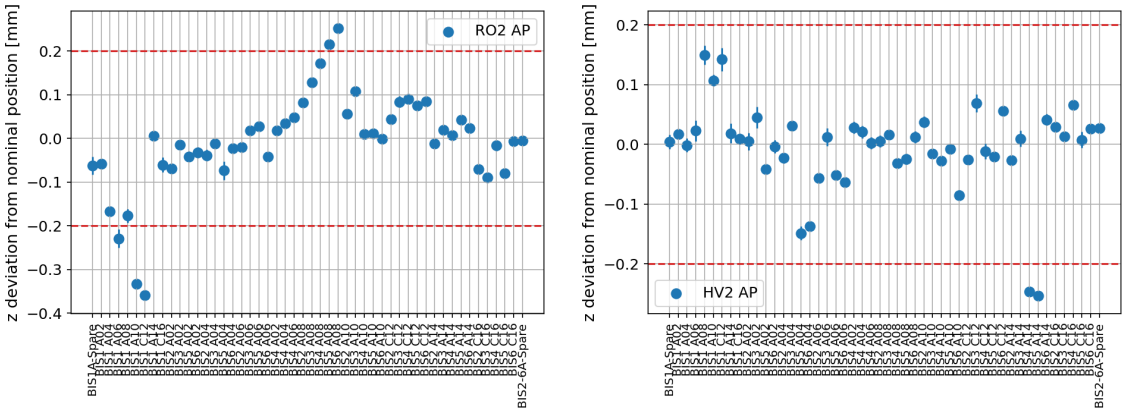

(a) RO2 AP z (b) HV2 AP z

Figure 5.41: Measured AP alignment platform positions in z for the different BIS1-6 chambers in the serial production.

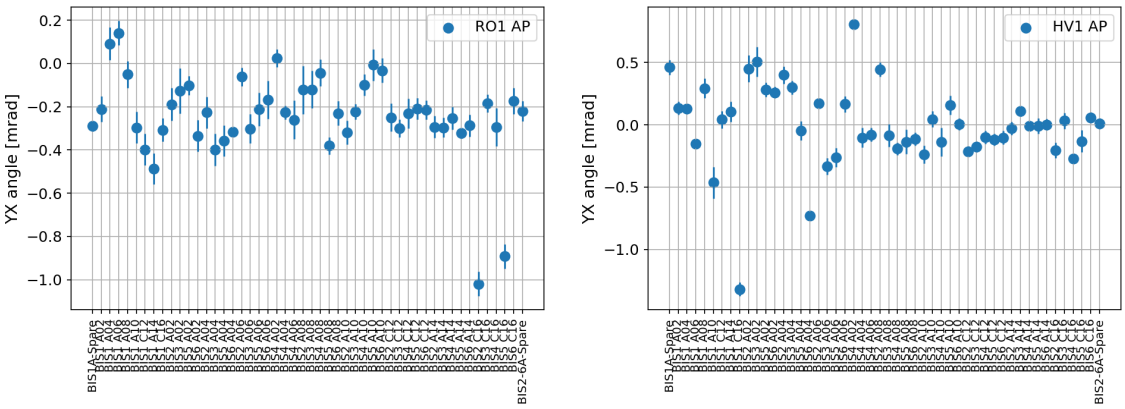

(a) RO1 AP angle α_z in x-y plane (b) HV1 AP angle α_z in x-y plane

Figure 5.42: Measured AP alignment platform angles in the x-y plane for the different BIS1-6 chambers in the serial production.

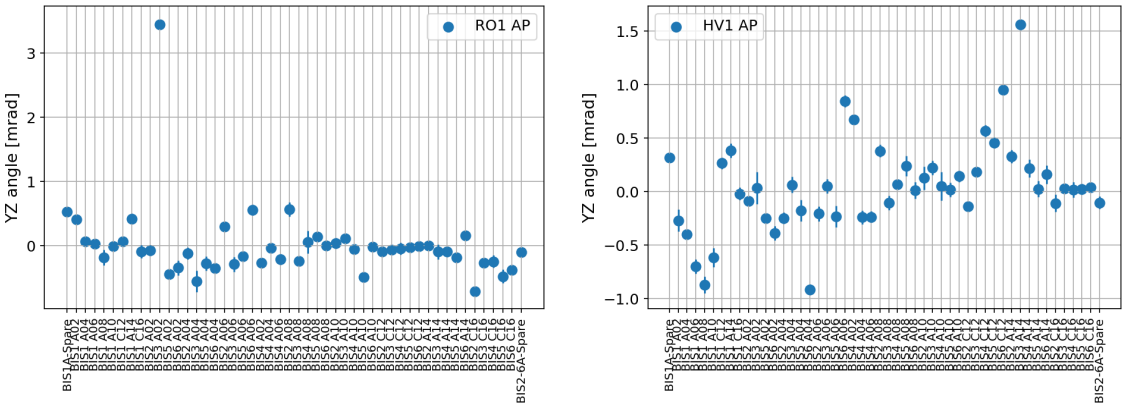

(a) RO1 AP angle α_x in y-z plane

(b) HV1 AP angle α_x in y-z plane

Figure 5.43: Measured AP alignment platform angles in the y-z plane for the different BIS1-6 chambers in the serial production.

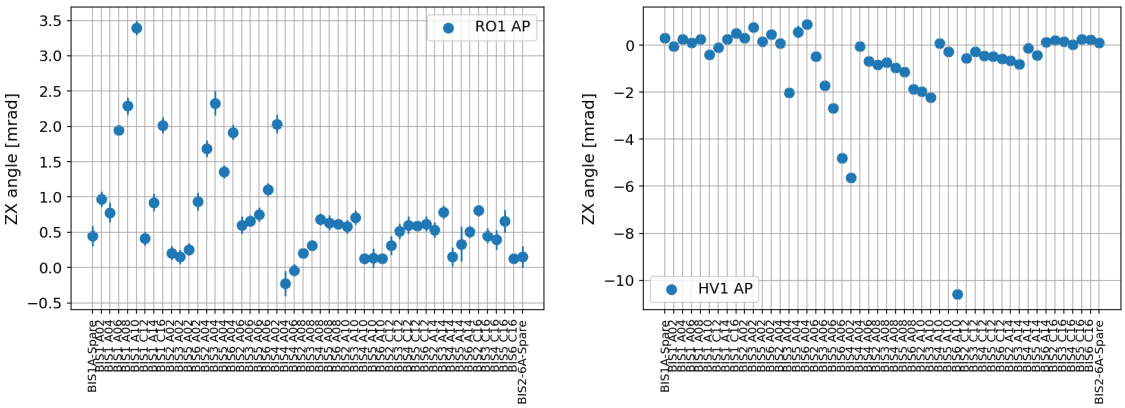

(a) RO1 AP angle α_y in x-z plane

(b) HV1 AP angle α_y in x-z plane

Figure 5.44: Measured AP alignment platform angles in the x-z plane for the different BIS1-6 chambers in the serial production.

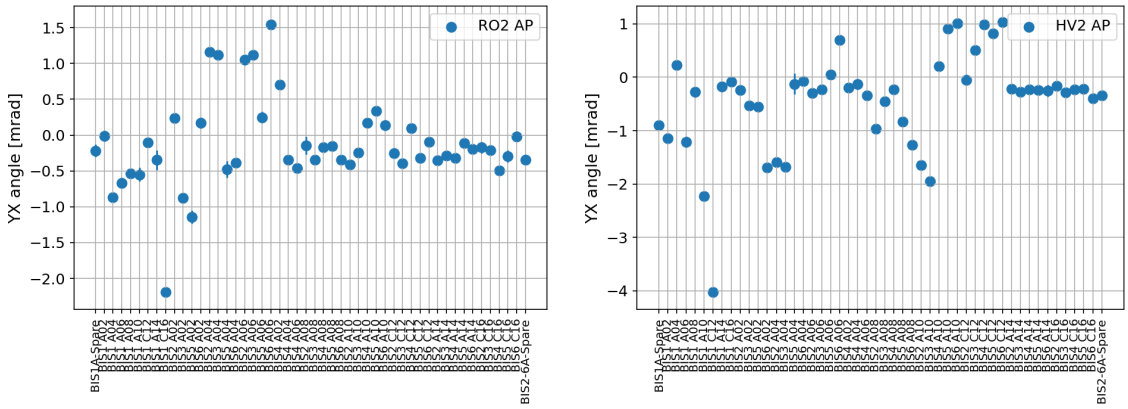

(a) RO2 AP angle α_z in x-y plane

(b) HV2 AP angle α_z in x-y plane

Figure 5.45: Measured AP alignment platform angles in the x-y for the different BIS1-6 chambers in the serial production.

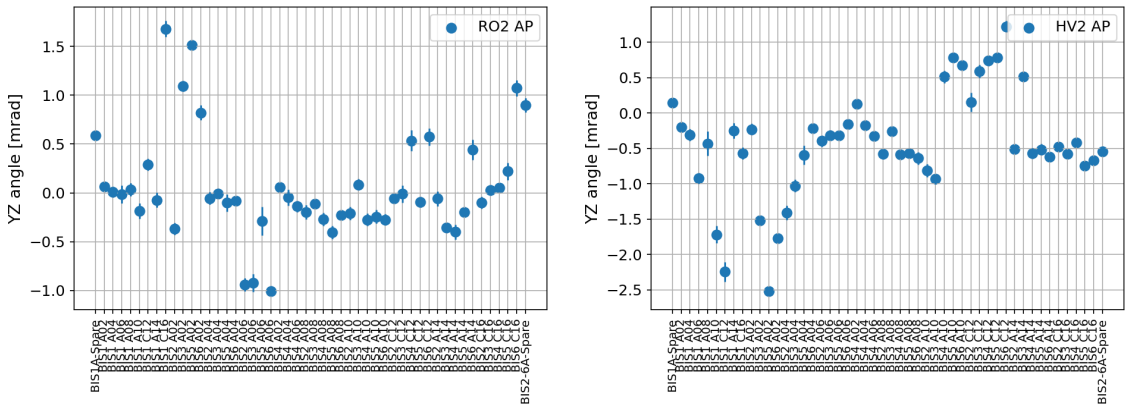

(a) RO2 AP angle α_x in y-z plane

(b) HV2 AP angle α_x in y-z plane

Figure 5.46: Measured AP alignment platform angles in the y-z for the different BIS1-6 chambers in the serial production.

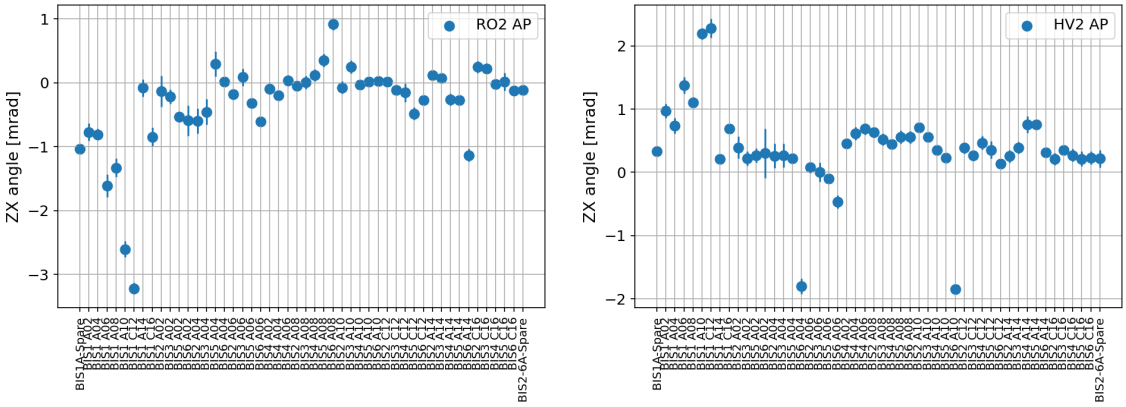

(a) RO2 AP angle α_y in x-z plane

(b) HV2 AP angle α_y in x-z plane

Figure 5.47: Measured AP alignment platform angles in the x-z for the different BIS1-6 chambers in the serial production.

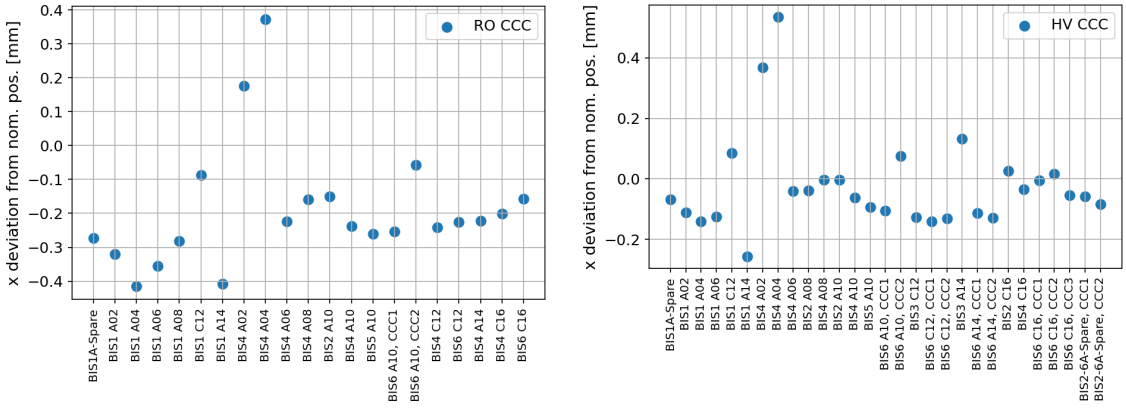

(a) RO1 CCC x

(b) HV1 CCC x

Figure 5.48: Measured CCC platform positions in x for the different BIS1-6 chambers in the serial production.

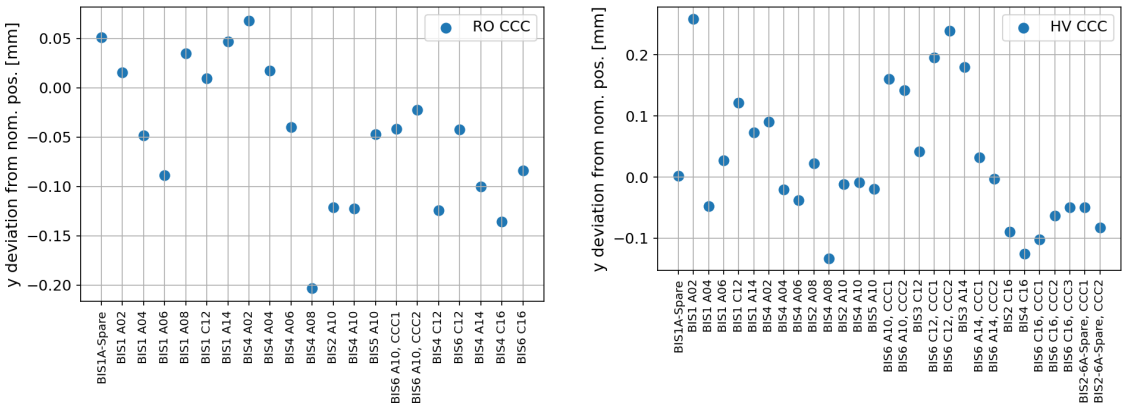

(a) RO1 CCC y (b) HV1 CCC y

Figure 5.49: Measured CCC platform positions in y for the different BIS1-6 chambers in the serial production.

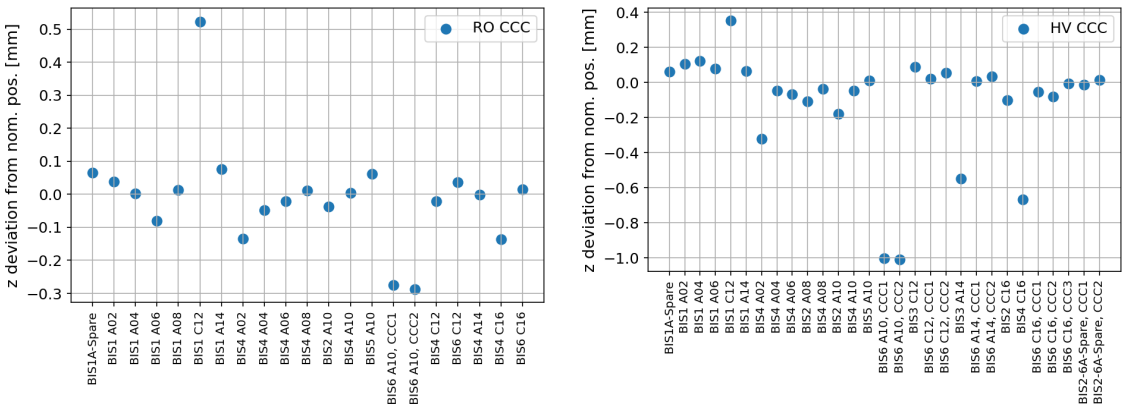

(a) RO1 CCC z (b) HV1 CCC z

Figure 5.50: Measured CCC platform positions in z for the different BIS1-6 chambers in the serial production.

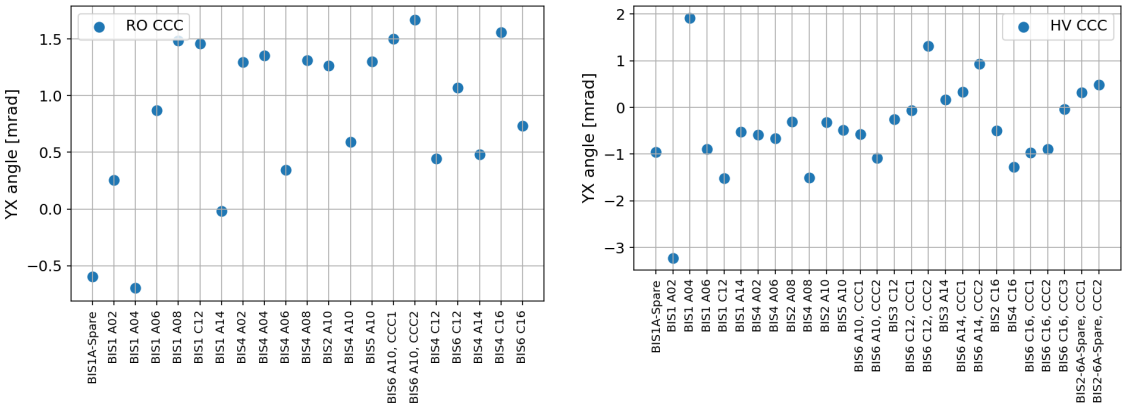

(a) RO1 CCC angle α_z in x-y plane

(b) HV1 CCC angle α_z in x-y plane

Figure 5.51: Measured CCC platform angles in the x-y plane for the different BIS1-6 chambers in the serial production.

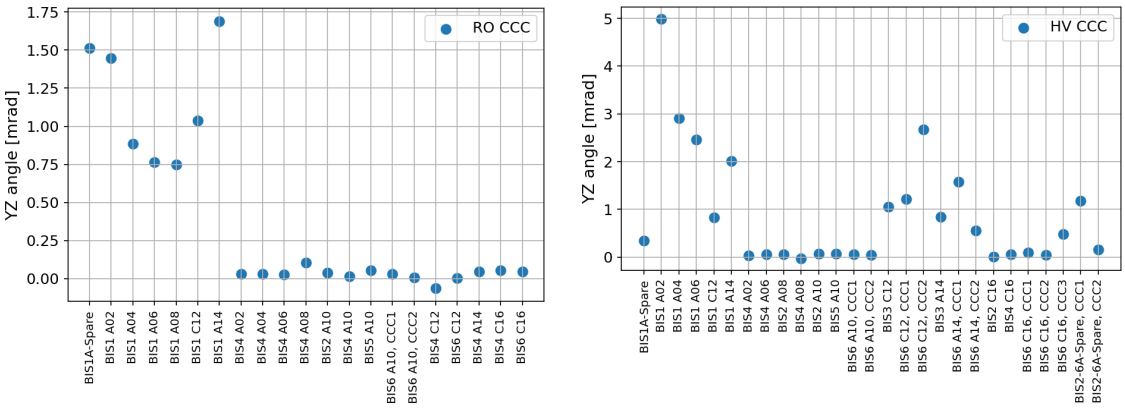

(a) RO1 CCC angle α_x in y-z plane

(b) HV1 CCC angle α_x in y-z plane

Figure 5.52: Measured CCC platform angles in the y-z plane for the different BIS1-6 chambers in the serial production.

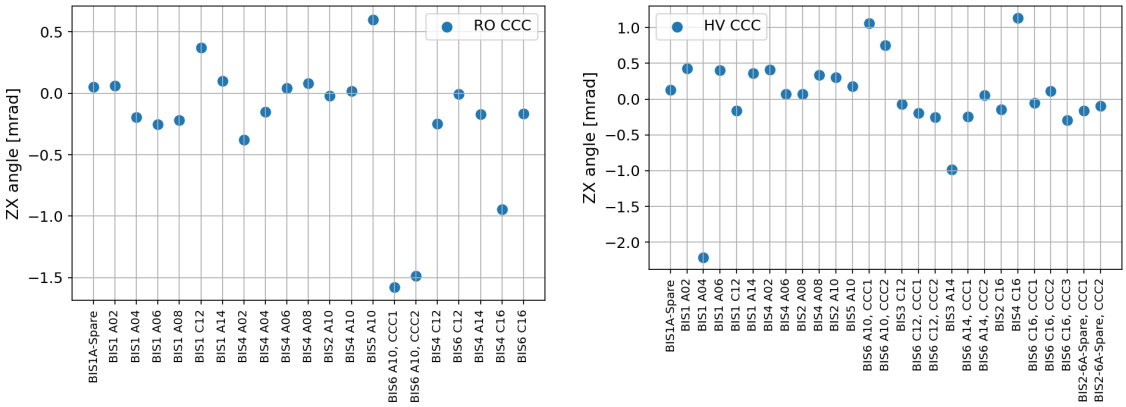

(a) RO1 CCC angle α_y in x-z plane

(b) HV1 CCC angle α_y in x-z plane

Figure 5.53: Measured CCC platform angles in the x-z plane for the different BIS1-6 chambers in the serial production.

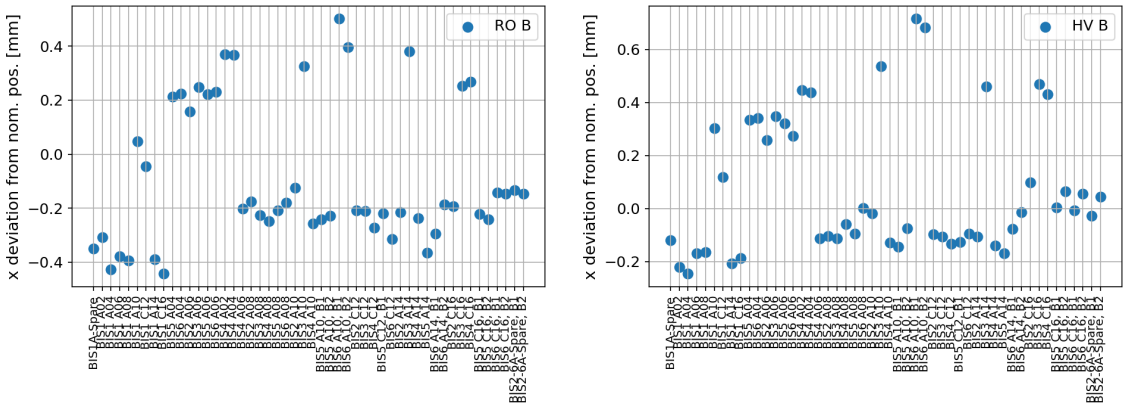

(a) RO B x

(b) HV B x

Figure 5.54: Measured B-field sensor platform positions in x for the different BIS1-6 chambers in the serial production.

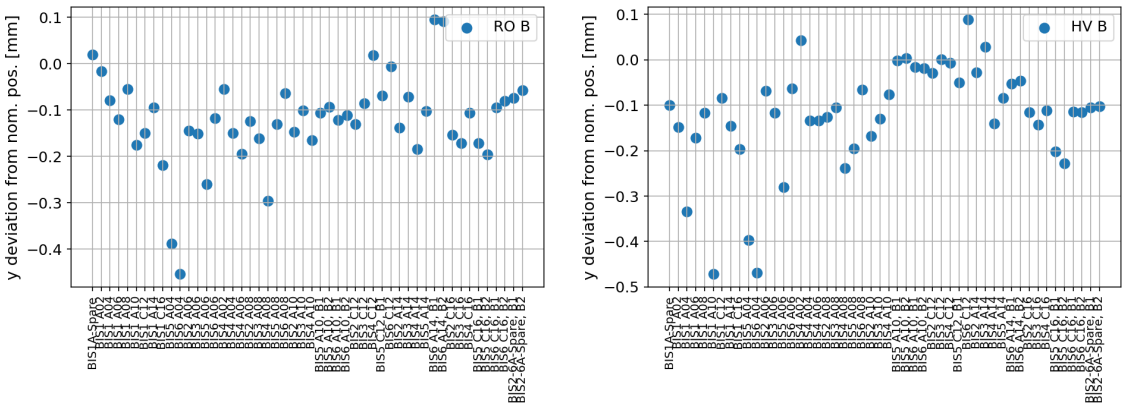

(a) RO B y (b) HV B y

Figure 5.55: Measured B-field sensor platform positions in y for the different BIS1-6 chambers in the serial production.

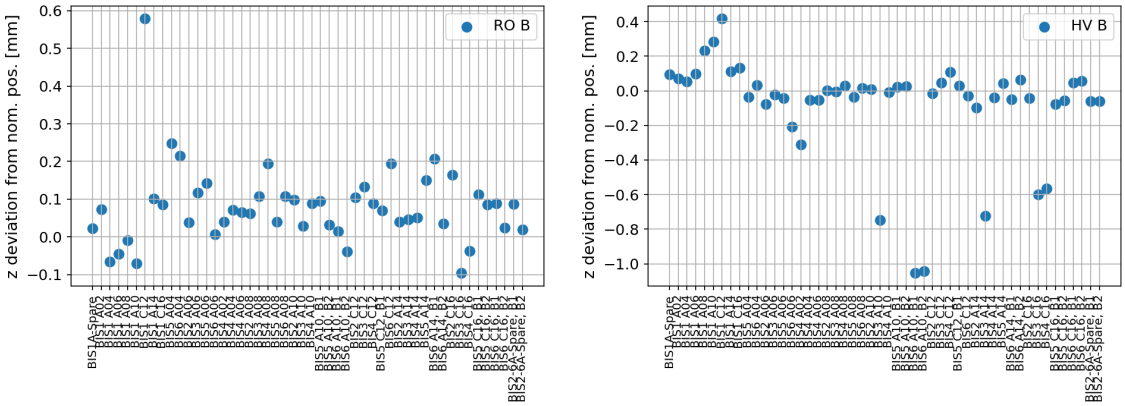

(a) RO B z (b) HV B z

Figure 5.56: Measured B-field sensor platform positions in z for the different BIS1-6 chambers in the serial production.

5.4.4 CMM Wire Position Measurements for BIS1-6 Chambers

The geometry of each BIS1-6 chamber is determined with an automated Coordinate Measuring Machine (CMM). The CMM has a feeler that allows to measure coordinates of objects within a 3D coordinate system. In comparison to the FARO arm, the CMM has a higher precision, especially over large distances of 1-2 m, the sizes of the BIS1-6 chambers. The chamber are mounted on the granite table of the CMM on rails in a transport frame like in ATLAS and gravitational deformation of the chamber occur. By measuring the coordinates of multiple points on the reference surface of each endplug, the positions of the centers of the endplugs and therefore the positions of the sense wire in the whole chamber on RO and HV side are determined. This allows checking the positioning accuracy of the drift tubes including the distances between the layers. Furthermore, the deformations of the chamber can be studied and the predictions of the in-plane system compared to the mechanical measurements. Potential deviations in the tube positioning in the course of the serial production can be spotted and corrected.

The sense wire positions of each side are fitted to the expected wire grid with the following free parameters:

- Origin of the coordinate system: y_0, z_0
- Rotation angle of the chamber: α

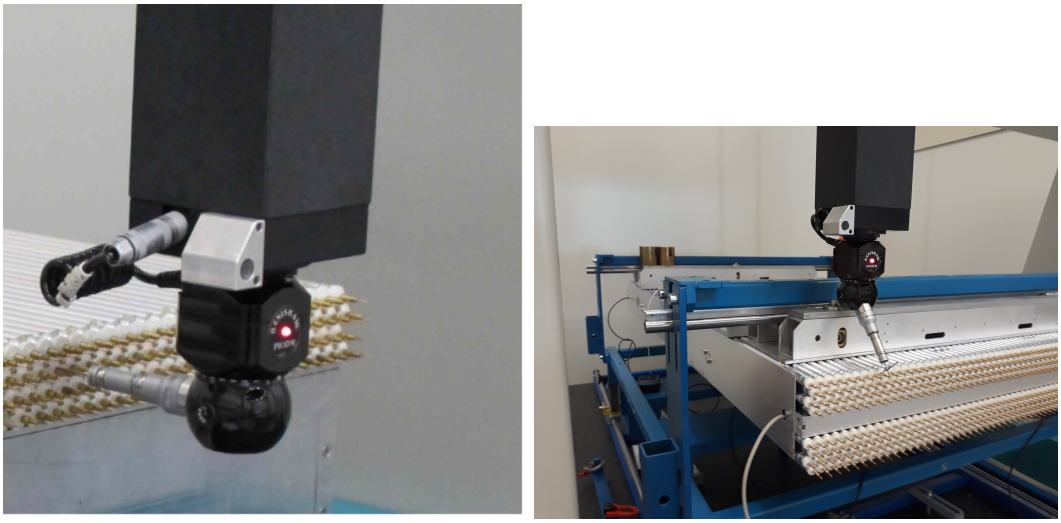

(a) (b)

Figure 5.57: (a) Measurement of the wire positions with the CMM. (b) Measurement of the wire positions of the top layer on both sides to determine the torsion angle between both sides. On one corner of the chamber weights are placed to change the torsion angle.

- Parabolic curvature of the wire grids, shared by all layers: c
- Position of the extremum of the parabola along the z-axis: a
- y-pitch: Δy
- z-pitch: Δz
- Multilayer distance, y-direction: Δy_m
- Multilayer shift, z-direction: Δz_m

The sense wire positions in the coordinate system of the CMM are

$$\begin{pmatrix} y \\ z \end{pmatrix} = \begin{pmatrix} y_0 \\ z_0 \end{pmatrix} + \begin{pmatrix} \cos\alpha & \sin\alpha \\ -\sin\alpha & \cos\alpha \end{pmatrix} \begin{pmatrix} y' \\ z' \end{pmatrix}, \tag{5.6}$$

relative to the positions y' and z' in the chamber coordinate system which can be parametrized as:

$$\begin{pmatrix} y' \\ z' \end{pmatrix} = \begin{pmatrix} \Delta y \cdot (i_{\text{layer}} - 1) + c \cdot (\Delta z \cdot (i_{\text{tube}} - 1) - a)^2 \\ \Delta z \cdot (i_{\text{tube}} - 1) \end{pmatrix}, \tag{5.7}$$

where i_{layer} is the drift tube layer index ranging from 1 to 8, starting with the bottom layer. i_{tube} is the index of the drift tubes within a layer ranging from 1 to 70 for BIS1 chambers and from 1 to 58 for BIS2-6 chambers. The drift tube with index 1 is the closest to the interaction point. Each even numbered layer is shifted in z by half of the value of the z-pitch, 7.55 mm nominally. For the second multilayer, Δy_m and Δz_m are added to the y and z coordinates, respectively. The fit is performed three times with different free parameter settings. In the first fit, the curvature is set to 0. A second fit takes the curvature into account. For the third fit, instead of an average layer distance Δy individual distances between adjacent layers are fitted and the curvature is also set to 0.

The chamber is too large for the CMM to reach all endplugs of both sides in one measurement. Between, these measurements on RO and HV side, the chamber has to be moved which affects their chamber torsion due to changing external forces. Therefore three separate CMM measurements are performed. In the first two measurements, the positions of all endplugs are measured on the RO or HV sides, to determine the pitches Δy and Δz, the distances between the layers and multilayer and the curvatures of the grid. The fits are performed independently for both sides and additionally for both sides combined. The combined fit of Δy, Δz, Δy_m, Δz_m on RO and HV side are relevant for the muon track reconstruction together with the relative torsion angle between the sides. The curvatures can be and are neglected.

Figure 5.58 shows the residual distributions of the wire position measurements of the first chamber BIS1-A02 (Module 1) in the coordinates y, z and the radial distance $r = \sqrt{y^2 + z^2}$ which is most

relevant for track reconstruction with cylindrical symmetric drift tubes. The distributions can be well described by a Gaussian function. From the widths of these distributions, the positioning accuracies of the wires are determined. For the BIS1-A02 chamber, the positioning accuracies are 11.0, 8.0 and 8.5 μm in y, z and r, respectively. Figures 5.59-5.61 show the positioning accuracies in y, z and r for each side for the assembled chamber. The RMS values of the residuals are between 8 and 13 μm in y, between 5 and 9 μm in z and between 5 and 11 μm in r, well below the required 20 μm.

Figures 5.62 and 5.63 show the measured wire pitches Δy and Δz for the assembled chambers for RO and HV side and for both sides combined. The y-pitches are between 13.085 and 13.094 mm with an average of 13.090 ± 0.002 mm, equally on RO and HV side. Only in the early production there was a larger difference between both sides for five subsequent chambers. There are very small differences between the z-pitches of the different chambers with values ranging from 15.0996 to 15.1003 mm and average of 15.1000 ± 0.0001 mm measured at 20 ± 1 °C. The RO side shows always slightly larger values than the HV side. The assembly combs have been measured with CMM and fitted to the same grid model before the start of the serial production. No difference in the z-pitches of both sides have been observed. A temperature difference of 1°C with the coefficient of thermal expansion of aluminium of $23.1 \cdot 10^{-6}$ K^{-1} would change the z-pitch by ≈ 0.3 μm, which is of the same order as the observed deviation. However, the temperature is measured during the CMM measurement and rarely changes by more than 0.1°C between the measurement of the two sides. Also this cannot explain the systematic difference between the HV side and RO side. This deviation might be caused by a systematic error of the CMM. This still under investigation.

Figures 5.64-5.67 shows the individual measured distances between adjacent layers for the produced chambers. The distances vary between 13.075 and 13.12 mm. In general, the measured distances on RO and HV side are similar. In the early production, there was a larger difference between the RO and HV side for five subsequent chambers between layers 2 and 3 and between layers 6 and 7. These are the same chambers that also showed differences between RO and HV in the y-pitches. The assembly combs were investigated and it was found that the combs were slightly deformed during the assembly of the tube layers due to the pushing of the tubes against the RO side comb. The procedure was changed such that such deformations are avoided.

For the third CMM measurement, the chamber is moved in a position in which the endplugs of the top layer 8 can be reached by the CMM feeler both on the RO and the HV side. During this measurement the in-plane alignment system is read out. This measurement is used to determine the torsion angle between the two sides and to validate the torsion measurement with in-plane alignment system. It is important to note that the torsions changes when the chamber is moved on the rails of the transport frame. This is also expected on the rails in the ATLAS detector. The torsion angle evaluated by this measurement is not stable. The third CMM measurement is repeated with a weight of 4 kg placed asymmetrically on one end on the HV side increasing the torsion angle and allowing for another

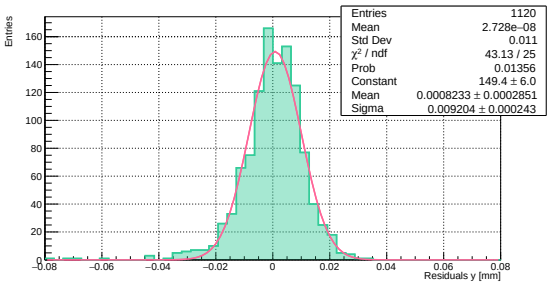

(a) Residuals y

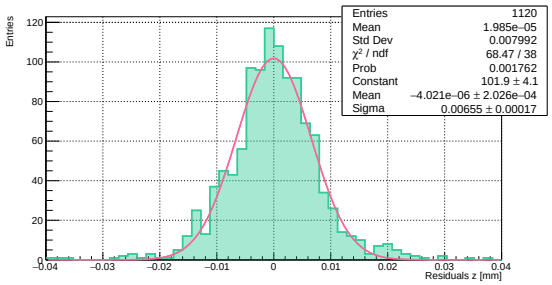

(b) Residuals z

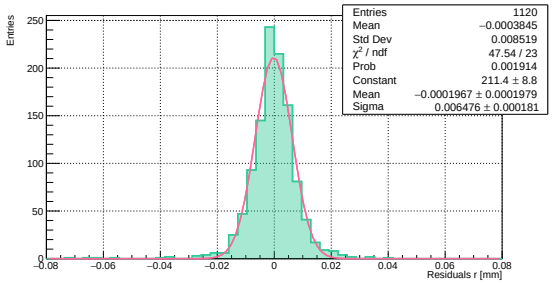

(c) Residuals r

Figure 5.58: Residual distributions in y, z and r of the CMM wire coordinate measurements for RO and HV side combined for the BIS1-A02 chamber.

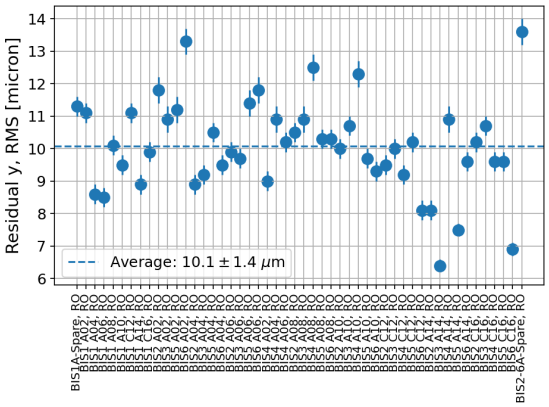

(a) RO, y

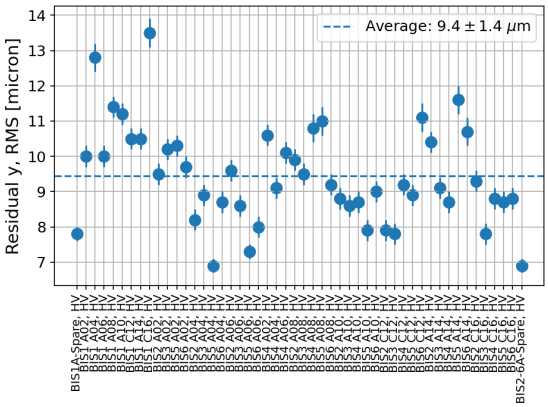

(b) HV, y

Figure 5.59: Widths of the residual distributions in y of the CMM wire coordinate measurements on the RO and HV side, i.e. the wire positioning accuracy of the BIS1-6 chambers in the sequence of construction.

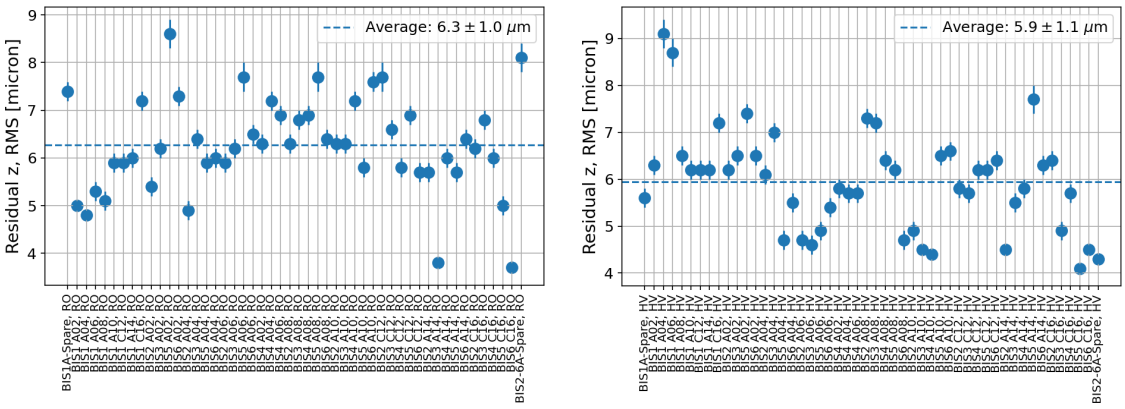

(a) RO, z (b) HV, z

Figure 5.60: Widths of the residual distributions in z of the CMM wire coordinate measurements on the RO and HV side, i.e. the wire positioning accuracy of the BIS1-6 chambers in the sequence of construction.

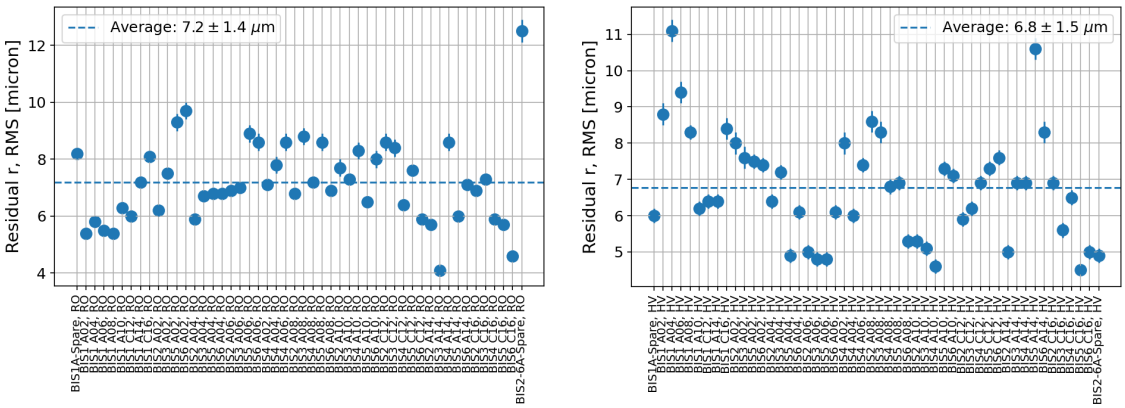

(a) RO, r (b) HV, r

Figure 5.61: Widths of the residual distributions in r of the CMM wire coordinate measurements on the RO and HV side, i.e. the wire positioning accuracy of the BIS1-6 chambers in the sequence of construction.

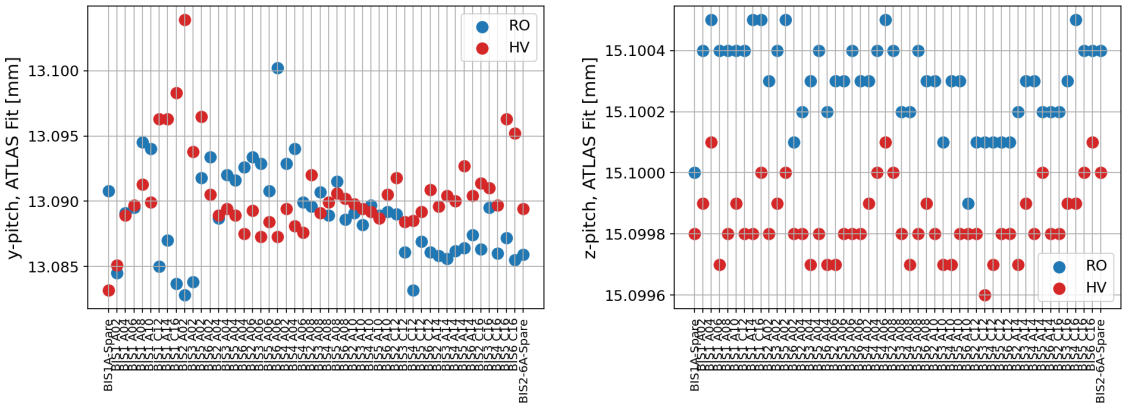

(a) y, splitted by side

(b) z, splitted by side

Figure 5.62: Wire pitches in y and z for RO and HV side for the BIS1-6 chambers in the sequence of construction.

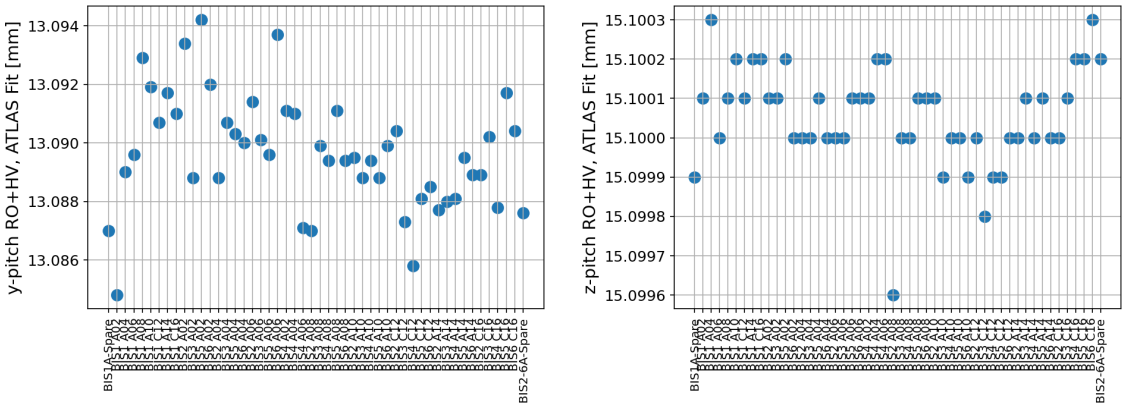

(a) y

(b) z

Figure 5.63: Wire pitches in y and z for RO and HV side combined for the BIS1-6 chambers in the sequence of construction.

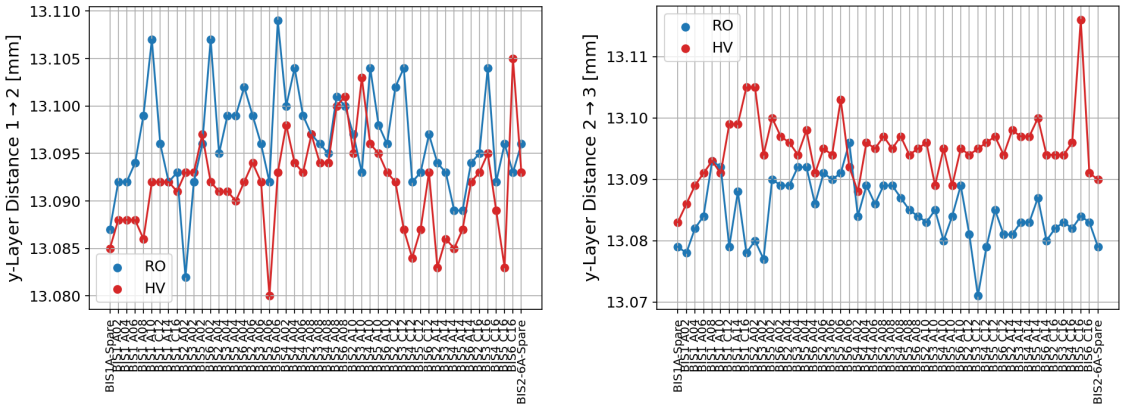

(a) Layer 1 → 2 (b) Layer 2 → 3

Figure 5.64: Individual wire layer distances in y for the BIS1-6 chambers in the sequence of construction.

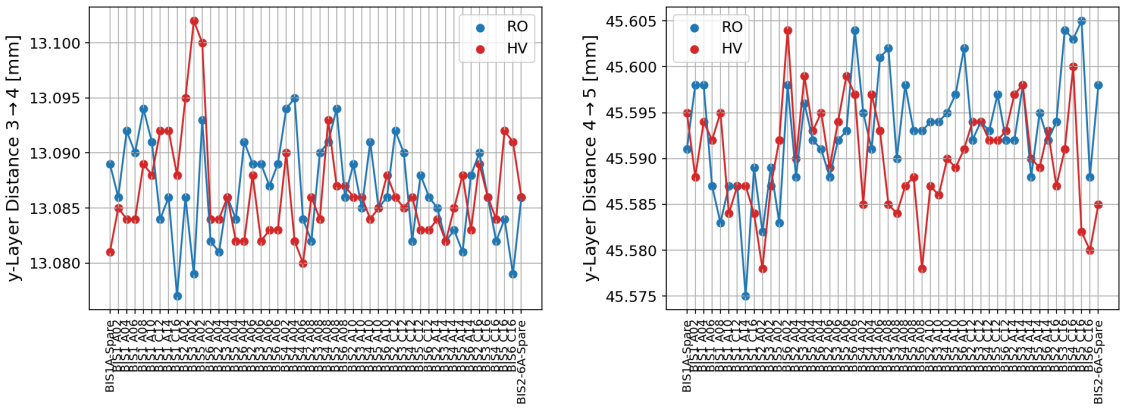

(a) Layer 3 → 4 (b) Layer 4 → 5

Figure 5.65: Individual wire layer distances in y for the BIS1-6 chambers in the sequence of construction.

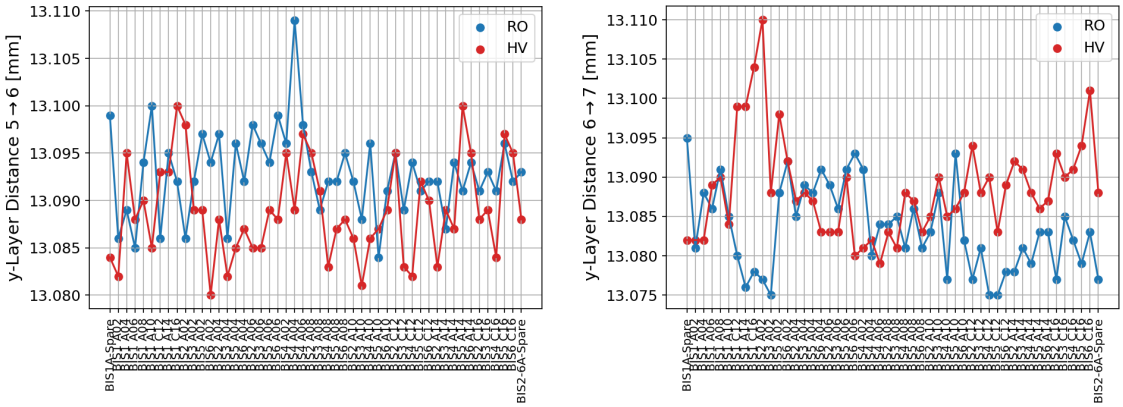

(a) Layer 5 → 6 (b) Layer 6 → 7

Figure 5.66: Individual wire layer distances in y for the BIS1-6 chambers in the sequence of construction.

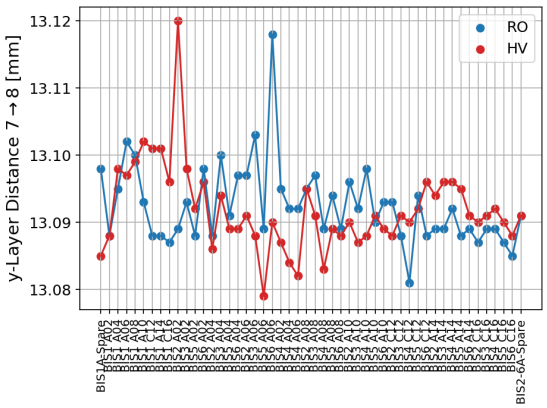

(a) Layer 7 → 8

Figure 5.67: Individual wire layer distances in y for the BIS1-6 chambers in the sequence of construction.

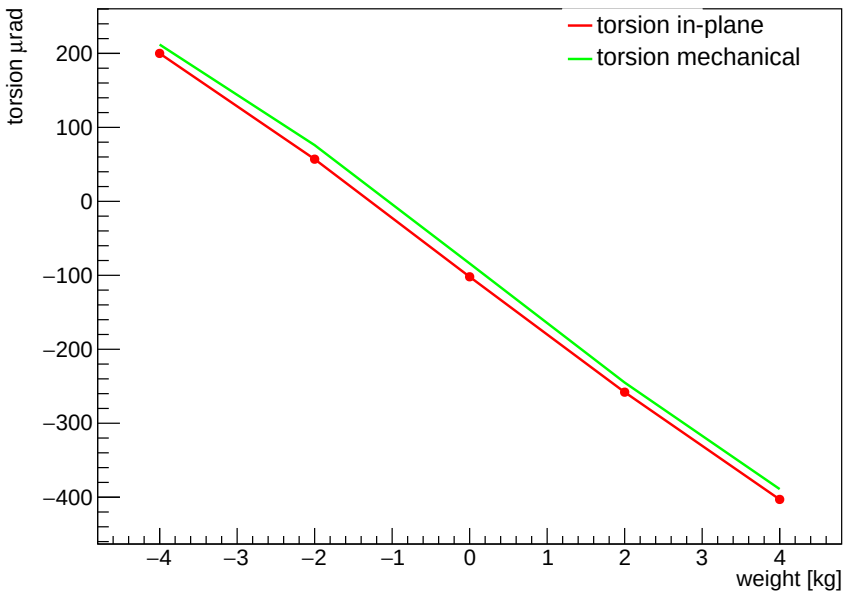

Figure 5.68: Torsion angles of the prototype BIS1 sMDT chamber as a function of additional weights placed on the HV side as measured with the CMM and with the in-plane alignment system at the same time. The different sign of the weigths correspond to the weights placed on opposite ends of the HV side.

validation of the in-plane torsion measurement. For the prototype BIS1 sMDT chamber, the so called Module 0 chamber, additional measurement with different weights have been performed. The torsion angles from the mechanical and the optical measurements are shown in Figure 5.68 as a function of the applied weight. There is a good agreement between the two measurement methods and the torsion angles in both cases depend linearly on the weight.

Figure 5.69 shows the torsion angles for the different chambers evaluated with the CMM and the in-plane alignment system without and with 4 kg weight. The torsion angle ranges between −150 and +150 μrad without weight. Applying the weight on the left corner on the HV side (as seen from the RO side) increases the torsion angle to values ranging from 50 to 400 μrad. Good agreement is found between the CMM and the in-plane alignment system measurements with deviations below 50 μrad demonstrating that the in-plane alignment works as intended.

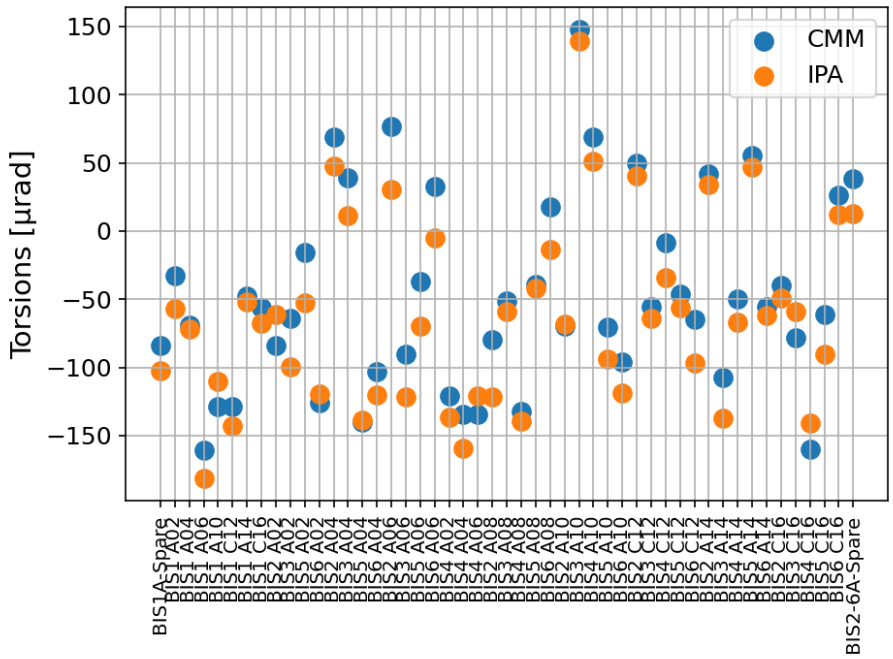

(a) Without weight applied.

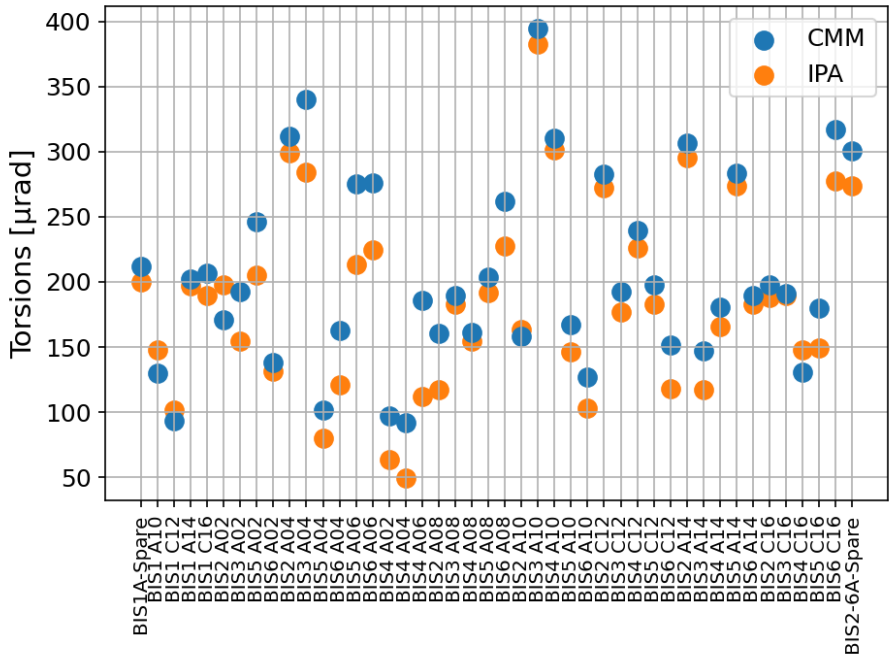

(b) With 4 kg applied on the left corner of the HV side as seen from the RO side.

Figure 5.69: Torsion angle measurements with CMM and in-plane alignment system (IPA) for the BIS1-6 chambers in the sequence of construction.

5.4.5 In-plane Alignment Measurement of the BIS1 Prototype Chamber Under Different Angles

Similar to the BIS78 chamber, the BIS1 prototype chamber was installed in the rotation frame, and the in-plane alignment system was readout for different rotation angles of the chamber. The torsion as a function of the rotation angle is shown in Figure 5.70. It again follows approximately a sine function varying between −110 and +100 μrad. After each full rotation by 360°, the chamber returns to the same deformation as expected.

5.4.6 Gas Leak Rate Measurement

The gas distribution is tested for tightness during several steps of the chamber construction. The first test is done immediately after the installation of the gas distribution system. A second test is performed after the installation of the electronics and the final test after the transport of the chamber from the construction site to CERN. The leak rate must not exceed $2N_{\text{tubes}} \cdot 10^{-5} \frac{\text{mbar}\cdot\text{l}}{\text{s}}$ for each multilayer separately.

For the leaktest, the chamber is filled with the nominal gas mixture of Ar/CO_2 (93/7) at absolute pressure of 3 bar. The gas pressure is monitored over at least 24 h while the temperature of the

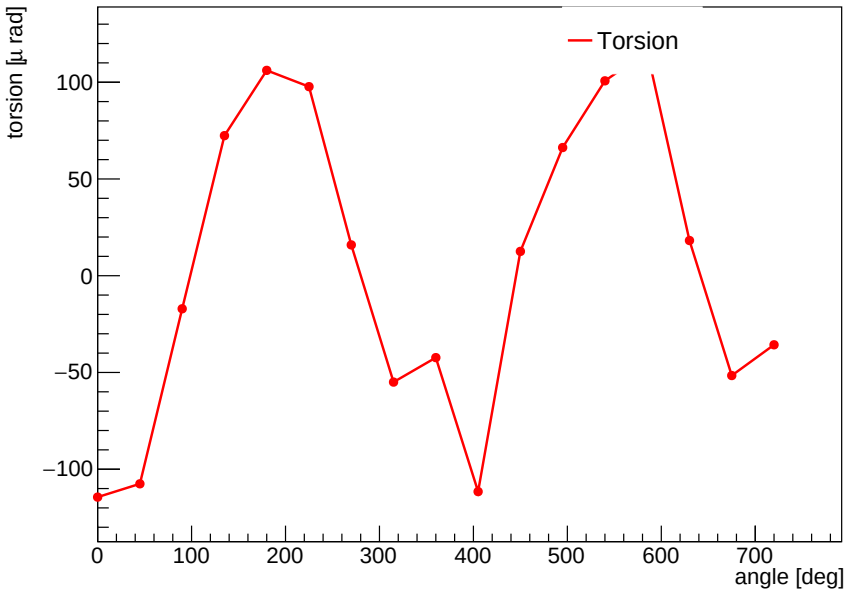

Figure 5.70: Torsion measured by the in-plane alignment system as a function of the rotation angle of the BIS1 prototype chamber.

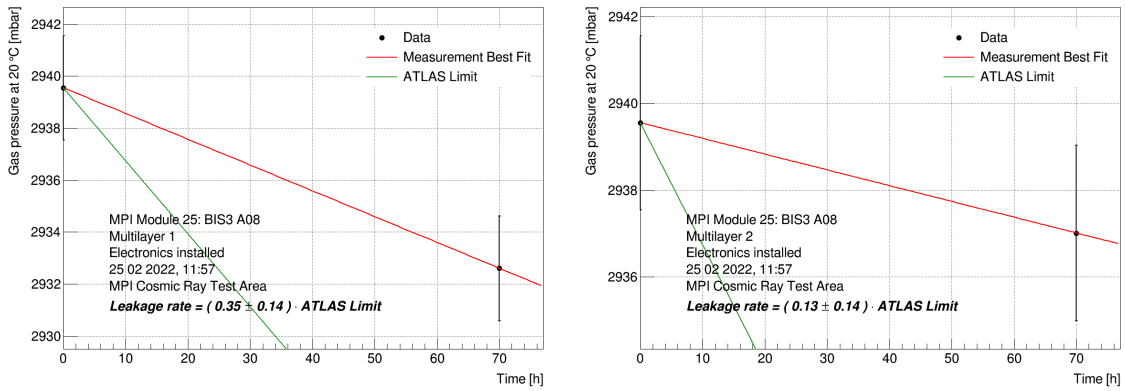

(a) Multilayer 1 (b) Multilayer 2

Figure 5.71: Gas leak rate measurements of the BIS3-A08 chamber (red) via pressure drop over > 24 h compared to the required limit (green).

chamber is measured using temperature sensors distributed over the chamber surfaces. The pressure is translated in to the pressure expected at the reference temperature of 20 °C assuming an ideal gas. Since the final temperature sensors are not yet installed during the first leaktest, temporary temperature sensor are attached on the top and bottom of the chamber. Figure 5.71 shows the pressure measurements over time of the BIS3 A08 chamber from which the gas leak rate is determined.

Figure 5.72 shows the gas leak rate of the produced chambers relative to the required limit. Leak rate are well below the requirements in both multilayers The largest observed leak rate is 80% of the limit.

5.4.7 Performance Measurements with Cosmic Muons

After the installation of the electronics, the chamber is moved to a test stand where the chamber is connected and is tested for the noise rate of the electronics as well as the spatial resolution and efficiency for each tube using cosmic muons. Scintillators are placed above and below the chamber providing a trigger signal for muons traversing both of the scintillators. A sMDT chamber in the cosmic test stand is shown in Figure 5.73. The chamber is operated with the nominal gas mixture and pressure. The gas pressure and temperature of the chamber is measured during the chamber operation, providing a gas leak rate measurement after the installation of the electronics.

For the measurement of the noise rate of the electronics, the readout is triggered by a periodic signal.

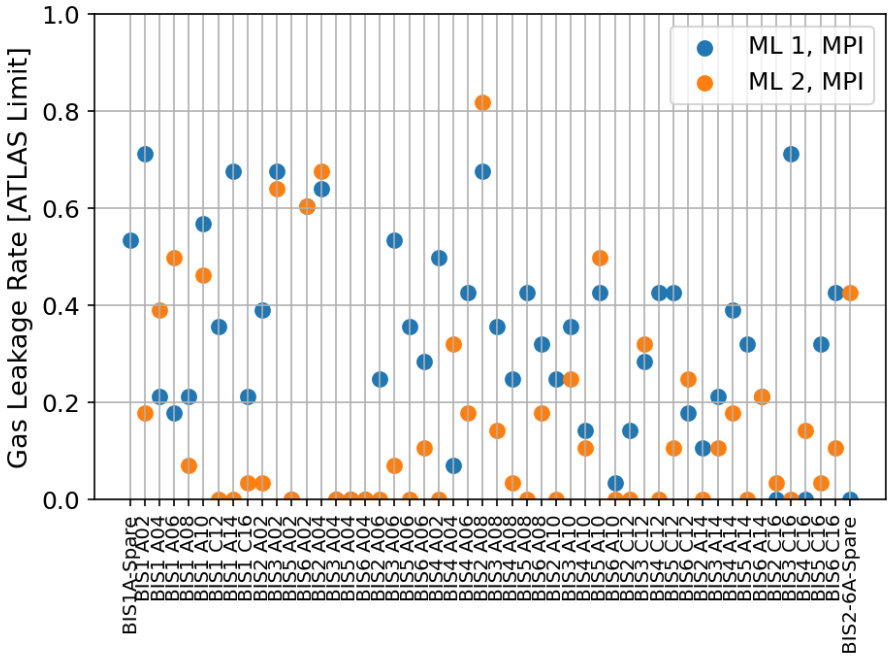

Figure 5.72: Measured gas leak rates of fully assembled BIS1-6 chambers in multilayer 1 and 2 in the sequence of construction.

The noise rate per readout channel is given by

$$f_{\text{noise}} = \frac{N_{\text{events}}}{\Delta t_{\text{RO}} \cdot N_{\text{triggers}}} \tag{5.8}$$

where N_{events} is the number of signals above the readout threshold after a trigger signal, Δt_{RO} denotes the active time window of the readout and N_{triggers} is the number of trigger signals. This test is performed with the high voltage disconnected and connected to the chamber. The noise rates with connected high voltage of the tested BIS1-6 chambers is shown in Figure 5.74. The noise rate is below 50 Hz per tube for all chambers with an average of about 10 Hz per tube. This is well below the requirement of < 1 kHz.

In order to measure the efficiency per tube the chamber measures cosmic muons using the scintillators as trigger. The muon tracks are reconstructed using the hits recorded by the chamber requiring at least 4 hits per track. The reconstruction is performed leaving out a single layer of drift tubes. It is tested for every track whether the drift tube in the tested layer traversed by the muon track provides a hit. The efficiency given by the ratio of the number of hits associated with the reconstructed tracks and the number of reconstructed tracks traversing the drift tube. The procedure is repeated leaving out another drift tube layer until all layers have been tested. Figure 5.75 shows the efficiency per tube for all tested

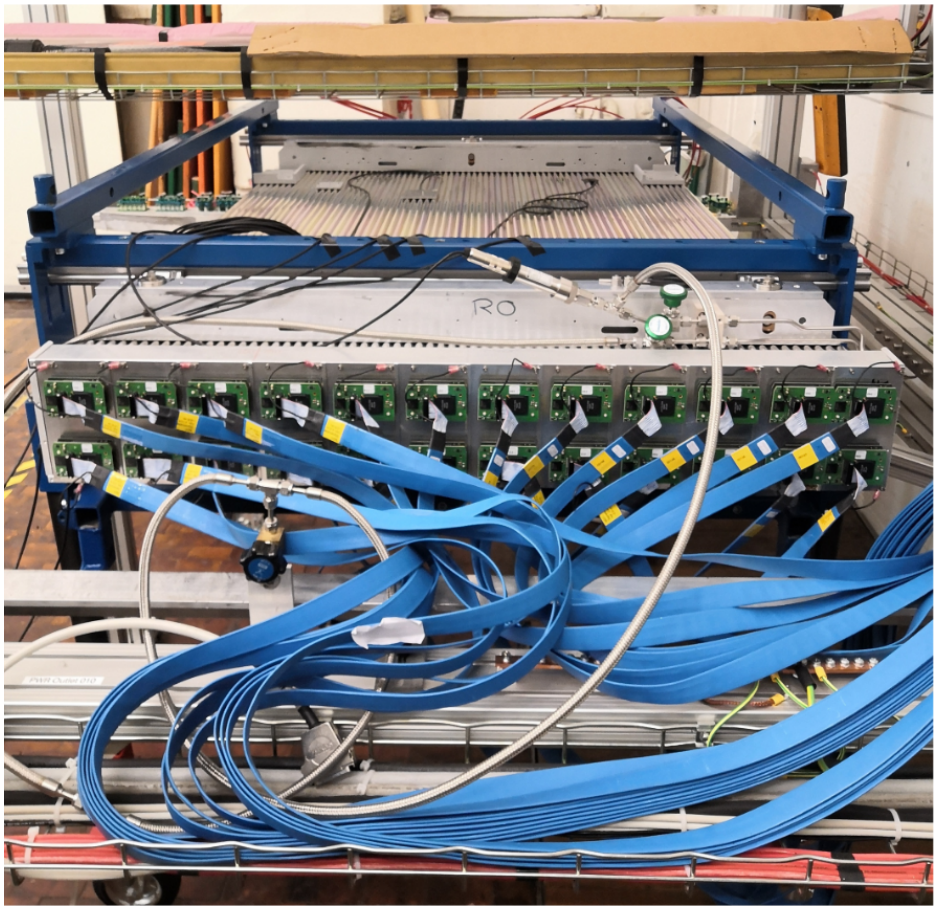

Figure 5.73: sMDT chamber in the cosmic test stand. Above and below the chamber scintillators are placed providing a trigger signal for muons traversing both scintillators.

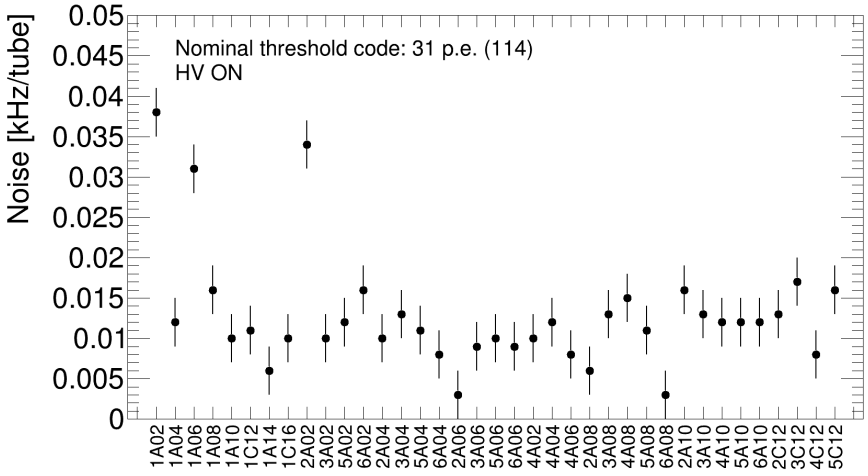

Figure 5.74: Measured noise rates of fully assembled BIS1-6 chambers.

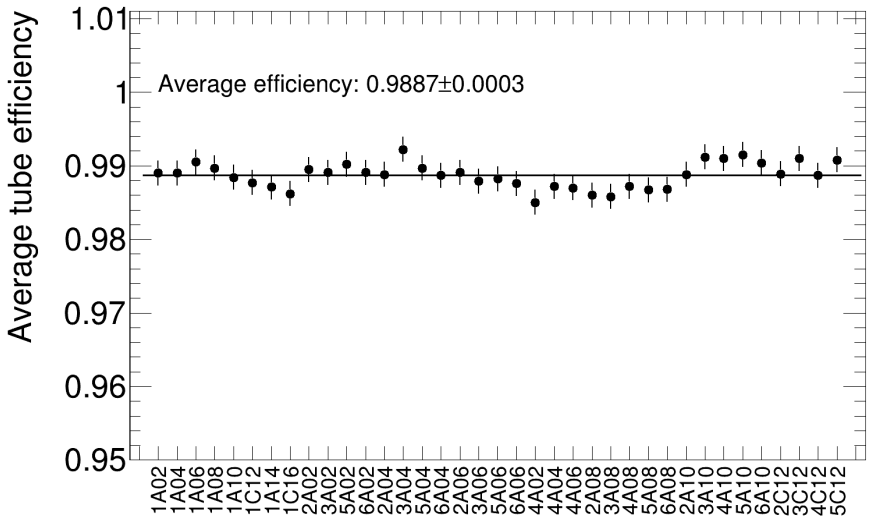

Figure 5.75: Measured efficiency per tube of fully assembled BIS1-6 chambers.

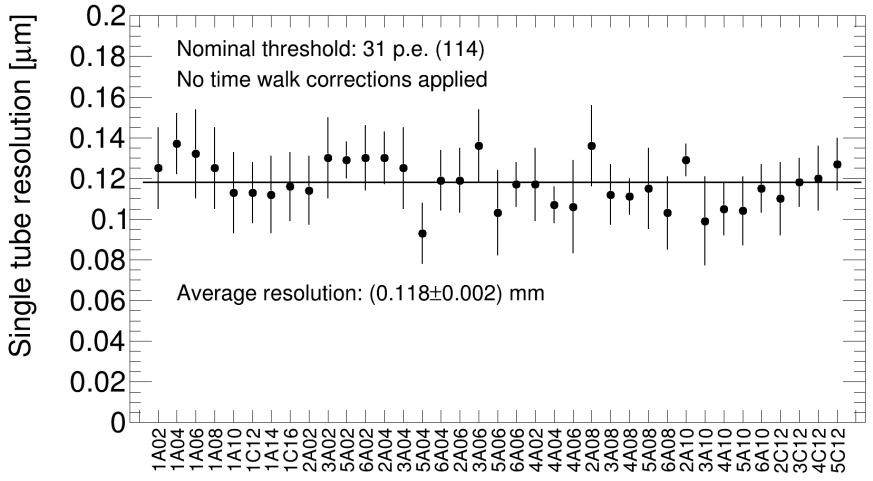

Figure 5.76: Measured spatial resolution per tube of fully assembled BIS1-6 chambers.

BIS1-6 chambers. The efficiency per tube is about 99%.

The spatial resolution is measured by comparing the drift radii of a drift tube measurement with the distance of the reconstructed track from the sense wire. The single tube resolution for all tested BIS1-6 chambers is shown in Figure 5.76. The average spatial resolution per tube is 0.119 ± 0.003 mm.

5.5 Summary of the Construction of new sMDT chambers

New sMDT chambers for the upgrade of the MS for the High Luminosity LHC are constructed. 16 BIS78 chambers were constructed in 2017-2019 and installed in the ATLAS detector in 2020. The production of 96 BIS1-6 chambers is still ongoing. As of september 2022 40 of 48 chambers have been built at the MPI. At the same time 26 of 48 have been constructed at the production site in Michigan. All chambers are expected to be assembled until end of 2022 at MPI and in 2023 in Michigan and are therefore, ready well before the start of LS3 in 2026. All chambers undergo several measurements during the construction in order to assure they fulfill the requirements on the precision of the sense wire positioning as well as gas leak rate, HV stability and electronic performance. So far all assembled chamber fulfill the requirements.

CHAPTER SIX

SEARCH FOR SUPERSYMMETRY IN FOUR LEPTON FINAL STATES

Final states with four or leptons are an excellent channel for the search for supersymmetry, due to the low SM background rates. The search presented in this chapter uses a dataset of 139 fb^{-1} of pp collisions at a center-of-mass energy of 13 TeV recorded between 2015 and 2018 with the ATLAS detector [123]. Similar searches have been already performed using the LHC Run 1 data and with a partial Run 2 dataset of 2015 and 2016 [124]. In addition to the increased amount data used by this analysis, the signal regions of the previous search have been reoptimized to increase the sensitivity to high SUSY masses. Furthermore, the dominant irreducible backgrounds ZZ and $t\bar{t}Z$ are normalized to data in dedicated control regions instead of relying on Monte Carlo only. The estimation of the reducible background has been improved.

6.1 Targeted SUSY models

The SUSY models considered for this search can be split into two types. General Gauge Mediated (GGM) SUSY breaking scenarios [125] consider a $\tilde{\chi}_1^0$, $\tilde{\chi}_2^0$ and $\tilde{\chi}_1^\pm$ higgsino triplet. The members of the higgsino triplet are close in mass and therefore decays of the $\tilde{\chi}_2^0/\tilde{\chi}_1^\pm$ to $\tilde{\chi}_1^0$ yield only low p_T SM particles that are difficult to reconstruct. In GGM scenarios the LSP is a nearly massless gravitino $\tilde{G}$, the fermionic superpartner of the graviton. The search presented in this thesis considers pair produced higgsinos that decays into gravitinos via Z/h bosons. The search targets events in which two Z bosons decay each into an electron or muon pair. The model is parametrized in the higgsino mass and the branching ratio of the higgsino decaying into Z bosons. The feynman diagrams of the GGM model are shown in Figure 6.1.

The second type of SUSY models considered in this thesis assume RPV which allows the LSP to decay into two charged leptons and a neutrino. Three possibilities for the NLSP are considered. The first scenario is wino pair production where the wino decays via W, Z or higgs bosons into the LSP.

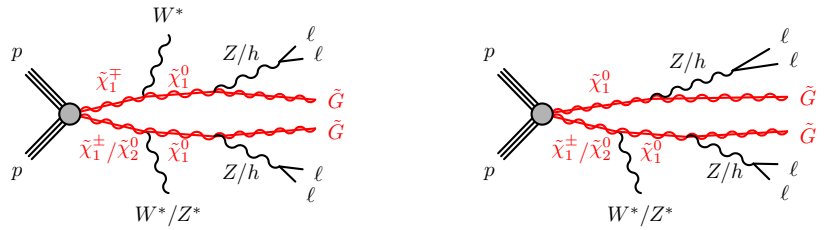

(a) (b)

Figure 6.1: Diagrams of the processes in the SUSY RPC GGM higgsino models. The W^*/ Z^* produced in the $\tilde{\chi}_1^{\pm}/\tilde{\chi}_2^0$ decays are off-shell and their decay products are usually not reconstructed.

The second model considers pair production of charged left-handed sleptons ($\tilde{\ell}_L$) and sneutrinos ($\tilde{\nu}$) decaying into the LSP and a charged lepton or neutrino. The third RPV model considers pair production of gluinos decaying into the LSP and two quarks. The feynman diagrams of the RPV models are shown in Figure 6.2.

For RPV models two scenarios for the RPV coupling are considered. The first scenario considers a non-zero λ_{12k} ($k = 1, 2$) coupling leading to decays of the LSP into light leptons only. The second scenario considers a non-zero λ_{i33} ($i = 1, 2$) coupling leading to decays of the LSP dominantly into τ leptons. The decay modes and branching ratios of the $\tilde{\chi}_1^0$ for the two scenarios for the RPV couplings are showns in Table 6.1.

Table 6.1: Decay modes and branching ratios of the $\tilde{\chi}_1^0$ for the two scenarios for the RPV coupling.

	$e^+e^-\nu$	$e^\pm\mu^\pm\nu$	$\mu^+\mu^-\nu$	$e^\pm\tau^\pm\nu$	$\tau^+\tau^-\nu$	$\mu^\pm\tau^\pm\nu$
λ_{12k}	1/4	1/2	1/4	0	0	0
λ_{i33}	0	0	0	1/4	1/2	1/4

6.2 Search Strategy

In general, the design of an analysis is guided by the final state that is expected by the decay chain of the considered SUSY models. In case of this analysis it is a final state with at least four leptons. The hypothetical production of SUSY particles in pp collisions, adds additional events to the expectation from the SM background to that final state. The production cross sections of the SUSY particles is expected to be much smaller than the production cross sections of SM particles decaying into the same final state. Therefore, signal regions (SR) are designed by applying additional selections to the considered events, in order to make the small SUSY contributions of the expected event yield comparable to that of the SM. Monte Carlo samples are used to optimize the signal regions (SRs),

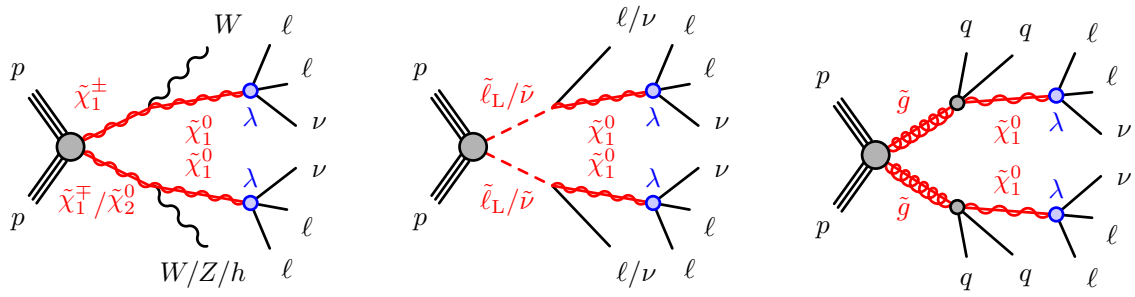

(a) Wino NLSP (b) $\tilde{\ell}_L/\tilde{\nu}$ NLSP (c) $\tilde{g}$ NLSP

Figure 6.2: Diagrams of the benchmark SUSY models of RPC NLSP pair-production of (a) winos, (b) sleptons/sneutrinos and (c) gluinos, followed by an RPV decay of the $\tilde{\chi}_1^0$ LSP. The LSP is assumed to decay as $\tilde{\chi}_1^0 \to \ell\ell\nu$ with 100% branching ratio.

such that a high expected signal sensitivity is reached for the considered models over are large signal parameter space. For the most dominant SM backgrounds, control regions (CRs) are used to determine the contributions of these backgrounds in data. The CRs are required to be enriched with the targeted background process with a negligible contamination from signal events. Furthermore, they are required to be close but orthogonal to the SR to constrain the backgrounds in a phase space similar to that of the SR. The background predictions in the CRs are then extrapolated to the SRs. Validation regions (VRs) are designed to validate the extrapolation. The VRs are required to be orthogonal to the CRs and SRs and to be depleted in signal. In case correct background modeling is observed in the VRs, the predictions in the SR can be compared to data.

6.3 Data and simulated Event Samples

The analysis uses pp collisions at $\sqrt{s}$ = 13 TeV, that were recorded during the Run 2 in 2015-2018. With the beam, detector and data-quality requirements applied [46], the total integrated luminosity used corresponds to 139.0 ± 2.4 fb^{-1} [126]. MC generators are used to simulate SM processes as well as new physics signals. The SUSY signals are generated using MadGraph5_aMC@NLO v2.2.2 [127] for the calculation of the leading-order (LO) matrix elements with up to two extra partons. The PDF set used is `NNPDF23LO` [94]. Parton showering, hadronization, the decay of the produced SUSY particles and the underlying event is modelled using Pythia v8.230 [128] with a set of tuned parameters called the tune A14 [129]. The matrix element is matched to parton showers following the CKKW-L prescription [130] with a matching scale set to one quarter of the mass of the pair-produced SUSY particles. The cross-sections are calculated at next-to-leading order (NLO), the resummation of soft gluon emission at next-to-leading logarithm accuracy (NLL) [131–138]. The simulated signals

are passed through the fast detector simulation [97]. For the gluino model mass ranges of 2.2-2.8 TeV (1.6-2.5 TeV) are simulated for For the Wino NLSP masses between 1 TeV (0.6 TeV) and 1.7 TeV (1.1 TeV) are generated for scenarios with λ_{12k} ($\lambda_i 33$) RPV coupling. For the $\tilde{\ell}_{\mathrm{L}}/\tilde{\nu}$ model, mass ranges from 400 GeV to 1.3 TeV (900 GeV) are considered for scenarios with λ_{12k} ($\lambda_i 33$) RPV coupling.

The dominant backgrounds that can produce four prompt and isolated charged leptons are ZZ, $t\bar{t}Z$, triboson (VVV) and Higgs production ($V = W, Z$). Diboson and triboson production are simulated using Sherpa v2.2.1 or v.2.2.2 [139]. The matrix elements for the ZZ simulation contains all diagrams with four electroweak vertices. They are calculated at NLO for up to one extra parton and at LO for up to three extra partons [140]. Triboson production includes the processes ZZZ, WZZ and WWZ with four to six charged leptons. Tribosons are generated at NLO and for up to two extra partons at LO [140]. For diboson and triboson production the `NNPDF30NNLO` PDF set [141] is used and the parton showering uses the Sherpa default tune. $t\bar{t}Z$ production as well as $t\bar{t}W$ production are simulated using MadGraph5_aMC@NLO v2.3.3 with the `NNPDF23LO` PDF set. Pythia v8.210 is used for the parton showering with the A14 tune.

The Higgs production includes Higgs production via gluon-gluon fusion (ggF) and vector-boson fusion (VBF) as well as associated production with a boson (WH,ZH) or $t\bar{t}$ ($t\bar{t}H$). They are simulated with Powheg-Box v2 [142–144] and Pythia v8.212 (v8.230 in case of $t\bar{t}H$) and is simulated at NNLO+NNLL [145–148] accuracy (NLO for $t\bar{t}H$ [145]). The `CTEQ6L1` PDF set [149] is used and the parton showering uses the AZNLO tune [150]. $t\bar{t}H$ uses instead the `NNPDF23LO` PDF set and the A14 tune.

Other backgrounds producing atleast four charged leptons are tWZ, $t\bar{t}WW$, $t\bar{t}ZZ$, $t\bar{t}WH$, $t\bar{t}HH$, $t\bar{t}tW$ and $t\bar{t}t\bar{t}$ processes. They are simulated using MadGraph5_aMC@NLO v2.2.2, v.2.3.3 or v2.6.7 together with Pythia v8.186, v8.212 or v8.240 at NLO [127, 151] using the `NNPDF23LO` PDF set and the for parton showering the A14 tune.

$t\bar{t}$, Z+jets and W+jets are used for the estimation of the reducible background (Section 6.6.2). $t\bar{t}$ is simulated using Powheg-Box v2 and Pythia v8.230 at NNLO+NNLL accuracy [152–158] Using the `NNPDF23LO` PDF set and the A14 tune of the parton showering. Z+jets and W+jets events are generated using Powheg-Box v2 and Pythia v8.186 at NNLO accuracy [159] using the `CTEQ6L1` PDF set with AZNLO tune.

All SM background samples are passed through the full ATLAS GEANT4 detector simulation [96]. An summary of the simulated MC samples is shown in Table 6.2.

Scale factor weights are applied to the simulated MC samples in order to account for differences from data regarding trigger efficiencies, b-quark jet identification efficiencies and the energy and

momentum measurements of leptons and jets. The samples are also reweighted such that the simulated pile-up matches the pile-up of the data.

Table 6.2: Summary of the simulated MC samples used in this analysis, where $V = W, Z$, and includes off-shell contributions. "Tune" refers to the set of parameter values used by the generator. Table adapted from Ref. [123]

Process	Generator(s)	Cross-section calculation	Tune	PDF set
ZZ, WZ, WW	Sherpa v2.2.2	NLO	Sherpa default	NNPDF30NNLO
VVV	Sherpa v2.2.1	NLO	Sherpa default	NNPDF30NNLO
H via ggF, VBF, VH	Powheg-Box v2 + Pythia v8.212	NNLO+NNLL	AZNLO	CTEQ6L1
$t\bar{t}H$	Powheg-Box v2 + Pythia v8.230	NLO	A14	NNPDF23LO
$t\bar{t}Z, t\bar{t}W$	MadGraph5_aMC@NLO v2.3.3 + Pythia v8.210	NLO	A14	NNPDF23LO
$t\bar{t}WW, t\bar{t}W$	MadGraph5_aMC@NLO v2.2.2 + Pythia v8.186	NLO	A14	NNPDF23LO
$t\bar{t}WZ, tWZ$	MadGraph5_aMC@NLO v2.3.3 + Pythia v8.212	NLO	A14	NNPDF23LO
$t\bar{t}ZZ, t\bar{t}WZ, t\bar{t}WH, t\bar{t}HH$	MadGraph5_aMC@NLO v2.6.7 + Pythia v8.240	NLO	A14	NNPDF23LO
$t\bar{t}tW, t\bar{t}t\bar{t}$	MadGraph5_aMC@NLO v2.2.2 + Pythia v8.186	NLO	A14	NNPDF23LO
$t\bar{t}$	Powheg-Box v2 + Pythia v8.230	NNLO+NNLL	A14	NNPDF23LO
Z+jets, W+jets	Powheg-Box v2 + Pythia v8.186	NNLO	AZNLO	CTEQ6L1
SUSY signals	MadGraph5_aMC@NLO v2.2.2 + Pythia v8.230	NLO+NLL	A14	NNPDF23LO

6.4 Event and Object Selection

The object selection is performed in three steps. In the particle preselection, the reconstructed objects have to fulfill minimal quality criteria. The different particle reconstruction algorithms run independent from each other, therefore the same energy deposits or tracks may be used in the reconstruction of different particles. In order to resolve these ambiguities preselected particles have to pass the so-called overlap removal. Particles passing this step are called baseline particles. After the overlap removal additional quality requirements are applied to the particles. Particles passing the final step are referred to as signal particles. Another category, referred to as loose leptons, is introduced to estimate the reducible background (section 6.6.2). Loose leptons are leptons that are baseline leptons but failing the signal requirements.

Preselected electrons are required to have $p_{\mathrm{T}} > 4.5$ GeV and $|\eta| < 2.47$ and satisfy the LooseAndBLayerLLH criteria [76]. Preselected muons fulfill $p_{\mathrm{T}} > 3$ GeV and $|\eta < 2.7|$ and pass the Medium identification criteria [77]. Both, preselected electrons and muons pass a cut on the longitudinal impact parameter $|z_0 \sin(\theta) < 0.5|$ mm in order to reduce the number of leptons from secondary vertices.

The anti-k_t algorithm with a radius parameter of 0.4 is used to reconstruct jets [78]. Preselected Jets are required to have $p_{\mathrm{T}} > 20$ GeV and are within $|\eta| < 2.8$.

Preselected hadronic τ leptons are required to have $p_{\mathrm{T}} > 20$ GeV and are within $|\eta| < 2.47$, excluding the region $1.37 < |\eta| < 1.52$ [84]. The τ has to be associated with 1 or 3 ID tracks, which charges sum up to ± 1. A loose cut on the RNN score of the τ identification classifier is applied, in order to reject fake jets [85].

The overlap removal procedure consists of the following steps:

1. τ leptons with $\Delta R < 0.2$ to an electron or muon are removed.
2. Electrons sharing an ID track with a muon are removed.
3. Jets with $\Delta R < 0.2$ to an electron are removed.
4. Electrons with $\Delta R < 0.4$ to a jet are removed to reject electrons from semileptonic decays of c- and b-hadrons.
5. Jets with less than 3 associated tracks are removed if there is a muon with $\Delta R < 0.2$ or if a muon can be matched to a track associated with the jet.
6. Muons with $\Delta R < 0.4$ to a jet are removed.
7. Jets overlaping with a τ lepton within $\Delta R < 0.4$ are removed, if the τ passes the Medium identification requirements. In case of the control regions with loose τ leptons, used to estimate the reducible background (section 6.6.2), it is sufficient that the τ passes the preselection.

After the overlap removal, opposite-sign (OS) light lepton pairs with $m_{\mathrm{OS}} < 4$ GeV are removed. Furthermore, same-flavor, opposite-sign (SFOS) light lepton pairs with $8.4 < m_{\mathrm{SFOS}} < 10.4$ GeV are discarded, to suppress leptons from Υ-decays.

Signal electrons (muons) must have $p_{\mathrm{T}} > 7$ (5) GeV. Additionally electrons have to pass the MediumLLH identification criteria [76]. In order to suppress electrons and muons from secondary vertices, the transvers impact parameter normalised to its uncertainty $|d_0|/\sigma_{d_0}$ must be < 5 (3) for electrons (muons). Both signal electrons and muons are required to pass the FCLoose isolation criteria, to reduce the amount of leptons from semileptonic decays of hadrons and jets misidentified as leptons [76, 77]. Contributions from nearby leptons, are removed for the isolation variables, which increases the sensitivity to RPV signals with low LSP mass. Signal τ leptons are required to pass the Medium identification criteria. Signal jets with $p_{\mathrm{T}} < 120$ GeV are required to pass the medium working point of the jet-vertex-tagging algorithm, in order to reduce the amount of pile-up jets.

Events considered for this analysis are required to have a primary vertex with at least two tracks with $p_{\mathrm{T}} > 500$ MeV. The primary vertex of an event is the vertex with the highest $\sum p_{\mathrm{T}}^2$ of associated tracks. Events are selected using single-lepton, dilepton and trilepton triggers [60, 61]. Dilepton

(trilepton) triggers are only used if the leptons fail the p_{T}-threshold requirements for the single-lepton (single-lepton and dilepton) triggers.

6.5 Signal Regions

In the GGM scenario each of the two higgsinos decays into a gravitino and either a higgs or a Z boson. This analysis focus on those events where both higgsinos decay into a Z boson, with both Z bosons decaying into a pair of charged light leptons. Decays of the Z boson into hadronically decaying τ are not considered, since the background for hadronically decaying τ is typically larger due to a larger amount of particles misidentified as τ and the Z boson decays into each lepton flavor with similar rate. The signal regions targeting the GGM scenario requires at least four light leptons with two pairs of same flavor opposite sign (SFOS) leptons that are consistent with a leptonic Z boson decay. The pair with the invariant mass closer to the Z boson mass is required to have an invariant mass of 81.2 GeV $< m_{\ell\ell} <$ 101.2 GeV. The requirement on the invariant mass of the second pair is looser with 61.2 GeV $< m_{\ell\ell} <$ 101.2 GeV. Since there are no b-tagged jets expected in this process, events containing b-jets are vetoed. A requirement on $E_{\mathrm{T}}^{\mathrm{miss}}$ is used to further discriminate signal from background. A loose signal region (SR0-ZZ$^{\mathrm{loose}}_{\mathrm{bveto}}$) with $E_{\mathrm{T}}^{\mathrm{miss}} > 100$ GeV and a tight signal region SR0-ZZ$^{\mathrm{tight}}_{\mathrm{bveto}}$ with $E_{\mathrm{T}}^{\mathrm{miss}} > 200$ GeV are defined targeting low- and high-mass GGM scenarios, respectively. There two additional regions (SR0-ZZ$^{\mathrm{loose}}$ and SR0-ZZ$^{\mathrm{tight}}$) without the veto on b-jets and with $E_{\mathrm{T}}^{\mathrm{miss}} > 50$ GeV and $E_{\mathrm{T}}^{\mathrm{miss}} > 100$ GeV, respectively. These two regions showed an excess of up to 2.3σ in the previous analysis using the dataset of 2015 and 2016. Therefore, these regions are included in this analysis, in order to check if this excess persists also in the full Run 2 dataset. It is important to note, although the event selection is the same, the reconstruction algorithm as well as the lepton identification was updated between the previous analysis and this analysis. Therefore, it is not expected to select the exact same events in the 2015 and 2016 dataset. However, it was tested and confirmed, that the results in the 2015 and 2016 were very similar and an excess can be observed in this partial dataset also with the updated algorithms.

For the RPV scenarios, the signal regions are categorized with respect to the number of hadronically decaying τ leptons. For the regions targeting scenarios with a non-zero λ_{12k} RPV coupling (the LSP decays into light leptons only), the events are required to have at least four light leptons. There is no requirement on the number of hadronically decaying τ leptons. The regions targeting scenarios with non-zero λ_{i33} RPV coupling (LSP decays dominantly into τ leptons), are required to have either exactly three light leptons and at least one hadronic τ or exactly two light leptons and at least two hadronic τ. The strict requirement on the number of light leptons ensures that the regions are orthogonal to those without τ leptons. Since the RPV models have no Z bosons in the decay, all regions targeting RPV scenarios have a veto on Z bosons by rejecting events with SFOS lepton pairs with an invariant mass

of 81.2 GeV $< m_{\ell\ell} <$ 101.2 GeV. The Z veto rejects also events with a $\ell^+\ell^-\ell'^{\pm}$ or $\ell^+\ell^-\ell'^+\ell'^-$ system with an invariant mass within 81.2-101.2 GeV, in order to supress events where a photon is radiated from the $Z \to \ell\ell$ decay. In order to separate the signal from the SM background, the effective mass m_{eff} is used

$$m_{\text{eff}} = \sum_{\ell=e,\mu,\tau} p_{\text{T}}(\ell) + \sum_{p_{\text{T}}(j)>40\,\text{GeV}} p_{\text{T}}(j) + E_{\text{T}}^{\text{miss}} \tag{6.1}$$

which is the scalar sum of $E_{\text{T}}^{\text{miss}}$ and the transverse momenta of the leptons and all jets with $p_{\text{T}} > 40$ GeV. There are three general signal regions ($\text{SR0}^{\text{loose}}_{\text{bveto}}$, $\text{SR1}^{\text{loose}}_{\text{bveto}}$, $\text{SR2}^{\text{loose}}_{\text{bveto}}$) with no b-jet, $m_{\text{eff}} > 600$ GeV and 0, 1 and 2 hadronic τ, respectively. These are not optimized for the SUSY scenarios but are sensitive to events from beyond SM processes decaying into four leptons in a model-independent way. There are two additional signal regions with no hadronic τ, one ($\text{SR0}^{\text{tight}}_{\text{bveto}}$) with no b-jet and $m_{\text{eff}} > 1250$ GeV requirement and one (SR0_{breq}) with at least one b-jet and $m_{\text{eff}} > 1300$ GeV. While the region without b-jet provides good sensitivity to the models with wino and slepton production, the region with at least one b-jet improves the sensitivity to the model with gluino production, since the gluino can decay to the LSP together with b quarks.

There are two signal regions with 1 hadronic τ, one ($\text{SR1}^{\text{tight}}_{\text{bveto}}$) without b-jet and $m_{\text{eff}} > 1000$ GeV and another region (SR1_{breq}) with at least one b-jet and $m_{\text{eff}} > 1300$ GeV. Finally two signal regions with at least 2 hadronic τ are defined, a region ($\text{SR2}^{\text{tight}}_{\text{bveto}}$) with no b-jet and $m_{\text{eff}} > 1000$ GeV and one (SR2_{breq}) with at least one b-jet and $m_{\text{eff}} > 1100$ GeV. The cut on m_{eff} are optimized in such a way that the region provides good sensitivity to all the RPV models.

Additionally SR5L is a region with at least five light leptons. No additional requirements are used on this region, since only a small number events is expected in this phase space. This region does not target any SUSY model specifically, but is used for a general search for new physics in five-lepton final states. For the considered SUSY models that can produce more than four leptons, the signal regions with four leptons are more sensitive than SR5L. A summary of the signal regions is shown in Table 6.3.

6.6 Background Estimation

The Standard Model background with four or more reconstructed leptons in the final state are classified into two categories. The irreducible background are processes that produces at least four prompt leptons that originate from the decay of the primary produced particles in the collision. The most dominant irreducible processes for this search are ZZ and $t\bar{t}Z$. Other processes with smaller contributions are $t\bar{t}WW$, $t\bar{t}ZZ$, $t\bar{t}WZ$, $t\bar{t}WH$, $t\bar{t}HH$, tWZ, VVZ (ZZZ, WZZ, WWZ), H via ggF, H via VBF, WH, ZH, $t\bar{t}H$, $t\bar{t}t\bar{t}$ and $t\bar{t}tW$. The reducible background are processes, where at least one

Table 6.3: Definition of the signal regions for the search for SUSY in final states with at least four charged leptons. Table adapted from Ref. [123].

Signature	Signal Region	$N(e,\mu)$	$N(\tau_{had})$	$N(b$-jets$)$	Z boson	Selection
$4L0T$	SR0-ZZ$^{\text{loose}}_{\text{bveto}}$	≥ 4	≥ 0	$= 0$	require 1st & 2nd	$E_{\text{T}}^{\text{miss}} > 100$ GeV
	SR0-ZZ$^{\text{tight}}_{\text{bveto}}$	≥ 4	≥ 0	$= 0$	require 1st & 2nd	$E_{\text{T}}^{\text{miss}} > 200$ GeV
	SR0-ZZ$^{\text{loose}}$	≥ 4	≥ 0	≥ 0	require 1st & 2nd	$E_{\text{T}}^{\text{miss}} > 50$ GeV
	SR0-ZZ$^{\text{tight}}$	≥ 4	≥ 0	≥ 0	require 1st & 2nd	$E_{\text{T}}^{\text{miss}} > 100$ GeV
	SR0$^{\text{loose}}_{\text{bveto}}$	≥ 4	≥ 0	$= 0$	veto	$m_{\text{eff}} > 600$ GeV
	SR0$^{\text{tight}}_{\text{bveto}}$	≥ 4	≥ 0	$= 0$	veto	$m_{\text{eff}} > 1250$ GeV
	SR0$_{\text{breq}}$	≥ 4	≥ 0	≥ 1	veto	$m_{\text{eff}} > 1300$ GeV
$3L1T$	SR1$^{\text{loose}}_{\text{bveto}}$	$= 3$	≥ 1	$= 0$	veto	$m_{\text{eff}} > 600$ GeV
	SR1$^{\text{tight}}_{\text{bveto}}$	$= 3$	≥ 1	$= 0$	veto	$m_{\text{eff}} > 1000$ GeV
	SR1$_{\text{breq}}$	$= 3$	≥ 1	≥ 1	veto	$m_{\text{eff}} > 1300$ GeV
$2L2T$	SR2$^{\text{loose}}_{\text{bveto}}$	$= 2$	≥ 2	$= 0$	veto	$m_{\text{eff}} > 600$ GeV
	SR2$^{\text{tight}}_{\text{bveto}}$	$= 2$	≥ 2	$= 0$	veto	$m_{\text{eff}} > 1000$ GeV
	SR2$_{\text{breq}}$	$= 2$	≥ 2	≥ 1	veto	$m_{\text{eff}} > 1100$ GeV
$5L0T$	SR5L	≥ 5	≥ 0	≥ 0	–	–

of the four leptons is a fake or non-prompt lepton. Non-prompt leptons are leptons that originate in secondary vertices from e.g. hadron decays while fake leptons are other signatures such as jets which have been misidentified. In the following these contributions are just referred to as fake leptons. The main contributions to the reducible background originate from $t\bar{t}$ and Z+jets events with two fake leptons. Smaller contributions originate from WZ, WW, WWW, $t\bar{t}W$, $t\bar{t}t$. This includes also processes listed as irreducible background that do not undergo a decay to four real leptons (e.g. $ZZ \rightarrow q\bar{q}\ell\ell$). Events with three or four fake leptons are very rare and are therefore neglected. However a systematic uncertainty is considered, estimating an upper limit on these contributions. The reducible background are especially dominant in the regions containing hadronically decaying τ leptons due to the lower fake lepton rejection of the τ identification algorithms with repect to their electron and muon counterparts.

6.6.1 Irreducible Background

The irreducible background is estimated using Monte Carlo simulations. The Monte Carlo predictions of the dominant contributions to the irreducible background, ZZ and $t\bar{t}Z$, are normalized to data in dedicated control regions (CRs). These CRs are required to be close but orthogonal to the SRs. Furthermore, the CRs are constructed to be enriched in the considered background and depleted in signal. The normalization factor is approximately given by

$$\mu_{\text{bkg}}^{\text{CR}} = \frac{N_{\text{data}}^{\text{CR}} - N_{\text{MC, other bkg}}^{\text{CR}}}{N_{\text{MC, bkg}}^{\text{CR}}}, \tag{6.2}$$

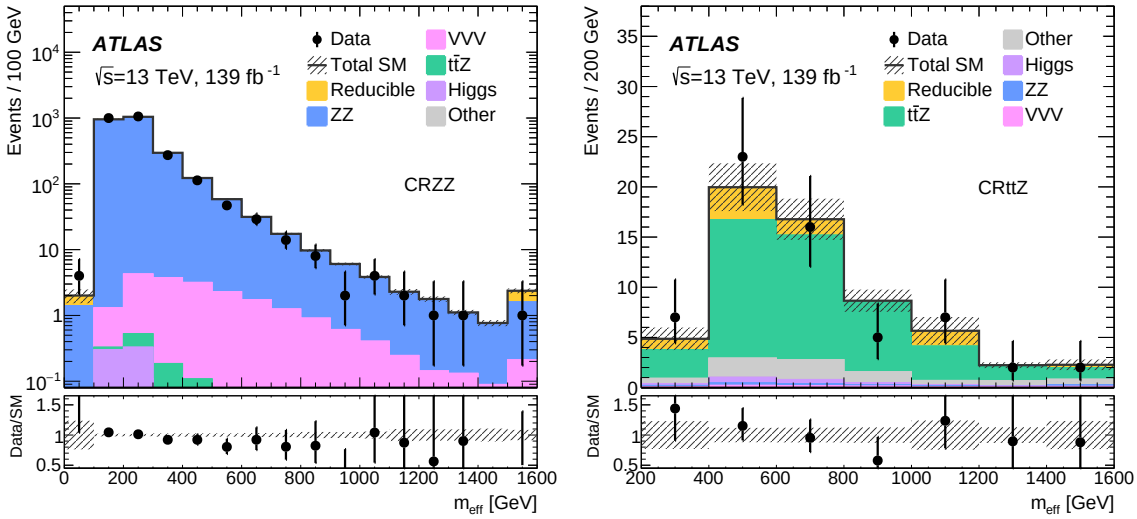

(a) CRZZ (b) CRttZ

Figure 6.3: m_{eff} distributions for data and SM backgrounds in CRZZ and CRttZ after the background-only fit. The last bin includes the overflow. The lower panel shows the ratio between observed data and expected SM background yields. Both statistical and systematic uncertainties in the SM background are included in the shaded band [123].

where $N^{\text{CR}}_{\text{data}}$ is the number of data events in the CR, $N^{\text{CR}}_{\text{MC, bkg}}$ the expected number of events of the the considered background and $N^{\text{CR}}_{\text{MC, other bkg}}$ the expected number of other background events. For the final results the normalization factors are derived by a likelihood fit to data (Section 6.9.1) which takes systematic uncertainties (Section 6.8) into account. The normalization factor measured in the CRs are then used to scale the background predictions in the signal regions. The definition of the control regions are summarized in Table 6.4. Both control regions require at least four light leptons. The region CRZZ requires two Z boson candidates and vetoes events with b-jets. Events with $E_{\text{T}}^{\text{miss}} < 50$ GeV are selected, which ensures that the region is orthogonal to the signal regions. CRttZ requires at least one b-jet, exactly one Z boson candidate and $E_{\text{T}}^{\text{miss}} > 100$ GeV.

Table 6.4: Definition of the control regions for the estimation of the irreducible background. Table adapted from Ref. [123].

Region	$N(e,\mu)$	$N(\tau_{had})$	$N(b\text{-jets})$	Z boson	Selection
CRZZ	≥ 4	≥ 0	$= 0$	require 1st & 2nd	$E_{\text{T}}^{\text{miss}} < 50$ GeV
CRttZ	≥ 4	≥ 0	≥ 1	require 1st & veto 2nd	$E_{\text{T}}^{\text{miss}} > 100$ GeV

Figure 6.3 shows the m_{eff} distributions in the CRs after the background-only fit. The obtained scale factors are 1.15 ± 0.09 and 1.06 ± 0.24 for ZZ and $t\bar{t}Z$, respectively.

To verify that the normalization factors derived in the CR are also applicable in the phase space of the

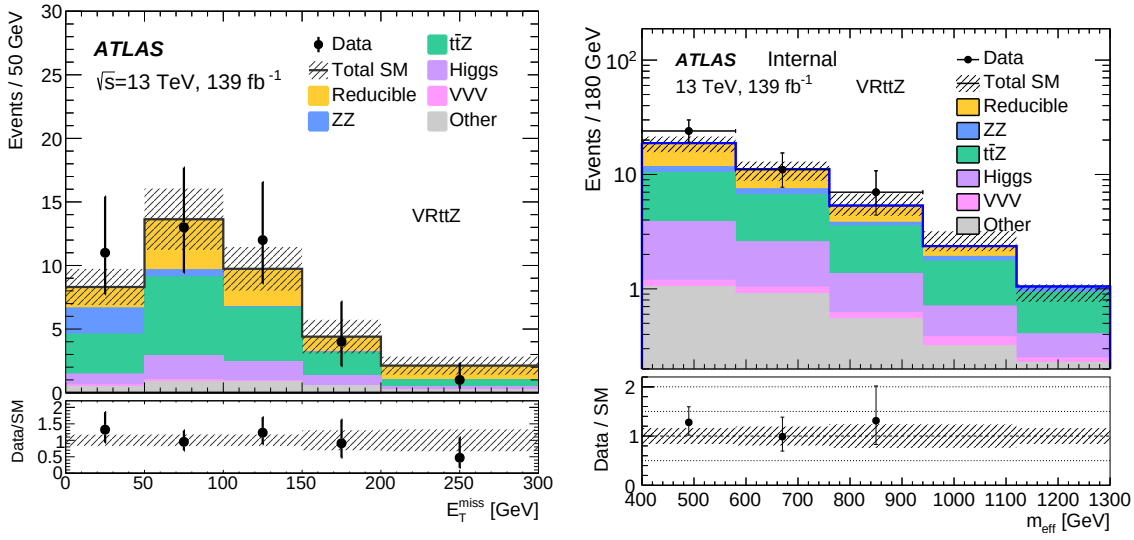

(a) VRZZ (b) VRttZ

Figure 6.4: m_{eff} distributions for data and SM backgrounds in VRZZ and VRttZ after the background-only fit. The last bin includes the overflow. The lower panel shows the ratio between observed data and expected SM background yields. Both statistical and systematic uncertainties in the SM background are included in the shaded band [123]. [123].

SR, validation regions (VRs) for each background are used. The definition of the validation regions are given in Table 6.5. VRZZ requires exactly one Z boson candidate and no b-jets. VRttZ vetoes events with a Z boson and requires at least one b-jet. Furthermore, m_{eff} is required to be between 400 and 1300 GeV in order to keep the region orthogonal to the signal regions with b-jets.

The m_{eff} distributions in the VRs after the normalization of the ZZ and $t\bar{t}Z$ is applied are shown in Figure 6.4. A good agreement between data and MC is observed which verifies that the extrapolation to the SRs is valid.

Table 6.5: Definition of the VRs for the estimation of the irreducible background. Table adapted from Ref. [123].

Region	$N(e,\mu)$	$N(\tau_{had})$	$N(b\text{-jets})$	Z boson	Selection
VRZZ	≥ 4	≥ 0	$= 0$	require 1st & veto 2nd	–
VRttZ	≥ 4	≥ 0	≥ 1	veto	$400 < m_{\text{eff}} < 1300$ GeV

6.6.2 Reducible Background

The reducible background is estimated using the so-called fake-factor method. For this method CRs with identical kinematic selection criteria as the SRs, but with one or two of the leptons to be of only

loose identification quality. The CRs have the following naming scheme: CR1 (CR2) requires exactly three (two) signal leptons and at least one (two) loose leptons. A sequence of capital (small) L or T letters indicates the number of signal (loose) light leptons or τ leptons. e.g. `CR2_LLll` is a region with four light leptons, two signal and two loose leptons. An overview of the used control regions is shown in Table 6.6.

Table 6.6: Definition of the CRs for the estimation of the reducible background. Table adapted from Ref. [123].

Reducible bkg. estimation for	Control Region	$N(e,\mu)$ signal	$N(e,\mu)$ loose	$N(\tau_{had})$ signal	$N(\tau_{had})$ loose
$4L0T$	`CR1_LLLl`	$= 3$	≥ 1	≥ 0	≥ 0
	`CR2_LLll`	$= 2$	≥ 2	≥ 0	≥ 0
$3L1T$	`CR1_LLLt`	$= 3$	$= 0$	$= 0$	≥ 1
	`CR1_LLTl`	$= 2$	$= 1$	≥ 1	≥ 0
	`CR2_LLlt`	$= 2$	$= 1$	$= 0$	≥ 1
$2L2T$	`CR1_LLTt`	$= 2$	$= 0$	$= 1$	≥ 1
	`CR2_LLtt`	$= 2$	$= 0$	$= 0$	≥ 2
$5L0T$	`CR1_LLLLl`	$= 4$	≥ 1	≥ 0	≥ 0

The loose leptons are expected to be fake leptons. The number of data events in these control regions after subtracting the irreducible background estimated from MC simulation, is extrapolated to the signal region using a fake factor as weight. The fake factor is defined as the ratio of signal to loose leptons: $F = \frac{N_{\text{signal}}}{N_{\text{loose}}}$. The fake factor is dependent on the lepton flavor, p_{T}, η, its proximity to other leptons (ΔR) and in case of τ leptons on its prong number. Additionally, the fake factor varies on the process in which the fake lepton is produced. In four-lepton events the two most important processes are $t\bar{t}$ and Z+jets, while for events with five leptons the dominant process is ZZ. Furthermore the fake factor depends on the source of the fake lepton. For fake light leptons, light-flavor quark (LF) jets, jets with bottom or charm quarks, so called heavy flavor jets (HF) and in case of electrons in addition photon conversions (CONV) are considered as potential sources. For fake τ leptons, HF jets, LF jets, gluon jets (GJ) and electrons misidentified as τ leptons (ELEC) are considered. In order to take the different fake lepton types and production processes into account, a weighted average F_w of fake factors is estimated for each CR defined as

$$F_w = \sum_{i,j} \left(F^{ij} \times R^{ij} \times s^i \right) \tag{6.3}$$

F^{ij} is the fake factor for fake leptons of type i (e.g. LF, HF) from process j ($t\bar{t}$, Z+jets), estimated from MC simulations. The weighted fake factor is evaluated separately for the different lepton flavors. The fake factor is weighted by the process fractions R^{ij}, which is the fraction of fake leptons of type i

from process j, estimated from MC, in CR2. CR2 instead of the signal region is used for the process fraction, since CR2 has lower statistical uncertainties, while having similar fake contributions. The scale factor s^i is used to correct the fake factor for fake leptons of type i in MC to data. The scale factors are estimated from CRs that are enriched in fake leptons of a certain type.

The final estimate for the number of reducible background events $N_{\text{red}}^{\text{SR}}$, using the fake factor method, is given by

$$N_{\text{red}}^{\text{SR}} = [N_{\text{data}}^{\text{CR1}} - N_{\text{irr}}^{\text{CR1}}] \times F_w - [N_{\text{data}}^{\text{CR2}} - N_{\text{irr}}^{\text{CR2}}] \times F_w \times F_w^{'} \tag{6.4}$$

using the number of events in data in the CRs $N_{\text{data}}^{\text{CR1}}$ and $N_{\text{data}}^{\text{CR2}}$. Contributions from irreducible backgrounds in the CRs, $N_{\text{irr}}^{\text{CR1}}$ and $N_{\text{irr}}^{\text{CR2}}$ are subtracted from the number of data events. These contributions are estimated from MC simulation and utilizing its truth information. To each CR event a weighted fake factor F_w for each of the loose leptons is applied. In CR2, two weighted fake factors are applied, one for each loose lepton. The negative sign of the second term, removes double-counted events with two fake leptons from the first term. Equation 6.4 is a schematic outline, since the fake factors are applied on an event-by-event basis rather than as an average. In the rare case of an additional loose lepton in the CR, all possible combination of applying the fake factor to the event are considered and the average is taken, e.g. in `CR2_LLll` with an additional third loose lepton, the combinations $F_1 \times F_2$, $F_1 \times F_3$ and $F_2 \times F_3$ are considered.

In the following, the estimation of the components of the weighted fake factor is described in detail.

The fake factor determination: The fake factors for the dominating $t\bar{t}$ and Z+jets processes and for each fake lepton source are calculated from MC events with at least one baseline lepton. The fake factor for electrons and muons for $t\bar{t}$ and Z+jets is shown in Figures 6.5 and 6.6. The fake factor for electrons increases with p_{T} in $t\bar{t}$, while the fake factor in Z+jets increases p_{T} for HF electrons while the fake factor for LF electrons has its maximum for p_{T} between 30 and 50 GeV. A moderate η dependence is observed with a slightly high fake factor in the transition region between barrel and forward region. The fake factor for conversion electrons is much higher. However, conversion electrons add only a small contribution to the fake leptons, as shown later. For electrons and muons a dependence on ΔR to the closest lepton can be observed as shown in Figures 6.7 and 6.8 for HF electrons and muons in $t\bar{t}$ events. The fake factor increases at low ΔR in case the closest lepton fulfills signal requirements. The fake factor decreases if the closest lepton is of loose quality. Similar behaviour is shown for the other fake types and in Z+jets events. Signal leptons are isolated from hadronic activity, therefore it is likely that a close lepton passes the isolation criteria as well and fulfills signal criteria. Correspondingly, lepton close to a non-isolated lepton are itself non-isolated. Figures 6.9 and 6.10 show the fake factor for 1-prong and 3-prong τ in $t\bar{t}$ and Z+jets. The fake factor

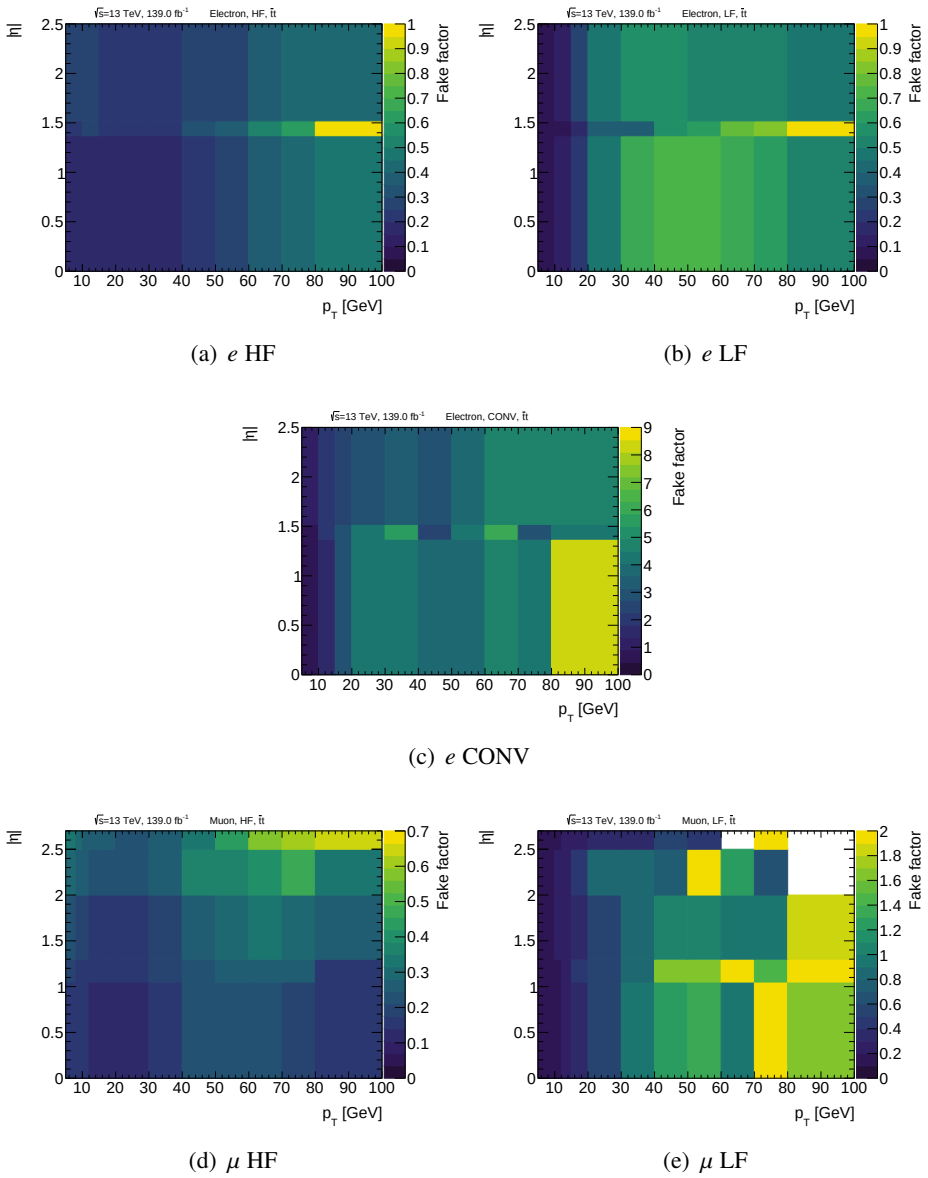

(a) e HF (b) e LF

(c) e CONV

(d) μ HF (e) μ LF

Figure 6.5: p_{T}-$|\eta|$ dependence of the Fake factors for electrons and muons in simulated $t\bar{t}$ events.

decreases with p_{T} with the exception of 3-prong GJ and ELEC τ. The fake factors are rather stable in η. Typically the fake factors for 3-prong τ leptons are smaller than for 1-prong τ leptons.

Figure 6.11 shows the fake factor for electrons and muons in ZZ events. These are only used for the fake estimate in the 5L region. The fake factor depends on p_{T} and η. In contrast to the fake factor in $t\bar{t}$ and Z+jets, no dependence on ΔR to the closest lepton is considered, since in the 5L region, events with only one fake lepton are expected to be dominant.

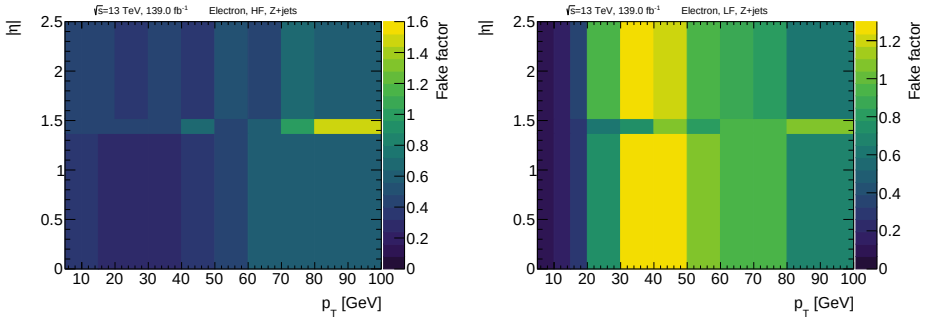

(a) e HF

(b) e LF

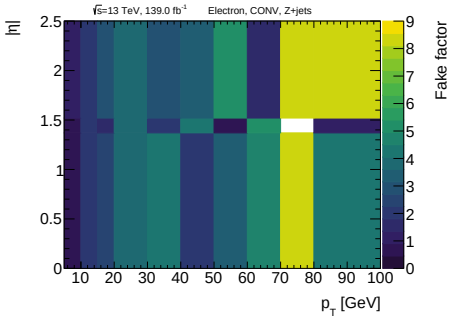

(c) e CONV

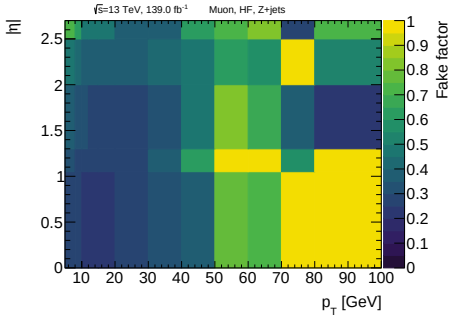

(d) μ HF

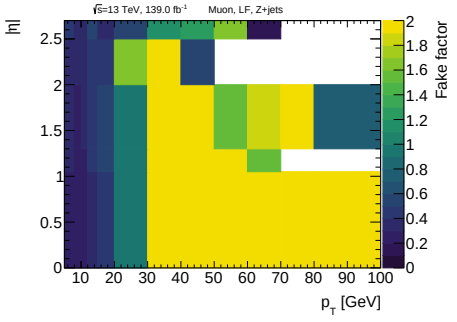

(e) μ LF

Figure 6.6: p_{T}-$|\eta|$ dependence of the Fake factors for electrons and muons in simulated Z+jets events.

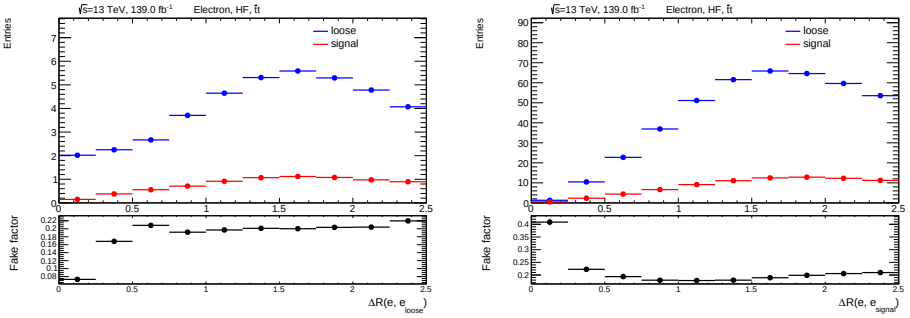

(a) closest lepton: e_{loose}

(b) closest lepton: e_{signal}

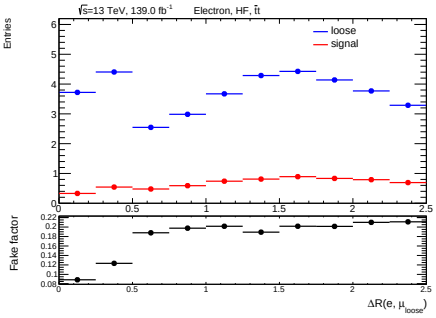

(c) closest lepton: μ_{loose}

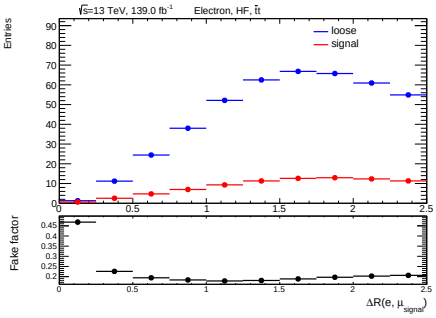

(d) closest lepton: μ_{signal}

Figure 6.7: ΔR dependence of the Fake factors for HF electrons in simulated $t\bar{t}$ events. (a),(b) Closest lepton is an electron of loose (a) or signal (b) quality. (c),(d) Closest lepton is a muon of loose (c) or signal (d) quality. The upper panel shows the distributions of loose and signal leptons, while the lower panel shows the fake factor.

Process fraction: The fraction of each fake type contributing to the reducible background is estimated for $t\bar{t}$ and Z+jets in the CRs. Figure 6.12 shows the fractions for electrons and muons in $t\bar{t}$ as a function of p_{T} and η. In $t\bar{t}$ fake electrons are dominantly originating from heavy-flavor decays with approximately 80%. Light-flavor fakes become more important at higher p_{T}, in the forward region and the transition region between barrel and endcap. Electrons from photon conversions have only a tiny contribution. Fake muons are dominantly originating from heavy-flavor decays with the light-flavor fake muons contributing with up to 20% only at very low p_{T}.

In Z+jets events, shown in Figure 6.13, light flavor electrons are more dominant, especially at high p_{T} and high η. Similar to $t\bar{t}$, fake muons dominantly originate from heavy-flavor decays. Only at very low p_{T} the light-flavor fake muons contribute with up to 20%. There is no large difference between the SR and CR distributions, therefore fractions from CR2 are used for the fake estimate, in order to maximize the available statistic.

For τ leptons in $t\bar{t}$ events, shown in Figures 6.14 and 6.15, fake τ from heavy-flavor jets are the

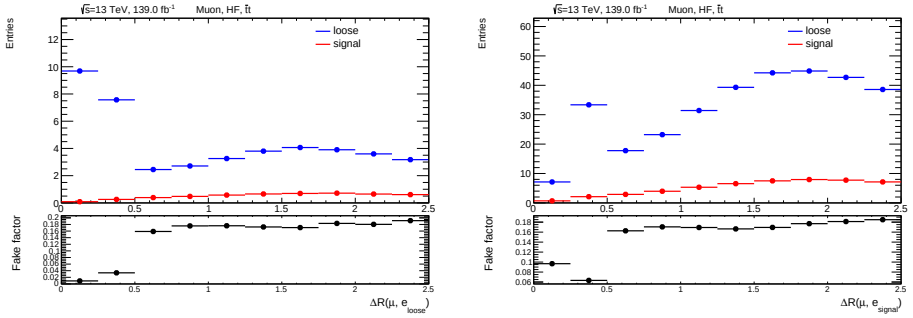

(a) closest lepton: e_{loose}

(b) closest lepton: e_{signal}

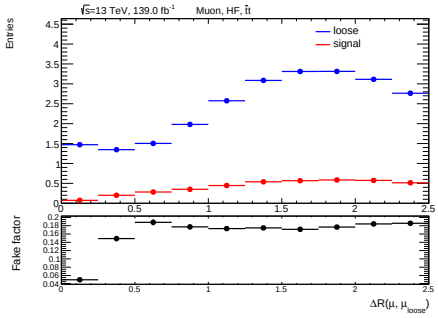

(c) closest lepton: μ_{loose}

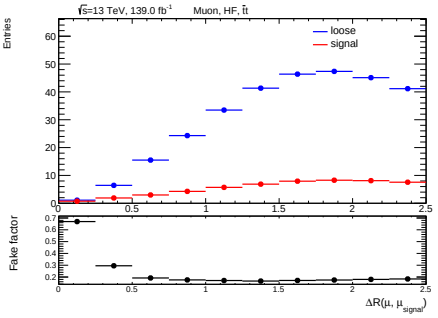

(d) closest lepton: μ_{signal}

Figure 6.8: ΔR dependence of the Fake factors for HF muons in simulated $t\bar{t}$ events. (a),(b) Closest lepton is an electron of loose (a) or signal (b) quality. (c),(d) Closest lepton is a muon of loose (c) or signal (d) quality. The upper panel shows the distributions of loose and signal leptons, while the lower panel shows the fake factor.

dominant type. For 1-prong τ also light-flavor fakes are an important contribution. At low p_{T} the fraction of fake τ from gluon jets increases. τ faked by electrons are only a small contribution. No large dependency on η is observed. Fake τ in Z+jets are dominated by light flavor fakes as shown in Figures 6.16 and 6.17.

For the final results, the process fractions used for the estimation of the reducible background in the CRs, VRs and SRs are splitted based on the selection of Z bosons and b-jets in the region. No large dependence on m_{eff} and $E_{\text{T}}^{\text{miss}}$ have been observed. Therefore, a selection based on these variables is not applied.

Closure test: Closure tests are performed in order to check the parametrizations for the fake factors and process fractions. For the closure test the weighted fake factors are applied to MC events from CR1 and CR2 in $t\bar{t}$ and Z+jets. The obtained distributions of the variables m_{eff} and $E_{\text{T}}^{\text{miss}}$ used in the SR definitions are then compared to the distributions of the MC events with four signal leptons

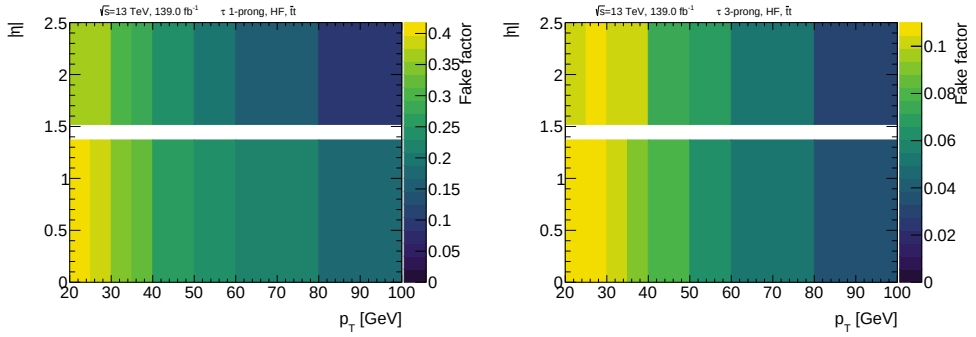

(a) 1-prong τ HF

(b) 3-prong τ HF

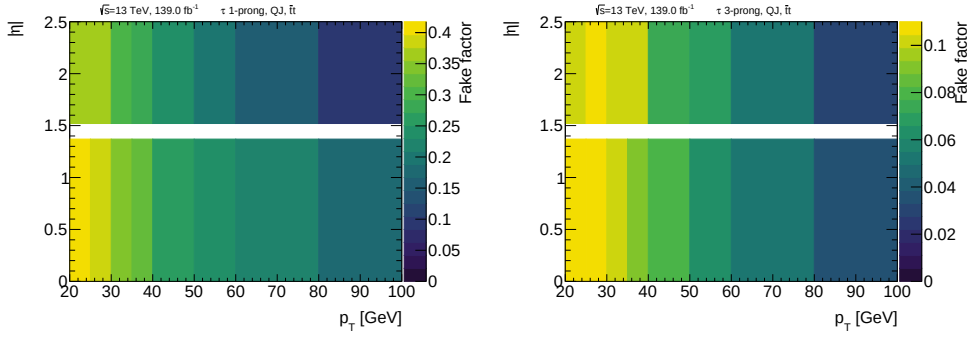

(c) 1-prong τ QJ

(d) 3-prong τ QJ

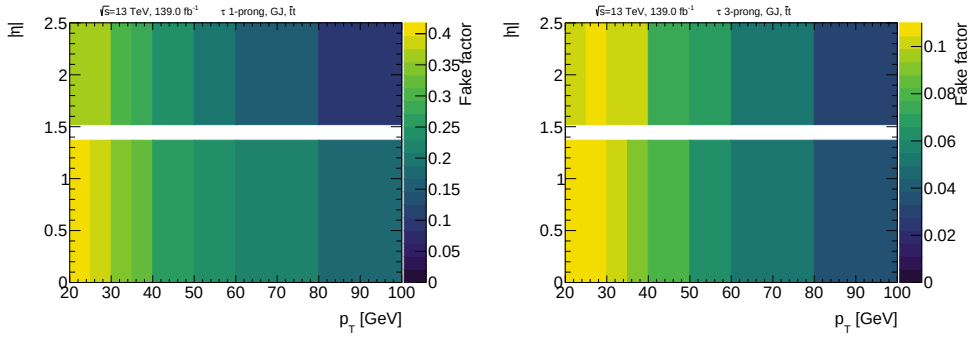

(e) 1-prong τ GJ

(f) 3-prong τ GJ

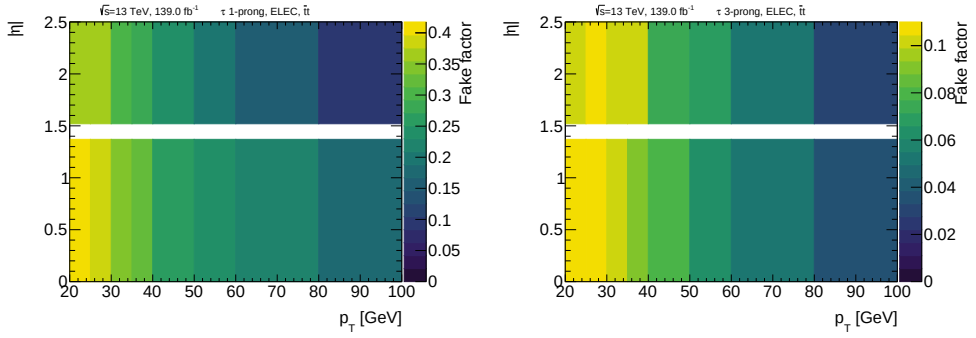

(g) 1-prong τ EL

(h) 3-prong τ EL

Figure 6.9: p_{T}-$|\eta|$ dependence of the Fake factors for τ leptons in simulated $t\bar{t}$ events.

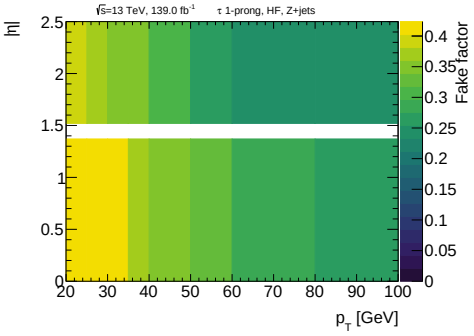

(a) 1-prong τ HF

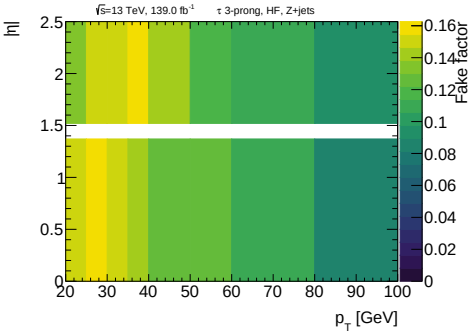

(b) 3-prong τ HF

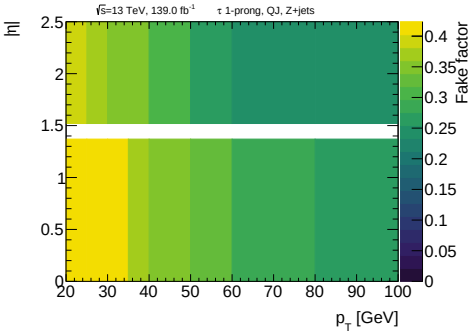

(c) 1-prong τ QJ

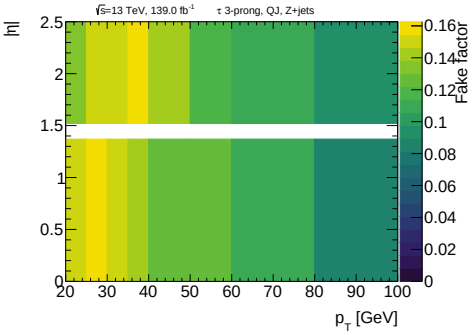

(d) 3-prong τ QJ

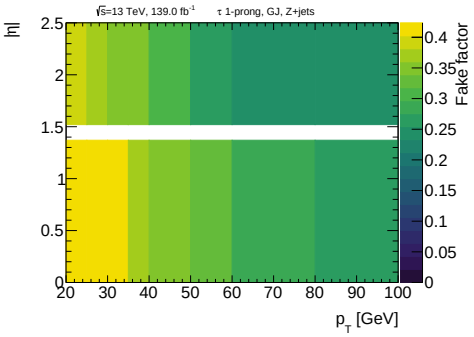

(e) 1-prong τ GJ

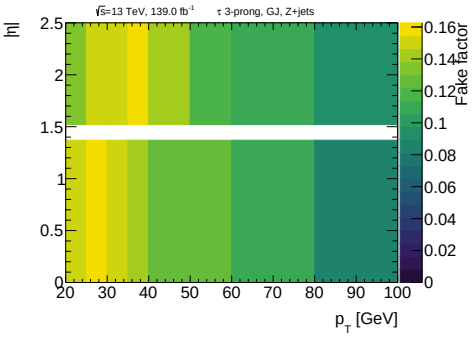

(f) 3-prong τ GJ

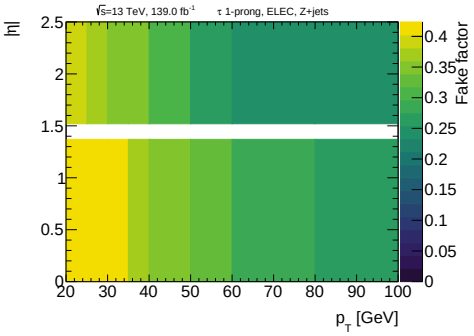

(g) 1-prong τ EL

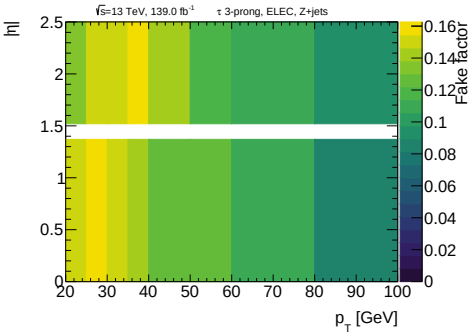

(h) 3-prong τ EL

Figure 6.10: p_{T}-$|\eta|$ dependence of the Fake factors for τ leptons in simulated Z+jets events.

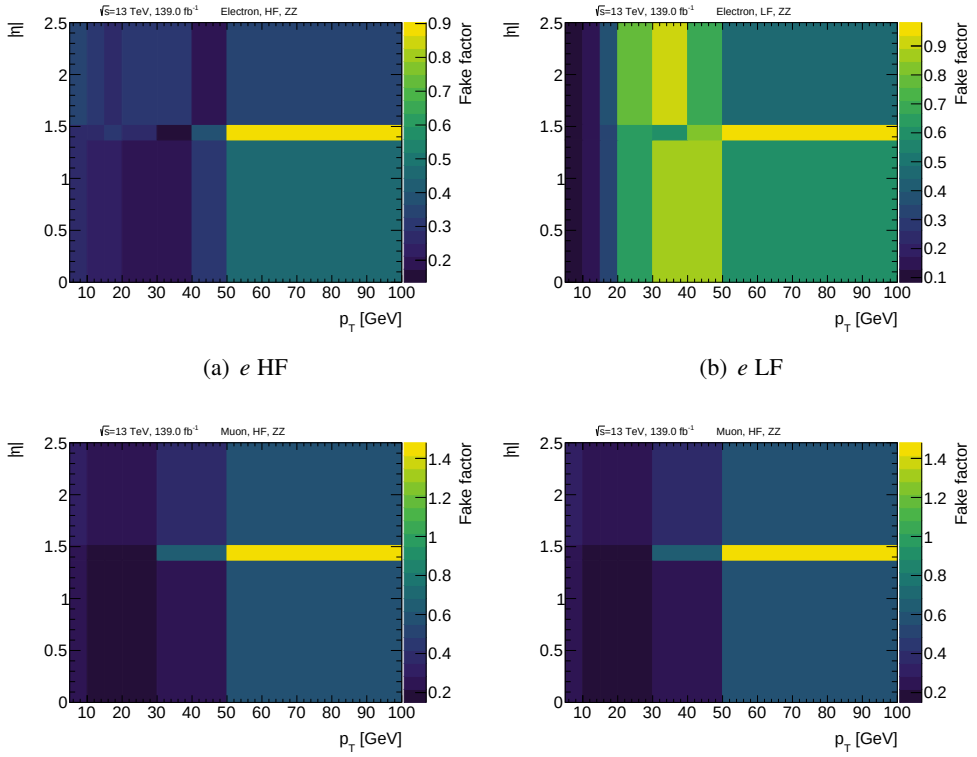

(a) e HF (b) e LF

(c) μ HF (d) μ LF

Figure 6.11: p_{T}-$|\eta|$ dependence of the Fake factors for electrons and muons in simulated ZZ events.

in the same MC sample. For the closure test only the fake factors and process fractions but not the scale factors are used, since a correction of the fake factors to data is not needed for this pure MC comparison The process fractions are restricted to the tested sample. The closure test distributions are in LLLL, LLLT and LLTT events are shown in Figures 6.18, 6.19 and 6.20, respectively. Overall there is a good agreement between the ”intrinsic” fake predictions of the MC and the predictions of the fake factor method. This is expected, since the fake factors and process fractions are obtained from the same sample. However, larger deviations between the distributions can indicate that an important dependency of a variable was not considered. The weighted distributions in CR2 is approximately half the events of CR1, which is expected from processes that are contributing to the SR with two fake leptons.

The fake factor scale factor estimation: The derived fake factors are based on MC simulations. Since fake leptons tend to be badly modelled in MC, fake factors in data might differ from the ones in simulation. In order to account for this, the fake factors are corrected with a scale factor for the dominant fake types. The scale factor is the ratio of the fake factors measured in data and MC.

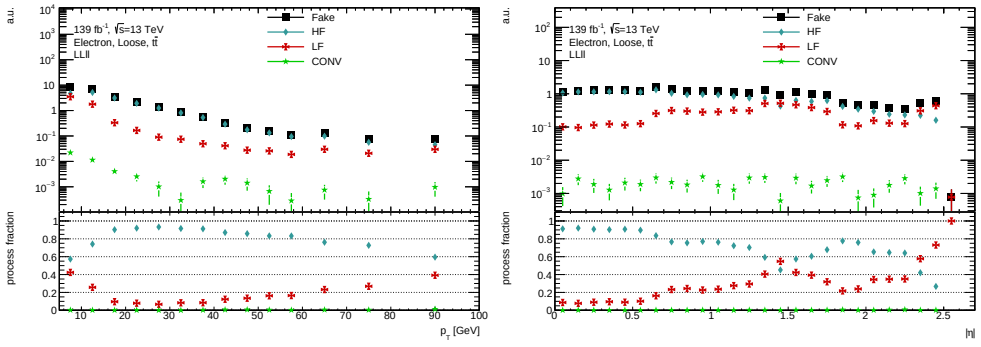

(a) CR2_LLll e p_{T} (b) CR2_LLll e $|\eta|$

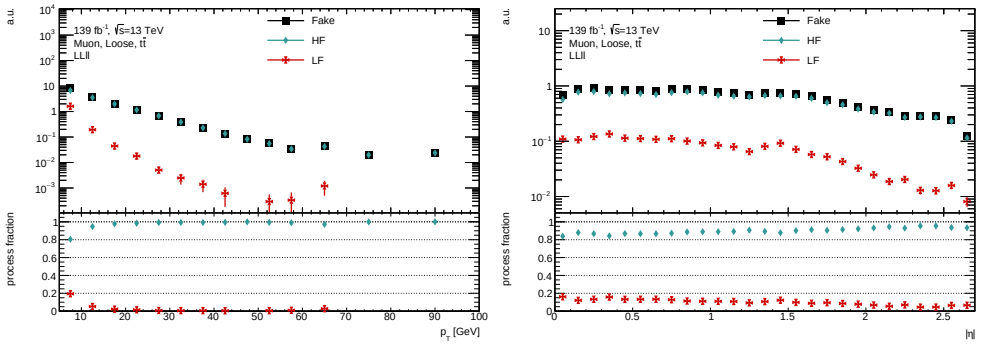

(c) CR2_LLll μ p_{T} (d) CR2_LLll μ $|\eta|$

Figure 6.12: Fake process fractions as a function of p_{T} and $|\eta|$ for electrons and muons in simulated $t\bar{t}$ events. The upper panel shows the p_{T} and $|\eta|$ distributions for fake electrons and muons for the different fake types. The process fraction shown in the lower panel is the fraction each fake type contributes to the reducible background in the region.

The scale factors are determined in a CR that is enriched with fake leptons of a particular type. It is assumed that the scale factor are the same for $t\bar{t}$ and Z+jets. For fake types that have only low contributions to the CRs, a scale factor of 1 ± 0.1 is considered. This affects CONV electrons, LF muons, GJ τ and ELEC τ. The scale factors are measured with respect to p_{T} and η. However, for the final results only the p_{T} dependency is considered, due to the otherwise high statistical uncertainty.

HF e,μ,τ scale factors The scale factors for fake leptons from HF decays are estimated in a $t\bar{t}$ enriched CR. The region selects events selected by lepton triggers with a signal e/μ pair with opposite charge, an additional third baseline lepton is used to calculate the fake factor. If the third lepton is an e/μ, its sign must match the sign of the same flavor signal lepton in order to avoid contamination from Z decays. Additionally, events are required to have at least one b-jet.

Before calculating the fake factor for MC and data, non-HF contamination is subtracted from both

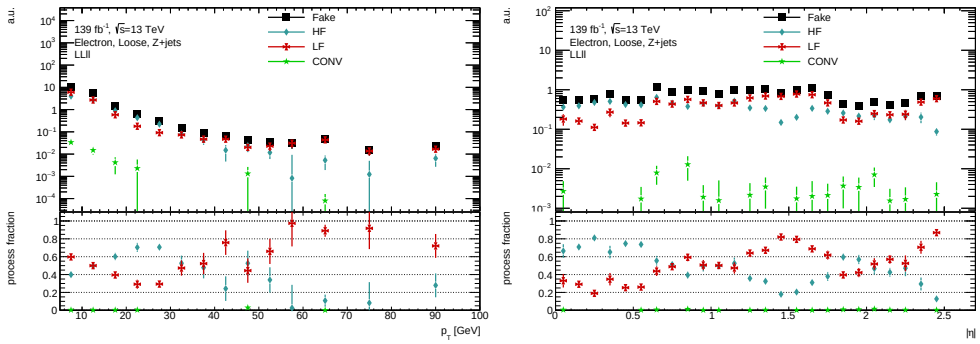

(a) CR2_LLll e p_{T} (b) CR2_LLll e $|\eta|$

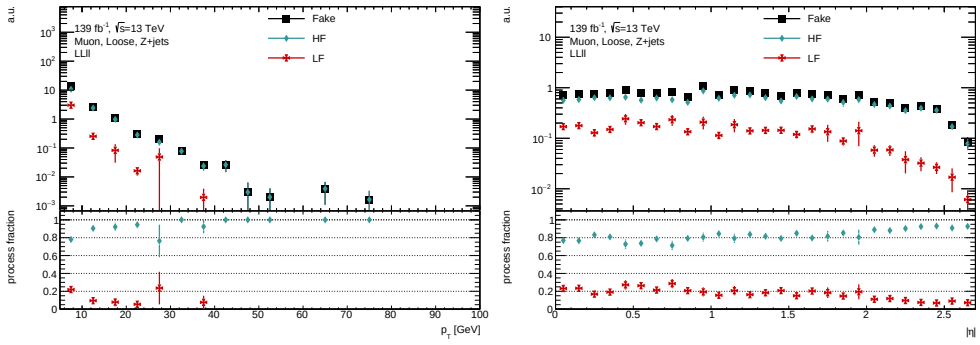

(c) CR2_LLll μ p_{T} (d) CR2_LLll μ $|\eta|$

Figure 6.13: Fake process fractions as a function of p_{T} and $|\eta|$ for electrons and muons in simulated Z+jets events. The upper panel shows the p_{T} and $|\eta|$ distributions for fake electrons and muons for the different fake types. The process fraction shown in the lower panel is the fraction each fake type contributes to the reducible background in the region.

MC and data, estimated MC. The MC samples considers all SM backgrounds in the region. The scale factor is the ratio of the fake factors measured in data and MC. The fake factors and scale factors are shown in Figure 6.21. The scale factor for electrons and muons is close to 1. The electron scale factor decreases slightly with p_{T}. In both cases the scale factor increases at high p_{T} to 2.2 and 1.7 for electrons and muons, respectively. For electrons the scale factor increases with η. For muons there is only a small dependency on η. For both flavors there is no large dependency on the distance to the closest lepton. The τ scale factor decreases with p_{T} and is between 1.25 and 0.95 for 1-prong τ leptons and between 1.16 and 0.98 for 3-prong τ leptons. 1-prong τ leptons show no dependency on η. For 3-prong τ leptons the scale factor decreases with η.

LF τ scale factors The scale factor for LF τ are estimated in a $Z \rightarrow \mu\mu$ CR. The events are selected by lepton triggers. The region requires two oppositely charged signal muons with an invariant mass consistent with a Z boson. An additional baseline τ is used to calculate the fake factor. Before

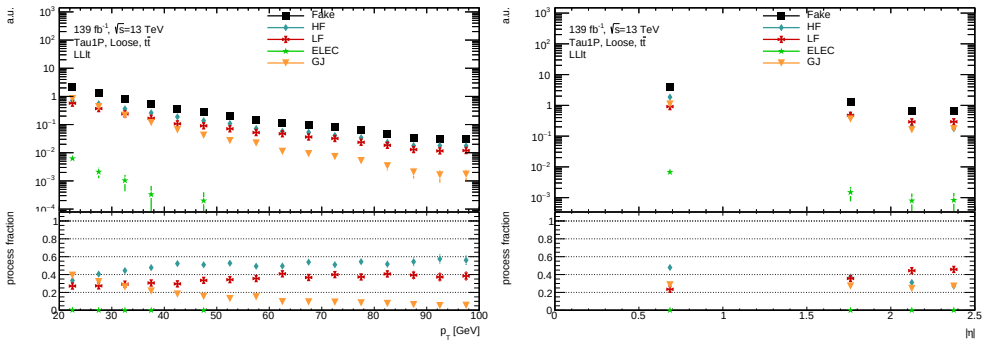

(a) CR2_LLlt p_{T} (b) CR2_LLlt η

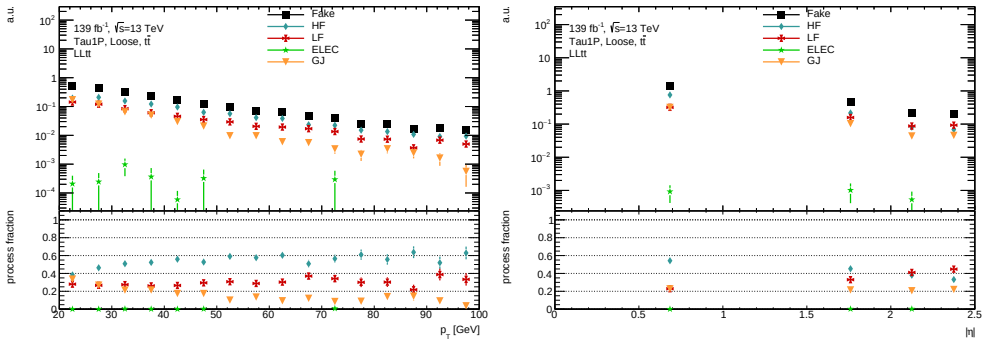

(c) CR2_LLtt p_{T} (d) CR2_LLtt η

Figure 6.14: Fake process fractions as a function of p_{T} and η for 1-prong τ leptons in simulated $t\bar{t}$ events. The upper panel shows the p_{T} and $|\eta|$ distributions for fake τ leptons for the different fake types. The process fraction shown in the lower panel is the fraction each fake type contributes to the reducible background in the region.

calculating the fake factor for MC and data, non-LF contamination is subtracted from both MC and data, using MC. As in the case of the HF e, μ, τ scale factors the MC samples of all SM backgrounds in the CR are used. The fake factors and scale factors are shown in Figure 6.22. The scale factor decreases with p_{T} and is between 1.1 and 0.9 and between 1.35 and 1.05 for 1-prong and 3-prong τ, respectively.

LF electron scale factors The scale factor for LF electrons is measured in a $W \rightarrow \mu\nu$ region. The region requires one signal muon with $p_{\mathrm{T}} > 28$ GeV that triggered the event. A second baseline electron with the same charge as the muon is used to measure the fake factors. The electron must be separated from the muon by $|\eta| > 0.2$. The invariant mass of the lepton pair has to be $m_{e\mu} > 20$ GeV. Furthermore, the events are required to have $m_{\mathrm{T}}(\mu) > 50$ GeV and $E_{\mathrm{T}}^{\mathrm{miss}} > 30$ GeV. Before calculating the fake factor for MC and data, non-LF contamination is subtracted from both MC and data, using MC. Similar to the other scale factors, the used MC samples cover all SM backgrounds in this region.

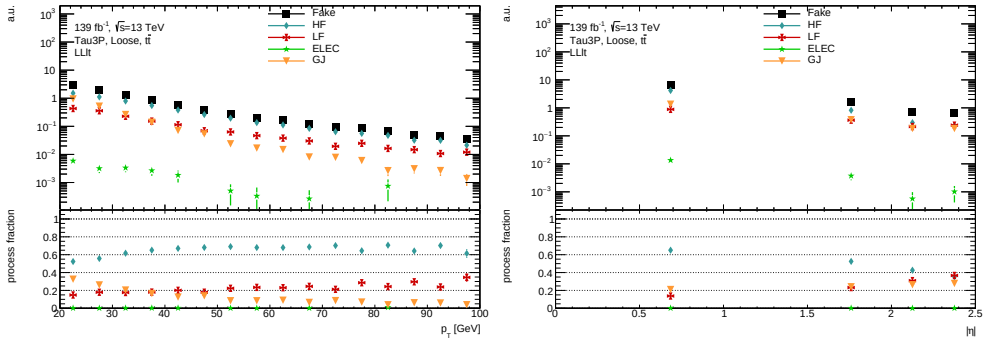

(a) CR2_LLlt p_{T} (b) CR2_LLlt η

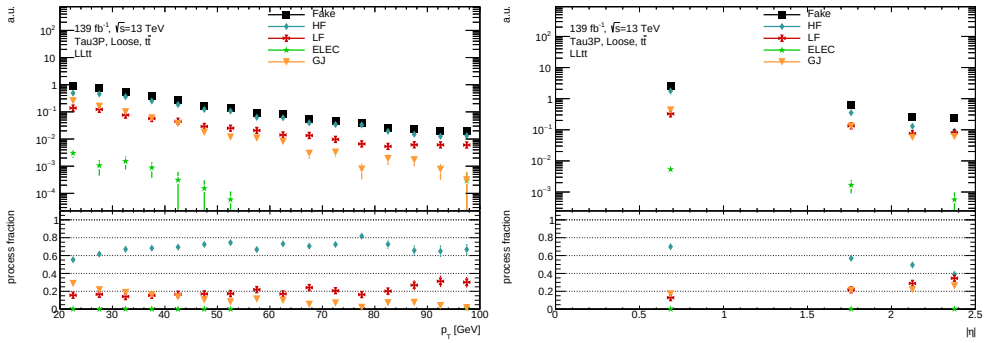

(c) CR2_LLtt p_{T} (d) CR2_LLtt η

Figure 6.15: Fake process fractions as a function of p_{T} and η for 3-prong τ leptons in simulated $t\bar{t}$ events. The upper panel shows the p_{T} and $|\eta|$ distributions for fake τ leptons for the different fake types. The process fraction shown in the lower panel is the fraction each fake type contributes to the reducible background in the region.

The scale factor is the ratio of the fake factors measured in data and MC. The fake factors and scale factors are shown in Figure 6.23. The obtained scale factor is between 1.05 and 1.4. In the transition region between barrel and endcap the scale factor decreases.

6.7 Background validation

The modeling of the reducible background is tested in VRs with four leptons with 0, 1 or 2 τ leptons. For LLLL, LLLT and LLTT events, the VRs veto the presence of a Z boson. To ensure orthogonality to the SRs the cut on m_{eff} is inverted. For LLLT and LLTT events, additional VRs with a Z boson requirement are used to check the fake lepton modeling across m_{eff}. The presence of a Z boson ensures the orthogonality of these regions with the SRs. The definition of the region are shown in Table 6.7. Figure 6.24 shows the m_{eff} distributions in the validation regions VR1-Z and VR2-Z, while Figure 6.25

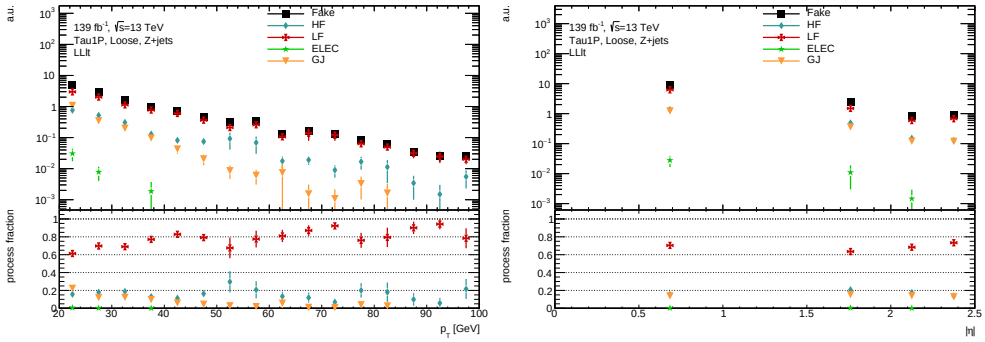

(a) CR2_LLlt p_{T} (b) CR2_LLlt η

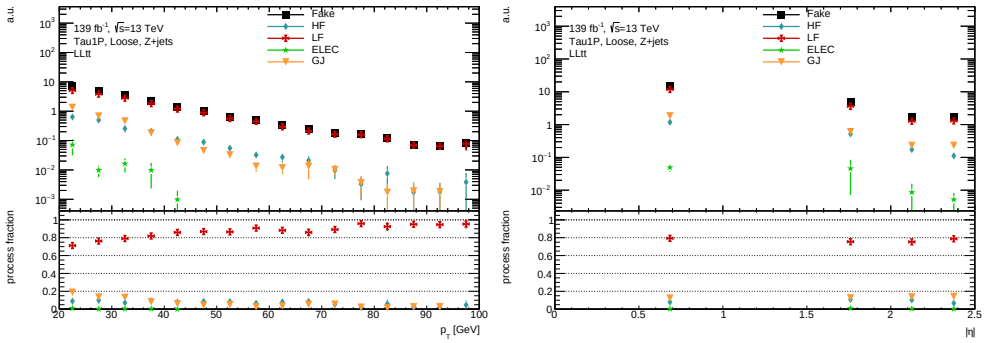

(c) CR2_LLtt p_{T} (d) CR2_LLtt η

Figure 6.16: Fake process fractions as a function of p_{T} and η for 1-prong τ leptons in simulated Z+jets events. The upper panel shows the p_{T} and $|\eta|$ distributions for fake τ leptons for the different fake types. The process fraction shown in the lower panel is the fraction each fake type contributes to the reducible background in the region.

shows the lepton p_{T} distributions in VR0-noZ, VR1-noZ and VR2-noZ. Good agreement is seen within statistical and systematic uncertainties (described in section 6.8). No significant deviations are observed showing the validity of the fake factor method.

Table 6.7: Definition of the validation regions to verify the fake estimation. Table adapted from Ref. [123].

Validation Region	$N(e,\mu)$	$N(\tau_{had})$	$N(b$-jets)	Z boson	Selection
VR0-noZ	≥ 4	$= 0$	$= 0$	veto	$m_{\mathrm{eff}} < 600$ GeV
VR1-noZ	$= 4$	≥ 1	$= 0$	veto	$m_{\mathrm{eff}} < 600$ GeV
VR1-Z	$= 4$	≥ 1	$= 0$	require 1st	–
VR2-noZ	$= 2$	≥ 2	$= 0$	veto	$m_{\mathrm{eff}} < 600$ GeV
VR2-Z	$= 2$	≥ 2	$= 0$	require 1st	–

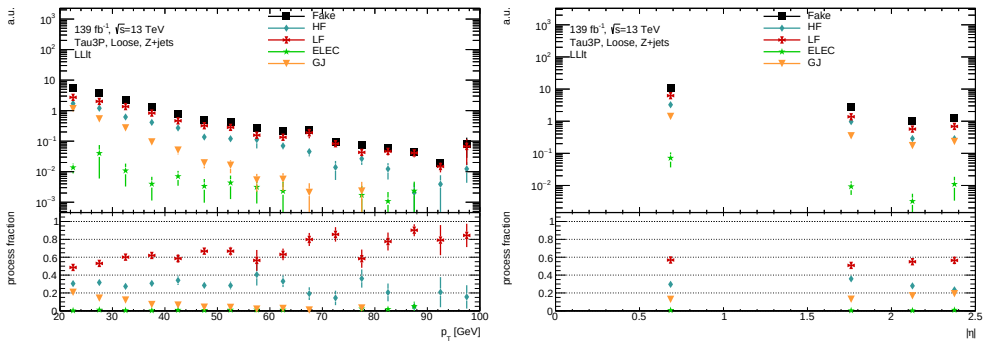

(a) CR2_LLlt p_{T} (b) CR2_LLlt η

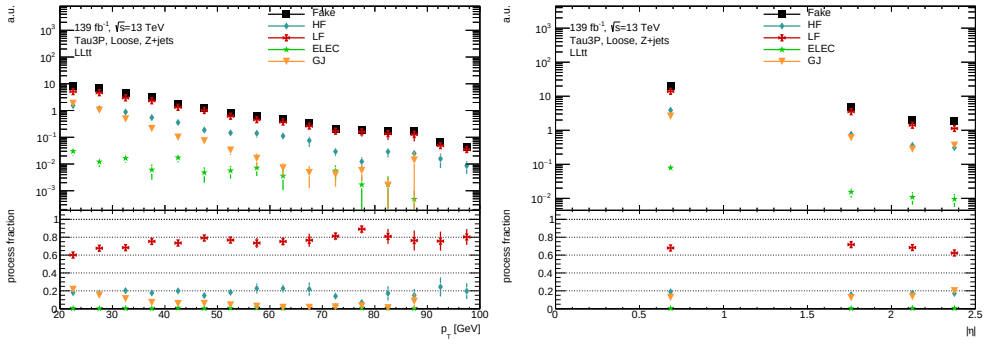

(c) CR2_LLtt p_{T} (d) CR2_LLtt η

Figure 6.17: Fake process fractions as a function of p_{T} and η for 3-prong τ leptons in simulated Z+jets events. The upper panel shows the p_{T} and $|\eta|$ distributions for fake τ leptons for the different fake types. The process fraction shown in the lower panel is the fraction each fake type contributes to the reducible background in the region.

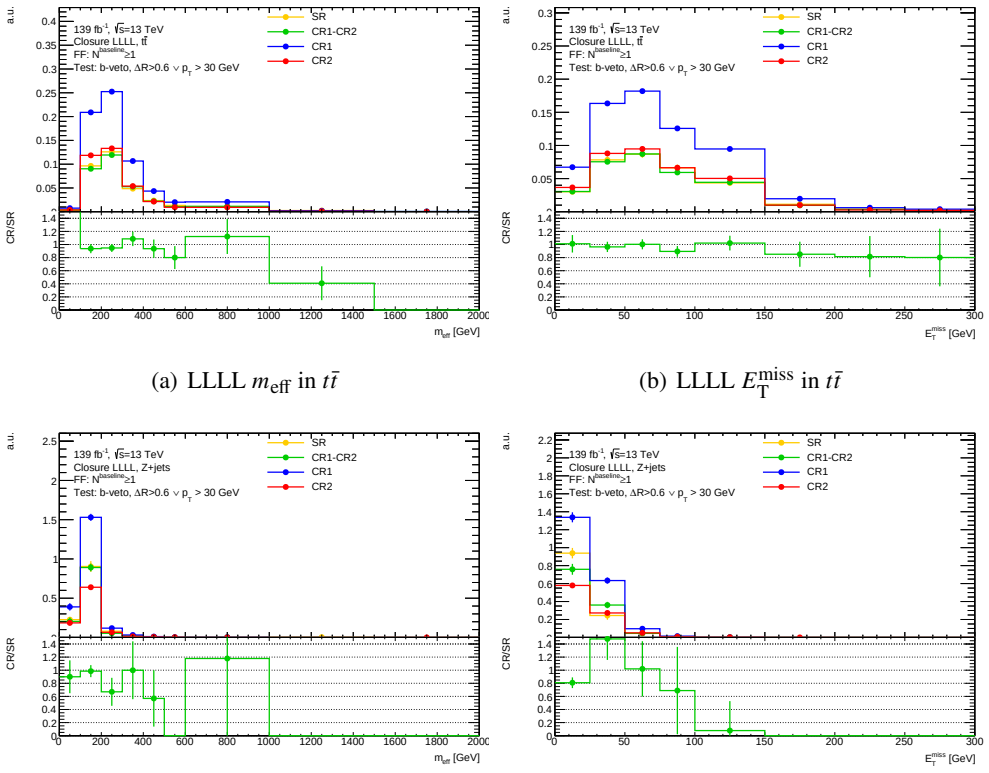

(a) LLLL m_{eff} in $t\bar{t}$

(b) LLLL $E_{\text{T}}^{\text{miss}}$ in $t\bar{t}$

(c) LLLL m_{eff} in Z+jets

(d) LLLL $E_{\text{T}}^{\text{miss}}$ in Z+jets

Figure 6.18: Closure in LLLL events in $t\bar{t}$ and Z+jets MC. The green (CR1-CR2) histogram is the prediction for the SR from the FF method and the yellow line is the prediction for the SR directly from the MC sample. The blue and red lines are the distributions from CR1 and CR2 weighted with the fake factors, respectively. The lower panel shows the ratio of the prediction of the FF method to the SR event selection.

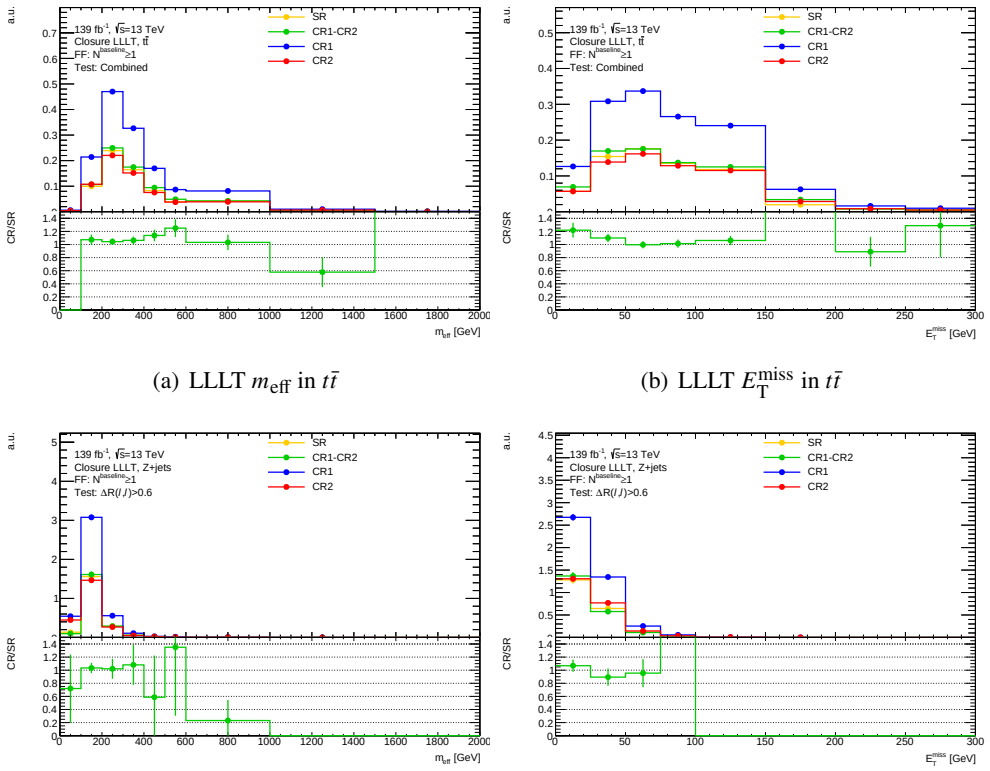

(a) LLLT m_{eff} in $t\bar{t}$

(b) LLLT $E_{\text{T}}^{\text{miss}}$ in $t\bar{t}$

(c) LLLT m_{eff} in Z+jets

(d) LLLT $E_{\text{T}}^{\text{miss}}$ in Z+jets

Figure 6.19: Closure in LLLT events in $t\bar{t}$ and Z+jets MC. The green (CR1-CR2) histogram is the prediction for the SR from the FF method and the yellow line is the prediction for the SR directly from the MC sample. The blue and red lines are the distributions from CR1 and CR2 weighted with the fake factors, respectively. The lower panel shows the ratio of the prediction of the FF method to the SR event selection.

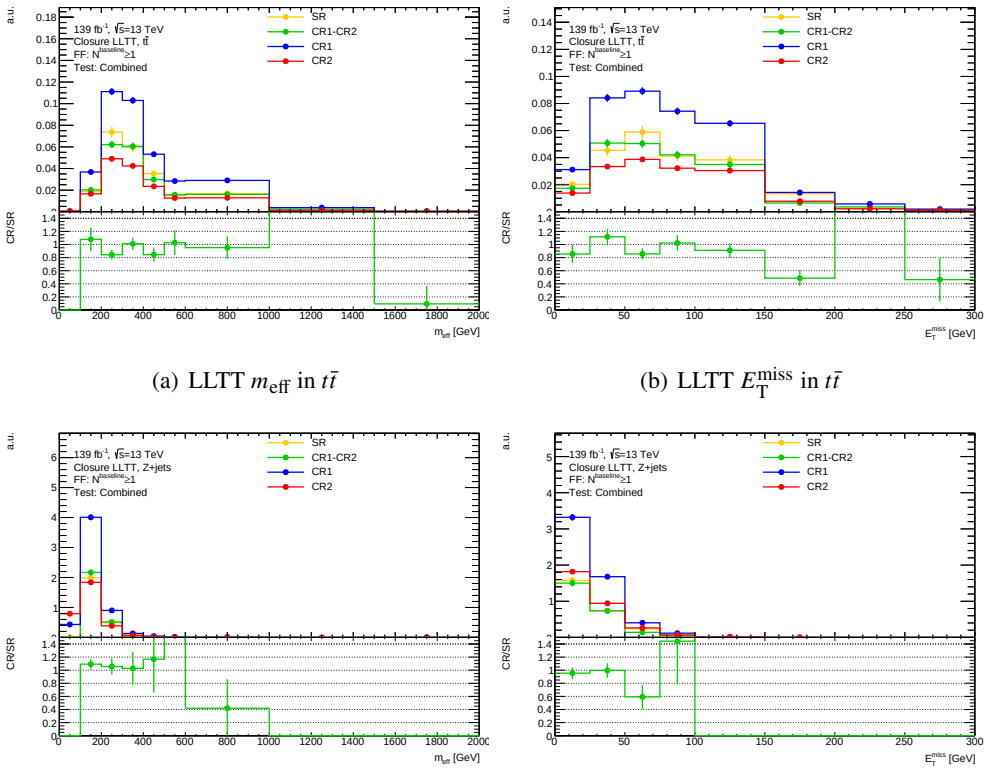

(a) LLTT m_{eff} in $t\bar{t}$

(b) LLTT $E_{\text{T}}^{\text{miss}}$ in $t\bar{t}$

(c) LLTT m_{eff} in Z+jets

(d) LLTT $E_{\text{T}}^{\text{miss}}$ in Z+jets

Figure 6.20: Closure in LLTT events in $t\bar{t}$ and Z+jets MC. The green (CR1-CR2) histogram is the prediction for the SR from the FF method and the yellow line is the prediction for the SR directly from the MC sample. The blue and red lines are the distributions from CR1 and CR2 weighted with the fake factors, respectively. The lower panel shows the ratio of the prediction of the FF method to the SR event selection.

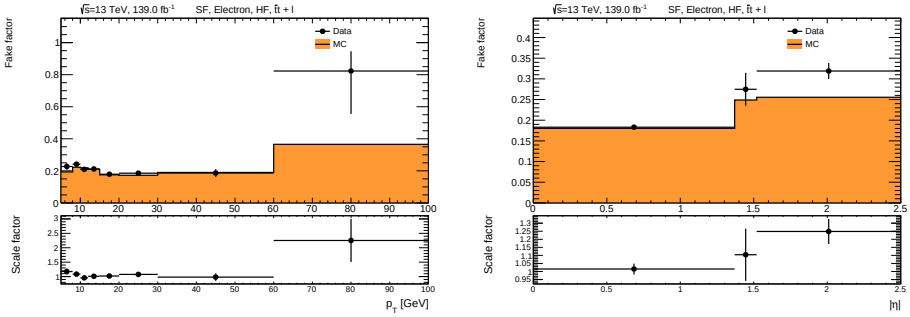

(a) e p_{T}

(b) e η

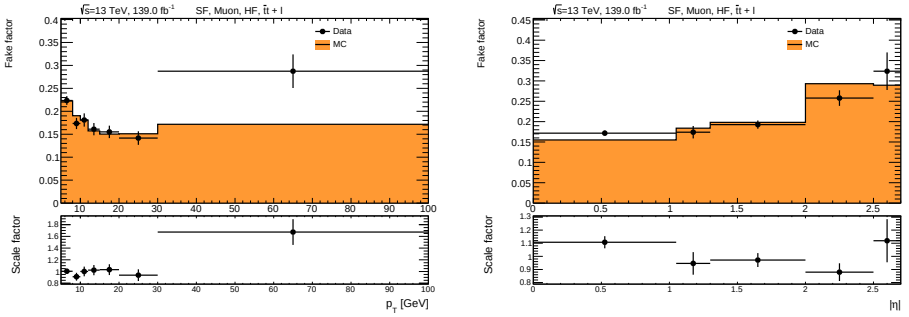

(c) μ p_{T}

(d) μ η

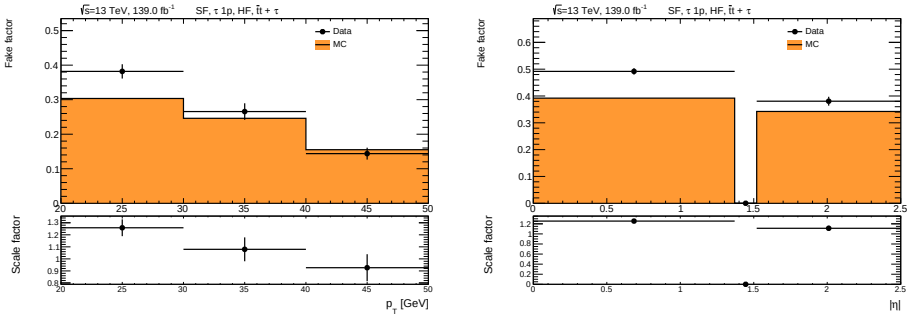

(e) 1P τ p_{T}

(f) 1P τ η

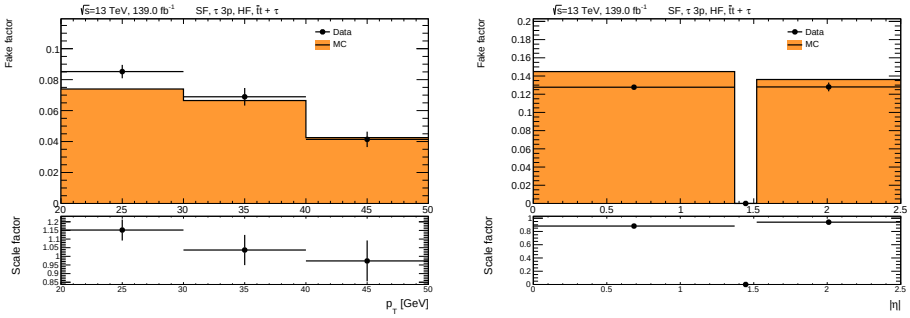

(g) 3P τ p_{T}

(h) 3P τ η

Figure 6.21: Heavy flavour scale-factor in a $t\bar{t}$ CR. The upper panel shows the fake factors measured in data and MC. The scale factor, shown in the lower panel, is the ratio between the two fake factors.

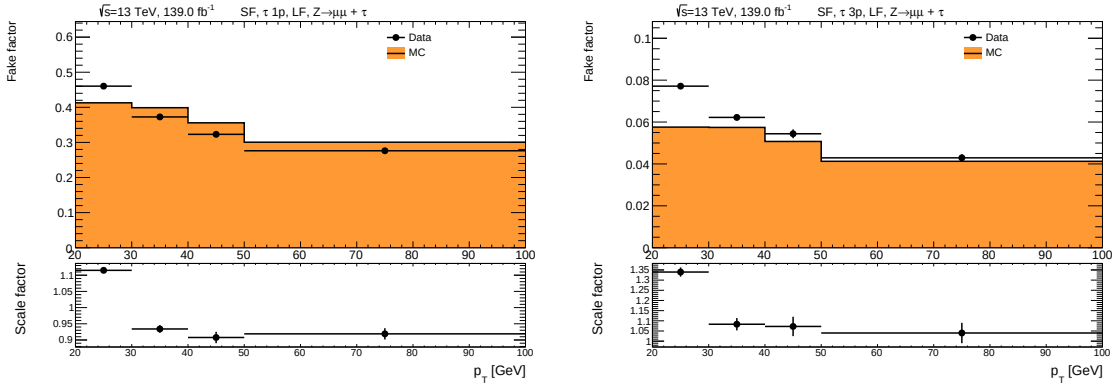

(a) 1P τ p_{T} (b) 3P τ p_{T}

Figure 6.22: The light flavor scale-factor for taus in a Z+jets CR in data and MC. The upper panel shows the fake factors measured in data and MC. The scale factor, shown in the lower panel, is the ratio between the two fake factors.

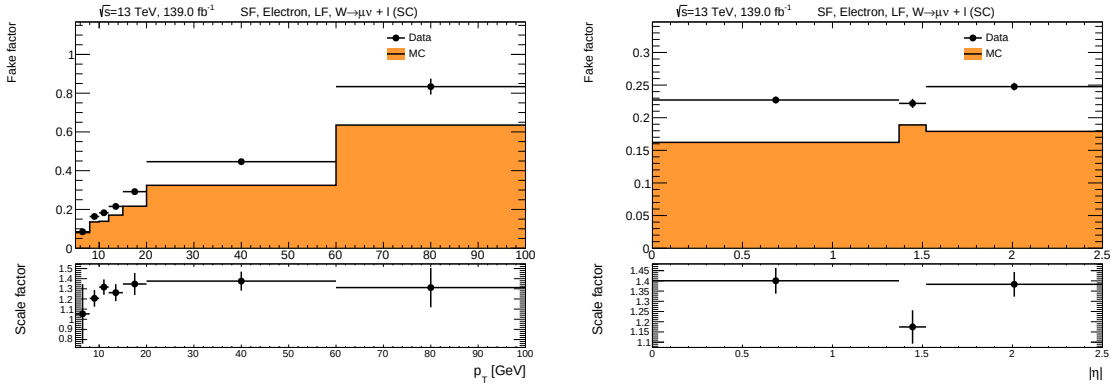

(a) p_{T} (b) η

Figure 6.23: The light flavor scale-factor for electrons in the $W \rightarrow \mu\nu$ CR in data and MC. The upper panel shows the fake factors measured in data and MC. The scale factor, shown in the lower panel, is the ratio between the two fake factors.

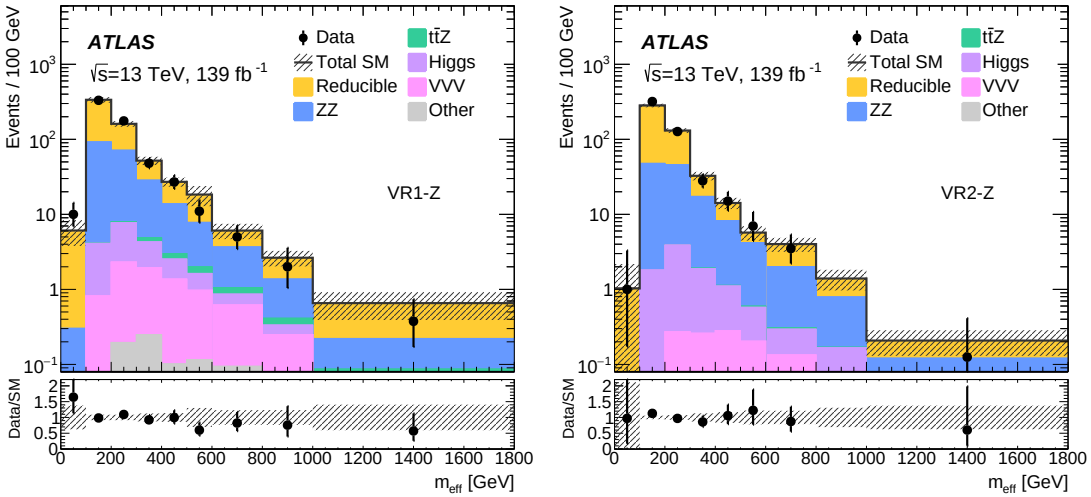

(a) VR1-Z (b) VR2-Z

Figure 6.24: m_{eff} distribution in the validation regions VR1-Z and VR2-Z after the background-only fit. The last bin includes the overflow. The lower panel shows the ratio of observed data to the expected SM background yields. Both the statistical and systematic uncertainties in the SM background are included in the shaded band [123].

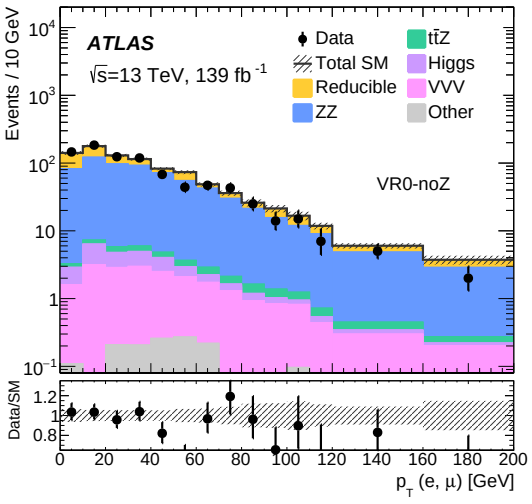

(a) $p_{\mathrm{T}}(e,\mu)$ in VR0-noZ

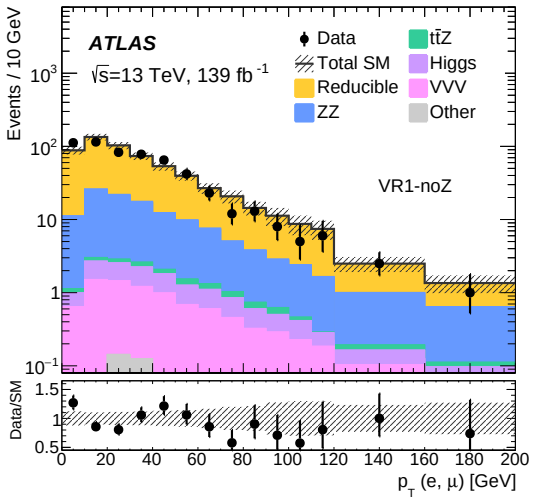

(b) $p_{\mathrm{T}}(e,\mu)$ in VR1-noZ

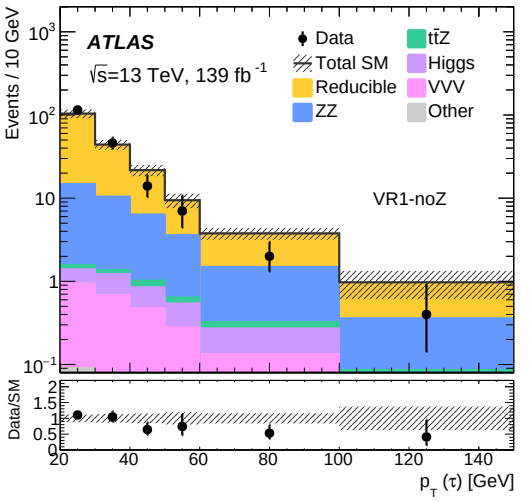

(c) $p_{\mathrm{T}}(\tau_{\mathrm{had}})$ in VR1-noZ

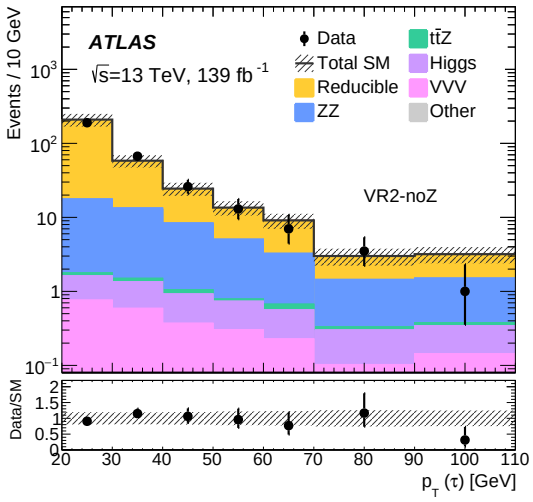

(d) $p_{\mathrm{T}}(\tau_{\mathrm{had}})$ in VR2-noZ

Figure 6.25: p_{T} distributions in the validation regions VR0-noZ, VR1-noZ and VR2-noZ after the background-only fit. The last bin includes the overflow. The lower panel shows the ratio of observed data to the expected SM background yields. Both the statistical and systematic uncertainties in the SM background are included in the shaded band [123].

6.8 Systematic uncertainties

The systematic uncertainties considered in this analysis can be divided into four components: statistical uncertainty of the MC simulation, experimental uncertainties in the event reconstruction, theoretical uncertainties and uncertainties in the reducible background. The statistical uncertainty is typically below 5% but rises up to 15% in regions with tight cuts on m_{eff}. The experimental uncertainties are associated with electrons, muons, τ, jets and $E_{\text{T}}^{\text{miss}}$ as well as uncertainties on the luminosity and the simulation of pile-up. The uncertainty on the luminosity is measured with the LUCID-2 detector [160]. The uncertainty on the luminosity is 1.7% for the Run 2 dataset [126]. The experimental uncertainties associated with electrons, muons and τ include uncertainties regarding the lepton identification efficiencies, lepton energy scale, energy resolution, isolation and trigger efficiencies and are generally of the order of a few percent in all signal regions [75–77, 84]. Uncertainties regarding jets are due to jet energy scale, jet energy resolution, jet vertex tagging and b-tagging [83, 161]. The jet energy resolution is a dominant uncertainty in the SRs targeting the GMM models, since uncertainties on object momenta are propagated to the $E_{\text{T}}^{\text{miss}}$ measurement [86]. Uncertainties in $E_{\text{T}}^{\text{miss}}$ are also arising from energy deposits not associated with any reconstructed object. Jet and $E_{\text{T}}^{\text{miss}}$ uncertainties are of the order of a few percent in the SRs but increases to 10-20% in the SRs with $E_{\text{T}}^{\text{miss}}$ selection. Theoretical uncertainties on the MC predictions originate from uncertainties on the cross-section, on the choice of the renormalization and factorization scales and the PDFs, as well as the choice of the MC generator used. These uncertainties have been determined to be of the order of the order of 20% in the SRs [140, 162].

The statistical uncertainties in data in CR1 and CR2 are the dominating uncertainties for the estimation of the reducible background. Furthermore, the statistical uncertainties of the fake factor and process fraction in the MC samples as well as the statistical uncertainties in MC and data in CRs for the estimation of the scale factors are considered. Additionally, there are systematic uncertainties due to neglected terms in the fake factor method. These terms are from regions with three or four loose leptons or in the case of regions with τ leptons, events with signal τ leptons and loose light leptons. The MC statistics in the corresponding control regions does not allow for accurate estimations, due to the very small contributions of events with three or four loose leptons. An upper limit on these uncertainties from neglected terms is estimated using data events from the neglected CRs weighted with the measured fake factors. Only those CRs that are expected to contribute the most are considered. For events with light leptons only, this corresponds to a region with one signal and three loose leptons. For regions with τ leptons there are also CRs with signal τ leptons and loose light leptons. The obtained yields plus its 1σ statistical uncertainty are the upper limits on the uncertainties from neglected terms, that are added to the reducible background uncertainty. The process fractions for the contributing processes and fake types considers no dependence on p_{T}, η and ΔR, since the MC

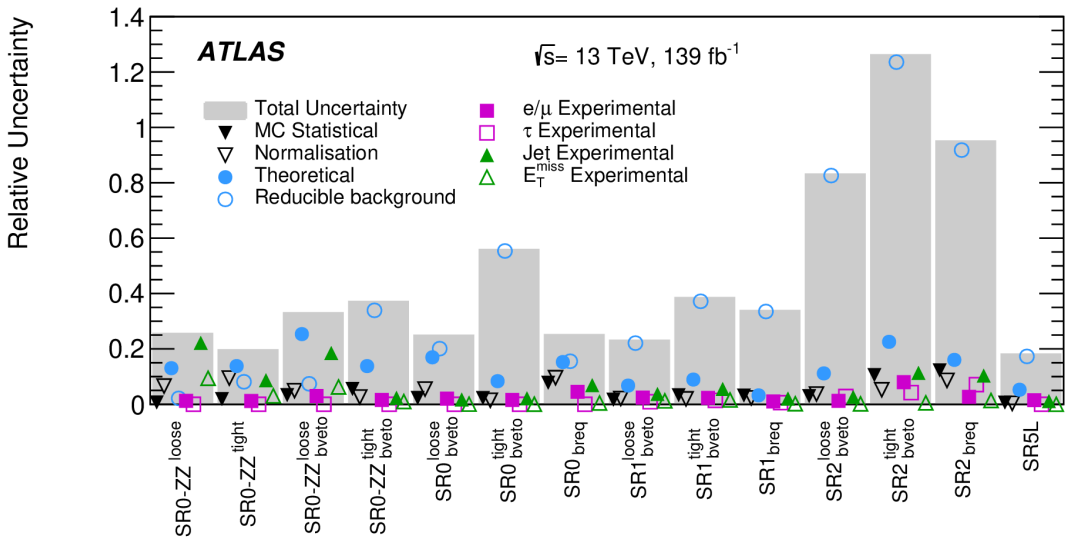

Figure 6.26: Systematic uncertainties in the SRs [123].

statistics do not allow for that parametrization. The obtained systematic uncertainties for each SR, VR and the ZZ and $t\bar{t}Z$ CRs, together with the used term which is neglected in the nominal fake estimate are shown in Table 6.8. In the regions with four light leptons, there are no or only very few data events in the CRs. Therefore, the obtained systematic is very small. For regions with τ leptons, the contributions from neglected terms are larger leading to a higher uncertainty.

Figure 6.26 shows the uncertainties for each SR. The uncertainties vary from 20% in regions with no or one τ lepton, to up to 120% in regions with two τ leptons. In most signal regions the uncertainty is dominated by the uncertainty on the reducible background, while in the regions with two Z bosons theoretical uncertainties and uncertainties on jets are dominant.

Table 6.8: Uncertainty on the fake estimation derived from neglected terms in the fake factor method. The obtained yields plus its 1σ statistical uncertainty are the upper limits on the uncertainties from neglected terms, that are added to the reducible background uncertainty.

Region	Calculation of Systematic	Obtained yields
CRZZ	$N^{\text{data}}_{\text{CR\_Lll1}} F_1 F_2 F_3$	0 ± 0
VRZZ	$N^{\text{data}}_{\text{CR\_Lll1}} F_1 F_2 F_3$	2.5 ± 0.44
CRttZ	$N^{\text{data}}_{\text{CR\_Lll1}} F_1 F_2 F_3$	0.19 ± 0.09
VRttZ	$N^{\text{data}}_{\text{CR\_Lll1}} F_1 F_2 F_3$	0.87 ± 0.47
VR0-noZ	$N^{\text{data}}_{\text{CR\_Lll1}} F_1 F_2 F_3$	5.8 ± 0.4
SR0-ZZ$^{\text{loose}}_{\text{bveto}}$	$N^{\text{data}}_{\text{CR\_Lll1}} F_1 F_2 F_3$	0 ± 0
SR0-ZZ$^{\text{tight}}_{\text{bveto}}$	$N^{\text{data}}_{\text{CR\_Lll1}} F_1 F_2 F_3$	0 ± 0
SR0-ZZ$^{\text{loose}}$	$N^{\text{data}}_{\text{CR\_Lll1}} F_1 F_2 F_3$	0 ± 0
SR0-ZZ$^{\text{tight}}$	$N^{\text{data}}_{\text{CR\_Lll1}} F_1 F_2 F_3$	0 ± 0
SR0$^{\text{loose}}_{\text{bveto}}$	$N^{\text{data}}_{\text{CR\_Lll1}} F_1 F_2 F_3$	0.09 ± 0.08
SR0$^{\text{tight}}_{\text{bveto}}$	$N^{\text{data}}_{\text{CR\_Lll1}} F_1 F_2 F_3$	0 ± 0
SR0$_{\text{breq}}$	$N^{\text{data}}_{\text{CR\_Lll1}} F_1 F_2 F_3$	0.009 ± 0.009
VR1-noZ	$N^{\text{data}}_{\text{CR\_LTll}} F_1 F_2 - N^{\text{data}}_{\text{CR\_Llll}} F_1 F_2 F_3$	20.4 ± 1.5
VR1-Z	$N^{\text{data}}_{\text{CR\_LTll}} F_1 F_2 - N^{\text{data}}_{\text{CR\_Llll}} F_1 F_2 F_3$	48.5 ± 3.6
SR1$^{\text{loose}}_{\text{bveto}}$	$N^{\text{data}}_{\text{CR\_LTll}} F_1 F_2 - N^{\text{data}}_{\text{CR\_Llll}} F_1 F_2 F_3$	0.42 ± 0.17
SR1$^{\text{tight}}_{\text{bveto}}$	$N^{\text{data}}_{\text{CR\_LTll}} F_1 F_2 - N^{\text{data}}_{\text{CR\_Llll}} F_1 F_2 F_3$	0.09 ± 0.09
SR1$_{\text{breq}}$	$N^{\text{data}}_{\text{CR\_LTll}} F_1 F_2 - N^{\text{data}}_{\text{CR\_Llll}} F_1 F_2 F_3$	0.03 ± 0.03
VR2-noZ	$N^{\text{data}}_{\text{CR\_LTTl}} F_1$	23.5 ± 3.1
VR2-Z	$N^{\text{data}}_{\text{CR\_LTTl}} F_1$	13.6 ± 12.6
SR2$^{\text{loose}}_{\text{bveto}}$	$N^{\text{data}}_{\text{CR\_LTTl}} F_1$	1.35 ± 1.18
SR2$^{\text{tight}}_{\text{bveto}}$	$N^{\text{data}}_{\text{CR\_LTTl}} F_1$	0 ± 0
SR2$_{\text{breq}}$	$N^{\text{data}}_{\text{CR\_LTTl}} F_1$	0.38 ± 0.38
SR5L	$N^{\text{data}}_{\text{CR\_LLlll}} F_1 F_2 F_3$	0.34 ± 0.18

6.9 Results

After the validity of the background estimation has been demonstrated by the good agreement between data and background in the VRs, the SRs can be unblinded.

6.9.1 Statistical Interpretation

The recorded data in the signal regions is statistically interpreted in order to check if the observations gives evidence for physics beyond the SM or is in agreement with the SM. For this the maximum likelihood fits are employed to fit the statistical model to the observed data [163]. The method is implemented in the HistFitter software framework [164]. For each region the expected number of events is the sum of the contributions of the individual physics processes (samples). The sample rates may depend on a set of free parameters $\boldsymbol{\eta}$, e.g. the normalization factors and constrained parameters $\boldsymbol{\chi}$ that account for systematic uncertainties. The constrained parameters are limited by constrained terms that can be viewed as auxillary measurements with global observable data $\boldsymbol{a}$. $\boldsymbol{a}$ is paired with data in the region $\boldsymbol{n}$ and is written as complete observation $\boldsymbol{x} = (\boldsymbol{n}, \boldsymbol{a})$. The likelihood function is given by

$$\mathcal{L}(\boldsymbol{x}|\boldsymbol{\eta}, \boldsymbol{\chi}) = \prod_{i \in \text{regions}} \text{Pois}(n_i|\nu_i(\boldsymbol{\eta}, \boldsymbol{\chi})) \prod_{\chi \in \boldsymbol{\chi}} c_\chi(a_\chi|\chi) \,, \tag{6.5}$$

where the Possion distribution $\text{Pois}(n_i|\nu_i(\boldsymbol{\eta}, \boldsymbol{\chi}))$ models the likelihood of the observed data n_i given the expected number of events in the region ν_i. The second term $\prod_{\chi \in \boldsymbol{\chi}} c_\chi(a_\chi|\chi)$ contrains the nuisance parameter χ using the auxiliary data a_χ and is modeled with a Gaussian with unit width.

The expected number of events ν_i in each region can be expressed as $\nu_i = \mu \cdot s + b$, where μ is the signal strength parameter, s the expected number of signal events and b the expected number of background events. Both s and b depend on the nuissance parameters $\boldsymbol{\chi}$. A signal strength of $\mu = 0$ corresponds to the background-only hypothesis while $\mu = 1$ corresponds to the signal-plus-background hypothesis.

By maximizing the likelihood function the values for the parameters $\boldsymbol{\eta}$ and $\boldsymbol{\chi}$ can be determined. The normalization factors for the irreducible backgrounds is determined in a background-only fit using the CRs as constraining regions.

In order to search for new signal processes, a null hypothesis H_0 is defined, which corresponds to the background-only hypothesis. H_0 is tested against the alternative hypothesis H_1, which corresponds to the signal-plus-background hypothesis. When setting limits on a particular signal model the signal-plus-background hypothesis is the null hypothesis H_0, which is tested against the background-only hypothesis H_1. The level of agreement of the observed data with a given hypothesis H is quantified by a p-value, i.e. a probability of finding data of equal or greater incompability under the assumption of

H. The hypothesis can be regarded as excluded if the observed p-value is below a specified threshold. Usually the p-value is converted into a significance Z defined as

$$Z = \Phi^{-1}(1 - p) \,, \tag{6.6}$$

where Φ^{-1} is the quantile of the standard Gaussian. In order to exclude a signal model a p-value threshold of 0.05 is used, which corresponds to the 95% confidence level (CL) and a significance of $Z = 1.64$.

A test statistic t is defined to evaluate the compability of data and the hypothesis. Large t values correspond to poor agreement with the data. The p-value is then calculated as

$$p = \int_{t_{\text{obs}}}^{\infty} f(t|H)dt \,, \tag{6.7}$$

where t_{obs} is the value of the test statistic observed in data and $f(t|H)$ is the probability density function of the test statistic under the assumption of H which can be obtained by sampling pseudo experiments. For large sampling numbers $f(t|H)$ can be approximated using asymptotic formulas [165].

In the test statistic the profile likelihood is used, which is defined as

$$\lambda(\mu) = \frac{\mathcal{L}(\mu, \hat{\hat{\boldsymbol{\theta}}}_{\mu}))}{\mathcal{L}(\hat{\mu}, \hat{\boldsymbol{\theta}})} \,, \tag{6.8}$$

where $\hat{\hat{\boldsymbol{\theta}}}_{\mu}$ denotes values of $\boldsymbol{\theta}$ that maximizes $\mathcal{L}$ for a given μ. $\hat{\mu}$ and $\hat{\boldsymbol{\theta}}$ are the parameter values that maximize the likelihood. For the purpose of setting upper limits, the test statistic is defined as

$$t_{\mu} = \begin{cases} -2\ln(\lambda(\mu)) & \text{if } \hat{\mu} \leq 0 \\ 0 & \hat{\mu} > \mu \end{cases} \,. \tag{6.9}$$

Setting $t_{\mu} = 0$ for $\hat{\mu} > \mu$ ensures that the hypothesis is not rejected in case of upward fluctuation of data [165]. However, signal points with small yields can potentially be excluded with this approach, although the analysis provides no sensitivity to those points. In order to avoid the exclusion to such signal points, the CL_s technique is used [166]. The CL_s is defined as

$$\text{CL}_s = \frac{p_{\mu}}{1 - p_b} \,, \tag{6.10}$$

which takes the $p - value$ of the background-only hypothesis p_b into account.

6.9.2 Observations

Table 6.9 shows the measured data and background expectations of the SRs. Figure 6.27 shows the data and background yields together with the significance for each SR. The observations are consistent with the SM expectations. The largest excess with respect to the SM predictions is observed in region SR5L which corresponds to a significance of 1.9σ. The 2.3σ excess in SR0-ZZ$^{\text{tight}}$ that was seen in the previous analysis with the 2015 and 2016 data [124], is not present in the full Run 2 dataset. The exclusion limits for the considered SUSY models are shown in Figure 6.28. For the GGM model the limit is shown as a function of the higgsino mass and the branch ratio of the decay via Z bosons. The observed limit obtained from this analysis is shown as red line while the observed limit from the previous search using 36.1 fb^{-1} is shown as grey area. The analysis is more sensitive to scenarios with high branching ratios of the decay to Z bosons. Higgsino masses up to 540 GeV are excluded for a branching ratio of 100%. The limit is weaker for lower branching ratios. Sensitivity down to branching ratios of 20% was achieved. The limits are increased by 200-260 GeV compared to the previous search and the sensitivity to lower branching ratios down to 20% is improved. The search for SUSY in final states with at least four lepton is not the only search targeting the GGM model. A comparison of the observed exclusion limits with other searches targeting this model is shown in Figure 6.29. In contrast to the search in final states with four leptons, the search in final states with at least three b-jets is sensitive to scenarios where the $\tilde{\chi}_1^0$ decays into Higgs [167]. It excludes scenarios where the branching ratio of the $\tilde{\chi}_1^0$ decaying into Higgs is above 50%. Higgsino masses up to 900 GeV are excluded. The search in final states with two hadronically decaying bosons is more sensitive to high masses excluding higgsino masses up to 950 GeV [168]. However, the search looses sensitivity at masses below 450 GeV. The search in two lepton final states excludes higgsino masses up to 900 GeV and branching ratios of the $\tilde{\chi}_1^0$ decaying into Higgs up to 90% [169] and covers roughly the phase space of the search in final states with four charged leptons as well as the search in final states with two hadronically decaying bosons.

The limits to the RPV models are shown as red line for the scenarios of the LSP decaying to light leptons, while the limit for the scenarios of the LSP decaying to τ is shown in blue. The limits are shown as function of the NLSP and LSP masses. Wino NLSP can be excluded for masses up to 1.6 TeV for the LSP decaying to light leptons. For scenarios with the LSP decaying to τ masses up to 1.1 TeV are excluded. The limits are lower for low LSP masses due as the leptons are more collimated in this parameter space and therefore more difficult to reconstruct. This effect is more pronounced for τ leptons since reconstructed τ leptons are separated by $\Delta R > 0.4$. $\tilde{\ell}_{\text{L}}/\tilde{\nu}$ are excluded up to 1.2 TeV and 0.87 TeV for the LSP decaying into light leptons and τ, respectively. Gluino masses up to 2.45 TeV and 1.8 TeV are excluded. These are one of the strongest constraints on gluinos at ATLAS [170].

For each signal region, the 95% CL upper limits on the expected and observed number of beyond-the-

SM events (S^{95}_{exp} and S^{95}_{obs}) are calculated using the model-independent signal fit. Also the 95% CL upper limits on the signal cross-section times efficiency ($\langle\epsilon\sigma\rangle^{95}_{\text{obs}}$) are calculated for each signal region. These results are shown in Table 6.10.

Table 6.9: Expected and observed events in the SRs after the background-only fit. Both statistical and systematic uncertainties are included. Table adapted from Ref. [123].

	SR0-ZZ$^{\text{loose}}$	SR0-ZZ$^{\text{tight}}$	SR0-ZZ$^{\text{loose}}_{\text{bveto}}$	SR0-ZZ$^{\text{tight}}_{\text{bveto}}$	SR0$^{\text{loose}}_{\text{bveto}}$	SR0$^{\text{tight}}_{\text{bveto}}$	SR0$_{\text{breq}}$
Observed	157	17	5	1	11	1	3
Total SM	161^{+41}_{-43}	$18.4^{+3.6}_{-3.3}$	$7.3^{+2.4}_{-1.9}$	1.1 ± 0.4	$11.5^{+2.9}_{-2.2}$	$3.5^{+2.0}_{-2.2}$	$1.19^{+0.30}_{-0.28}$
ZZ	125^{+40}_{-42}	$4.5^{+2.6}_{-2.1}$	$3.7^{+2.2}_{-1.7}$	$0.05^{+0.11}_{-0.04}$	$7.6^{+1.6}_{-1.7}$	$0.64^{+0.28}_{-0.29}$	$0.19^{+0.15}_{-0.19}$
$t\bar{t}Z$	15 ± 4	7.4 ± 1.8	0.87 ± 0.24	$0.12^{+0.05}_{-0.04}$	$0.7^{+0.18}_{-0.19}$	$0.02^{+0.014}_{-0.015}$	0.49 ± 0.13
Higgs	0.79 ± 0.1	0.29 ± 0.05	$0.09^{+0.028}_{-0.027}$	$0.0046^{+0.0019}_{-0.0018}$	0.24 ± 0.04	$0.02^{+0.007}_{-0.006}$	$0.16^{+0.05}_{-0.06}$
VVV	$7.9^{+1.9}_{-2.0}$	2.4 ± 0.6	2.2 ± 0.5	0.44 ± 0.12	1.6 ± 0.4	0.21 ± 0.06	$0.083^{+0.027}_{-0.029}$
Other	3.3 ± 0.7	1.7 ± 0.4	0.32 ± 0.09	$0.04^{+0.013}_{-0.014}$	$0.142^{+0.029}_{-0.032}$	$0.032^{+0.019}_{-0.022}$	$0.27^{+0.06}_{-0.05}$
Reducible	$9.1^{+3.4}_{-4.4}$	$2.0^{+1.5}_{-1.7}$	$0.15^{+0.54}_{-0.15}$	0.4 ± 0.4	$1.2^{+2.3}_{-1.2}$	$2.6^{+1.9}_{-2.2}$	$0.00^{+0.19}_{-0.00}$

	SR1$^{\text{loose}}_{\text{bveto}}$	SR1$^{\text{tight}}_{\text{bveto}}$	SR1$_{\text{breq}}$	SR2$^{\text{loose}}_{\text{bveto}}$	SR2$^{\text{tight}}_{\text{bveto}}$	SR2$_{\text{breq}}$	SR5L
Observed	7	2	2	5	2	1	21
Total SM	$7.7^{+1.8}_{-1.9}$	$1.6^{+0.6}_{-0.7}$	2.2 ± 0.7	$3.4^{+2.8}_{-1.6}$	$0.35^{+44}_{-0.13}$	$0.52^{+0.50}_{-0.13}$	12.4 ± 2.3
ZZ	$2.0^{+0.4}_{-0.6}$	$0.39^{+0.13}_{-0.19}$	0.04 ± 0.04	$1.54^{+0.3}_{-0.4}$	$0.23^{+0.08}_{-013}$	0.06 ± 0.06	0.49 ± 0.04
$t\bar{t}Z$	0.19 ± 0.1	$0.029^{+0.047}_{-0.029}$	0.22 ± 0.06	$0.058^{+0.024}_{-0.025}$	0.0 ± 0.0	0.19 ± 0.07	0.034 ± 0.009
Higgs	0.24 ± 0.07	$0.033^{+0.019}_{-0.020}$	$0.14^{+0.05}_{-0.06}$	0.2 ± 0.04	$0.033^{+0.010}_{-0.011}$	0.2 ± 0.07	0.96 ± 0.14
VVV	$0.66^{+0.16}_{-0.17}$	$0.16^{+0.04}_{-0.05}$	0.021 ± 0.008	$0.38^{+0.09}_{-0.10}$	$0.084^{+0.025}_{-0.027}$	$0.024^{+0.009}_{-0.010}$	$3.0^{+0.6}_{-0.7}$
Other	0.009 ± 0.005	$0.02^{+0.013}_{-0.018}$	$0.183^{+0.039}_{-0.034}$	0.005 ± 0.005	0.0014 ± 0.0012	$0.054^{+0.019}_{-0.015}$	0.22 ± 0.19
Reducible	4.7 ± 1.7	1.0 ± 0.6	1.6 ± 0.7	$1.2^{+2.8}_{-1.2}$	$0.0^{+0.4}_{-0.0}$	$0.0^{+0.5}_{-0.0}$	7.7 ± 2.1

6.10 Summary

A search for SUSY in events with at least four charged leptons has been performed using the full Run 2 dataset. The search targets R-parity violating scenarios where the LSPs decay each into two charged leptons and a neutrino, as well as R-parity conserving general gauge mediated SUSY scenarios where a pair produced mass degenerated higgsino triplet decays into a nearly massless gravitino and a Z or Higgs bosons. No significance excess over the expected SM background was observed and exclusion limits at 95% confidence level were derived. In the RPV models, gluino, wino and slepton masses up to 2.5 TeV, 1.6 TeV and 1.2 TeV have been excluded, respectively, for the case of the LSP decaying only into light leptons. For the scenario of the LSP decaying dominantly into τ leptons the corresponding limits are up to 1.8 TeV, 1.1 TeV and 0.87 TeV, respectively. This improves upon previous limits by around 100-350 GeV. For the GGM model higgsino masses up to 540 GeV are excluded, improving upon previous limits by around 200-260 GeV.

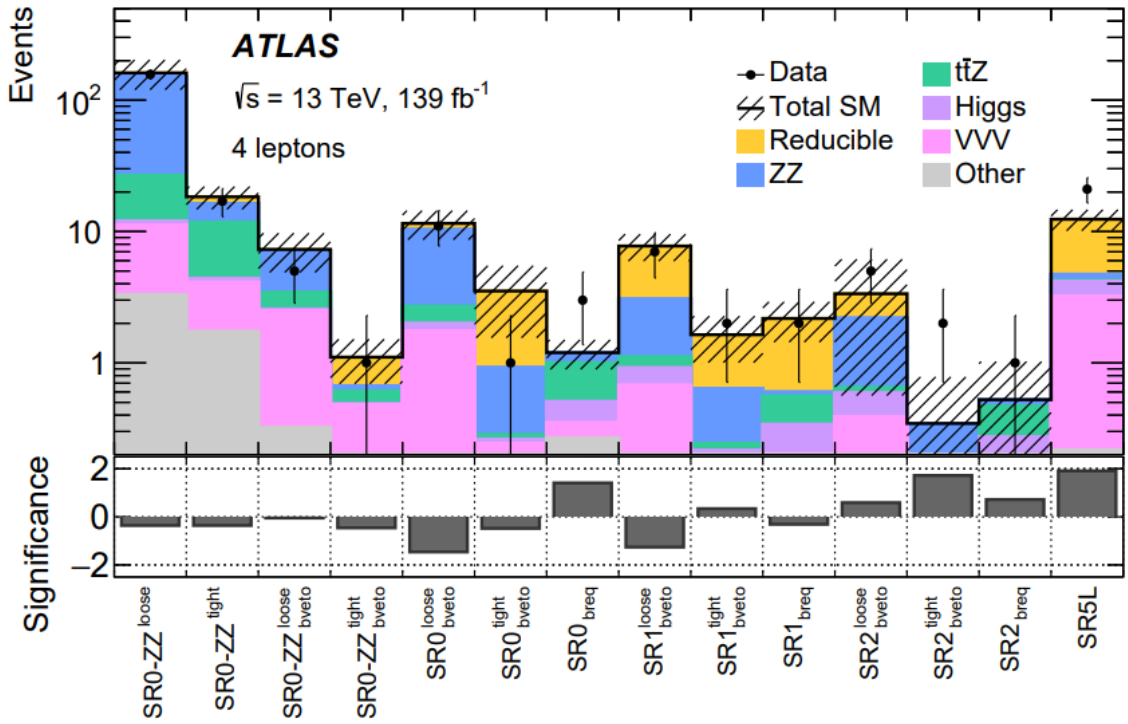

Figure 6.27: Expected and observed events in the SRs after the background-only fit. Both the statistical and systematic uncertainties in the SM background are included in uncertainties shown. The bottom panel shows the significance of any deviation of the observed data to the expected SM background yields [123].

Table 6.10: Model-independent limits calculated from the signal region observations. 95% CL upper limit on the visible cross-section times efficiency ($\langle\epsilon\sigma\rangle^{95}_{\text{obs}}$), the observed number of signal events (S^{95}_{obs}) and the signal events given the expected number of background events (S^{95}_{exp} and the $\pm1\sigma$ variations of the expected number). Table adapted from Ref. [123].

	$\langle\epsilon\sigma\rangle^{95}_{\text{obs}}$ [fb]	S^{95}_{obs}	S^{95}_{exp}
SR0-ZZ$^{\text{loose}}$	0.481	66.86	$67.43^{+20.43}_{-15.71}$
SR0-ZZ$^{\text{tight}}$	0.081	11.28	$11.52^{+4.81}_{-3.34}$
SR0-ZZ$^{\text{loose}}_{\text{bveto}}$	0.043	6.01	$7.10^{+2.82}_{-1.90}$
SR0-ZZ$^{\text{tight}}_{\text{bveto}}$	0.028	3.87	$3.63^{+1.44}_{-0.63}$
SR0$^{\text{loose}}_{\text{bveto}}$	0.070	9.79	$8.28^{+3.58}_{-2.30}$
SR0$^{\text{tight}}_{\text{bveto}}$	0.028	3.87	$4.29^{+1.56}_{-0.86}$
SR0$_{\text{breq}}$	0.046	6.33	$3.78^{+1.59}_{-0.66}$
SR1$^{\text{loose}}_{\text{bveto}}$	0.046	6.37	$7.46^{+2.92}_{-2.04}$
SR1$^{\text{tight}}_{\text{bveto}}$	0.032	4.47	$4.22^{+1.63}_{-1.04}$
SR1$_{\text{breq}}$	0.033	4.56	$4.59^{+1.77}_{-1.22}$
SR2$^{\text{loose}}_{\text{bveto}}$	0.061	8.45	$7.45^{+2.36}_{-1.24}$
SR2$^{\text{tight}}_{\text{bveto}}$	0.041	5.63	$3.53^{+1.06}_{-0.15}$
SR2$_{\text{breq}}$	0.030	4.17	$3.16^{+1.20}_{-0.16}$
SR5L	0.129	17.88	$9.88^{+4.08}_{-2.44}$

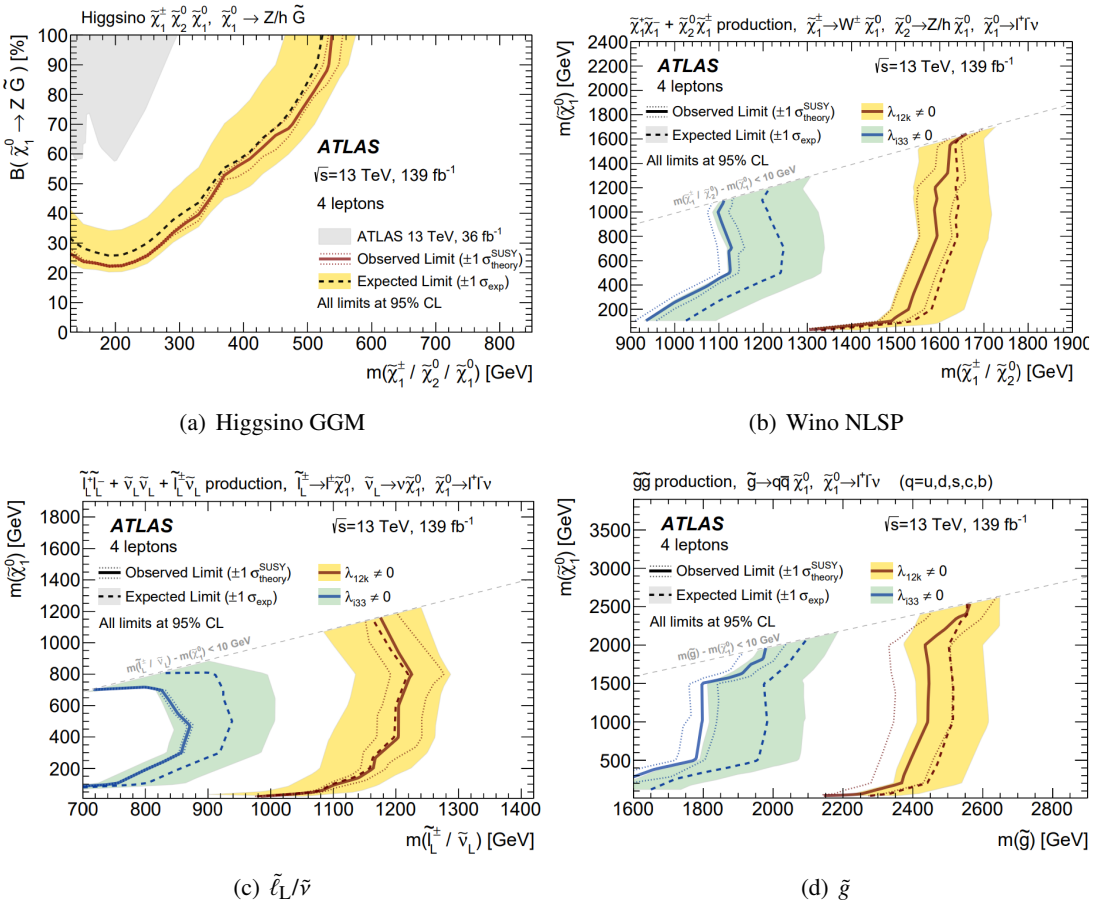

(a) Higgsino GGM

(b) Wino NLSP

(c) $\tilde{\ell}_L/\tilde{\nu}$

(d) $\tilde{g}$

Figure 6.28: Expected (dashed) and observed (solid) 95% CL exclusion limits on (a) the higgsino GGM models, and (b) wino NLSP, (c) $\tilde{\ell}_L/\tilde{\nu}$ and (d) gluino NLSP pair production with RPV $\tilde{\chi}_1^0$ decays via λ_{12k} (red), or λ_{i33} (blue) couplings. The limits are set using a statistical combination of disjoint regions. Where the signal regions overlap, the observed CL_s value is taken from the signal region with the better expected CL_s value is used. For all limits the $\pm 1\sigma$ uncertainty band is shown [123].

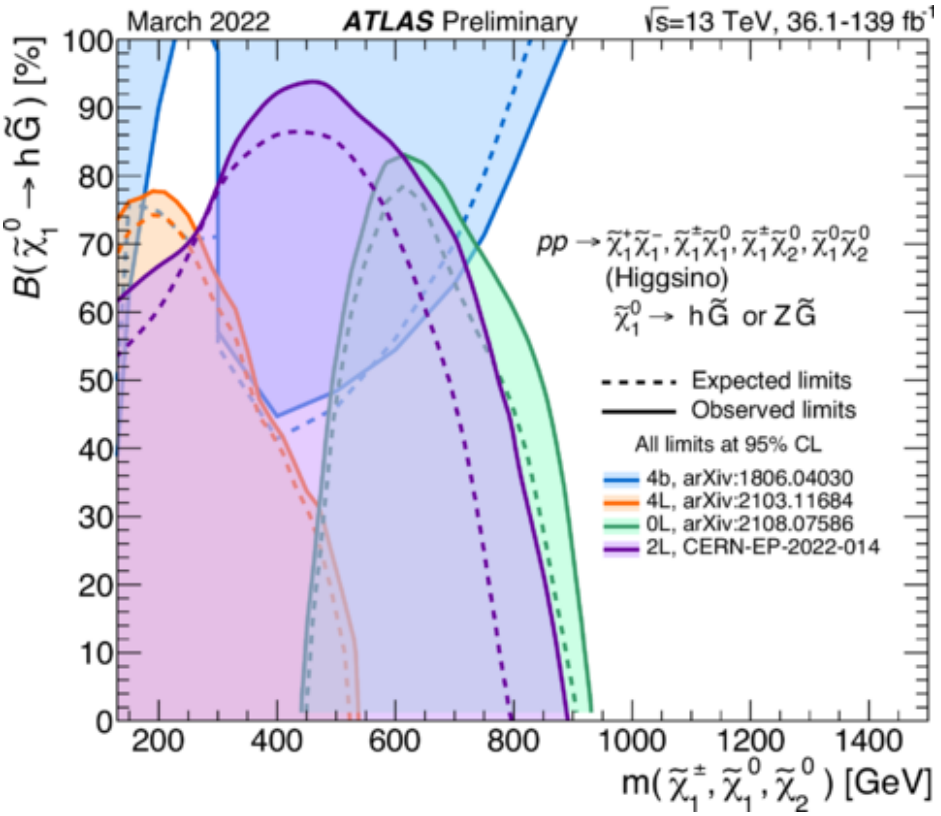

Figure 6.29: Comparison of the expected (dashed) and observed (observed) exclusion limits on the GGM model between this analysis (orange area) and a search in final states with at least three *b*-jets (blue area) [167], in final states with two boosted hadronically decaying bosons (green area) [168] and in final states with two leptons (violett area) [169]. Figure taken from Ref. [170]

CHAPTER SEVEN

SEARCH FOR SLEPTONS

The search for smuons is of particular interest, because SUSY scenarios featuring light smuons are capable of providing an explanation for the observed deviation of the measured value of the anomalous magnetic moment of the muon in the muon g-2 experiment at Fermilab, which differs significantly from the SM prediction. Loop corrections in the coupling of the muon to the photon, featuring the smuons and neutralinos, shown in Figure 7.2, might lead to a SUSY contributions to a_μ which makes the prediction consistent with the observed value [171]. Figure 7.3 shows the current mass constraints on smuons overlayed with scenarios, derived using pMSSM scans, that are consistent with the observed a_μ value. While some of the scenarios that would yield an a_μ matching to the measured value are already excluded by the previous searches, there are also scenarios with smuon and neutralino masses within the sensitivity gap between the yellow and orange areas. Therefore, a search for smuons targeting this gap is well motivated. In principle, a similar loop correction with selectrons, would lead to corrections to the anomalous magnetic moment the electron. However, due to the much smaller mass of the electron compared to the mass of the muon, this correction is much smaller and therefore, SUSY contributions to anomalous magnetic moment of the electron are negligible and no conflicts with the measured value which is in agreement with the SM prediction arises [171].

The supersymmetric partners of the SM leptons are targeted by several searches with the ATLAS detector. Figure 7.1 shows a summary of the constraints on sleptons by previous searches. With the full Run 2 dataset, two searches for selectrons and smuons were performed. These searches assume pair production of mass degenerate selectrons and smuons that each decay into a $\tilde{\chi}_1^0$ LSP and their corresponding SM lepton. One limit shown by the yellow area, was set by a search with events with two high p_{T} leptons, targeting scenarios where the mass difference between the slepton and the lightest neutralino is large [172]. This analysis excludes sleptons up to mass of $m_{\tilde{\ell}} = 700$ GeV and a mass splitting between slepton and LSP of $\Delta m(\tilde{\ell}, \tilde{\chi}_1^0) > 50$ GeV. The search was later reoptimized for scenarios with a mass splittings around the W-mass shown by the purple area [173] excluding mass splitting above 20 GeV for a slepton mass of 100 GeV. Another search, shown in orange, targets scenarios with a very small mass splitting, so called compressed scenarios [174]. Compressed

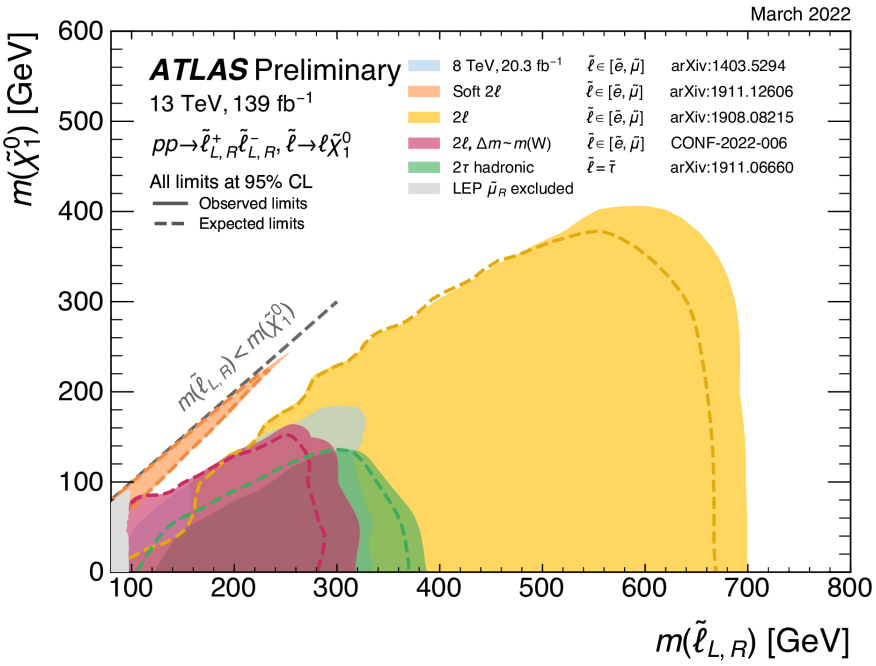

Figure 7.1: Current limits on slepton searches [170].

scenarios, lead to events with rather soft objects in the final states and are therefore challenging to reconstruct. This analysis excludes sleptons with masses up to 260 GeV with mass splittings of $\Delta m(\tilde{\ell}, \tilde{\chi}^0_1)$ up to 30 GeV. There is still a gap in the mass splitting, that is not targeted by the previous searches.

The search for sleptons within the sensitivity gap follows the strategy of the previous search for compressed scenarios by concentrating on events where a jet from initial state radiation boosts the sleptons allowing the usage of $E_{\mathrm{T}}^{\mathrm{miss}}$ trigger to select the events [174]. A common signal selection was developed for selectron and smuon production as the SM background as well as the reconstruction and identification efficiencies for electrons and muons are very similar.

7.1 Considered SUSY model

The analysis considers the pair production of mass degenerated selectrons and smuons. Each slepton decays in its SM counter part and the lightest neutralino, leading to a final state with two charged leptons and two neutralinos, contributing to $E_{\mathrm{T}}^{\mathrm{miss}}$. Slepton masses between 100 and 300 GeV with a mass splitting between slepton and neutralino between 10 and 75 GeV are considered. Due to the low mass splitting, typical events have soft leptons and low $E_{\mathrm{T}}^{\mathrm{miss}}$ and are therefore difficult to reconstruct or to select with the triggers. Therefore, this analysis concentrates on events that have an additional

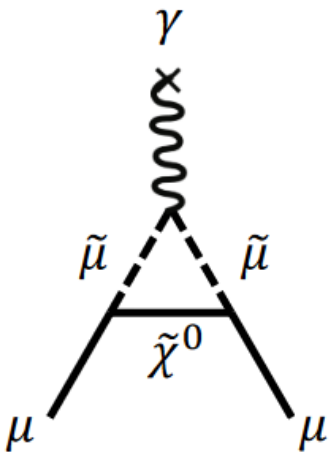

Figure 7.2: Loop correction to the coupling of the muon to the photon, featuring smuons and neutralinos.

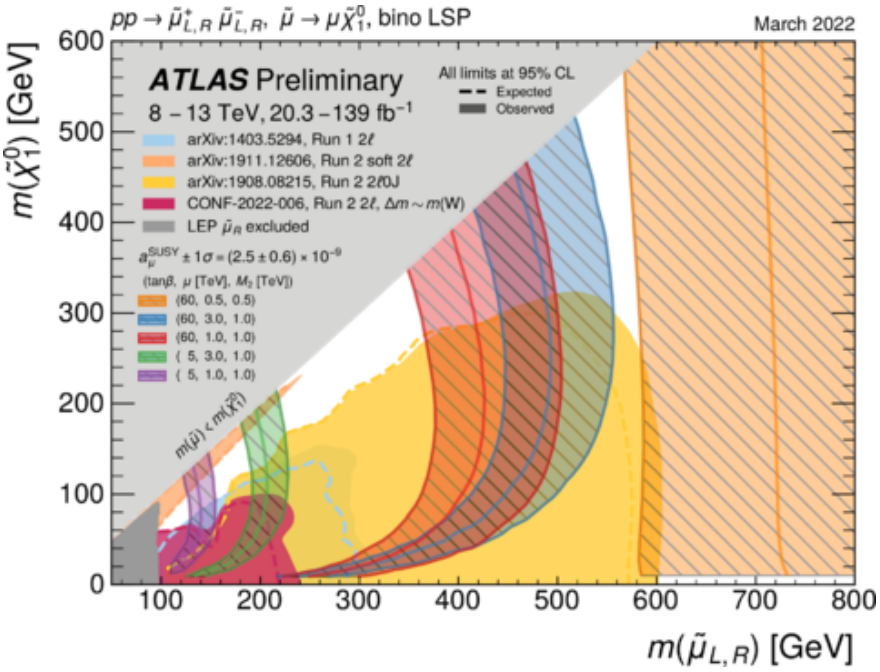

Figure 7.3: Current limits on slepton searches overlayed with SUSY scenarios that are consistent with the observed value of the anomalous magnetic moment of the muon [170].

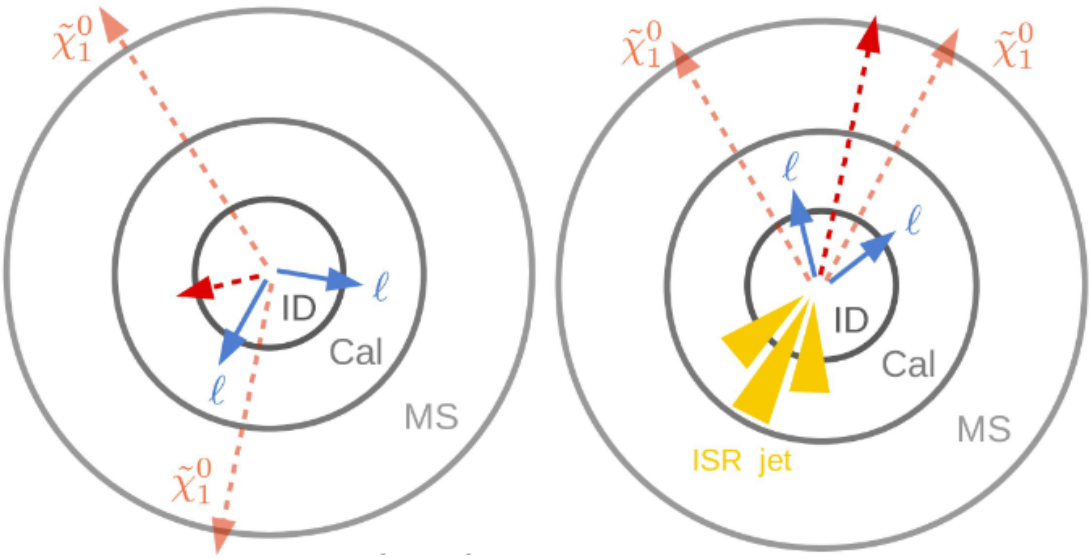

(a) without ISR jet, low $E_{\mathrm{T}}^{\mathrm{miss}}$ (b) with ISR jet, high $E_{\mathrm{T}}^{\mathrm{miss}}$

Figure 7.4: Schematic comparison of the event topology between events without an ISR jet and with ISR jet.

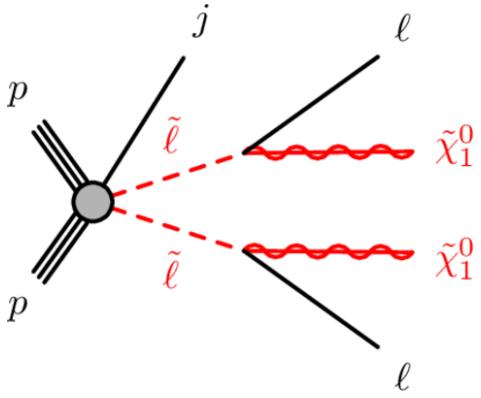

Figure 7.5: Feynman diagram of the slepton pair production with an ISR jet.

jet originating from initial state radiation (ISR). Such an ISR jet boosts the slepton-slepton system, leading to leptons with higher p_{T} and higher $E_{\mathrm{T}}^{\mathrm{miss}}$, which allows to select the events with the $E_{\mathrm{T}}^{\mathrm{miss}}$ trigger. Figure 7.4 shows a schematic comparison between the typical event without and with ISR jet. The previous search for compressed sleptons also used the approach with the ISR jet. Figure 7.5 shows the feynman diagram of the considered SUSY model with an ISR jet.

7.2 Data and simulated Event Samples

The analysis uses the full Run 2 dataset which contains pp collisions at $\sqrt{s}$ = 13 TeV, that were recorded during the Run 2 in 2015-2018. With the beam, detector and data-quality requirements applied [46], the total integrated luminosity used corresponds to 139.0 ± 2.4 fb^{-1} [126]. MC generators are used to simulate SM processes as well as new physics signals. The slepton samples are generated using MadGraph5_aMC@NLO v2.7.3 [127] using the NNPDF23LO PDF set [94] with up to two additional partons. The parton showering, hadronization and the underlying event are modeled with Pythia v8.244 [128] using the A14 tune [129]. The matrix element is matched to parton showers following the CKKW-L prescription [130]. The cross-sections are calculated at next-to-leading order (NLO) in the strong coupling constant, the resummation of soft gluon emission at next-to-leading logarithm accuracy (NLL) [138]. Slepton masses between 100 and 300 GeV and mass splittings between 10 and 75 GeV are considered. The detector response is modelled with the fast detector simulation [97].

Backgrounds considered for this analysis are from vector boson production V+jets ($V = W, Z, \gamma^*$), diboson production (VV), triboson production (VVV) as well as $t\bar{t}$, single top, $t\bar{t}V$, $t\bar{t}t$, $t\bar{t}t\bar{t}$, $t\bar{t}WW$ tZ, tW and tWZ. V+jets, VV and VVV production are simulated with Sherpa v2.2.1 or v2.2.2 with the NNPDF30NNLO PDF set at NLO. $t\bar{t}$, single-top and tW are simulated with Powheg-Box v2 with the NNPDF23LO and Pythia v8.230 with the A14 tune. The remaining top related backgrounds are simulated with MadGraph5_aMC@NLO with the NNPDF23LO PDF set and Pythia with the A14 tune.

All backgrounds are passed through the full ATLAS GEANT4 detector simulation [96]. A summary of the simulated MC samples is shown in Table 7.1.

The simulated MC samples are corrected to account for differences from data regarding the trigger efficiencies, reconstruction and identification efficiencies of the reconstructed objects as well the energy and momentum measurements of leptons and jets. The samples are also reweighted such that the simulated pile-up matches the pile-up of the data.

7.3 Object and Event Selection

Similar to the object selection of the search for SUSY in final states with at least four charged leptons, the object selection is performed in three steps. In the first step, preselected particles that fulfill minimal quality criterias are selected. In the next step, the overlap removal resolves ambiguities between preselected particles. Particles that passes the overlap removal are referred to as baseline particles. In the final step, additional quality requirements are applied. Particles that fulfill these

Table 7.1: Summary of the simulated MC samples used in this analysis, where $V = W, Z, \gamma^*$. "Tune" refers to the set of parameter values used by the generator.

Process	Generator(s)	Cross-section calculation	tune	PDF set
V+jets	Sherpa v2.2.1	NNLO		NNPDF30NNLO
VV	Sherpa v2.2.1/2.2.2	NLO		NNPDF30NNLO
VVV	Sherpa v2.2.1	NLO		NNPDF30NNLO
$t\bar{t}$	Powheg-Box v2 + Pythia v8.230	NNLO+NNLL	A14	NNPDF23LO
t	Powheg-Box v2 + Pythia v8.230	NNLO+NNLL	A14	NNPDF23LO
tW	Powheg-Box v2 + Pythia v8.230	NNLO+NNLL	A14	NNPDF23LO
$t\bar{t}V$	MadGraph5_aMC@NLO v2.3.3 + Pythia v8.210/8.212	NLO	A14	NNPDF23LO
$t\bar{t}t$	MadGraph5_aMC@NLO v2.2.2 + Pythia v8.186	LO	A14	NNPDF23LO
$t\bar{t}t\bar{t}$	MadGraph5_aMC@NLO v2.2.2 + Pythia v8.186	NLO	A14	NNPDF23LO
$t\bar{t}WW$	MadGraph5_aMC@NLO v2.2.2 + Pythia v8.186	NLO	A14	NNPDF23LO
tZ	MadGraph5_aMC@NLO v2.3.3 + Pythia v8.212	NLO	A14	NNPDF23LO
tWZ	MadGraph5_aMC@NLO v2.7.3 + Pythia v8.244	NLO	A14	NNPDF23LO
SUSY signals	MadGraph5_aMC@NLO v2.7.3 + Pythia v8.244	NLO+NLL	A14	NNPDF23LO

requirements are called signal or tight particles, while baseline particles passing the overlap removal but not the signal selection are referred to as loose leptons. Loose leptons are used to estimate the reducible background.

Electrons are required to have $p_{\mathrm{T}} > 4.5$ GeV and $|\eta| < 2.47$ and satisfy the LooseAndBLayerLLH criteria. Muons are required to have $p_{\mathrm{T}} > 3$ GeV, $|\eta| < 2.7$ and pass the Medium identification working point. Both, preselected electrons and muons pass a cut on the longitudinal impact parameter $|z_0 \sin(\theta) < 0.5|$ mm in order to reduce the number of leptons from secondary vertices. The overlap removal procedure consists of the following steps:

1. Electrons sharing an ID track with a muon are removed.
2. Non-b-tagged Jets with $\Delta R_y < 0.2$ to an electron are removed.
3. Jets with less than 3 associated tracks are removed if there is a muon with $\Delta R_y < 0.2$ or if a muon can be matched to a track associated with the jet.
4. Electrons and Muons with $\Delta R_y < 0.4$ to a jet are removed to reject leptons from semileptonic decays of c- and b-hadrons.

Signal electrons satisfy the MediumLLLH identification criteria. In order to suppress electrons and muons from secondary vertices, the transvers impact parameter normalised to its uncertainty $|d_0|/\sigma_{d_0}$ must be < 5 (3) for electrons (muons). Both signal electrons and muons are required to pass the PLVLoose isolation criteria, to reduce the amount of leptons form semileptonic decays of hadrons and jets misidentified as leptons. Jets are reconstructed with the anti-k_t algorithm with a radius parameter of 0.4. Preselected jets have $p_{\mathrm{T}} > 20$ GeV and $|\eta < 2.8|$. Signal jets with $p_{\mathrm{T}} < 120$ GeV are required

to pass the medium working point of the jet-vertex-tagging algorithm, in order to reduce the amount of pile-up jets. Events considered for this analysis are required to have one collision vertex with $\sum_{\text{tracks}} p_{\text{T}} > 400$ MeV. The data has to be recorded under stable beam and detector conditions. Events with muons that likely originated from cosmic rays, with $|d_0| > 0.2$ mm and $z_0 > 1$ mm are discarded. Also events with badly measured jets are rejected.

For the slepton search events that are triggered by $E_{\text{T}}^{\text{miss}}$ triggers. The events are required to have exactly two leptons with same flavor, either electrons or muons, with opposite charge. In order to select events with an ISR-jet, a jet with a p_{T} with more than 100 GeV that is in opposite direction of $E_{\text{T}}^{\text{miss}}$ with $\Delta\phi(\text{leading jet}, E_{\text{T}}^{\text{miss}}) > 2.0$. Since events from slepton production is expected to have high $E_{\text{T}}^{\text{miss}}$. Therefore to reduce the SM background $E_{\text{T}}^{\text{miss}} > 200$ GeV is required. Further reduction of the amount of SM background can be achieved by limiting the number of jets with $p_{\text{T}} > 30$ GeV to a maximum of two. The angular separation between the jets and $E_{\text{T}}^{\text{miss}}$, $\Delta\phi(\text{jet}, E_{\text{T}}^{\text{miss}}) > 0.4$ is used. The separation between the leptons $\Delta R_{\ell\ell}$ is larger than 0.75. Only events without a b-tagged jet are selected in order to reduce the amount background from processes involving top-quarks. This selection is referred as preselection.

7.4 Signal Regions

In order to find a selection that provides good sensitivity to the considered SUSY models, the significance is used, given by

$$Z = \sqrt{2\left(n \ln \frac{n(B+\sigma^2)}{B^2+n\sigma^2} - \frac{B^2}{\sigma^2} \ln\left[1 + \frac{\sigma(n-B)}{B(B+\sigma^2)}\right]\right)} \tag{7.1}$$

where B is the number of background events, n is the sum of signal and background events and σ the uncertainty on the background [175]. For this optimization for the uncertainty is the statistical uncertainty and a flat systematic uncertainty of 30 %. As benchmark signals, points with $m_{\tilde{\ell}} = 150$ GeV and $m_{\tilde{\chi}_1^0}$ of 130 and 110 GeV are used. Since the background modeling using monte carlo shows good agreement to data at preselection level, the background predictions taken from MC are used during the signal region optimization.

The signal region optimization in an iterative way utilizing N-1 plots. In N-1 plots all current selection criterias are applied with exception of the one on the plotted variable. The bottom panel of these plots shows the significance yielded by a requirement on the variable across the spectrum shown. The optimization iterates over the considered discriminating variables, like $E_{\text{T}}^{\text{miss}}$, the transverse mass of one of the leptons $m_{\text{T}}(\ell_i) = \sqrt{2(E_{\text{T}}^{\text{miss}} E_{\text{T}}^{\ell_i} - \boldsymbol{p}_{\text{T}}^{\text{miss}} \boldsymbol{p}_{\text{T}}^{\ell_i})}$ or $m_{\ell\ell}$. The selection requirements are chosen such that a high significance for the benchmark signal points are yielded.

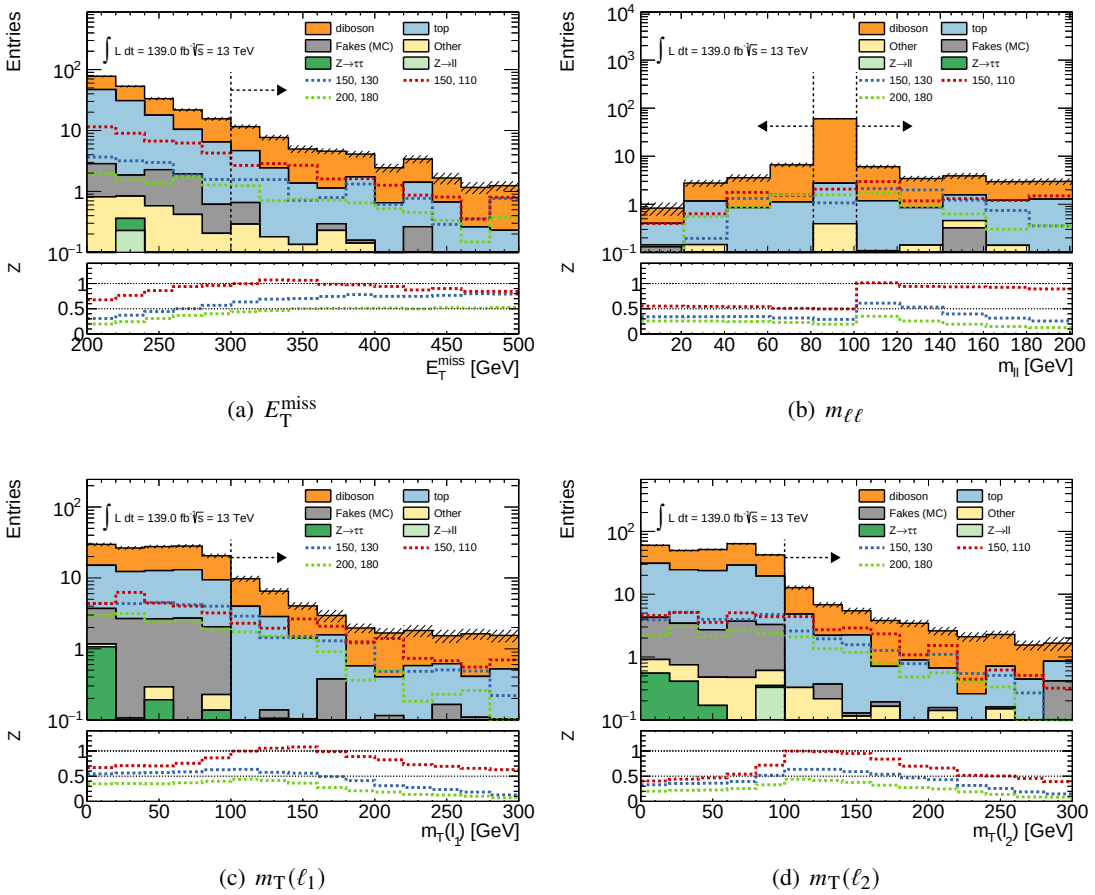

(a) $E_{\mathrm{T}}^{\mathrm{miss}}$ (b) $m_{\ell\ell}$

(c) $m_{\mathrm{T}}(\ell_1)$ (d) $m_{\mathrm{T}}(\ell_2)$

Figure 7.6: N-1 plots for the signal region. All requirements of the signal region with exception of the requirement on the shown variable are applied. The arrows indicate the chosen requirement on the variable shown. the The bottom panel shows the significance of the benchmark signal points yielded by a requirement on the variable across the spectrum.

The signal region requires $E_{\mathrm{T}}^{\mathrm{miss}} > 300$ GeV, $m_{\mathrm{T}}(\ell_1) > 100$ GeV and $m_{\mathrm{T}}(\ell_2) > 100$ GeV. Furthermore, events with $81.2 < m_{\ell\ell} < 101.2$ are vetoed to reduce the background involving Z-boson. Figure 7.6 shows N-1 plots of the used discriminating variables.

As discriminating variable m_{T2} is used which is variable constructed for processes where a pair of particles is produces, both decaying into a visible (lepton) and an invisible particle (neutralino). m_{T2} is given by:

$$m_{\mathrm{T2}} = \min_{\boldsymbol{q}_{\mathrm{T}}}(\max[m_{\mathrm{T}}(\boldsymbol{p}_{\mathrm{T}}^{\ell_1}, \boldsymbol{q}_{\mathrm{T}}, m_{\chi}), m_{\mathrm{T}}(\boldsymbol{p}_{\mathrm{T}}^{\ell_2}, \boldsymbol{p}_{\mathrm{T}}^{\mathrm{miss}} - \boldsymbol{q}_{\mathrm{T}}, m_{\chi})]) \tag{7.2}$$

where $\boldsymbol{p}_{\mathrm{T}}^{\ell_1}$ and $\boldsymbol{p}_{\mathrm{T}}^{\ell_2}$ are the transverse momenta of the leading and subleading lepton, q_{T} is the momentum of the invisible particle which is produced in the decay associated with the leading lepton.

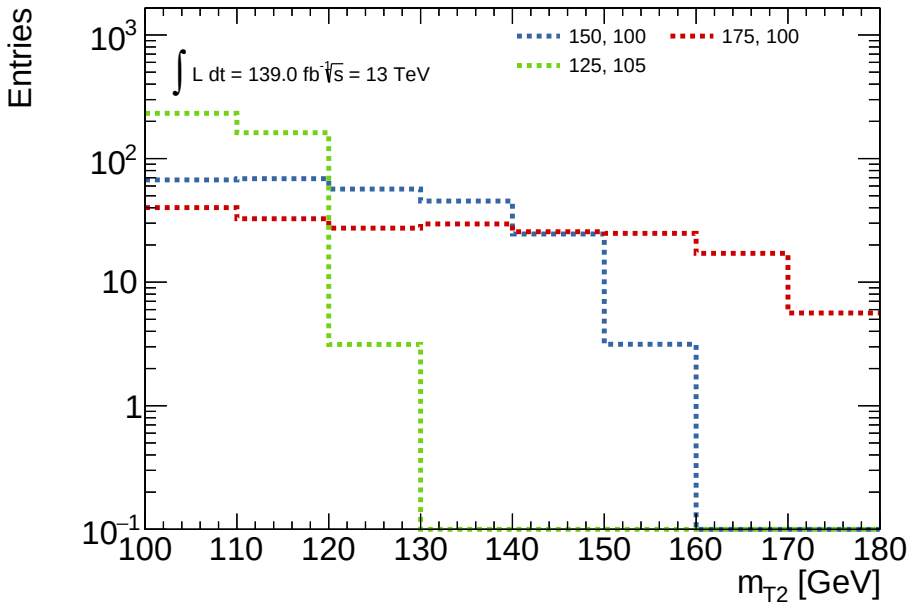

Figure 7.7: m_{T2} distribution for different slepton signal points.

The momentum of second invisible particle is given by the momentum of first invisible particle and $\boldsymbol{p}_{\mathrm{T}}^{\mathrm{miss}}$. m_{χ} is an assumed mass for the invisible particle. For m_{T2} a scan over all possible values for the momenta of the invisible particles is done [176].

The variable is constructed is such a way that if the mass parameter m_{χ} is chosen correctly the distribution of m_{T2} has a kinematic endpoint of the slepton mass. The lowest possible value of m_{T2} is the mass parameter. Therefore the width of the distribution corresponds to the mass splitting. Since the mass of the neutralino is not known, a mass parameter of 100 GeV is chosen. Therefore the endpoint of the distribution is only approximately the slepton mass. The m_{T2} distribution for different slepton signals is shown in Figure 7.7.

In order to increase the sensitivity to the considered signal points, the signal region is split in m_{T2} between 100 and 180 GeV into eight bins of equal size. The m_{T2} distribution in the signal region is shown in Figure 7.8.

7.5 Background Estimation

The SM background for the slepton search can be classified into two categories. The irreducible background consists of processes that produces the exact same final state as the considered signal,

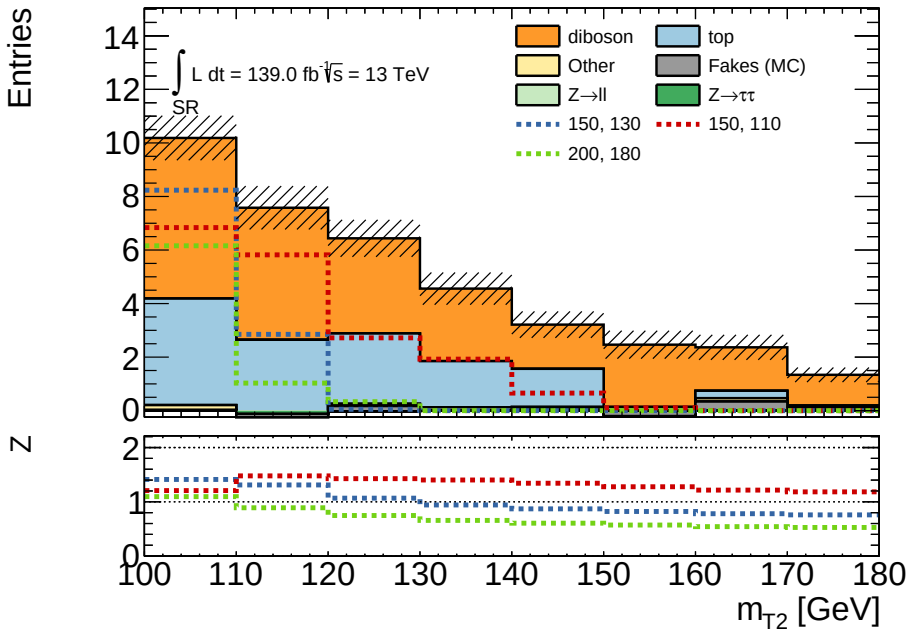

Figure 7.8: m_{T2} distribution in the signal region.

i.e. two same flavor opposite sign leptons with at least and $E_{\mathrm{T}}^{\mathrm{miss}} > 300$ GeV. The main contribution to the irreducible are from diboson and top production, where the latter includes $t\bar{t}$ and single top production. Further but minor contributions originates from $Z \to \tau\tau$ and $Z \to \ell\ell$ events. The second category is the reducible background in which at least one of the two leptons is a fake or non-prompt lepton. For the slepton search the main contribution to the reducible background comes from W+jets, where one lepton is a misidentified jet.

7.5.1 Irreducible background

The MC predictions for the dominant processes of the irreducible background, are normalized to data in dedicated CR. The selections for the two CRs are similar to the signal region selection. For the CR targeting the top background (CRtop), a b-jet is required instead of the b-veto of the signal region. For the diboson CR (CRVV) the cut on $m_T(\ell_2)$ is inverted. In order to increase the statistics in both CRs the cut on $E_{\mathrm{T}}^{\mathrm{miss}}$ is relaxed to $E_{\mathrm{T}}^{\mathrm{miss}} > 200$ GeV. Furthermore, also events with lepton pairs of different flavor, i.e. $e\mu$ events, are included. Figures 7.9 and 7.10 show the $E_{\mathrm{T}}^{\mathrm{miss}}$ and m_{T2} distributions in CRVV and CRtop. While CRtop is almost completely pure in top, CRVV has a purity of about 50%. However, the remaining non-diboson background in CRVV is dominantly from top, which is constrained by CRtop. Therefore, the comparable low purity in CRVV is not problematic. In

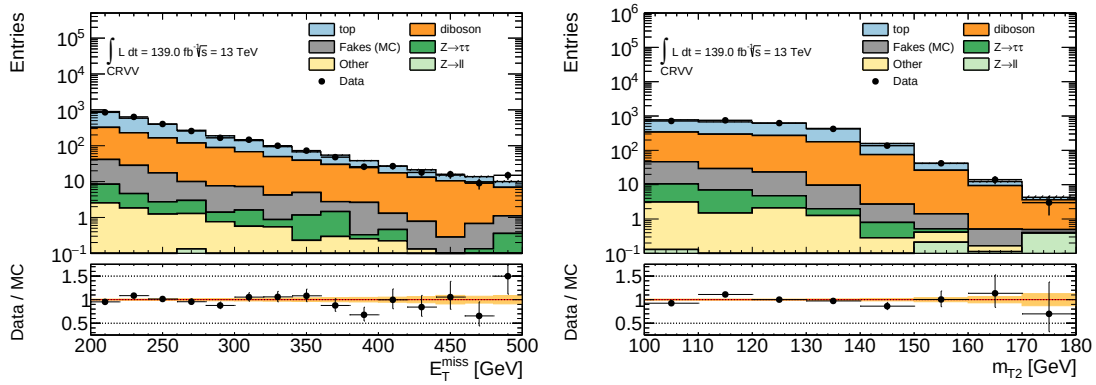

(a) $E_{\mathrm{T}}^{\mathrm{miss}}$ (b) m_{T2}

Figure 7.9: $E_{\mathrm{T}}^{\mathrm{miss}}$ and m_{T2} distributions in CRVV.

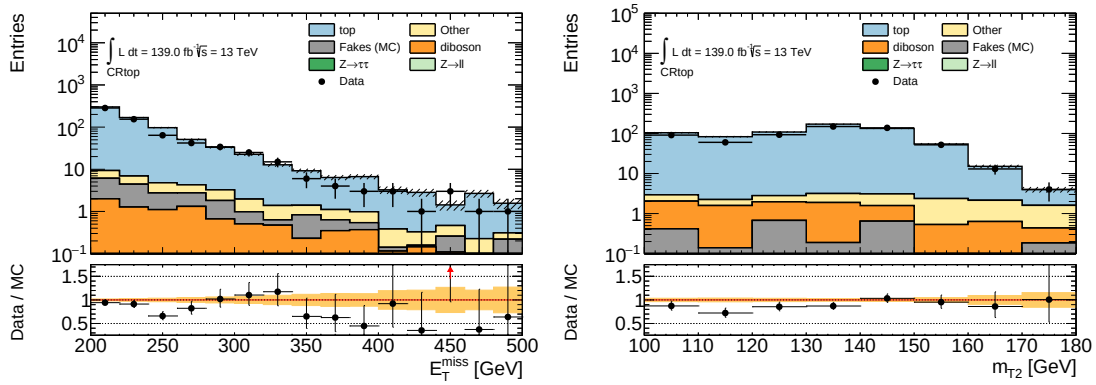

(a) $E_{\mathrm{T}}^{\mathrm{miss}}$ (b) m_{T2}

Figure 7.10: $E_{\mathrm{T}}^{\mathrm{miss}}$ and m_{T2} distributions in CRtop.

both regions a good agreement between data and MC is observed. The resulting normalization factors are 1.1 and 0.91 for diboson and top, respectively.

7.5.2 Reducible background

The reducible background is estimated using the fake factor method, similar to the approach described for the four-lepton search in section 6.6.2. Events from control regions, where one or both of leptons are not passing the signal requirements, are weighted with a fake factor. Similar to the approach described for the search in four-lepton events the reducible background is given by

$$N_{\mathrm{reducible}} = (N_{\mathrm{TL}}^{\mathrm{data}} - N_{\mathrm{TL}}^{\mathrm{MC}} + N_{\mathrm{LT}}^{\mathrm{data}} - N_{\mathrm{LT}}^{\mathrm{MC}})F - (N_{\mathrm{LL}}^{\mathrm{data}} - N_{\mathrm{LL}}^{\mathrm{MC}})F_1F_2 \tag{7.3}$$

where the L and T subscripts indicate if the leading or subleading lepton is a tight or loose lepton. The applied fake factors weight depends on the kinematic of the loose lepton. In case of events with two loose leptons, two fake factors, one for each lepton, are applied.

In contrast to the fake factor in the four lepton search, the fake factor for the slepton search is directly measured in data. The fake factor is measured with respect to p_{T}.

Two regions for measuring fake factors have been tested. The first region uses Z+jets events, in which the Z boson decays leptonically and an additional lepton is considered as fake lepton. For this region events are selected by lepton triggers and are required to have exactly three charged leptons. Two of the leptons are required to fulfill signal requirements and forming a same-flavor opposite-sign lepton pair with an invariant mass of $|m_{\ell\ell} - m_Z| < 10$ GeV. The third lepton, not consistent with a lepton from a Z boson decay, is assumed to be a fake lepton and can be either loose or signal quality. Contributions from other background processes are suppressed by requiring the events to have $E_{\mathrm{T}}^{\mathrm{miss}} < 60$ GeV and $m_{\mathrm{T}}(\ell_3) < 40$ GeV.

The p_{T} distributions of the selected fake lepton are shown in Figure 7.11. While the distribution for loose leptons is very pure in fakes over the whole p_{T} range, contributions from real leptons from diboson events became important at $p_{\mathrm{T}} > 20$ GeV for tight leptons.

The fake factors calculated using these distribution after substracting the contributions from real leptons are shown in Figure 7.12. The fake factor for electrons is about 0.2, decreases to 0.1 for $10 < p_{\mathrm{T}} < 40$ GeV and rises again at higher p_{T}. The muon fake factors rapidly decrease from 0.8 at low p_{T} to about 0.1 at high p_{T}.

The second region tested for the fake background estimation, uses multi-jet events selected by prescaled single-lepton triggers. As already described in section refsec:Trigger, prescaled trigger are triggers that are prescaled with a factor n selecting only every n-th event. Otherwise these triggers would exceed the trigger rate limit due to their lower p_{T} threshold and quality requirements compared to the unprescaled triggers. Using these triggers allows to select events with very loose quality criteria or very low p_{T}. The events are required exactly one lepton. To select events that are more similar to the events in the main analysis with an ISR topology, events are required to have at least one jet with $p_{\mathrm{T}} > 100$ GeV. Furthermore, events with b-jets are vetoed. Most events in this selection are assumed from multi-jet events in which the lepton is a fake lepton. The important background with a real prompt lepton in this region are from W+jets and $t\bar{t}$ events. Events with $m_{\mathrm{T}}(\ell) > 100$ GeV are used to normalize the background to data, while events with $m_{\mathrm{T}}(\ell) < 40$ GeV are used to calculate the fake factors.

The p_{T} distributions of the selected lepton is shown in Figure 7.13. While the distributions for loose leptons is very pure in fakes over the whole p_{T} range, contributions from real leptons from W+jets

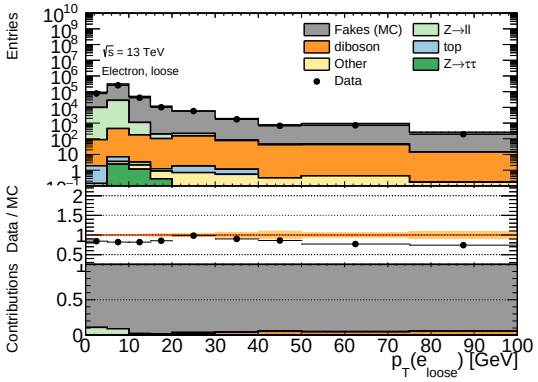

(a) Loose electrons

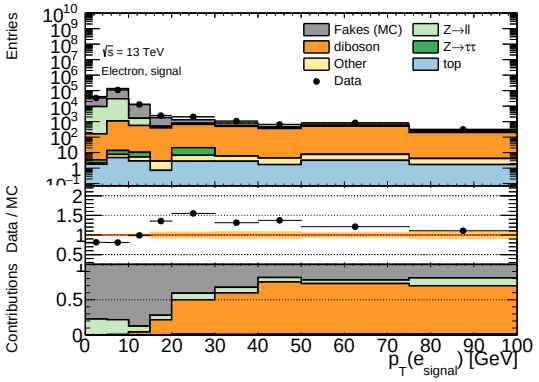

(b) Signal electrons

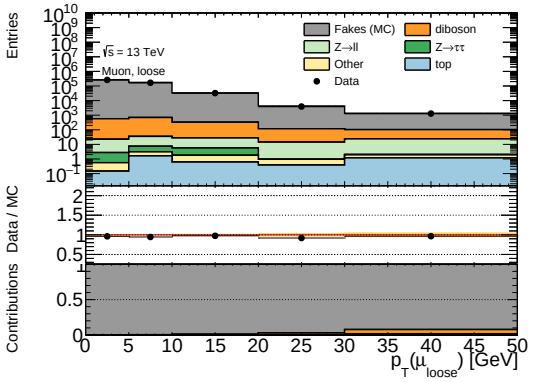

(c) Loose muons

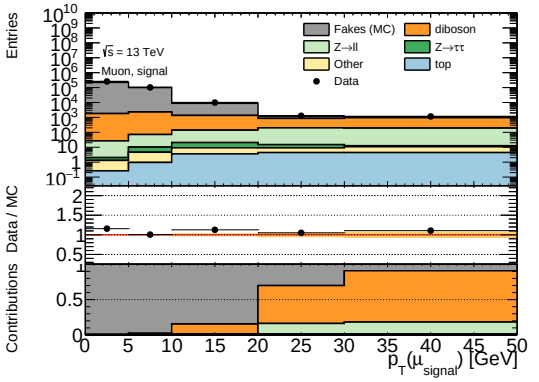

(d) Signal muons

Figure 7.11: p_{T} distribution of the selected fake lepton in the $Z\ell\ell$+fake region.

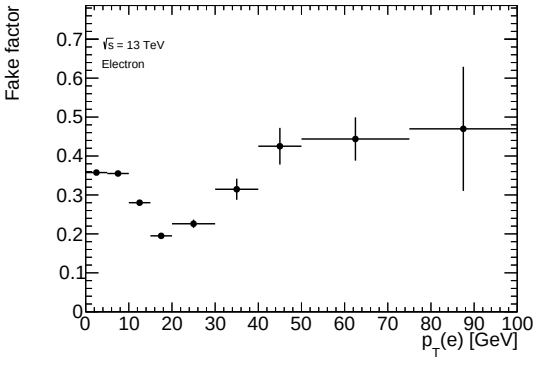

(a) Electrons

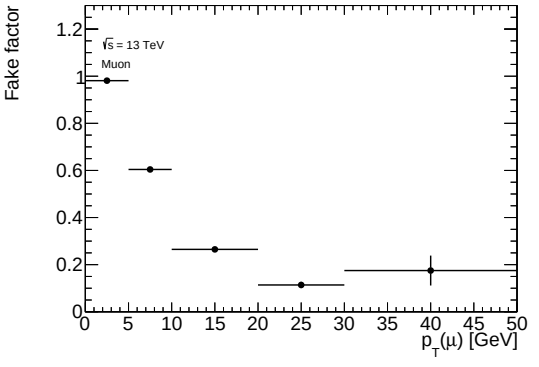

(b) Muons

Figure 7.12: Fake factor for electrons and muons in dependence of p_{T} estimated in the $Z\ell\ell$+fake region.

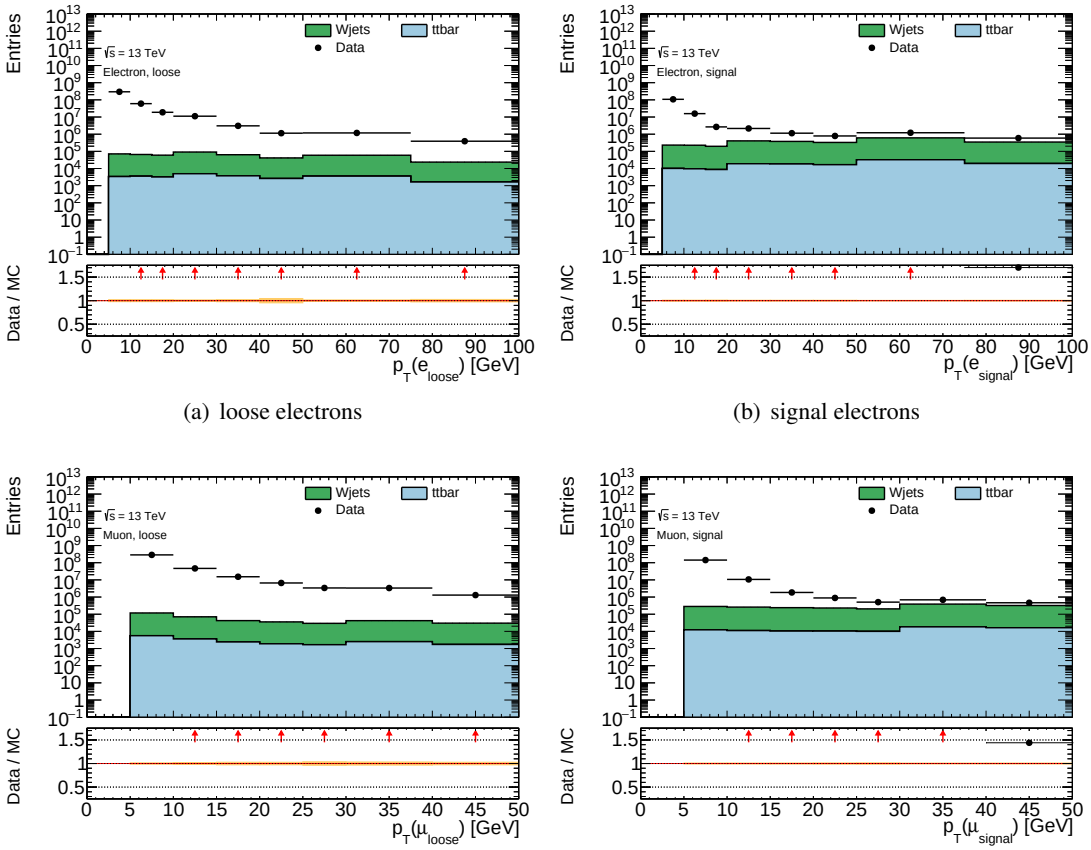

(a) loose electrons

(b) signal electrons

(c) loose muons

(d) signal muons

Figure 7.13: p_{T} distribution of the selected fake lepton in the QCD dijet region.

events contribute notably for $p_{\mathrm{T}} > 50$ GeV for tight leptons.

The fake factors calculated using these distribution after substracting the prompt-lepton contribution are shown in Figure 7.14. The fake factors for electrons are about 0.4 at low p_{T}, decrease to 0.1 for $10 < p_{\mathrm{T}} < 40$ GeV and increase to 0.8 at high p_{T}. The muon fake factors rapidly decreases from 0.5 at low p_{T} to about 0.1 at high p_{T}.

The estimation of the reducible background with the derived fake factors is validated in fake-enriched region. This VR is based on the preselection but requires a same-sign instead of an opposite-sign lepton pair. Since most processes of the irreducible background produces leptons with opposite charge and the charge of the fake lepton is independent of the charge of the other lepton, the region with same-sign leptons is enriched in reducible background.

The p_{T} distribution of the subleading lepton in this same sign validation region with the fake background estimated with fake factors calculated from the Z+jets and the multi-jet events, are shown

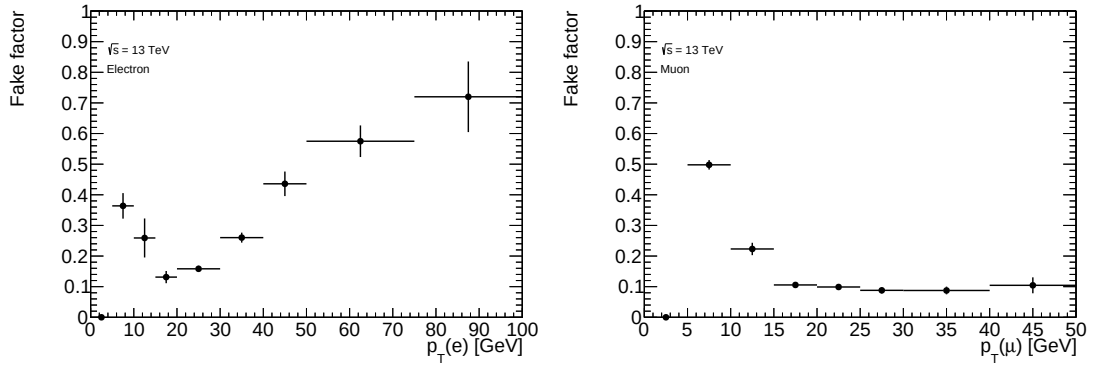

(a) electrons (b) muons

Figure 7.14: Fake factor for electrons and muons in dependence of p_{T} estimated in the QCD dijet region.

in Figure 7.15 and Figure 7.16, respectively. At low p_{T} the fake lepton estimate based on the Z+jets fake factors is underestimated by about 20-30%. The estimation of the fake lepton background based on the multi-jet fake factors performs significantly better in this p_{T} range. For muons the background for $p_{\mathrm{T}} > 30$ GeV is clearly underestimated in both appoaches. Only small contributions from fake muons are expected at high p_{T}. Studies indicate that this discrepancy originates from charge-flipped muons which are heavily underrepresented in the used MC simulation.

The comparison between the two approaches for the measurement of the fake factors, shows that the fake factors from multi-jet events perform better in the phase space targeted by this analysis and are hence used in the estimation for the fake lepton background. It is assumed that the origin of fake leptons in the multi-jet events is more similar to the origin in the signal region. In the Z+jets events fake leptons might for example stem much more likely from photon conversions which originate from the prompt leptons of the Z decay.

7.6 Sensitivity Reach

To quantify the sensitivity reach the analysis has to slepton production, the exclusion power to the considered SUSY models is estimated. For this the significance given in equation 7.1 is calculated using the predicted signal yield for each of the signal points. Assuming that the measured data corresponds to the background prediction, signal points with a significance of larger than 1.64 are expected to be excluded. As a rough estimation, one expects that signal points with a significance larger than 1.67 can be excluded in case no new physics are present in the data. The expected exclusion reach is shown in Figure 7.17 in the plane of of the slepton mass and the mass splitting as red line.

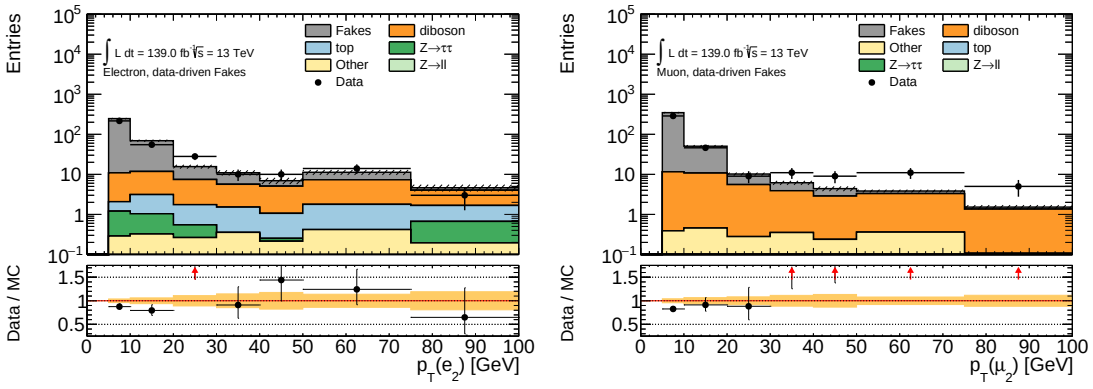

(a) electrons (b) muons

Figure 7.15: p_{T} distribution of the subleading lepton in the same sign validation region. The fake background is estimated using fake factors calculated from the $Z\ell\ell$+fake region.

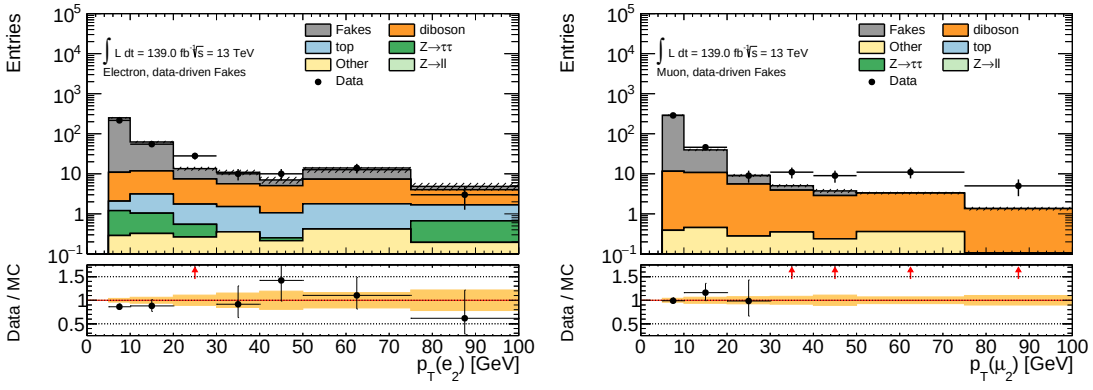

(a) electrons (b) muons

Figure 7.16: p_{T} distribution of the subleading lepton in the same sign validation region. The fake background is estimated using fake factors calculated from the QCD dijet region.

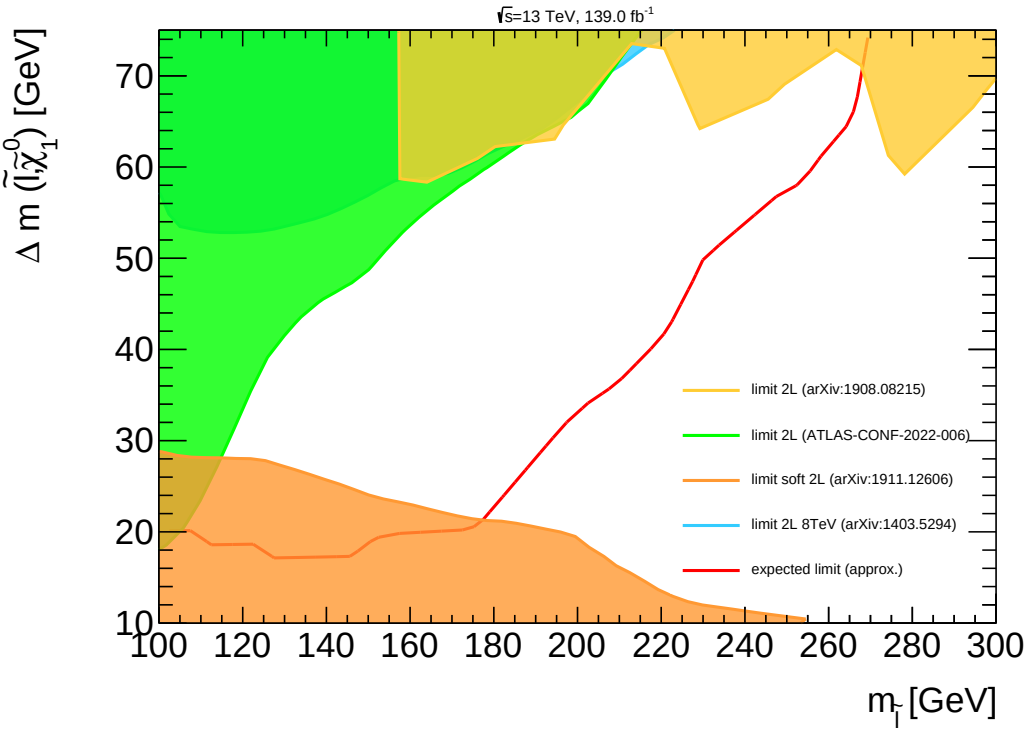

Figure 7.17: Expected limits (red line). The colored areas are excluded by previous searches [172–174, 177].

The colored areas show the exclusion limits from previous searches for sleptons. Sleptons with masses up to 260 GeV with mass splittings of 60 GeV and up to 180 GeV with mass splittings of 20 GeV are excluded. Hence, the current analysis promises sensitivity in the signal parameter space well beyond the current ATLAS constraints. The sensitivity decreases for lower mass splittings, but a re-optimization for lower mass splittings is possible. The limit for smuons-only will be less stringent but will still cover a notable portion of the phase space with valid SUSY solutions to the muon g-2 experiment results.

7.7 Summary

A search for sleptons in final states with two charged leptons, a jet from ISR and $E_{\mathrm{T}}^{\mathrm{miss}}$ using the full Run 2 dataset has been presented. The search targets a sensitivity gap for scenarios with mass splitting between 20 and 60 GeV that has not been covered by previous searches. The analysis has not been finalized, yet. Therefore, no results are available. But the search strategy, including the design of a signal region targeting the sensitivity gap as well as the strategy to estimate the dominant SM backgrounds from top, dibosons as well as from fake leptons has been presented. An estimation of the

expected limits shows that good sensitivity to the current sensitivity gap can be achieved. In order to finalize the analysis and unblind the data in the signal region, the systematic uncertainties have to be estimated and the remaining problems in the estimation of the fake muon background have to be understood.

CHAPTER EIGHT

CONCLUSIONS

This thesis presented the construction of new small-diameter Monitored Drift Tube (sMDT) chambers for the upgrade of the ATLAS Muon Spectrometer for the High Luminosity LHC, as well two analyses to search for physics beyond the SM. Both searches have been optimized for models of SUSY a well-studied extension of the SM, and have been performed using proton-proton collisions at $\sqrt{s}$ = 13 TeV at the LHC recorded by the ATLAS experiment during the Run 2 in 2015–2018. The first search considered final states with at least four charged leptons. The second search targeted sleptons in final states in final states with two charged leptons and a jet from initial-state radiation (ISR).

The current MDT chambers in the small sectors of the inner layer of the central part of the MS will be replaced by new thinner sMDT chambers that are integrated with new RPC trigger chambers. The drift tubes of the sMDT chambers have half the diameter compared to the drift tubes of the MDT, which increases the background capability. 16 BIS78 chambers were built between 2017 and 2019 at the MPI and were installed at the edges of the barrel inner layer in 2020 for the Run 3 of the LHC. The production of the 96 BIS1-6 chambers is still ongoing with the two production sites at MPI and in Michigan each constructing half of the chambers. As of september 2022 40 and 26 chambers have been produced at MPI and in Michigan, respectively. MPI will finish the assembly end of 2022, while the production in Michigan will be finished in 2023. The BIS1-6 chambers will be installed during the long shutdown 3 of the LHC in 2026-2028. The thesis focuses on the mechanical measurements of the chamber geometry, which includes the measurement of the positions of the platforms for alignment sensors as well as the measurement of the positions of the sense wires. The measurements show that the platforms for the alignment sensors are positioned within ±0.1 mm of the nominal positions. The measured sense wire positioning accuracy is about 10 μm which is well below the requirement of < 20 μm. So far all assembled chamber fulfill the requirements.

The search for SUSY in final states with at least four charged leptons targets general gauge mediated (GGM) SUSY models where pair produced higgsinos decay into a gravitino and a Z or Higgs boson, as well as R-parity violating (RPV) SUSY models where the lightest neutralino $\tilde{\chi}_1^0$ decays into two charged leptons and a neutrino. In the latter case, the pair production of winos, sleptons and gluinos

have been considered. Scenarios for the RPV coupling are distinguished. In the first scenario the LSP decays only into electrons and muons, while in the second case the LSP decays dominantly into τ leptons. Furthermore, an additional region selecting five charged light leptons has been defined, which is model agnostic, but is used for a general search for new physics in five-lepton final states. The dominant irreducible backgrounds from ZZ and $t\bar{t}Z$ are normalized to data in dedicated CRs. The background from fake and non-prompt leptons, dominantly originating from $t\bar{t}$ and Z+jets are estimated from data using the fake factor method, where the fake factors are derived from Monte Carlo and are corrected to data for the most important fake types. The observations are in agreement with the SM expectations and exclusion limits at 95% confidence level were derived. In the RPV models, for the case of the LSP decaying only into light leptons, gluino, wino and slepton masses up to 2.5 TeV, 1.6 TeV and 1.2 TeV have been excluded, respectively. For the scenario of the LSP decaying dominantly into τ leptons the corresponding limits are up to 1.8 TeV, 1.1 TeV and 0.87 TeV, respectively. This improves upon previous limits by around 100-350 GeV. F For the GGM model higgsino masses up to 540 GeV are excluded, improving upon previous limits by around 200–260 GeV. The sensitivity decreases with increasing branching ratios of the higgsino decaying into Higgs bosons. In comparison to other analyses, the four-lepton search excluded the region of phase space with low higgsino masses and high branching ratios of the higgsino decaying into Z bosons [170]. A search in final states with at least three b-jets excluded scenarios with high branching ratios of the higgsino decaying into Higgs boson [167]. A search in final states with two hadroncally decaying bosons is sensitive to higher higgsino masses but looses sensitivity at low higgsino masses, where the four-lepton search is sensitive [168]. So both searches are complementary to the four-lepton search. A search in final states with two leptons excluded approximately the phase space covered by the four-lepton search and the search in final states with two hadronically decaying bosons [169]. The results of the four-lepton search have been published in Ref. [123].

The searches for sleptons are of particular interest as SUSY scenarios featuring light smuons are capable of providing an explanation for the observed deviation of the measured anomalous magnetic moment of the muon from the SM prediction. Sleptons have been already targeted in previous searches, using simplified models of slepton pair production in which the slepton decays into a SM and the $\tilde{\chi}_1^0$, but there is still a gap in sensitivity remaining for mass differences between the slepton and the LSP (mass splitting) between 20 and 60 GeV which is targeted with this analysis. The analysis focuses on final states where a jet from ISR boosts the slepton system which allows to utilize $E_{\mathrm{T}}^{\mathrm{miss}}$ trigger to select the events. A signal region optimized for signals in the sensitivity gap was designed. Most important backgrounds originate from top and diboson processes which are normalized to data in dedicated CRs. The background from fake and non-prompt leptons is estimated directly from data. The signal region promises good sensitivity within the mass gap. Slepton masses up to 260 GeV at a mass splittings between 20 and 60 GeV fall into the expected exclusion reach. In order to finalize the

analysis the systematic uncertainties have to be estimated and the remaining problems in the estimation of the fake muon background have to be understood.

With the start of the Run 3 of the LHC more collision data will be collected in the next years. For both of the searches discussed in this thesis, it is expected that with an increased dataset the sensitivity to higher SUSY masses can be gained and the exclusion limits can be extended.

BIBLIOGRAPHY

[1] ATLAS Collaboration, G. Aad et al., *Observation of a new particle in the search for the Standard Model Higgs boson with the ATLAS detector at the LHC*, Phys. Lett. B **716** (2012) 1, arXiv: 1207.7214.

[2] CMS Collaboration,
Observation of a new boson at a mass of 125 GeV with the CMS experiment at the LHC,
Phys. Lett. B **716** (2012) 30, arXiv: 1207.7235.

[3] I. Zurbano Fernandez et al.,
High-Luminosity Large Hadron Collider (HL-LHC): Technical design report,
10/2020 (2020), ed. by I. Béjar Alonso et al.,
URL: https://cds.cern.ch/record/2749422.

[4] L. Rossi and O. Brüning, *High Luminosity Large Hadron Collider: A description for the European Strategy Preparatory Group*, tech. rep., CERN, 2012,
URL: https://cds.cern.ch/record/1471000.

[5] S. Weinberg, *A Model of Leptons*, Phys. Rev. Lett. **19** (21 1967) 1264,
URL: https://link.aps.org/doi/10.1103/PhysRevLett.19.1264.

[6] S. L. Glashow, *Partial-symmetries of weak interactions*, Nuclear Physics **22** (1961) 579,
ISSN: 0029-5582, URL:
https://www.sciencedirect.com/science/article/pii/0029558261904692.

[7] A. Salam, *Weak and Electromagnetic Interactions*, Conf. Proc. **C680519** (1968) 367.

[8] M. E. Peskin and D. V. Schroeder,
An Introduction To Quantum Field Theory (Frontiers in Physics), Westview Press, 1995,
ISBN: 0201503972.

[9] D. J. Griffiths, *Introduction to elementary particles; 2nd rev. version*, Physics textbook, Wiley, 2008.

[10] W. Hollik, 'Quantum field theory and the Standard Model', *2009 European School of High-Energy Physics*, 2010, arXiv: 1012.3883.

[11] M. Gell-Mann, *A schematic model of baryons and mesons*, Physics Letters **8** (1964) 214, ISSN: 0031-9163, URL: https://www.sciencedirect.com/science/article/pii/S0031916364920013.

[12] K. G. Wilson, *Confinement of quarks*, Phys. Rev. D **10** (8 1974) 2445, URL: https://link.aps.org/doi/10.1103/PhysRevD.10.2445.

[13] R. Pasechnik and M. Šumbera, *Phenomenological Review on Quark–Gluon Plasma: Concepts vs. Observations*, Universe **3** (2017) 7, arXiv: 1611.01533.

[14] *Observation of $J/\psi\phi$ Structures Consistent with Exotic States from Amplitude Analysis of $B^+ \to J/\psi\phi K^+$ Decays*, Phys. Rev. Lett. **118** (2 2017) 022003, URL: https://link.aps.org/doi/10.1103/PhysRevLett.118.022003.

[15] *Amplitude analysis of $B^+ \to J/\psi\phi K^+$ decays*, Phys. Rev. D **95** (1 2017) 012002, URL: https://link.aps.org/doi/10.1103/PhysRevD.95.012002.

[16] *Evidence for Exotic Hadron Contributions to $\Lambda_b^0 \to J/\psi p\pi^-$ Decays*, Phys. Rev. Lett. **117** (8 2016) 082003, URL: https://link.aps.org/doi/10.1103/PhysRevLett.117.082003.

[17] F. Englert and R. Brout, *Broken Symmetry and the Mass of Gauge Vector Mesons*, Phys. Rev. Lett. **13** (9 1964) 321, URL: https://link.aps.org/doi/10.1103/PhysRevLett.13.321.

[18] P. W. Higgs, *Broken Symmetries and the Masses of Gauge Bosons*, Phys. Rev. Lett. **13** (16 1964) 508, URL: https://link.aps.org/doi/10.1103/PhysRevLett.13.508.

[19] P. W. Higgs, *Spontaneous Symmetry Breakdown without Massless Bosons*, Phys. Rev. **145** (4 1966) 1156, URL: https://link.aps.org/doi/10.1103/PhysRev.145.1156.

[20] N. Cabibbo, *Unitary Symmetry and Leptonic Decays*, Phys. Rev. Lett. **10** (12 1963) 531, URL: https://link.aps.org/doi/10.1103/PhysRevLett.10.531.

[21] M. Kobayashi and T. Maskawa, *CP Violation in the Renormalizable Theory of Weak Interaction*, Prog. Theor. Phys. **49** (1973) 652.

[22] Y. Fukuda et al., *Evidence for oscillation of atmospheric neutrinos*, Phys. Rev. Lett. **81** (1998) 1562, arXiv: hep-ex/9807003.

[23] Q. R. Ahmad et al., *Direct evidence for neutrino flavor transformation from neutral current interactions in the Sudbury Neutrino Observatory*, Phys. Rev. Lett. **89** (2002) 011301, arXiv: nucl-ex/0204008.

[24] I. Esteban, M. C. Gonzalez-Garcia, A. Hernandez-Cabezudo, M. Maltoni and T. Schwetz, *Global analysis of three-flavour neutrino oscillations: synergies and tensions in the determination of θ_{23}, δ_{CP}, and the mass ordering*, JHEP **01** (2019) 106, arXiv: 1811.05487.

[25] M. Aker et al., *Improved Upper Limit on the Neutrino Mass from a Direct Kinematic Method by KATRIN*, Phys. Rev. Lett. **123** (2019) 221802, arXiv: 1909.06048.

[26] F. Zwicky, *Republication of: The redshift of extragalactic nebulae*, English, General Relativity and Gravitation **41** (2009) 207, ISSN: 0001-7701.

[27] K. G. Begeman, A. H. Broeils and R. H. Sanders, *Extended rotation curves of spiral galaxies: dark haloes and modified dynamics*, Monthly Notices of the Royal Astronomical Society **249** (1991) 523, ISSN: 0035-8711.

[28] G. Bertone, D. Hooper and J. Silk, *Particle dark matter: Evidence, candidates and constraints*, Phys. Rept. **405** (2005) 279, arXiv: hep-ph/0404175.

[29] P. A. R. Ade et al., *Planck 2015 results. XIII. Cosmological parameters*, Astron. Astrophys. **594** (2016) A13, arXiv: 1502.01589.

[30] R. L. Workman, *Review of Particle Physics*, PTEP **2022** (2022) 083C01.

[31] G. W. Bennett et al., *Final Report of the Muon E821 Anomalous Magnetic Moment Measurement at BNL*, Phys. Rev. D **73** (2006) 072003, arXiv: hep-ex/0602035.

[32] B. Abi et al., *Measurement of the Positive Muon Anomalous Magnetic Moment to 0.46 ppm*, Phys. Rev. Lett. **126** (2021) 141801, arXiv: 2104.03281.

[33] S. P. Martin, *A Supersymmetry primer*, Adv. Ser. Direct. High Energy Phys. **18** (1998) 1, ed. by G. L. Kane, arXiv: hep-ph/9709356.

[34] D. Volkov and V. Akulov, *Is the neutrino a goldstone particle?*, Physics Letters B **46** (1973) 109, ISSN: 0370-2693.

[35] A. Salam and J. Strathdee, *Super-symmetry and non-Abelian gauges*, Physics Letters B **51** (1974) 353, ISSN: 0370-2693.

[36] J. Wess and B. Zumino, *Supergauge invariant extension of quantum electrodynamics*, Nuclear Physics B **78** (1974) 1, ISSN: 0550-3213.

[37] J. Wess and B. Zumino, *Supergauge transformations in four dimensions*, Nuclear Physics B **70** (1974) 39, ISSN: 0550-3213.

[38] S. Ferrara and B. Zumino, *Supergauge invariant Yang-Mills theories*, Nuclear Physics B **79** (1974) 413, ISSN: 0550-3213.

[39] K. Abe et al., *Search for proton decay via $p \to e^+\pi^0$ and $p \to \mu^+\pi^0$ in 0.31 megaton·years exposure of the Super-Kamiokande water Cherenkov detector*, Phys. Rev. D **95** (2017) 012004, arXiv: 1610.03597.

[40] R. Barbier et al., *R-parity violating supersymmetry*, Phys. Rept. **420** (2005) 1, arXiv: hep-ph/0406039.

[41] L. Evans and P. Bryant, *LHC Machine*, JINST **3** (2008) S08001.

[42] ATLAS Collaboration, G. Aad et al., *The ATLAS Experiment at the CERN Large Hadron Collider*, JINST **3** (2008) S08003.

[43] CMS Collaboration, *The CMS experiment at the CERN LHC*, JINST **3** (2008) S08004.

[44] *The LHCb Detector at the LHC*, JINST **3** (2008) S08005.

[45] *The ALICE experiment at the CERN LHC. A Large Ion Collider Experiment*, JINST **3** (2008) S08002. 259 p, Also published by CERN Geneva in 2010, URL: http://cds.cern.ch/record/1129812.

[46] ATLAS Collaboration, G. Aad et al., *ATLAS data quality operations and performance for 2015–2018 data-taking*, JINST **15** (2020) P04003, arXiv: 1911.04632.

[47] E. Mobs, *The CERN accelerator complex. Complexe des accélérateurs du CERN*, (2016), General Photo, URL: https://cds.cern.ch/record/2197559.

[48] *Luminosity Public Results Run2*, URL: https://twiki.cern.ch/twiki/bin/view/AtlasPublic/LuminosityPublicResultsRun2 (visited on 15/08/2022).

[49] J. Pequenao, 'Computer generated image of the ATLAS inner detector', 2008, URL: https://cds.cern.ch/record/1095926.

[50] K. Potamianos, *The upgraded Pixel detector and the commissioning of the Inner Detector tracking of the ATLAS experiment for Run-2 at the Large Hadron Collider*, PoS **EPS-HEP2015** (2015) 261, arXiv: 1608.07850.

[51] M. Capeans et al., *ATLAS Insertable B-Layer Technical Design Report*, (2010), URL: https://cds.cern.ch/record/1291633.

[52] B. Abbott et al., *Production and Integration of the ATLAS Insertable B-Layer*, JINST **13** (2018) T05008, arXiv: 1803.00844.

[53] ATLAS Collaboration, M. Aaboud et al., *Performance of the ATLAS Transition Radiation Tracker in Run 1 of the LHC: tracker properties*, JINST **12** (2017) P05002, arXiv: 1702.06473.

[54] *Particle Identification Performance of the ATLAS Transition Radiation Tracker*, (2011).

[55] A. Vogel, *ATLAS Transition Radiation Tracker (TRT): Straw tube gaseous detectors at high rates*, Nuclear Instruments and Methods in Physics Research Section A: Accelerators, Spectrometers, Detectors and Associated Equipment **732** (2013) 277, Vienna Conference on Instrumentation 2013, ISSN: 0168-9002.

[56] A. Airapetian et al., *ATLAS calorimeter performance Technical Design Report*, (1996), URL: https://cds.cern.ch/record/331059.

[57] *ATLAS liquid argon calorimeter: Technical design report*, (1996), URL: https://cds.cern.ch/record/331061.

[58] *ATLAS tile calorimeter: Technical design report*, (1996), URL: https://cds.cern.ch/record/331062.

[59] *ATLAS muon spectrometer: Technical design report*, (1997).

[60] ATLAS Collaboration, G. Aad et al., *Performance of electron and photon triggers in ATLAS during LHC Run 2*, Eur. Phys. J. C **80** (2020) 47, arXiv: 1909.00761.

[61] ATLAS Collaboration, G. Aad et al., *Performance of the ATLAS muon triggers in Run 2*, JINST **15** (2020) P09015, arXiv: 2004.13447.

[62] ATLAS Collaboration, M. Aaboud et al., *Performance of the ATLAS Trigger System in 2015*, Eur. Phys. J. C **77** (2017) 317, arXiv: 1611.09661.

[63] *Trigger monitoring and rate predictions using Enhanced Bias data from the ATLAS Detector at the LHC*, tech. rep., CERN, 2016, URL: https://cds.cern.ch/record/2223498.

[64] *Trigger Menu in 2016*, tech. rep., CERN, 2017, URL: https://cds.cern.ch/record/2242069.

[65] *Trigger Menu in 2017*, tech. rep., CERN, 2018, URL: https://cds.cern.ch/record/2625986.

[66] J. Pequenao and P. Schaffner,
'How ATLAS detects particles: diagram of particle paths in the detector', 2013,
URL: https://cds.cern.ch/record/1505342.

[67] *Performance of the ATLAS Inner Detector Track and Vertex Reconstruction in the High Pile-Up LHC Environment*, tech. rep., CERN, 2012,
URL: https://cds.cern.ch/record/1435196.

[68] M. Aaboud et al., *Performance of the ATLAS Track Reconstruction Algorithms in Dense Environments in LHC Run 2*, Eur. Phys. J. C **77** (2017) 673, arXiv: 1704.07983.

[69] *Track Reconstruction Performance of the ATLAS Inner Detector at* $\sqrt{s} = 13$ *TeV*, tech. rep., CERN, 2015, URL: https://cds.cern.ch/record/2037683.

[70] T. Cornelissen et al., *The new ATLAS track reconstruction (NEWT)*,
J. Phys. Conf. Ser. **119** (2008) 032014, ed. by R. Sobie, R. Tafirout and J. Thomson.

[71] R. Frühwirth, *Application of Kalman filtering to track and vertex fitting*,
Nuclear Instruments and Methods in Physics Research Section A: Accelerators, Spectrometers, Detectors and Associated Equipment **262** (1987) 444, ISSN: 0168-9002.

[72] G. Aad et al., *A neural network clustering algorithm for the ATLAS silicon pixel detector*,
JINST **9** (2014) P09009, arXiv: 1406.7690.

[73] *Vertex Reconstruction Performance of the ATLAS Detector at* $\sqrt{s} = 13$ *TeV*, tech. rep., CERN, 2015, URL: https://cds.cern.ch/record/2037717.

[74] G. Piacquadio, K. Prokofiev and A. Wildauer,
Primary vertex reconstruction in the ATLAS experiment at LHC,
Journal of Physics: Conference Series **119** (2008) 032033.

[75] ATLAS Collaboration, M. Aaboud et al., *Electron and photon energy calibration with the ATLAS detector using 2015–2016 LHC proton-proton collision data*,
JINST **14** (2019) P03017, arXiv: 1812.03848.

[76] ATLAS Collaboration, G. Aad et al., *Electron and photon performance measurements with the ATLAS detector using the 2015–2017 LHC proton-proton collision data*,
JINST **14** (2019) P12006, arXiv: 1908.00005.

[77] ATLAS Collaboration, G. Aad et al., *Muon reconstruction and identification efficiency in ATLAS using the full Run 2 pp collision data set at* $\sqrt{s} = 13$ *TeV*,
Eur. Phys. J. C **81** (2021) 578, arXiv: 2012.00578.

[78] M. Cacciari, G. P. Salam and G. Soyez, *The anti-k_t jet clustering algorithm*,
JHEP **04** (2008) 063, arXiv: 0802.1189.

[79] ATLAS Collaboration, G. Aad et al., *Jet energy scale and resolution measured in proton–proton collisions at $\sqrt{s}$ = 13 TeV with the ATLAS detector*, Eur. Phys. J. C **81** (2021) 689, arXiv: 2007.02645.

[80] ATLAS Collaboration, M. Aaboud et al., *Jet reconstruction and performance using particle flow with the ATLAS Detector*, Eur. Phys. J. C **77** (2017) 466, arXiv: 1703.10485.

[81] ATLAS Collaboration, G. Aad et al., *Topological cell clustering in the ATLAS calorimeters and its performance in LHC Run 1*, Eur. Phys. J. C **77** (2017) 490, arXiv: 1603.02934.

[82] *Tagging and suppression of pileup jets*, (2014), URL: https://cds.cern.ch/record/1700870.

[83] ATLAS Collaboration, G. Aad et al., *ATLAS b-jet identification performance and efficiency measurement with $t\bar{t}$ events in pp collisions at $\sqrt{s}$ = 13 TeV*, Eur. Phys. J. C **79** (2019) 970, arXiv: 1907.05120.

[84] *Measurement of the tau lepton reconstruction and identification performance in the ATLAS experiment using pp collisions at $\sqrt{s}$ = 13 TeV*, tech. rep., CERN, 2017, URL: https://cds.cern.ch/record/2261772.

[85] *Identification of hadronic tau lepton decays using neural networks in the ATLAS experiment*, tech. rep., CERN, 2019, URL: https://cds.cern.ch/record/2688062.

[86] *E_T^{miss} performance in the ATLAS detector using 2015-2016 LHC p-p collisions*, tech. rep., CERN, 2018, URL: https://cds.cern.ch/record/2625233.

[87] ATLAS Collaboration, M. Aaboud et al., *Evidence for the associated production of the Higgs boson and a top quark pair with the ATLAS detector*, Phys. Rev. D **97** (2018) 072003, arXiv: 1712.08891.

[88] A. Buckley et al., *General-purpose event generators for LHC physics*, Phys. Rept. **504** (2011) 145, arXiv: 1101.2599.

[89] J. C. Collins, D. E. Soper and G. Sterman, *Factorization of Hard Processes in QCD*, 2004, arXiv: hep-ph/0409313.

[90] A. D. Martin, W. J. Stirling, R. S. Thorne and G. Watt, *Parton distributions for the LHC*, The European Physical Journal C **63** (2009) 189, ISSN: 1434-6052.

[91] A. D. Martin, W. J. Stirling, R. S. Thorne and G. Watt, *Heavy-quark mass dependence in global PDF analyses and 3- and 4-flavour parton distributions*, The European Physical Journal C **70** (2010) 51, ISSN: 1434-6052.

[92] A. D. Martin, W. J. Stirling, R. S. Thorne and G. Watt, *Uncertainties on α_S in global PDF analyses and implications for predicted hadronic cross sections*, The European Physical Journal C **64** (2009) 653, ISSN: 1434-6052.

[93] H.-L. Lai, M. Guzzi, J. Huston, Z. Li, P. M. Nadolsky et al., *New parton distributions for collider physics*, Phys. Rev. D **82** (2010) 074024, arXiv: 1007.2241.

[94] R. D. Ball et al., *Parton distributions with LHC data*, Nucl. Phys. B **867** (2013) 244, arXiv: 1207.1303.

[95] R. D. Ball et al., *Parton distributions for the LHC Run II*, JHEP **04** (2015) 040, arXiv: 1410.8849.

[96] S. Agostinelli et al., *GEANT4 – a simulation toolkit*, Nucl. Instrum. Meth. A **506** (2003) 250.

[97] M. Beckingham et al., *The simulation principle and performance of the ATLAS fast calorimeter simulation FastCaloSim*, (2010), URL: https://cds.cern.ch/record/1300517.

[98] *Sherpa and Open Science Grid: Predicting the emergence of jets*, URL: https://sciencenode.org/feature/sherpa-and-open-science-grid-predicting-emergence-jets.php (visited on 15/08/2022).

[99] T. Gleisberg et al., *Event generation with SHERPA 1.1*, JHEP **02** (2009) 007, arXiv: 0811.4622.

[100] T. Kawamoto et al., *New Small Wheel Technical Design Report*, tech. rep., 2013, URL: https://cds.cern.ch/record/1552862.

[101] *Technical Design Report for the Phase-II Upgrade of the ATLAS Muon Spectrometer*, tech. rep., CERN, 2017, URL: https://cds.cern.ch/record/2285580.

[102] C. Ferretti and H. Kroha, *Upgrades of the ATLAS Muon Spectrometer with sMDT Chambers*, Nucl. Instrum. Meth. A **824** (2016) 538, arXiv: 1603.09544.

[103] P. Gadow, O. Kortner, H. Kroha and R. Richter, *Precision Muon Tracking Detectors for High-Energy Hadron Colliders*, Nucl. Instrum. Meth. A **845** (2017) 246, arXiv: 1603.08765.

[104] H. Kroha, O. Kortner, K. Schmidt-Sommerfeld and E. Takasugi, 'Performance of New High-Precision Muon Tracking Detectors for the ATLAS Experiment.', 2016 IEEE Nuclear Science Symposium, Strasbourg, France, November 2016, 2017, arXiv: 1701.08971.

[105] H. Kroha, O. Kortner, K. Schmidt-Sommerfeld and E. Takasugi, *Construction and Test of New Precision Drift-Tube Chambers for the ATLAS Muon Spectrometer*, Nucl. Instrum. Meth. A **845** (2017) 244, arXiv: 1603.08760.

[106] H. Kroha, R. Fakhrutdinov and A. Kozhin, *New High-Precision Drift-Tube Detectors for the ATLAS Muon Spectrometer*, JINST **12** (2017) C06007, arXiv: 1705.05656.

[107] H. Kroha, *Design and construction of integrated small-diameter drift tube and thin-gap resistive plate chambers for the phase-1 upgrade of the ATLAS muon spectrometer*, Nuclear Instruments and Methods in Physics Research Section A: Accelerators, Spectrometers, Detectors and Associated Equipment **936** (2019) 445, Frontier Detectors for Frontier Physics: 14th Pisa Meeting on Advanced Detectors, ISSN: 0168-9002.

[108] O. Kortner et al., *Upgrades of the ATLAS muon spectrometer with new small-diameter drift tube chambers*, Nuclear Instruments and Methods in Physics Research Section A: Accelerators, Spectrometers, Detectors and Associated Equipment **936** (2019) 509, Frontier Detectors for Frontier Physics: 14th Pisa Meeting on Advanced Detectors, ISSN: 0168-9002.

[109] P. Rieck, *Design, construction and test of small-diameter Muon Drift Tube chambers (sMDT) for the Phase-1 upgrade of the ATLAS muon spectrometer*, Nucl. Instrum. Meth. A **958** (2020) 162791.

[110] G. Eberwein et al., *High-precision large-area muon tracking and triggering with drift-tube chambers at future colliders*, Nuclear Instruments and Methods in Physics Research Section A: Accelerators, Spectrometers, Detectors and Associated Equipment **1044** (2022) 167482, ISSN: 0168-9002.

[111] K. R. Schmidt-Sommerfeld, 'Study of Muon Drift Tube Detectors and Fast Readout Electronics for Very High Counting Rates', PhD thesis: Munich, Tech. U., 2020, URL: https://cds.cern.ch/record/2713422.

[112] *High Luminosity LHC Project*, URL: https://hilumilhc.web.cern.ch/content/hl-lhc-project (visited on 13/10/2022).

[113] W. R. Leo, *Techniques for nuclear and particle physics experiments: a how-to approach; 2nd ed.* Springer, 1994, ISBN: 3540572805.

[114] W. Diethorn, *A Methane Proportional Counter System for Natural Radiocarbon Measurements*, 1956.

[115] S. Aefsky et al., *The Optical Alignment System of the ATLAS Muon Spectrometer Endcaps*, Journal of Instrumentation **3** (2008) P11005.

[116] J. C. Barriere et al., *The alignment system of the barrel part of the ATLAS muon spectrometer*, tech. rep., CERN, 2008, URL: https://cds.cern.ch/record/1081769.

[117] M. Beker et al., *The Rasnik 3-point optical alignment system*, Journal of Instrumentation **14** (2019) P08010.

[118] C. Amelung, *ARAMyS - Alignment reconstruction software for the ATLAS muon spectrometer*, Nuclear Physics B - Proceedings Supplements **172** (2007) 132.

[119] G. H. Eberwein et al., 'Commissioning and installation of the new small-Diameter Muon Drift Tube (sMDT) detectors for the Phase-I upgrade of the ATLAS Muon Spectrometer', *2021 IEEE Nuclear Science Symposium (NSS) and Medical Imaging Conference (MIC) and 28th International Symposium on Room-Temperature Semiconductor Detectors*, 2021, arXiv: 2112.07026.

[120] *sMDT Chamber Parameter Book*, URL: https://wwwatlas.mpp.mpg.de/ftp/outgoing/sMDT/sMDT_ATLAS_param_v1.5.pdf (visited on 06/10/2022).

[121] P. Schwegler, 'High-Rate Performance of Muon Drift Tube Detectors', PhD thesis: Munich, Tech. U., 2014.

[122] *ATLAS sMDT Phase-2 Upgrade Quality Control*, URL: https://atlas-mdt-phase2-qc.web.cern.ch (visited on 20/09/2022).

[123] ATLAS Collaboration, G. Aad et al., *Search for supersymmetry in events with four or more charged leptons in 139 fb^{-1} of $\sqrt{s}$ = 13 TeV pp collisions with the ATLAS detector*, JHEP **07** (2021) 167, arXiv: 2103.11684.

[124] ATLAS Collaboration, M. Aaboud et al., *Search for supersymmetry in events with four or more leptons in $\sqrt{s}$ = 13 TeV pp collisions with ATLAS*, Phys. Rev. D **98** (2018) 032009, arXiv: 1804.03602.

[125] P. Meade, N. Seiberg and D. Shih, *General Gauge Mediation*, Prog. Theor. Phys. Suppl. **177** (2009) 143, ed. by T. Takayanagi and S. Yahikozawa, arXiv: 0801.3278.

[126] *Luminosity determination in pp collisions at $\sqrt{s}$ = 13 TeV using the ATLAS detector at the LHC*, tech. rep., CERN, 2019, URL: https://cds.cern.ch/record/2677054.

[127] J. Alwall et al., *The automated computation of tree-level and next-to-leading order differential cross sections, and their matching to parton shower simulations*, JHEP **07** (2014) 079, arXiv: 1405.0301.

[128] T. Sjöstrand et al., *An introduction to PYTHIA 8.2*, Comput. Phys. Commun. **191** (2015) 159, arXiv: 1410.3012.

[129] *ATLAS Pythia 8 tunes to 7 TeV data*, tech. rep., CERN, 2014, URL: https://cds.cern.ch/record/1966419.

[130] L. Lönnblad and S. Prestel, *Merging Multi-leg NLO Matrix Elements with Parton Showers*, JHEP **03** (2013) 166, arXiv: 1211.7278.

[131] W. Beenakker, R. Hopker, M. Spira and P. M. Zerwas, *Squark and gluino production at hadron colliders*, Nucl. Phys. B **492** (1997) 51, arXiv: hep-ph/9610490.

[132] A. Kulesza and L. Motyka, *Threshold resummation for squark-antisquark and gluino-pair production at the LHC*, Phys. Rev. Lett. **102** (2009) 111802, arXiv: 0807.2405.

[133] A. Kulesza and L. Motyka, *Soft gluon resummation for the production of gluino-gluino and squark-antisquark pairs at the LHC*, Phys. Rev. D **80** (2009) 095004, arXiv: 0905.4749.

[134] W. Beenakker et al., *Soft-gluon resummation for squark and gluino hadroproduction*, JHEP **12** (2009) 041, arXiv: 0909.4418.

[135] W. Beenakker et al., *Squark and Gluino Hadroproduction*, Int. J. Mod. Phys. A **26** (2011) 2637, arXiv: 1105.1110.

[136] B. Fuks, M. Klasen, D. R. Lamprea and M. Rothering, *Gaugino production in proton-proton collisions at a center-of-mass energy of 8 TeV*, JHEP **10** (2012) 081, arXiv: 1207.2159.

[137] B. Fuks, M. Klasen, D. R. Lamprea and M. Rothering, *Precision predictions for electroweak superpartner production at hadron colliders with Resummino*, Eur. Phys. J. C **73** (2013) 2480, arXiv: 1304.0790.

[138] B. Fuks, M. Klasen, D. R. Lamprea and M. Rothering, *Revisiting slepton pair production at the Large Hadron Collider*, JHEP **01** (2014) 168, arXiv: 1310.2621.

[139] E. Bothmann et al., *Event Generation with Sherpa 2.2*, SciPost Phys. **7** (2019) 034, arXiv: 1905.09127.

[140] *Multi-Boson Simulation for 13 TeV ATLAS Analyses*, tech. rep., CERN, 2016, URL: https://cds.cern.ch/record/2119986.

[141] R. D. Ball et al., *Parton distributions for the LHC Run II*, JHEP **04** (2015) 040, arXiv: 1410.8849.

[142] P. Nason, *A New method for combining NLO QCD with shower Monte Carlo algorithms*, JHEP **11** (2004) 040, arXiv: hep-ph/0409146.

[143] S. Frixione, P. Nason and C. Oleari, *Matching NLO QCD computations with Parton Shower simulations: the POWHEG method*, JHEP **11** (2007) 070, arXiv: 0709.2092.

[144] S. Alioli, P. Nason, C. Oleari and E. Re, *A general framework for implementing NLO calculations in shower Monte Carlo programs: the POWHEG BOX*, JHEP **06** (2010) 043, arXiv: 1002.2581.

[145] D. de Florian et al., *Handbook of LHC Higgs Cross Sections: 4. Deciphering the Nature of the Higgs Sector*, **2/2017** (2016), arXiv: 1610.07922.

[146] C. Anastasiou et al., *High precision determination of the gluon fusion Higgs boson cross-section at the LHC*, JHEP **05** (2016) 058, arXiv: 1602.00695.

[147] C. Anastasiou, C. Duhr, F. Dulat, F. Herzog and B. Mistlberger, *Higgs Boson Gluon-Fusion Production in QCD at Three Loops*, Phys. Rev. Lett. **114** (2015) 212001, arXiv: 1503.06056.

[148] F. Dulat, A. Lazopoulos and B. Mistlberger, *iHixs 2 — Inclusive Higgs cross sections*, Comput. Phys. Commun. **233** (2018) 243, arXiv: 1802.00827.

[149] J. Pumplin et al., *New generation of parton distributions with uncertainties from global QCD analysis*, JHEP **07** (2002) 012, arXiv: hep-ph/0201195.

[150] ATLAS Collaboration, G. Aad et al., *Measurement of the Z/γ^* boson transverse momentum distribution in pp collisions at $\sqrt{s} = 7$ TeV with the ATLAS detector*, JHEP **09** (2014) 145, arXiv: 1406.3660.

[151] *Modelling of the $t\bar{t}H$ and $t\bar{t}V$ ($V = W, Z$) processes for $\sqrt{s} = 13$ TeV ATLAS analyses*, tech. rep., CERN, 2016, URL: https://cds.cern.ch/record/2120826.

[152] M. Beneke, P. Falgari, S. Klein and C. Schwinn, *Hadronic top-quark pair production with NNLL threshold resummation*, Nucl. Phys. B **855** (2012) 695, arXiv: 1109.1536.

[153] M. Cacciari, M. Czakon, M. Mangano, A. Mitov and P. Nason, *Top-pair production at hadron colliders with next-to-next-to-leading logarithmic soft-gluon resummation*, Phys. Lett. B **710** (2012) 612, arXiv: 1111.5869.

[154] P. Bärnreuther, M. Czakon and A. Mitov, *Percent Level Precision Physics at the Tevatron: First Genuine NNLO QCD Corrections to $q\bar{q} \to t\bar{t} + X$*, Phys. Rev. Lett. **109** (2012) 132001, arXiv: 1204.5201.

[155] M. Czakon and A. Mitov, *NNLO corrections to top-pair production at hadron colliders: the all-fermionic scattering channels*, JHEP **12** (2012) 054, arXiv: 1207.0236.

[156] M. Czakon and A. Mitov, *NNLO corrections to top pair production at hadron colliders: the quark-gluon reaction*, JHEP **01** (2013) 080, arXiv: 1210.6832.

[157] M. Czakon, P. Fiedler and A. Mitov, *Total Top-Quark Pair-Production Cross Section at Hadron Colliders Through $O(\alpha_S^4)$*, Phys. Rev. Lett. **110** (2013) 252004, arXiv: 1303.6254.

[158] M. Czakon and A. Mitov, *Top++: A Program for the Calculation of the Top-Pair Cross-Section at Hadron Colliders*, Comput. Phys. Commun. **185** (2014) 2930, arXiv: 1112.5675.

[159] C. Anastasiou, L. J. Dixon, K. Melnikov and F. Petriello, *High precision QCD at hadron colliders: Electroweak gauge boson rapidity distributions at NNLO*, Phys. Rev. D **69** (2004) 094008, arXiv: hep-ph/0312266.

[160] G. Avoni et al., *The new LUCID-2 detector for luminosity measurement and monitoring in ATLAS*, JINST **13** (2018) P07017.

[161] ATLAS Collaboration, M. Aaboud et al., *Jet energy scale measurements and their systematic uncertainties in proton-proton collisions at $\sqrt{s} = 13$ TeV with the ATLAS detector*, Phys. Rev. D **96** (2017) 072002, arXiv: 1703.09665.

[162] S. Dittmaier et al., *Handbook of LHC Higgs Cross Sections: 2. Differential Distributions*, (2012), arXiv: 1201.3084.

[163] *Reproducing searches for new physics with the ATLAS experiment through publication of full statistical likelihoods*, tech. rep., CERN, 2019, URL: https://cds.cern.ch/record/2684863.

[164] M. Baak et al., *HistFitter software framework for statistical data analysis*, Eur. Phys. J. C **75** (2015) 153, arXiv: 1410.1280.

[165] G. Cowan, K. Cranmer, E. Gross and O. Vitells, *Asymptotic formulae for likelihood-based tests of new physics*, Eur. Phys. J. C **71** (2011) 1554, [Erratum: Eur.Phys.J.C 73, 2501 (2013)], arXiv: 1007.1727.

[166] A. L. Read, *Presentation of search results: The CL(s) technique*, J. Phys. G **28** (2002) 2693.

[167] ATLAS Collaboration, M. Aaboud et al., *Search for pair production of higgsinos in final states with at least three b-tagged jets in $\sqrt{s}$ = 13 TeV pp collisions using the ATLAS detector*, Phys. Rev. D **98** (2018) 092002, arXiv: 1806.04030.

[168] ATLAS Collaboration, G. Aad et al., *Search for charginos and neutralinos in final states with two boosted hadronically decaying bosons and missing transverse momentum in pp collisions at $\sqrt{s}$ = 13 TeV with the ATLAS detector*, Phys. Rev. D **104** (2021) 112010, arXiv: 2108.07586.

[169] *Searches for new phenomena in events with two leptons, jets, and missing transverse momentum in 139 fb^{-1} of $\sqrt{s}$ = 13 TeV pp collisions with the ATLAS detector*, tech. rep., 2022, arXiv: 2204.13072.

[170] *SUSY Summary Plots March 2022*, (2022), URL: http://cds.cern.ch/record/2805985.

[171] A. Czarnecki and W. J. Marciano, *The Muon anomalous magnetic moment: A Harbinger for 'new physics'*, Phys. Rev. D **64** (2001) 013014, arXiv: hep-ph/0102122.

[172] ATLAS Collaboration, G. Aad et al., *Search for electroweak production of charginos and sleptons decaying into final states with two leptons and missing transverse momentum in $\sqrt{s}$ = 13 TeV pp collisions using the ATLAS detector*, Eur. Phys. J. C **80** (2020) 123, arXiv: 1908.08215.

[173] ATLAS Collaboration, G. Aad et al., *Search for direct pair production of sleptons and charginos decaying to two leptons and neutralinos with mass splittings near the W-boson mass in $\sqrt{s}$ = 13 TeV pp collisions with the ATLAS detector*, (2022), arXiv: 2209.13935.

[174] ATLAS Collaboration, G. Aad et al., *Searches for electroweak production of supersymmetric particles with compressed mass spectra in $\sqrt{s}$ = 13 TeV pp collisions with the ATLAS detector*, Phys. Rev. D **101** (2020) 052005, arXiv: 1911.12606.

[175] *Formulae for Estimating Significance*, (2020), URL: http://cds.cern.ch/record/2736148.

[176] C. G. Lester and B. Nachman, *Bisection-based asymmetric M_{T2} computation: a higher precision calculator than existing symmetric methods*, JHEP **03** (2015) 100, arXiv: 1411.4312.

[177] ATLAS Collaboration, G. Aad et al., *Search for direct production of charginos, neutralinos and sleptons in final states with two leptons and missing transverse momentum in pp collisions at $\sqrt{s}$ = 8 TeV with the ATLAS detector*, JHEP **05** (2014) 071, arXiv: 1403.5294.